Experimentelle Physik

Energy calibration and stability monitoring of the KATRIN experiment

Inaugural-Dissertation
zur Erlangung des Doktorgrades der Naturwissenschaften
im Fachbereich Physik
der Mathematisch-Naturwissenschaftlichen Fakultät
der Westfälischen Wilhelms-Universität Münster

vorgelegt von
Stephan Bauer
aus Münster

–2013–

Westfälische
Wilhelms-Universität
Münster

Dekan:	**Prof. Dr. M. Donath**
Erster Gutachter:	**Prof. Dr. C. Weinheimer**
Zweiter Gutachter:	**Prof. Dr. J. P. Wessels**
Tag der mündlichen Prüfung:	**31.01.2014**
Tag der Promotion:	**31.01.2014**

Abstract

Neutrino oscillation experiments have shown, that neutrinos are not massless, but they are not able to determine the neutrino mass values. Since the masses of neutrinos are very important for astrophysics and cosmology as well as for particle and nuclear physics, several experiments try to determine their mass. A direct and model independent way to determine the average electron neutrino mass (m_{ν_e}) is to measure the β-decay spectrum in its endpoint region. Choosing tritium as β-emitter in combination with an electric retarding spectrometer of the MAC-E filter type provides the lowest upper limit for the neutrino mass measured in an laboratory experiment up to now. This limit of about 2 eV was measured independently at Mainz and Troitsk. In order to improve the sensitivity by one order of magnitude the experiment has to be improved by two orders of magnitude, because the measured value is the squared neutrino mass. This will be realized with the **KA**rlsruhe **TRI**tium **N**eutrino experiment (KATRIN) which will measure the neutrino mass with a sensitivity of 200 meV (90% C.L.). KATRIN will measure the energy of β-decay electrons emitted in a **W**indowless **G**aseous **T**ritium **S**ource (WGTS) with the help of a tandem set-up of MAC-E filter spectrometers. A double-layered wire electrode system will screen the electron flux of the source from secondary electrons generated in the vessel hull by cosmic muons and radioactivity in the materials. The wire electrode system is connected to a multichannel high voltage distribution system which provides up to 48 different voltages. This system was installed at the KATRIN experiment and integrated in the slow control system within this work. In order to achieve the necessary sensitivity the retarding potential of −18.6 kV has to be monitored with a precision of at least 3 ppm (≈ 60 mV) for each two months measurement interval. Several aspects of the energy calibration and stability monitoring of the KATRIN experiment were covered within this work. On the one hand the ppm stability of the redundant monitoring concept of the retarding potential could be demonstrated with the high precision KATRIN voltage dividers and the ion implanted ^{83}Rb/^{83m}Kr sources operated at the KATRIN Monitor Spectrometer. These ppm-class high voltage dividers (developed in cooperation with the Physikalisch Technische Bundesanstalt) are calibrated by different methods and the results of these measurements are presented. On the other hand important work for a second calibration source, the condensed ^{83m}Kr conversion electron source (CKrS) in the KATRIN beam line, has been done within this work: A novel ellipsometry variant has been developed in order to characterize film properties for a condensed ^{83m}Kr calibration source. With this ellipsometry variant it was possible to obtain the optical properties of **H**ighly **O**rdered **P**yrolytic **G**raphite (HOPG) and quench-condensed krypton. The results are in good agreement with values found in literature. The condensed krypton calibration source was also redesigned to meet the technical constraints at the cryogenic pumping section and to allow for an absolute calibration of the KATRIN experiment. The design is ready to be build and tested in the laboratory of the Institut für Kernphysik Münster. The interplay of all these methods for calibration and stability monitoring is able to provide the required accuracy needed for the high sensitivity of the KATRIN experiment.

Zusammenfassung

Neutrinooszillations Experimente haben gezeigt, dass Neutrinos nicht masselos sind aber sie sind nicht in der Lage die absolute Neutrinomasse zu bestimmen. Da die Massen der Neutrinos sehr wichtig für die Astrophysik und Kosmologie sowie für die Kern- und Teilchenphysik sind, versuchen verschiedene Experimente diese zu bestimmen. Eine direkte und modellunabhängige Möglichkeit, die durchschnittliche Elektronneutrino Masse (m_{ν_e}) zu bestimmen, ist das β-Spektrum in seinem Endpunktbereich zu vermessen. Die Kombination eines elektrostatischen Retardierungspektrometer vom MAC-E Filter Typ zusammen mit Tritium als β-Strahler erbringt bis heute die sensitivsten Obergrenzen für die Neutrinomasse. Die aktuelle Grenze liegt bei 2 eV und wurde unabhängig in Mainz und Troisk gemessen. Um die Sensitivität um eine Größenordnung zu erhöhen ist es nötig das Experiment um zwei Größenordnungen zu verbessern, da die Messgröße das Neutrinomassenquadrat ist. Dies wird durch das **KA**rlsruhe **TRI**tium **N**eutrino Experiment (KATRIN) realisiert, welches die Neutrinomasse mit einer Senistivität von 200 meV (90% C.L.) messen wird. KATRIN wird die Energie der β-Zerfallselektronen aus einer fensterlosen gasförmigen Tritiumquelle (WGTS) mithilfe eines Tandemaufbaus bestehend aus zwei MAC-E Filter Spektrometern messen. Ein zweilagiges Drahtelektrodensystem schirmt den Flussschlauch der Quelle von Sekundärelektronen ab, die in der Tankwand durch kosmische Myonen oder durch Radioaktivität im Material ausgelöst werden. Das Drahtelektrodensystem ist an einen Hochspannungsverteiler angeschlossen welcher bis zu 48 Spannungen bereit stellt. Dieses System wurde im Rahmen dieser Arbeit am KATRIN Experiment aufgebaut und in die Experimentsteuerung integriert. Um die hohe Sensitivität des KATRIN Experiments zu erreichen muss das Retardierungspotential von −18.6 kV mit einer Genauigkeit von mindestens 3 ppm (≈ 60 mV) innerhalb jedes zweimonatigen Messzyklus überwacht werden. Verschiedene Aspekte der Energiekalibrierung und der Stabilitätsüberwachung des KATRIN Experiments wurden in dieser Dissertation bearbeitet. Einerseits konnte die Funktionalität des redundanten Konzeptes zur Stabilitätsüberwachung mit den hochpräzisions KATRIN Spannungsteilern und den ionenimplantierten $^{83}Rb/^{83m}Kr$ Quellen am KATRIN Monitor Spektrometer demonstriert werden. Diese Spannungsteiler in der ppm-Klasse (entwickelt in Zusammenarbeit mit der Physikalisch Technischen Bundesanstalt) wurden mit unterschiedlichen Methoden kalibriert und die Ergebnisse dieser Messungen vorgestellt. Auf der anderen Seite wurden wichtige Vorbereitungen für eine zweite Kalibrationsquelle, der kondensierten ^{83m}Kr Konversionselektronen Quelle in der KATRIN Strahllinie, getroffen: Eine neue Ellipsometrievariante wurde entwickelt um Filmeigenschaften einer kondensierte Krypton Quelle (CKrS) zu bestimmen. Mit dieser Ellipsometrievariante war es möglich, die optischen Konstanten von **H**ighly **O**rdered **P**yrolytic **G**raphite (HOPG) und schockkondensiertem Krypton zu bestimmen, welche gut mit den Literaturwerten überein stimmen. Weiterhin wurde das Design der kondensierten Krypton Quelle überarbeitet, um den technischen Einschränkungen an der kryogenen Pumpstrecke zu genügen und damit eine Absolutkalibrierung des KATRIN Experiments zu erlauben. Das Design ist fertig und die Quelle kann im Institut für Kernphysik Münster aufgebaut und getestet werden. Das Zusammenspiel all dieser Methoden zur Energiekalibrierung und Stabilitätsüberwachung ist in der Lage, die geforderte Genauigkeit bereit zu stellen um die hohe Sensitivität des KATRIN Experiments zu erreichen.

Contents

Chapter 1

Neutrino physics

1.1 History of the neutrino

The history of the neutrino started when Chadwick discovered discrepancies in the β-decay spectrum. He expected a discrete spectrum like in a two-body decay, e.g. the α-decay. Instead he discovered a continuous spectrum overlain by a weak spectrum of discrete lines [Cha14].
This put the entire knowledge of energy and momentum conservation in question. In his famous letter to the "radiative ladies and gentlemen" Pauli proposed the existence of an electrical neutral spin 1/2 particle. This particle should be emitted together with the electron and thus the β-decay can be explained by a three body decay. With this new particle, which Pauli named "neutron", the continuous spectra of the β-decay could be described [Pau30]. After Chadwick discovered the particle which is nowadays known as the neutron in 1932 [Cha32], not only a new name but also the missing particle itself had to be found.

In 1934 Fermi was able to describe the β-decay as a three-body decay in theory. He came to the conclusion that the mass of the new particle, which he gave the name "neutrino", has to be zero or at least very small compared to the mass of an electron [Fer34]. Further he showed that the neutrino mass has a significant influence on the shape of the β-spectrum in the region of the endpoint. This will play an important role in the direct mass determination of the neutrino.

1.2 Discovery of the neutrino

It took another 22 years to detect the neutrino, and so to prove its existence. Reines and Cowan measured the cross section of the inverse β-decay

$$\overline{\nu}_e + p \rightarrow e^+ + n \tag{1.1}$$

with the "Poltergeist-experiment" [Cow56]. Tanks filled with liquid scintillator served as detector and Cd-loaded water as target for this experiment. This set-up was placed close to the reactor of the Savannah River Plant which provided the antineutrinos for the inverse β-decay. Via the capture of an antineutrino, a proton converts into a neutron and a positron. For the proof of this reaction characteristic signals were recorded. The prompt signal of the 511 keV photons caused by e^+e^--annihilation and some μs later the gamma rays due to the neutron capture in Cd were observed [Cow56].

The muon neutrino (ν_μ) was discovered by Lederman, Schwartz and Steinberger in 1962 during the investigation of the interaction of high energy particles with matter at the Brookhaven AGS (Alternating Gradient Syncrotron). The neutrinos from pion decay do not generate electrons but muons when interacting with matter [Led62]. Today we know that because of parity violation the dominant pion decay channel is into muons and muon neutrinos:

$$\pi^\pm \rightarrow \mu^\pm + \nu_\mu/\overline{\nu}_\mu\,. \tag{1.2}$$

After the discovery of the tau also a tau neutrino (ν_τ) was expected to exist. Finally in the year 2000 the DONUT experiment (Direct Observation of the NU Tau) at Fermilab could prove the existence of the third neutrino [Kod01]. A 800 GeV proton beam hit a tungsten target in order to generate a particle shower. This particle beam crossed many different shieldings before hitting an emulsion lead target. By crossing those different shields all particles except for the ν are stopped. Finally taus are produced by the interaction of the ν_τ with the emulsion lead target, which can only be produced by the ν_τ:

$$\nu_\tau + n \rightarrow p + \tau \,. \tag{1.3}$$

These taus were detected via their decay in the emulsion target. After the existence of all three neutrinos was proven, there was still the open question of their mass. The standard model assumes the neutrino to be massless but what if the neutrinos have a very small mass? Since the neutrino is the most abundant particle in the universe (336 relic neutrinos per cm^3 remained from the Big Bang) after the photons, it contributes to the dark matter and would have played an important role during structure formation in the early universe depending on the mass of the neutrinos. The following section will introduce the solar neutrino problem and neutrino oscillation which proved that neutrinos have a non-zero mass.

1.3 Solar neutrino problem and neutrino oscillation

The Homestake solar neutrino experiment was set up in order to measure the solar (electron) neutrino flux and to compare the measured flux with predictions from solar models. The measurements were carried out with a 615 t radiochemical detector filled with tetrachloroethylene (C_2Cl_4) in the Homestake mine. The underlying reaction to detect the neutrino flux is the neutrino capture of the chlorine $^{37}Cl(\nu_e, e^-)^{37}Ar$. The ^{37}Ar ($t_{1/2} = 50,5$d) was extracted by purging the liquid with gaseous helium. The activity of the ^{37}Ar was measured over 200-400 days and the whole experiment measured from 1970 to 1994. The average ^{37}Ar production rate during this period of time was [Dav96]:

$$0.482 \pm 0.042 \text{ atoms/day} \,.$$

This production rate and hence the solar neutrino flux was about one-third of the neutrino flux predicted by solar models. This large deficit made history as the "solar neutrino problem". During that time it was not obvious whether the solar models or the experiment were wrong. The answer to this solar neutrino problem was given during the famous Neutrino conference (Tokyo, Japan) in 1998, where the Super-Kamiokande Experiment announced first evidences for neutrino oscillation based on measurements of the atmospheric neutrino flux [Fuk98]. The experiment was done by observing final state leptons from charge interactions of the neutrinos with the nuclei. The flavor of the neutrino is determined by the flavor of the final state lepton, created in a 50 kt water Cherenkov detector located in the Kamioka mine in Japan. The analyzed data are consistent with a two-flavor ($\nu_\mu \leftrightarrow \nu_\tau$) neutrino oscillation.

In order to find a precise experimental proof of neutrino oscillation not only one flavor but all have to be measured. This great opportunity was given to the **S**udbury **N**eutrino **O**bservatory and the precise measurement of the solar neutrino flux [SC00]. The SNO experiment uses also a huge water Cherenkov detector like Super-Kamiokande but this time with 1 kt of heavy water (D_2O). Due to the neutrons of the deuterium three different reactions could be observed:

$$\begin{array}{lcll} \nu_e + d & \rightarrow & p + p + e^- & \text{charged current (CC)} \quad \Phi_{CC} = \Phi_e, \\ \nu_x + d & \rightarrow & p + n + \nu_x & \text{neutral current (NC)} \quad \Phi_{NC} = \Phi_e + \Phi_{\mu\tau}, \\ \nu_x + e^- & \rightarrow & \nu_x + e^- & \text{elastic scattering (ES)} \quad \Phi_{ES} = \Phi_e + 0.16 \cdot \Phi_{\mu\tau}. \end{array}$$

Thereby the electron neutrinos (Φ_e) can be measured via the charged current reaction and the total neutrino flux ($\Phi_e + \Phi_{\mu\tau}$) via the neutral current. The measured total ^{8}B solar neutrino flux agreed well with the flux predicted by the standard solar model (see figure 1) and neutrino oscillation was finally proven.

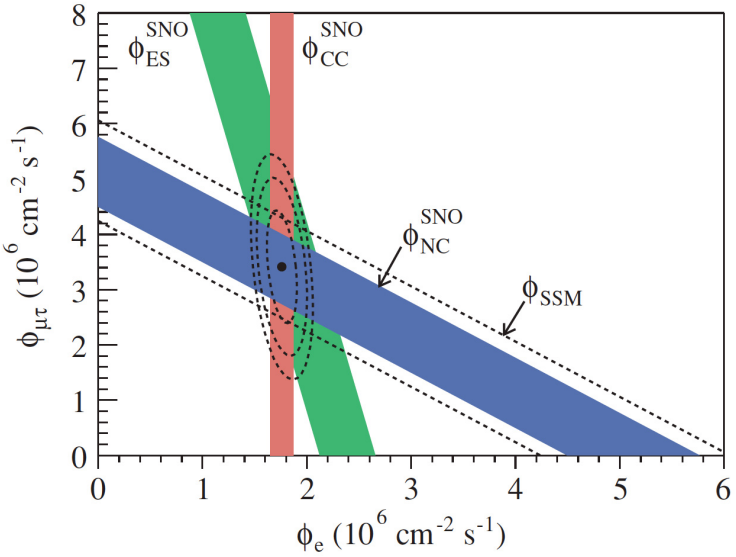

Figure 1: Results of the SNO phase 1 dataset. Shown is the flux of ^{8}B solar neutrinos that are μ or τ flavor vs. the flux of electron neutrinos. The prediction of the standard solar model (BP2000) is drawn as diagonal bands (dashed lines) and that measured with the NC reaction in SNO (solid blue band). The bands intersect at the fit values for Φ_e and $\Phi_{\mu\tau}$, indicating that the combined flux results are consistent with neutrino flavor oscillation. (Source: [SC07])

Since neutrino flavor oscillation is proven it is also proven that neutrinos have a non-zero mass. The reason for this will be shown in the following. If neutrinos are able to change their flavor they will be a superposition of a spectrum of mass eigenstates ν_i (probably more than three). Therefore the neutrino flavor $\alpha = e, \mu, \tau$ is a superposition of mass eigenstates:

$$\begin{pmatrix} \nu_e \\ \nu_\mu \\ \nu_\tau \end{pmatrix} = U \begin{pmatrix} \nu_1 \\ \nu_2 \\ \nu_3 \end{pmatrix} = \begin{pmatrix} U^*_{e1} & U^*_{e2} & U^*_{e3} \\ U^*_{\mu 1} & U^*_{\mu 2} & U^*_{\mu 3} \\ U^*_{\tau 1} & U^*_{\tau 2} & U^*_{\tau 3} \end{pmatrix} \begin{pmatrix} \nu_1 \\ \nu_2 \\ \nu_3 \end{pmatrix} \tag{1.4}$$

where U is the unitary PMNS[1] Matrix. This matrix contains three mixing angles (Θ_{ij}) and one complex phase (δ_D; Dirac-phase).

[1] Pontecorvo-Maki-Nakagawa-Sakata Matrix

A neutrino of a certain flavor α can be written as:

$$|\nu_\alpha\rangle = \sum_i U^*_{\alpha i} \, |\nu_i\rangle \ . \tag{1.5}$$

In order to see the time dependent development and hence the propagation through space of this neutrino with an energy (E_i), one has to apply Schrödinger's equation to the mass eigenstates ν_1:

$$|\nu_i(t)\rangle = e^{-iE_i t} \, |\nu_i(t=0)\rangle \ . \tag{1.6}$$

Therefore follows the presentation of a neutrino flavor in the base of its mass eigenstates:

$$|\nu_\alpha(t)\rangle = \sum_i U^*_{\alpha i} \, e^{-iE_i t} \, |\nu_i\rangle \ . \tag{1.7}$$

For extremely relativistic neutrinos ($p >> m_\mathrm{i}$) the following relations for the distance L and the energy E_i hold:

$$t \approx L \tag{1.8}$$

$$E_i \approx E + \frac{m_i^2}{2E} \, , \tag{1.9}$$

where E is the average energy of the mass eigenstates of the neutrino.

The probability to detect a neutrino with the flavor β, which was originally generated with the flavor α, is [Kay08]:

$$\begin{aligned} P(\nu_\alpha \to \nu_\beta) &= |\langle \nu_\beta | \nu_\alpha(t) \rangle|^2 \\ &= \ \delta_{\alpha\beta} \\ &\quad - 4 \sum_{i>j} \Re(U^*_{\alpha i} U_{\beta i} U_{\alpha j} U^*_{\beta j}) \sin^2 \left(1.27 \Delta m^2_{ij} \frac{L}{E} \right) \\ &\quad + 2 \sum_{i>j} \Im(U^*_{\alpha i} U_{\beta i} U_{\alpha j} U^*_{\beta j}) \sin \left(2.54 \Delta m^2_{ij} \frac{L}{E} \right) , \end{aligned} \tag{1.10}$$

where L is the travelled distance in km, E is the energy in GeV and $\Delta m^2_{ij} = |m_i^2 - m_j^2|$ is the difference in squared neutrino mass in eV^2. This shows that the probability to detect a neutrino flavor different from the original one depends on the difference in squared neutrino mass (Δm^2_{ij}) and that this probability would vanish if all of the neutrinos would have no mass [Kay08].

For the more simple case of a two flavor mixing the PNMS matrix is replaced by a 2x2 matrix. The probability $P(\nu_e \to \nu_\mu)$ that an electron neutrino is detected as a muon neutrino is than given by:

$$\begin{aligned} P(\nu_e \to \nu_\mu) = & \left| \begin{pmatrix} 0 \\ 1 \end{pmatrix} U \begin{pmatrix} e^{-iE_1 t} & 0 \\ 0 & e^{-iE_2 t} \end{pmatrix} U^{-1} \begin{pmatrix} 1 \\ 0 \end{pmatrix} \right|^2 \\ = & \sin^2(2\theta) \sin^2\left(\tfrac{\Delta m^2 L}{4E}\right) \qquad (1.11) \\ = & \sin^2(2\theta) \sin^2\left(\pi \tfrac{L}{\lambda_{\text{osc}}}\right) \quad \text{with} \quad \lambda_{\text{osc}} = \tfrac{4\pi E}{\Delta m^2}\,. \qquad (1.12) \end{aligned}$$

The principle of two flavor neutrino vacuum oscillation can be demonstrated by the propagation difference of the ordinary and extraordinary beam of a laser in a birefringent crystal [Wei10].

Unfortunately neutrino oscillation experiments can not give an absolute value on the neutrino mass but they can measure the three mixing angles (Θ_{ij}) and the Δm^2_{ij}. The recent values listed in the Particle Data Group Booklet [Ber12] are:

$$\begin{aligned} \Delta m^2_{21} &= 7.50^{+0.19}_{-0.20} \cdot 10^{-5}\ \text{eV}^2 \\ \Delta m^2_{32} &= 2.32^{+0.12}_{-0.08} \cdot 10^{-3}\ \text{eV}^2 \end{aligned}$$

$$\begin{aligned} \sin^2(2\Theta_{12}) &= 0.857^{+0.023}_{-0.025} \\ \sin^2(2\Theta_{23}) &> 0.95 \\ \sin^2(2\Theta_{13}) &= 0.095 \pm 0.01 \end{aligned}$$

These values do not give any hint about the absolute value of the neutrino mass or about the "hierarchy", which describes the order of the mass eigenstates. In principle there are two different possible hierarchies. The first one know as the "normal hierarchy", where $m_1 < m_2 < m_3$ and secondly the "inverted hierarchy" where $m_3 < m_1 < m_2$. The fact that $m_1 < m_2$ is given by the neutrino oscillation in matter (MSW effect[2]), which assumes that $\Delta m^2_{21} = m_2^2 - m_1^2$ is positive and hence $m_2^2 > m_1^2$.

1.4 Determination of the neutrino mass

Since neutrino oscillation experiments showed that neutrinos have a non-zero mass, the absolute mass of the neutrinos is still to be determined. The knowledge of the neutrino masses will give answers to many fields in physics, for example to cosmology and structure formation in the early universe or the mass generation of particle in the standard model

[2] Mikheyev–Smirnov–Wolfenstein effect

beyond the Higgs mechanism. This section will briefly present the different opportunities to determine the masses and is mainly based on [Wei13] and [Dre13]. The focus will be on the direct determination of the neutrino mass since this is the aim of the KATRIN experiment which will be presented in chapter 2.

1.4.1 Neutrino mass from cosmology

Neutrino masses obtained from cosmology are model dependent and therefore no replacement for a distinguished experiment. These models give limits on the sum of all three neutrino mass states by different probes, as for example the cosmic microwave background (CMB), galaxy distribution or supernovae. These constrains span a large region on upper limits for $\sum m(\nu_\mathrm{i})$ but the majority of them is in the order of less than a few 100 meV [Aba11].

1.4.2 Neutrino mass from neutrinoless double beta decays

Some nuclei can only decay via two simultaneous β-decays into a nucleus with higher binding energy. This decay is the double β-decay and is experimentally proven for the case that two neutrinos are emitted. For a neutrinoless double β^--decay ($0\nu\beta\beta$) the antineutrino from one decay vertex is absorbed as neutrino at the other decay vertex:

$$(Z, A) \longrightarrow (Z + 2, A) + 2\,\mathrm{e}^- \,. \tag{1.13}$$

This process assumes that the neutrino is its own antiparticle ("Majorana paricle"). This process will violate lepton number conservation and is therefore forbidden in the standard model of particle physics [Wei13]. For the neutrinoless double β-decay the decay rate will be proportional to the absolute square of the so-called effective Majorana neutrino mass (M^2_ee) [Dre13]:

$$\Gamma_{0\nu\beta\beta} \propto \left| \sum U^2_\mathrm{ei}\, m(\nu_\mathrm{i}) \right|^2 := m^2_\mathrm{ee} \tag{1.14}$$

where Majorana-phases appear in the U_ei for Majorana neutrinos and could cause partial cancellation. For the search of neutrinoless double β-decay the most common arrangement is the "detector = source" arrangement. For such a set-up the double β-decay nuclei are integrated in the detector. This kind of experiments are for example the GERDA experiment [Ack13] and MAJORANA experiment [Phi12] using ^{76}Ge or KamLAND-Zen [Gan12] and EXO-200 [Aug12] using ^{136}Xe. An update on the already mentioned SNO experiment is the SNO+ experiment [Che08] using ^{150}Nd.

A different approach is to use a source separated from the detector. This is for example done for the NEMO3 experiment [Sim12].

1.4.3 Direct mass determination

The previous mentioned methods to determine the neutrino mass are strongly model dependent or assume that the neutrino is a Majorana particle and depend on Majorana-phases. The direct and model independent neutrino mass determination can be realized by investigations of the endpoint region of the β-spectrum. By this only energy and momentum conservation is used to determine the "average electron neutrino mass squared" $m^2(\nu_\mathrm{e})$ [Ott08]:

$$m^2(\nu_\mathrm{e}) := \sum |U_\mathrm{ei}^2| m^2(\nu_\mathrm{i})\,. \tag{1.15}$$

Beta spectrum

At the β^- decay the nucleus (Z, A) decays into a daughter nucleus $(Z+1, A)$ and emits an electron (e^-) and an electron antineutrino $(\overline{\nu}_e)$:

$$(Z, A) \longrightarrow (Z+1, A) + \mathrm{e}^- + \overline{\nu}_\mathrm{e}\,. \tag{1.16}$$

Following Fermis golden rule, the transition rate within a time interval dt and an energy interval between E and $E + dE$ can be derived by the use of the phase-space density $\rho(E)$ and the nuclear matrix element M [Wei03]:

$$\frac{d^2N}{dtdE} = \frac{d\dot{N}}{dE} = \frac{2\pi}{\hbar}\left|M^2\right|\rho\,(E)\ . \tag{1.17}$$

As presented in [Wei03] one obtains for the β-spectrum, neglecting the nuclear recoil energy:

$$\frac{d\dot{N}}{dE} = R\,(E)\sqrt{(E_0 - E)^2 - m_{\nu_\mathrm{e}}^2 c^4}\;\Theta\left(E_0 - E - m_{\nu_\mathrm{e}}c^2\right) \tag{1.18}$$

with

$$R\,(E) = \frac{G_F^2}{2\pi^3\hbar^7 c^5}\cos^2(\theta_C)\,|M|^2\,F\,(Z+1, E)\,p\left(E + m_\mathrm{e}c^2\right)(E_0 - E)\,. \tag{1.19}$$

In this context is:

G_F	the Fermi coupling constant,
θ_C	the Cabibbo angle,
M	the nuclear matrix element,
F	the Fermi function,
p	the momentum of the electron,
E	the kinetic energy of the electron,
E_0	the endpoint of the β-spectrum (maximum electron energy for $m_\nu = 0$),
$m_\mathrm{e}c^2$, $m_{\nu_\mathrm{e}}c^2$	the rest energy of the electron and the electron antineutrino.

The energy conservation is ensured by the Heaviside step function $\Theta\left(E_0 - E - m_{\nu_e}c^2\right)$. The Fermi function describes the Coulomb interaction between the electron and the daughter nucleus. The neutrino mass affects the spectrum only by the phase space factor:

$$p_\nu = \sqrt{\left(E_0 - E\right)^2 - m_{\nu_e}^2 c^4}\,.$$

The influence of the neutrino mass is more significant for electron energies closer to the endpoint energy of the spectrum. Thus the measurement of the β-spectrum is ideal for the direct measurement of the neutrino mass. This consideration neglects influences caused by the finite mass of the nucleus, orbital electrons as well as the influence of additional atoms like inside a molecule as it is the case for tritium T_2. A detailed consideration of these effects is presented in [Dre13].

For the direct neutrino mass determination isotopes with low endpoint energies are favoured. From the theoretical point of view the absolute endpoint energy does not matter but since the mass has to be determined experimentally this value plays an important role. The endpoint region of the spectrum has to be measured with high accuracy (see figure 2) which is more feasible for lower energies than higher ones. Since the total count rate will increase and the relative fraction in the last eV will decrease, electrons which energies are not in the endpoint region could cause additional background. Also the energy resolution (ΔE) will be much higher at lower E_0. All this favors β-emitters with low endpoint energies [Dre13].

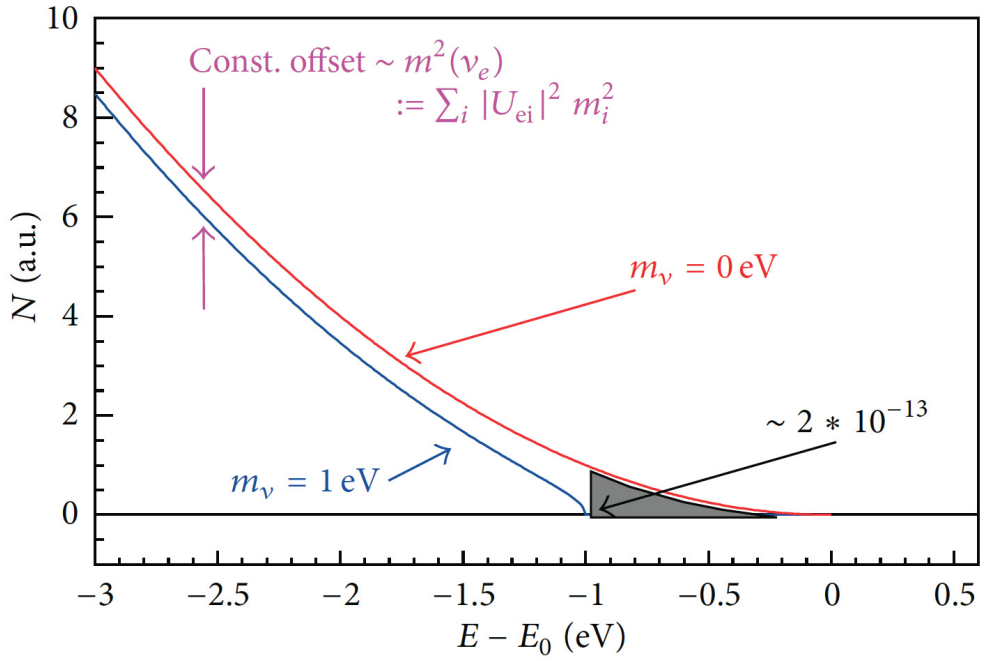

Figure 2: Endpoint region of the β-spectrum for an allowed or superallowed β-decay. The plot shows the spectrum for a zero neutrino mass (red line) and for an arbitrary chosen neutrino mass of 1 eV (blue line). The gray shaded area denotes the amount of decay electrons which are in the last 1 eV of the spectrum for zero neutrino mass. In the case of tritium this fraction is $2 \cdot 10^{-13}$ of all β-decays. (Source: [Dre13])

The β-emitter with the lowest endpoint energy is ^{187}Re ($E_0(^{187}Re) = 2.47\,\mathrm{keV}$), but it also implicates two significant disadvantages. The half-life of ^{187}Re is in the order of 10^{10} years and exhibits a complicated electronic structure which makes it unsuitable for the measurement with an integration spectrometer (like the MAC-E filter of the KATRIN experiment). This problems can be circumvent to some extend by measurements with cryo-bolometers which is the aim of the MARE project [Mon06]. Recently the ECHo experiment, that wants to measure the electronic de-excitation spectrum after the electron capture of ^{163}Ho, which exhibits a similar phase space spectrum at the upper end as figure 2, gets a lot of attention [Bla13].

The isotope with the second lowest endpoint energy is tritium with $E_0(T_2) = 18.6\,\mathrm{keV}$. Tritium offers with its half-life of 12.3 years reasonable count rates without having huge amounts of tritium. Its supperallowed shape of the β-spectrum and its simple electronic structure allow the tritium β-spectrum to be measured with small systematic uncertainties [Dre13].

The most recent upper limits on the neutrino mass are determined with MAC-E filters measuring the tritium β-decay. These limits were obtained independently in Mainz and Troitsk:

$$\begin{aligned} &\text{Mainz: } m_\nu < 2.3\,\mathrm{eV/c^2} \quad (95\%\text{C.L.}) \text{ [Kra05]} \\ &\text{Troisk: } m_\nu < 2.1\,\mathrm{eV/c^2} \quad (95\%\text{C.L.}) \text{ [Lob03]} \end{aligned}$$

A further improvement by one order of magnitude in sensitivity requires an improvement of these experiments by two orders of magnitude since the observable is $m^2(\nu_\mathrm{e})$. This is the aim of the KATRIN experiment, which wants to measure the neutrino mass with a sensitivity of 200 meV. This experiment uses the same type of spectrometer as the Mainz and Troisk group and will be presented in the next chapter.

1.5 Thesis outline

This thesis will have the following outline:

Chapter 2 will present how the KATRIN experiment is realized in order to determine the neutrino mass. The major subcomponents will be introduced and the basic concept of a MAC-E filter will be illustrated. Furthermore the statistical and systematic uncertainties will be described and an overview of the calibration and monitoring tasks will be given.

The complex high voltage system which will provide all necessary voltages for the main spectrometer of the KATRIN experiment will be presented in chapter 3.

The high voltage dividers custom developed for the KATRIN experiment will serve as one method of a redundant system for the stability monitoring. The design as well as the calibration and therefore the performance of these dividers will be presented in chapter 4.

The conversion electron lines of ^{83m}Kr and their use for the calibration of the KATRIN experiment will be introduced in Chapter 5. The KATRIN monitor spectrometer and measurements with ion implanted ^{83}Rb/^{83m}Kr will also be presented.

As a different approach for a calibration electron source the condensed krypton calibration source will be presented in chapter 6. An overview of the current set-up will be given and also the new design of the condensed krypton source at the cryogenic pumping section will be shown.

Due to technical constraints at the application of the condensed krypton source at the cryogenic pumping section a novel variant of reflection ellipsometry had to be developed and tested which will be shown in chapter 7.

Finally a conclusion and outlook will be given in chapter 8.

Chapter 2

The KATRIN experiment

2.1 Overview

The KATRIN experiment aims to determine the mass of the electron anti-neutrino or at least to give a new upper limit with a sensitivity of 200 meV ($c = 1$ throughout this thesis), which is one order of magnitude lower than the actual one (see section 1.4). The KATRIN experiment is located at the Karlsruhe Institute of Technologies (KIT). This location was chosen because the Tritium Laboratory Karlsruhe (TLK) has both a high degree of experience and the license for the use of the required amounts of tritium. To reach the desired sensitivity of 200 meV (90% C.L.)[KC04] at almost every part of the experiment one has to go to the limit of what is technically feasible. The experiment consist of a Windowless Gaseous Tritium Source (WGTS) as a high luminosity source of β-electrons, the transport section with its two pumping systems to reduce the tritium flow and a tandem set-up of spectrometers followed by the detector (see figure 3). This chapter will describe the major components of the KATRIN-experiment.

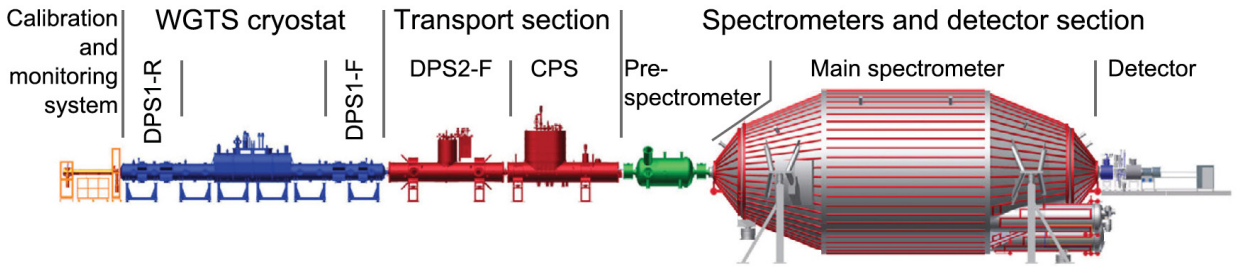

Figure 3: Overview of the KATRIN-experiment. The set-up is divided into three major parts. The WGTS as source, the transport section with the differential pumping section (DPS2-F) and the cryogenic pumping section (CPS) and the Spectrometer and detector section with the pre and main spectrometer and the detector. The calibration and monitoring system (rear section) for the source is placed at the rear side of the WGTS. The monitor spectrometer is not shown. (Source: [Bab12])

2.2 Rear section

The rear section is the first part of the KATRIN-experiment. It is located at the rear side of the WGTS (see section 2.3) and will be used to monitor several source parameters. Electrons with well-defined energies from an electron gun are used to investigate the transmission function of the main spectrometer and the inelastic scattering cross section inside the tritium source. The principle is based on the angular selective eGun which was tested at the former Mainz Neutrino Mass experiment [Kra05, Bec13] and is currently used for the commissioning of the main spectrometer. Also a detector will be installed to monitor the source activity and a so-called rear wall will control the plasma effects within the source [KC04].

2.3 Source and transport section

The source and transport section (STS) consists of the Windowless Gaseous Tritium Source as high luminosity source of β-decay electrons and two pumping sections DPS2-F and CPS. The pumping sections are designed to reduce the flux of tritium in the direction of the spectrometers by a factor of 10^{14}. The STS is followed by the pre-spectrometer (see section 2.4).

The Windowless Gaseous Tritium Source

The Windowless Gaseous Tritium Source (WGTS), shown in figure 4, will provide the high luminosity which is needed to reach the high statistical sensitivity of KATRIN. With a yearly throughput of 10 kg tritium, in a closed loop system. The column density of the WGTS for an inlet pressure $p_{\text{in}} = 3.4 \times 10^{-3}$ mbar and $T = 30$ K is $\rho d = 5 \times 10^{17}$ molecules/cm^2, corresponding to a total activity in the beam tube of 10^{11} Bq. The column density must be known with a precision of ±0.1 %[KC04].

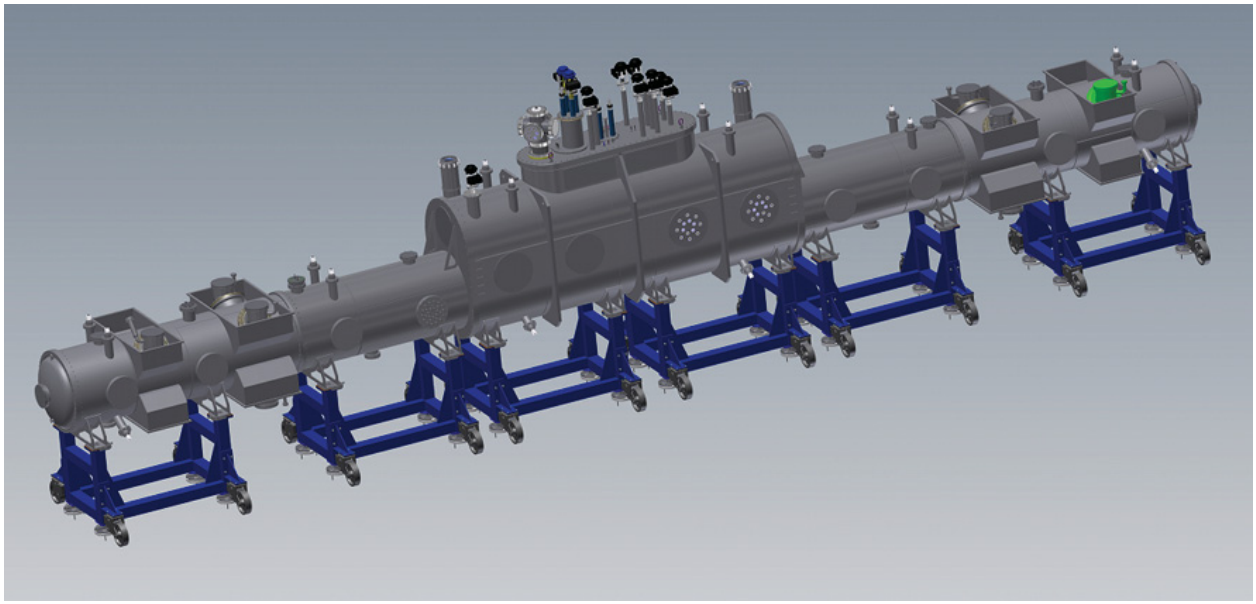

Figure 4: CAD drawing of the WGTS cryostat. The cryostat holds the 10 m long beam tube, with its surrounding superconducting magnets and also the first two differential pumping sections to pump the tritium back into the closed loop system.

The main part of the WGTS is a beam tube with a length of 10 m and a diameter of 90 mm which is cooled by a two-phase neon cooling system (see figure 6). With this cooling system the temperate of the beam tube is regulated by the pressure of the two-phase neon This beam tube is enclosed by superconducting solenoids with a field of 3.6 T (figure 5a). The tritium is injected in the middle of the beam tube. At both ends of the source the injected tritium is pumped back into the closed tritium loop by the differential pumping sections (DPS1-R and DSP1-F). Both first stage DPS systems are located inside the WGTS cryostat.

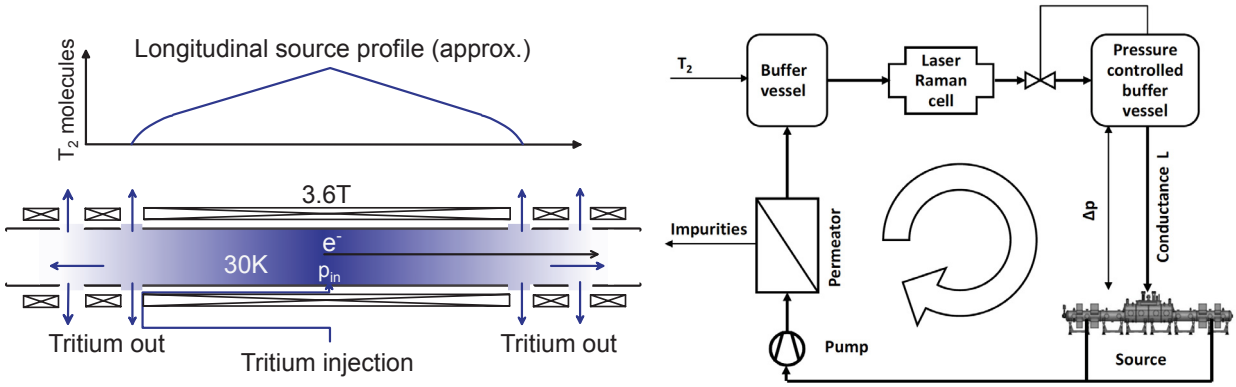

(a) (b)

Figure 5: WGTS schematic view on the left (Source: [KC04]). The tritium is injected in the center of the source tube. The longitudinal source profile (upper part of the left piture) is kept constant by continuously pumping out and injecting tritium. The right picture shows the simplified flow diagram of the inner tritium loop. (Source: [Stu11]).

In order not to exceed the required amount of the uncertainty budget which is requested, many operating parameters must be known with an accuracy of 10^{-3}. These are for example temperature, injection pressure, purity of tritium composition and activity. The tritium purity ($> 95\%$) will be monitored in-line by means of Laser-Raman spectroscopy [Bab12]. This so called LARA-System reached the required sensitivity of 0.1 % within a measurement period of 250 s [Fis12] and it is placed at the inner part of the closed loop (see figure 5b). Further investigations are ongoing and the measurement period will be reduced to less than 60 s [Fis14].

At a temperature of $T = 30\,\mathrm{K}$ the required temperature stability of the WGTS is $30\,\mathrm{mK\,h^{-1}}$ and will be measured by a system of PT500 and vapour pressure sensors. The behaviour of the system was tested with "Demonstrator", a system composed of the beam tube and a test cryostat. With this Demonstrator a stability of $1.5\,\mathrm{mK\,h^{-1}}$ could be achieved [Gro13].

The activity will be measured by three detectors. All operating parameters of the WGTS and their monitoring are summarized in [Bab12]. The use of a windowless source makes it necessary to reduce the flow of Tritium from the source to the spectrometers by a factor 10^{14}. This is achieved by differential and cryogenic pumping in the transport section which is described in the following sections.

Differential pumping section 2-F

The first stages of differential pumping are integrated into the WGTS. On the way down to the spectrometers a second differential pumping section follows. This is the DPS2-F, consisting of five segments of 1 m length surrounded by superconducting coils. Each of these five segments is installed with an angle of 20° to the next segment (see figure 7b) to avoid a direct line of sight for the tritium, whereas the electrons are guided by the magnetic field of the superconducting coils. Between these segments four pump ports are installed which are

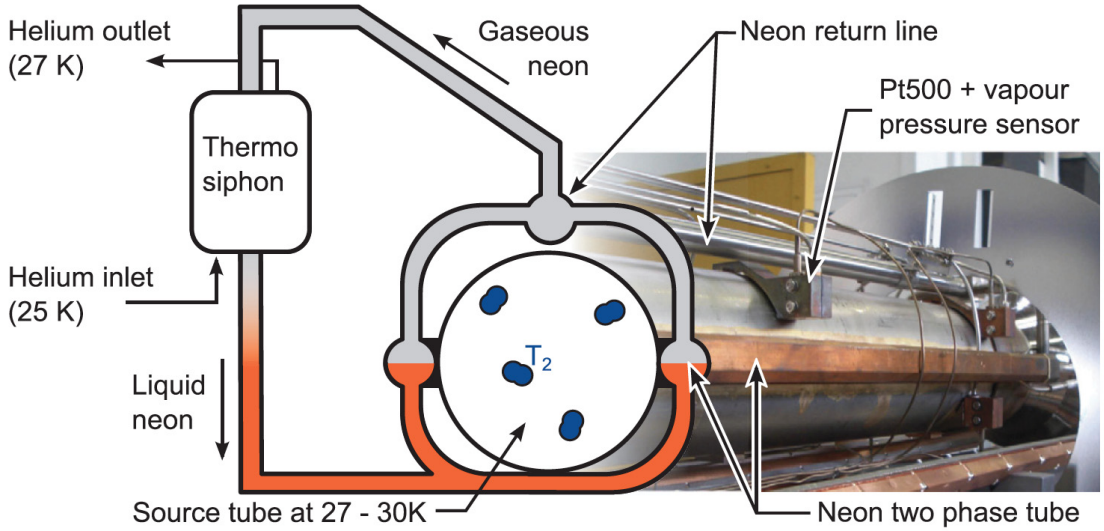

Figure 6: Principle of the two-phase neon cooling and picture of the WGTS-tube. The two-phase neon tubes are brazed to the source tube. The neon is cooled via thermo siphon by gaseous helium with a temperature of 25 K. The temperature can be regulated and stabilized via the pressure of the two-phase neon. The temperature is monitored by Pt500 and vapour pressure sensors. (Source: [Bab12])

equipped with four TURBOVAC MAG W 2800 turbo-molecular pumps (Leybold Vacuum) as primary pumps, with a pumping speed for He of 2400 L s^{-1} each. The **D**ifferential **P**umping **S**ection **2** in **F**orward direction (DPS2-F), is designed to have a reduction factor of 10^5. The reduction factor for DPS1-F and DPS2-F sums up to 10^7 [KC04]. After delivery of the DPS2-F intensive commissioning tests were performed. The reduction factor for tritium was interpolated based on the experimentally determined reduction factors for He, D_2, Ne, Ar and Kr to be :

$$R_{T_2} = (2.32 \pm 0.23_{sys} \pm 0.09_{fit}) \times 10^4 \quad \text{[Kos12]}$$

This is approximately a factor 4 smaller than the requested value from the Design Report. Possible explanations are discussed in [Kos12]. Unfortunately one of the protection circuits of the superconducting magnets broke during test. Because of a very complicated and cost-intensive repair, a new design of the DPS2-F was chosen. In this version the DPS2-F is not enclosed by a cryostat because of the use of five stand-alone, warm bore magnets. These magnets are cooled by liquid helium which is re-condensed by cryo-coolers. The new design is shown in figure 7.

Cryogenic pumping section

To reach the desired reduction factor of 10^{14} a **C**ryogenic **P**umping **S**ection (CPS) will reduce the tritium flow further by seven orders of magnitude. The basic concept of cryogenic pumping it to adsorb atoms on a cold surface. In order to increase the surface and thus

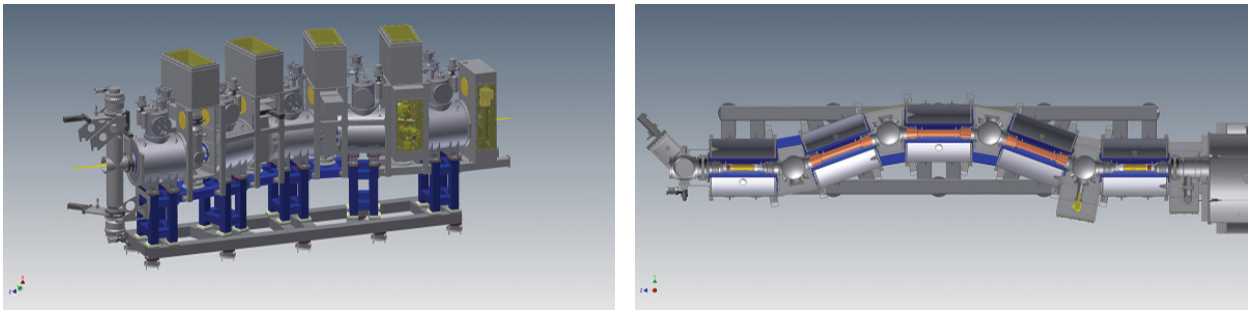

(a) (b)

Figure 7: CAD drawings of the new design of the DPS2-F. The left picture shows the side view of the DPS and its five magnets. A sectional view from the top is shown in the right picture. This new design uses five superconducting magnets cooled by liquid helium which is re-condensed by cryo-coolers.

the efficiency of pumping, the beam tube of the CPS will be covered by argon frost. This pre-condensed layer will be renewed monthly. The set-up is divided into seven sections and mainly consist of seven superconducting magnet modules, the beam tube, the cold gate valve V3, two pumping ports, and the cryogenic cooling system. The beam tube is bent in order to avoid a direct line of sight for tritium molecules as at the DPS (see figure 8). By this tritium is forced to hit the argon frost covered walls of the pumping section while the electrons are guided on the magnetic field lines through the CPS. The cold gate valve denotes the end of the tritium area and is used as barrier while refreshing the argon frost or if a failure occurs [Gil10].

The condensed krypton calibration source will be located at pump port 2 (P2 in fig. 8) at the CPS. It will immerse from the top of the CPS into the flux tube. The condensed krypton source at the CPS will be discussed in section 6.2.

2.4 Spectrometer

For the KATRIN-experiment three spectrometers, based on the principle of **M**agnetic **A**diabatic **C**ollimation combined with an **E**lectrostatic **Filter** (MAC-E-Filter [Pic92b]), are used. The pre and main spectrometer are working in a tandem set-up where the pre-spectrometer acts as a pre-filter to reduce the flux of electrons going into the main spectrometer. A third one, the so called monitor spectrometer (MoS), is used to monitor the energy stability by tracing the retarding voltage back to an atomic/nuclear standard. Before the spectrometers are presented, the principle of the MAC-E-Filter technique will be briefly introduced.

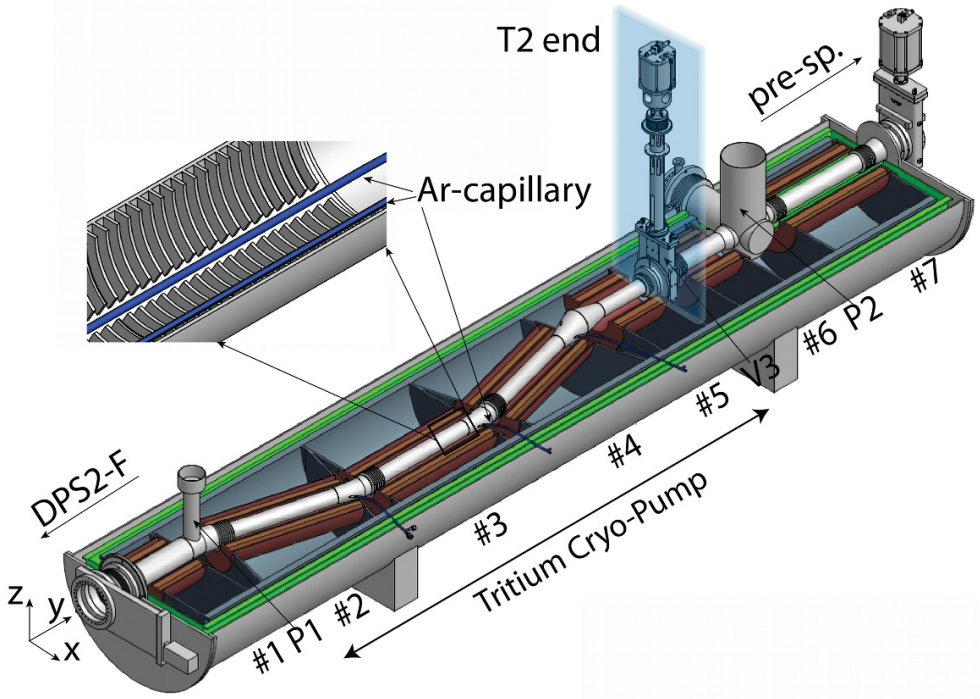

Figure 8: Sectional view of the CPS. The CPS beam tube consists of seven segments and is bend in order to avoid a direct line of sight for tritium. The signal electrons are guided by the magnetic field of the seven superconducting magnets (brown). The inset shows an enlargement of the beam tube and the argon capillaries (blue). The cold gate valve V3 denotes the end of the tritium area. (Source [Gil10]).

The principle of a MAC-E-Filter

The principle of a new high resolution spectrometer was proposed by Beamson et al. for photoelectron spectroscopy in 1980 [Bea80]. For this spectrometer two superconducting solenoids form an axial symmetric inhomogeneous magnetic field. The source is placed in the center of one solenoid and the detector in the other one. This magnetic field drops by orders of magnitude to the middle of the spectrometer. To describe the way of an electron through such a spectrometer the kinetic energy of an electron is split up into a longitudinal and a perpendicular component relative to the magnetic field direction:

$$E_{\mathrm{kin}} = E_{\perp} + E_{\parallel} \tag{2.1}$$

Where $E_{\perp} = E_{\mathrm{kin}} \cdot \sin^2 \Theta$ is the energy stored in the cyclotron motion, $E_{\parallel} = E_{\mathrm{kin}} \cos^2 \Theta$ is the energy along the guiding field and Θ is the angle between the velocity vector and the magnetic field. The cyclotron motion of the electron leads to a helical movement of the electron along the magnetic guiding field (see figure 9). The radius of that motion is given in non-relativistic limit by:

$$r_{\mathrm{cyc}} = \frac{\sqrt{2 \cdot m_{\mathrm{e}} \cdot E_{\perp}}}{e \cdot B} \,. \tag{2.2}$$

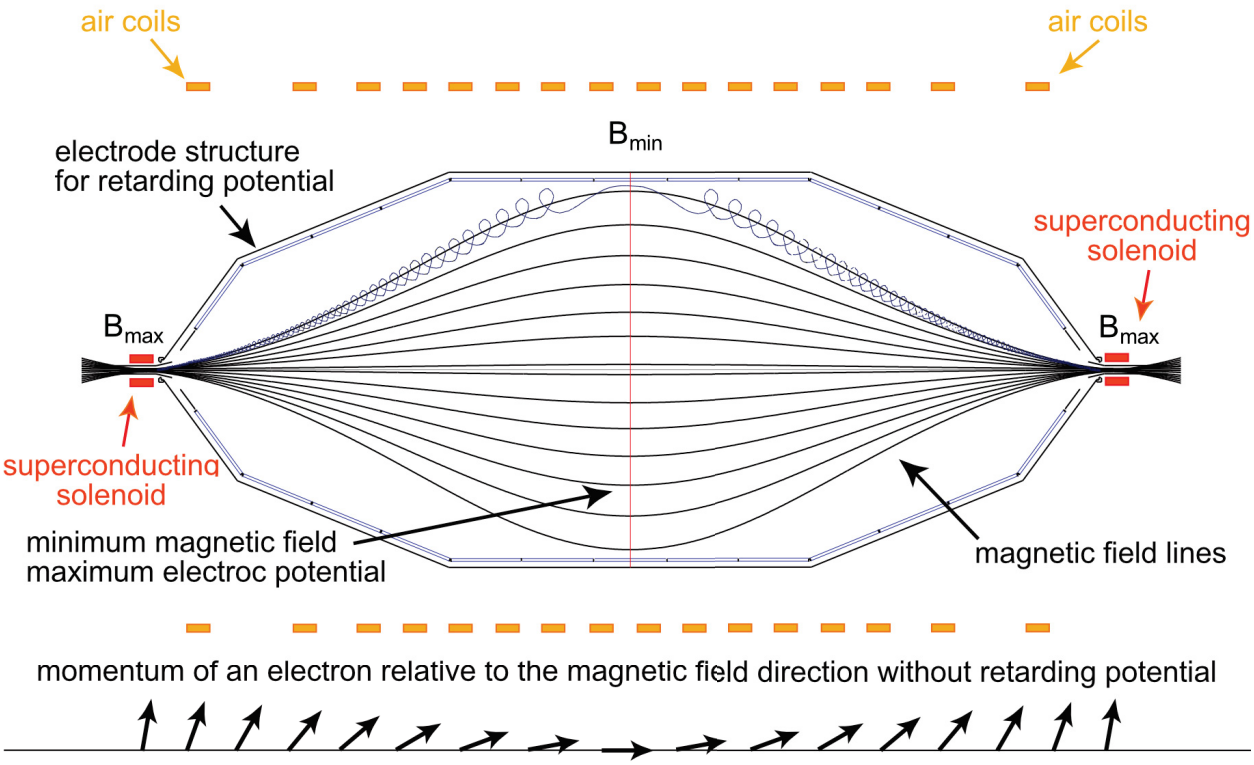

Figure 9: The principle of the MAC-E-Filter shown at the example of the KATRIN-experiment. The KATRIN main spectrometer with its superconducting solenoids (red), air coils (yellow) and the electrodes (blue) is shown. The black lines denotes the magnetic field and the blue line the motion of the electron along the magnetic field. In the minimum of the magnetic field almost all momentum is transferred into longitudinal momentum. (Source: [Hug08])

Because of the slow change of the magnetic field the transformation of cyclotron energy into longitudinal energy happens adiabatic. Hence the magnetic moment μ keeps constant. This is given for the non-relativistic case by:

$$\mu = |\vec{\mu}| = \frac{e}{2m_e} \cdot |\vec{l}| = \frac{E_\perp}{B} = const\,. \tag{2.3}$$

Due to the constant magnetic moment the following equation can be established:

$$\frac{E_{\perp,\mathrm{source}}}{B_{\mathrm{source}}} = \frac{E_{\perp,\mathrm{ana}}}{B_{\mathrm{ana}}} = \frac{E_{\perp,\mathrm{pinch}}}{B_{\mathrm{pinch}}} \tag{2.4}$$

Where $E_{\perp,\mathrm{source}}$, $E_{\perp,\mathrm{ana}}$ and $E_{\perp,\mathrm{pinch}}$ are the transversal energies at the source, the analysing plane and at the pinch magnet (placed in front of the detector) and B_{source}, B_{ana} and B_{pinch} the corresponding magnetic fields. The resolution of a MAC-E-Filter is given by the energy interval in which the transmission goes from 0 to 1.

The width of this energy interval is given by the remaining transversal energy of an electron in the analysing plane:

$$\Delta E = E_{\perp,\mathrm{ana}}^{\max} \tag{2.5}$$

$$= E_{\perp,\mathrm{pinch}}^{\max} \cdot \frac{B_{\mathrm{ana}}}{B_{\mathrm{pinch}}} \tag{2.6}$$

$$= E \cdot \frac{B_{\mathrm{ana}}}{B_{\mathrm{pinch}}} \tag{2.7}$$

$$\frac{\Delta E}{E} = \frac{B_{\mathrm{ana}}}{B_{\mathrm{pinch}}} \,. \tag{2.8}$$

With the given values $E = 18.6\,\mathrm{keV}$, $B_{\mathrm{ana}} = 3 \times 10^{-4}\,\mathrm{T}$ and $B_{\mathrm{pinch}} = 6\,\mathrm{T}$ this gives an energy resolution of $0.93\,\mathrm{eV}$ or a relative resolution of 5×10^{-5} for the KATRIN main spectrometer.

The magnetic flux tube is enclosed by a system of wire electrodes inside the spectrometer. This system of electrodes enables an energy analysis/separation by a retarding field. Only electrons whose longitudinal energy is greater than the energy of the retarding field overcome the analysing plane of the spectrometer. On their way to the detector these electrons are accelerated back to their initial energy. Because all electrons with an energy higher than the retarding field are transmitted, this spectrometer acts as integrating high-pass filter. This principle of **M**agnetic **A**diabatic **C**ollimation with **E**lectrostatic Filter (MAC-E-Filter) was used for neutrino mass measurements the first time in Mainz [Pic92b] and Troisk [Lob85].

In principle a MAC-E-Filter is able to accept electrons with starting angles up to 90° if the source is inside the maximum of the magnetic field. However for large starting angles the path length inside the source is long and this causes a higher scattering probability for the electrons. Therefore at the KATRIN-experiment the WGTS has a magnetic field of 3.6 T but the maximum field is 6 T at the pinch magnet. Thus the maximum acceptance angle is given by equation (2.4):

$$\Theta_{\max} = \arcsin \sqrt{\frac{B_{\mathrm{source}}}{B_{\mathrm{pinch}}}} = 50.77^{\circ} \tag{2.9}$$

The analytical transmission function for such a spectrometer is given by [KC04]:

$$T(E_{\mathrm{start}}, qU_0) = \begin{cases} 0 & E_{\mathrm{start}} < q\,U_0 \\ \dfrac{1 - \sqrt{1 - \dfrac{E_{\mathrm{start}} - q\,U_0}{E_{\mathrm{start}}} \dfrac{B_{\mathrm{source}}}{B_{\mathrm{min}}}}}{1 - \sqrt{1 - \dfrac{B_{\mathrm{source}}}{B_{\mathrm{pinch}}}}} & \text{for} \quad q\,U_0 \le E_{\mathrm{start}} \le q\,U_0 \dfrac{B_{\mathrm{pinch}}}{B_{\mathrm{pinch}} - B_{\mathrm{ana}}} \\ 1 & E_{\mathrm{start}} > q\,U_0 \dfrac{B_{\mathrm{pinch}}}{B_{\mathrm{pinch}} - B_{\mathrm{ana}}} \end{cases} \tag{2.10}$$

In this case qU_0 is the retarding energy of the spectrometer when the voltage U_0 is applied. Electrons with energies less than $E_{\text{start}} \leq q\,U_0$ are rejected and all electrons with energies $E_{\text{start}} > q\,U_0 \dfrac{B_{\text{pinch}}}{B_{\text{pinch}} - B_{\text{ana}}}$ are fully transmitted. In the intermediate energy range, the transmission of the electrons depends on their starting angle and therefore on the amount of remaining transversal energy in the center of the spectrometer. A plot of the transmission function for the main spectrometer is shown in figure 10 and 15.

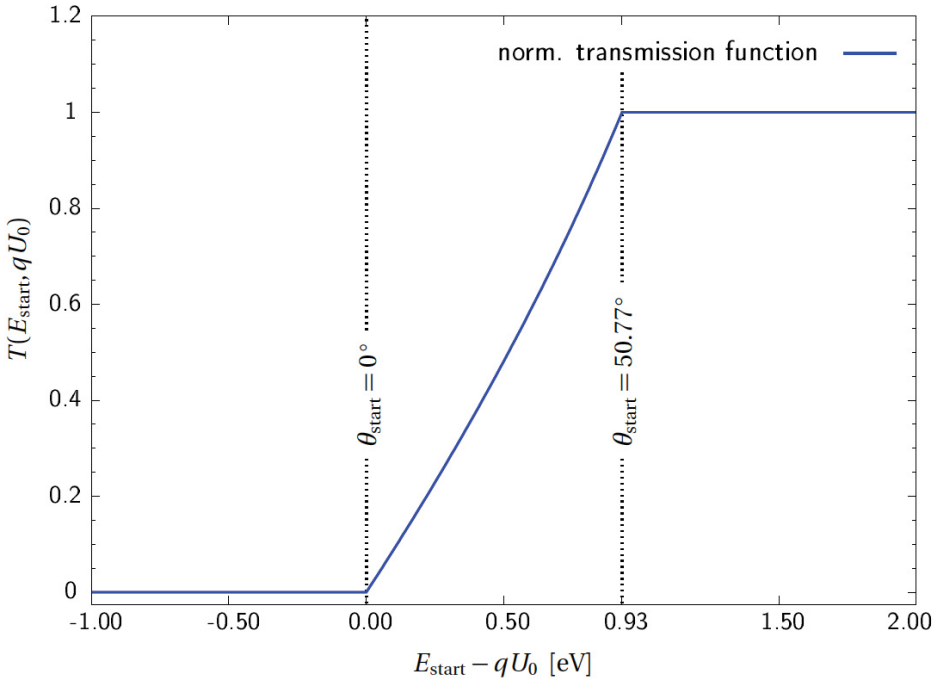

Figure 10: Normalized transmission function T $(E_{\text{start}}, q\,U_0)$ of the KATRIN main spectrometer. According to equation (2.10), the magnetic field parameters (here: $B_{\text{source}} = 3.6\,\text{T}$, $B_{\text{ana}} = 0.3\,\text{mT}$ and $B_{\text{pinch}} = 6\,\text{T}$) enter the analytical expression for T $(E_{\text{start}}, q\,U_0)$ [Val09].

Pre-spectrometer

The pre-spectrometer (see figure 11) is designed as pre-filter to reduce the flux of electrons by a factor 10^7 by setting the retardation voltage 300 V below the endpoint of the tritium decay. This strong reduction of electrons entering the main spectrometer reduces the possibility to ionize residual gas and thus to fill Penning-traps. A very promising measurement mode is the time-of-flight mode (TOF mode) where the main spectrometer acts as non-integration spectrometer. For this mode the pre-spectrometer can act as switch to periodically block the electron flux and thus imprint a time structure on the electron beam [Ste13].

For the purpose of a pre-filter the requirements for the energy resolution of the pre-spectrometer are very low. The resolution is approx. 100 eV which is sufficient. The length of the pre-spectrometer is 3.38 m and the diameter is 1.68 m. The vacuum system is build to reach

the 10^{-11} mbar level. This is achieved by differential pumping and a Non-Evaporable Getter pump (NEG pump). Also all materials are selected to reach a low outgassing rate in the order of $10^{-12}\,\frac{\mathrm{mbar\,L}}{\mathrm{s\,cm^2}}$. The pre-spectrometer is equipped with a wire electrode system to reduce muon induced background (monopole mode) and to remove stored particles (dipole mode) [KC04]. Also the pre-spectrometer was used for many test before the main spectrometer was commissioned. For example the influence of the ground electrode shape [Zac14] and the decay of ^{219}Rn, emanating from the NEG pump, on the background was investigated [Frä10].

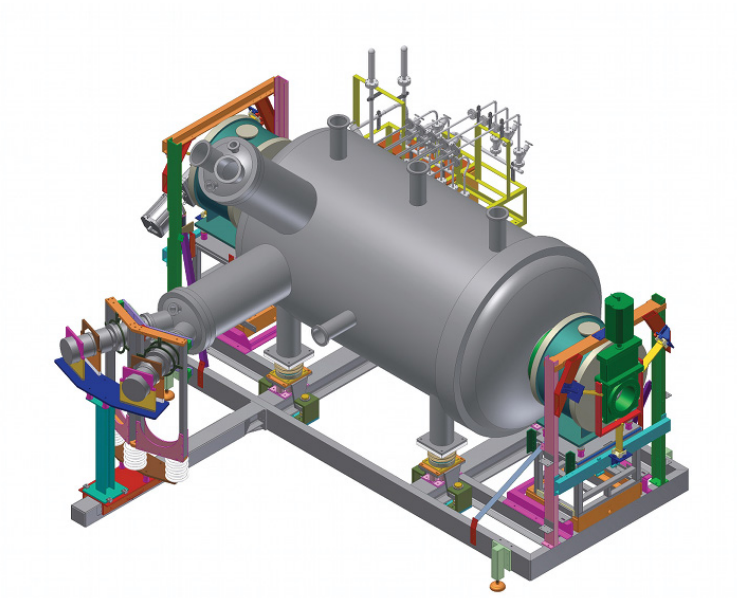

Figure 11: CAD drawing of the pre-spectrometer. The two pump ports (upper left part) are equipped with TMPs and NEG pumps. The superconducting magnets are placed at both sides of the spectrometer (green). The pre-spectrometer can be closed by two CF250 gate valves (dark green). In order to apply high voltage to the spectrometer the whole set-up is insulated by ceramic insulators.

Main spectrometer

The main spectrometer for the KATRIN-experiment (see figure 12a) has a length of 23.4 m and a diameter of 10 m. It is made from stainless steel (1.4429) with a thickness of 25 mm in the conical parts and 32 mm in the cylindrical part (analysing plane). The inner surface of the spectrometer is electro-polished to reduce field emission and outgassing. The out-gassing rate of hydrogen was measured to be $1.2 \times 10^{-12}\,\frac{\mathrm{mbar\,L}}{\mathrm{s\,cm^2}}$ at 20 °C [Wol09]. The volume of the main spectrometer is pumped by 2x3 Turbo Molecular Pumps (TMP) with a combined effective pumping speed of 10000 l/s. Three of these TMPs at a time are cascade by another TMP which is pumped by a fore-pump. In order to increase the pumping efficiency for hydrogen about 3 km of NEG strips are installed. This NEG pump will have a pumping speed for hydrogen in the order of $10^6\,\mathrm{L\,s^{-1}}$ [KC04].

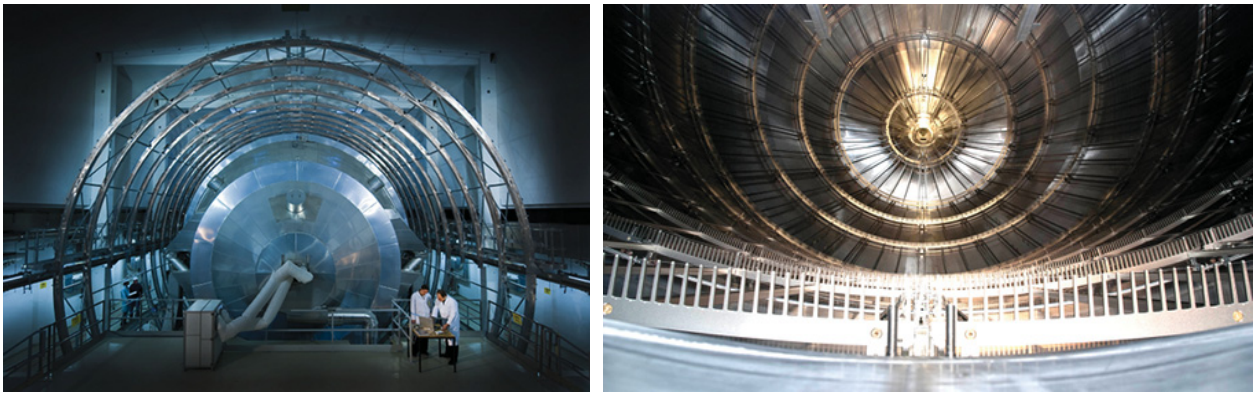

(a) **(b)**

Figure 12: The main spectrometer enclosed by the air coil system **(a)**. View over the wire electrode system from detector to source side along the beam axis **(b)**. In the front part of the picture the comb structure of the double-layered wire electrode is visible.

The main spectrometer is equipped with a double layer wire electrode system [Hil11, Pra11]. This system consists of 248 modules separated into 15 rings holding a total of approx. 23000 wires (see figure 12b). The whole electrode system is split vertically into two halves, which allows to apply an electric dipole field to the electrode system and thus to remove stored electrons by the $E \times B$ drift. More details on the wire electrode system are presented in section 3.1.

Monitor spectrometer

The spectrometer of the former Mainz Neutrino Mass experiment [Pic92b] is used as one possibility to monitor the stability of the retarding voltage. This is done by applying the same retarding voltage to the main spectrometer and the monitor spectrometer. To trace back the applied voltage to an atomic standard the position of the K-32 conversion electron line of ^{83m}Kr is measured. This is achieved by scanning the voltage which is applied to the ^{83m}Kr source. If the stability of the used source is well known, the stability of the line position is directly correlated to the stability of the retarding voltage. The best choice of such a source turned out to be an implanted source where the mother isotope ^{83}Rb is implanted into a foil of gold or platinum. This implanted sources are investigated in detail in [Zbo13] and further measurements at the monitor spectrometer are presented in chapter 5. To measure the line position the potential of the source must be scanned because the retarding potential will be fixed during the measurement. Also the line position of the K-32 line is approx. 800 V below the endpoint of tritium so the electrons have to be accelerated to a higher kinetic energy to pass the filter potential. For that purpose a voltage source with a variable output voltage of up to 1 kV is used. Thus the scanning voltage can be measured by commercial voltage dividers with a precision of 0.5 ppm (e.g. Fluke 752A Reference Divider) and a state-of-the-art voltmeter. A detailed description and scheme of the monitoring system will be given in section 2.8. More details on the monitor spectrometer set-up will be given in section 5.4.

2.5 Detector

The main component ot the Focal Plane Detector (FPD) at the KATRIN-experiment is an array of 148 PIN-diodes on a single wafer (see figure 13b). Each of the ion-implanted p-type pixels has an area of 44 mm^2 and the pixels are separated by 50 µm. The FPD is enclosed by the pinch magnet ($B_{\text{pinch}} = 6\,\text{T}$) and the detector magnet ($B_{\text{det}} = 3.6\,\text{T}$). The detector is installed in a vacuum chamber in which the separation is achieved by the so called detector flange.

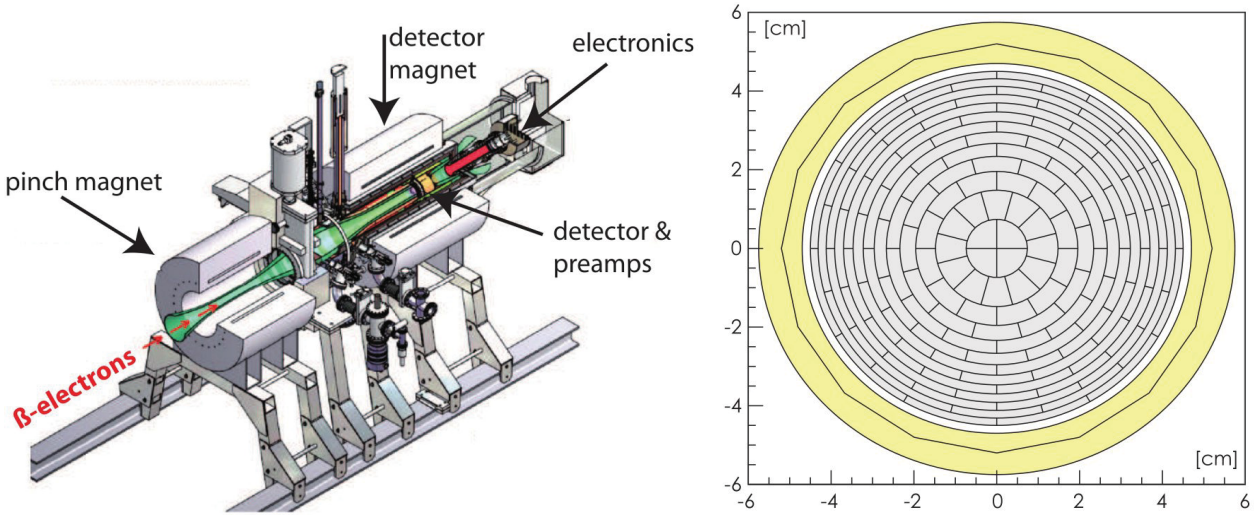

(a) **(b)**

Figure 13: Overview of the KATRIN Focal Plane Detector (FPD). The detector system is shown inside the both magnets. The detector wafer is placed inside the detector magnet The flux tube is pictured in green **(a)** (Source: [Leb10]). The segmentation of the FPD is shown in **(b)**. Each pixel has a size of 44 mm^2.

The custom made pre-amplifiers are directly mounted onto the detector flange to keep connections as short as possible. To reduce noise these pre-amplifiers are cooled. The pre-amplifiers are followed by further electronic boards which are connected via optical fibres to the DAQ system. The FPD achieves a RMS timing resolution of 46 ns and an energy resolution of 1.60(2) keV (FWHM) at 18.6 keV [Par].

2.6 KATRIN's sensitivity to the neutrino mass

For the KATRIN-experiment there are two possible outcomes after 5 years of data taking. In the optimal case KATRIN measures the neutrino mass. To get the lowest mass that could be measured with a sufficient significance the statistical and systematic uncertainties have to be summed up quadratically. This results in a total uncertainty of $\sigma_{\text{tot}} \approx 0.025\,\text{eV}^2$ (see section 2.7) which leads to a discovery potential of:

$$m_\nu = 0.35\,\text{eV} \qquad (5\sigma)$$

An overview of the discovery potential in dependence of the neutrino mass is shown in figure 14).

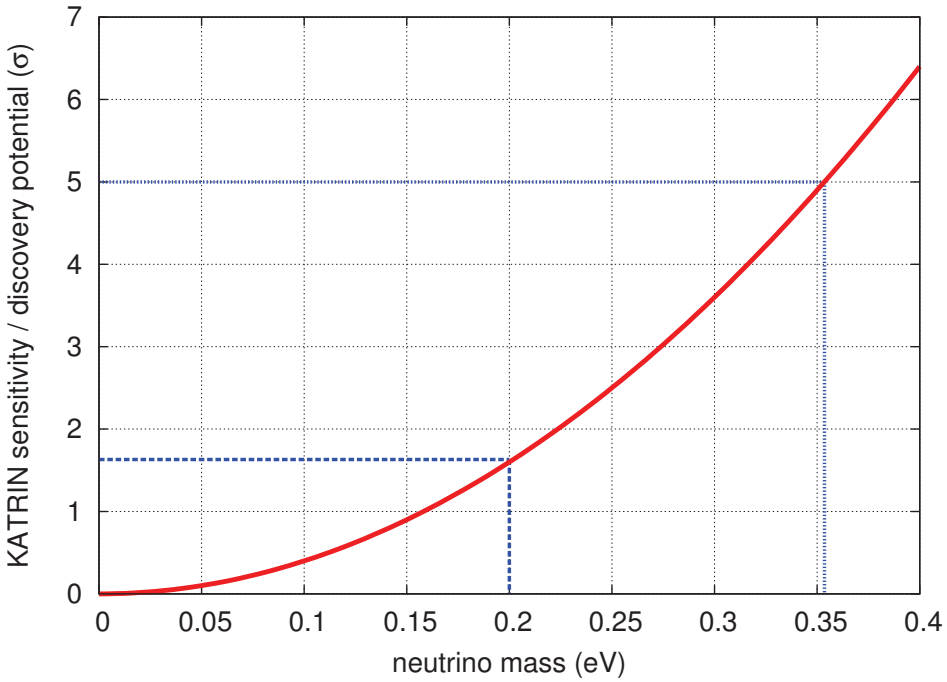

Figure 14: Discovery potential of the KATRIN-experiment. The upper 90% C.L. limit for the neutrino mass is 0.2 eV and denoted as the blue dashed line. The five σ level for a neutrino mass signal (0.35 eV) as blue dotted line.

For the case of no observed neutrino mass signal KATRIN will give an upper limit of:

$$m_\nu = \sqrt{1.64 \cdot \sigma_{\mathrm{tot}}} < 0.2\,\mathrm{eV} \qquad (90\,\%\ \mathrm{C.L.})$$

This sensitivity can only be achieved if several constraints to the systematic and statistical errors are fulfilled. The statistical and systematic uncertainties are discussed in the next section.

2.7 Statistical and systematic uncertainties

For the KATRIN-experiment the total uncertainty is the quadratic sum of the systematic (σ_{sys}) and the statistical uncertainty (σ_{stat}). If the analyzing interval is chosen to be $[E_0 - 30\,\mathrm{eV}, E_0 + 5\,\mathrm{eV}]$ than the statistical uncertainty will be:

$$\sigma_{\mathrm{stat}} = 0.018\,\mathrm{eV}^2$$

for a three years worth of data at a background rate of 10 mHz [KC04]. For a given statistical uncertainty KATRIN will reach the highest sensitivity if $\sigma_{\mathrm{sys}} \approx \sigma_{\mathrm{stat}}$. Therefore the overall systematic uncertainty is anticipated to be less than:

$$\sigma_{\mathrm{sys,tot}} \leq 0.017\,\mathrm{eV}^2$$

This value splits up into limits for the five major sources of uncertainties of:

$$\sigma_{\mathrm{sys,single}} \leq 0.0075\,\mathrm{eV}^2.$$

These five uncertainty components are added quadratically, since they are not correlated with each other. Four of them are connected to the WGTS and the last one concerns the high voltage stability which is one major topic in this work.

- **Transmission and response function:** The sharp analytical transmission function of the main spectrometer is broadened by different influences like inhomogeneities of the magnetic and electric field in the analyzing plane (see figure 15a). Influences caused by this inhomogeneities can be reduced by the use of a radial segmented detector. This transmission function, also if experimental effects are considered, does not consider any interaction of the electrons coming from the source. Therefore the transmission function must be folded by the energy loss function of the electrons which results in the response function (see figure 15b) of the KATRIN-experiment [KC04].

- **Column density of the WGTS:**
  The column density inside the WGTS determines the decay rate and the inelastic scattering fraction and hence influences directly the measured spectrum. This makes the monitoring of the column density to one of the most important issues. The amount of inelastic scattering processes of the signal electrons and by that the energy loss function of the source will directly be influenced by the column density. For the normal operating parameters of the WGTS 41.3% of the electrons moving through the source without inelastic scattering. A fraction of 29.3% are scattered once and 16.7% twice [Bab12]. To monitor the column density many different on- and off-line methods will be used. A detailed overview of these methods is given in [Bab12].

- **Description of final states:**
  During the β-decay not all of the energy is distributed among the outgoing electron and neutrino. Also a small fraction can go into the excited states of the daughter molecule. Due to the simple structure of tritium molecules this part is calculable and will be considered in the analysis. The first electronic excitation exist at an energy of 27 eV and can be ignored if the analysis interval is chosen right. Thus only the decay into the ground state, which is populated in 57% of the decays, has to be taken into account. This ground state also posses many rotational and vibrational excitations with mean excitation energy of 1.7 eV and a standard deviation of 0.36 eV [KC04].

- **Ions inside the WGTS:**
  Inside the WGTS both positive and negative ions are produced by β-decay and by electron scattering. These Ions contribute to the total decay rate but with their individual endpoint energies. Because of the lower endpoint energies and the small analysing interval only the negative ions contribute to a non-negligible fraction. Also positive ions can accumulate in front of the WGTS and create positive space charge resulting in a time dependent electric field. By this positive charge the energy of the electrons will be reduced [KC04].

- **High voltage variations and potential difference between source and main spectrometer:**
  Fluctuations in the potential difference between the WGTS and the main spectrometer will influence the measurement of the β-spectrum . If there is an unknown fluctuation of the retarding potential with the Gaussian width σ the squared neutrino mass will be shifted [Rob88]:

  $$\Delta m^2_{\nu_e} c^4 = -2\sigma^2$$

  The calculation will be shown in the following and the methods to monitor the variations of the retarding potential will be presented in this work.

There are further contributions to the uncertainty budget like energy dependence of the background count rate or fluctuations of the electric and magnetic fields inside the source. All sources of uncertainties are described in detail in the KATRIN Design Report [KC04].

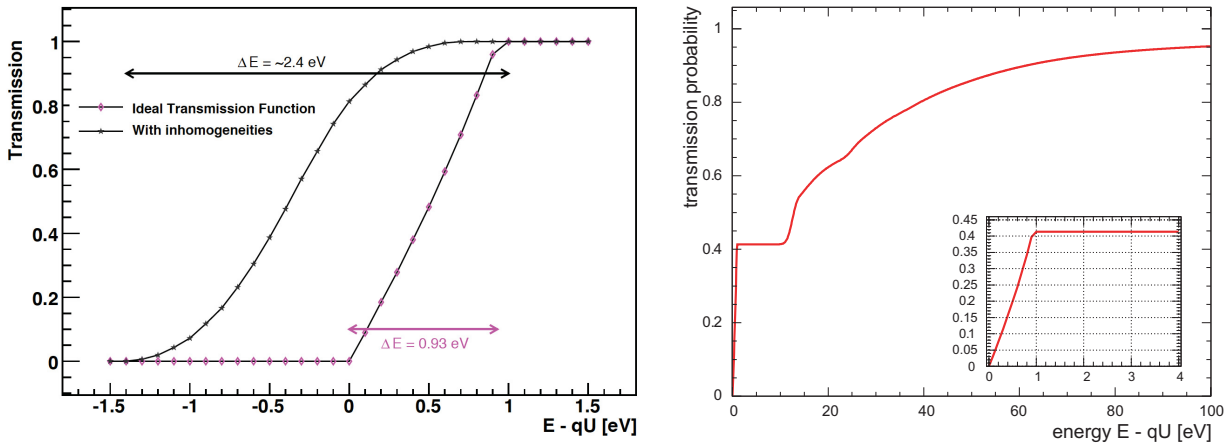

(a) **(b)**

Figure 15: The transmission function with the expected inhomogeneities in the analyzing plane ($\Delta U \approx 1.2\,\mathrm{V}$ and $\Delta B \approx 4 \times 10^{-5}\,\mathrm{T}$) taken into account ($\Delta E \approx 2.4\,\mathrm{eV}$). The influence of the inhomogeneities will be reduced by the pixelation of the detector into 12 rings and a central circle. The transmission function for each detector ring is shown as ideal Transmission function ($\Delta E = 0.93\,\mathrm{eV}$) [Dun07] **(a)**. Response function with fixed energy E as a function of the retarding energy qU **(b)**. The energy loss of electrons in the WGTS (at standard operation parameters) is folded into the response function. The inlay shows the transmission of non scattered electrons to the plateau of $P_0 = 41.33\%$ [KC04].

Because the stability of the high voltage system represents 20% of the systematic uncertainty this is a very important task at the KATRIN-experiment. Therefore the retarding voltage at the KATRIN-experiment will be monitored by two redundant methods in parallel:

- **Direct measurement of the retarding voltage:**
  To measure the retarding voltage directly, two high precision voltage dividers are used. They divide the retarding voltage down to approx. 10 V which can be measured precisely with state-of-the-art digital voltmeters. The KATRIN high voltage dividers are described in detail in chapter 4.
- **Monitor spectrometer:**
  The stability of the retarding voltage will also be monitored by comparing it to the line position of well known and sharp lines of conversion electrons out of ^{83m}Kr sources. For that purpose the monitor spectrometer will be connected to the same high voltage as the main spectrometer. Thus a shift in line position is correlated to a change in retarding voltage. The concept of the monitor spectrometer and the properties of the calibration sources are shown in chapter 5.

Section 2.8 will focus on the possibilities to monitor the stability of the high voltage system and the calibration of the experiment. To determine the influence of a fluctuation of the retarding potential to the neutrino mass a simplified form of the β-spectrum(1.18) near the E_0:

$$S_{\text{theo}}\left(E, m_{\nu_e}\right) = \frac{d\dot{N}}{dE} = a \cdot (E_0 - E)\sqrt{(E_0 - E)^2 - m_{\nu_e}^2 c^4}. \tag{2.11}$$

is considered. Here E is the kinetic energy of the β-electron, m_{ν_e} the neutrino mass and E_0 the endpoint energy. All other parameters are included in the constant a. A Taylor expansion up to the first order in $m_{\nu_e}^2$ around $m_{\nu_e}^2 = 0$ gives:

$$S_2\left(E, m_{\nu_e}\right) = a \cdot (E_0 - E)^2 - a \cdot \frac{1}{2} m_{\nu_e}^2 c^4 + \mathcal{O}(m_{\nu_e}^4). \tag{2.12}$$

Now this is compared with a β-spectrum with $m_{\nu_e}^2 = 0$ but with an additional fluctuation which is assumed to be Gaussian (with the mean value $\mu = 0$ and the width σ)

$$f(x) = \frac{1}{\sqrt{2\pi} \cdot \sigma} \cdot e^{-\frac{1}{2}\left(\frac{x}{\sigma}\right)^2} \tag{2.13}$$

This fluctuation is convoluted with the β-spectrum (for $m_{\nu_e} = 0$).

$$
\begin{aligned}
S_{\mathrm{sim}}(E,0) &= f(x) \otimes S_{\mathrm{theo}}(E,0) \\
&= \int_{-\infty}^{\infty} f(x) \cdot S_{theo}(E-x,0)\, dx \\
&= \int_{-\infty}^{\infty} \frac{1}{\sigma\sqrt{2\pi}} e^{-\frac{1}{2}\left(\frac{x}{\sigma}\right)^2} a \cdot (E_0 - E + x)^2\, dx \\
&= a(E_0-E)^2 \underbrace{\frac{1}{\sigma\sqrt{2\pi}} \int_{-\infty}^{\infty} e^{-\frac{1}{2}\left(\frac{x}{\sigma}\right)^2} dx}_{=1} + 2a(E_0-E) \underbrace{\frac{1}{\sigma\sqrt{2\pi}} \int_{-\infty}^{\infty} x e^{-\frac{1}{2}\left(\frac{x}{\sigma}\right)^2} dx}_{=0} \\
&\quad + a \underbrace{\frac{1}{\sigma\sqrt{2\pi}} \int_{-\infty}^{\infty} x^2 e^{-\frac{1}{2}\left(\frac{x}{\sigma}\right)^2} dx}_{=\sigma^2} \\
S_{\mathrm{sim}}(E,0) &= f(x) \otimes S_{\mathrm{theo}}(E,0) = a(E_0-E)^2 + a\sigma^2. \qquad (2.14)
\end{aligned}
$$

If now the coefficients of the Taylor expansion are compared (2.12) with the convolution (2.14) it follows:

$$m_{\nu_e}^2 c^4 = -2\sigma^2 \qquad (2.15)$$

This implies that an unconsidered but existing Gaussian fluctuation will reduce the neutrino mass by:

$$\Delta m_{\nu_e}^2 c^4 = -2\sigma^2 \qquad (2.16)$$

With the maximum allowable contribution of the high voltage of $0.0075\,\mathrm{eV}^2$ to the overall uncertainty budget it follows:

$$
\begin{aligned}
\sigma &= \sqrt{\frac{0.0075\,\mathrm{eV}^2}{2}} = 0.061\,\mathrm{eV} \\
&\Rightarrow \sigma_{\mathrm{U_{ret}}} \leq 61\,\mathrm{mV} \qquad (2.17)
\end{aligned}
$$

For the retarding voltage of $-18.6\,\mathrm{kV}$ the allowed fluctuation of 61 mV corresponds to a relative uncertainty of 3.3×10^{-6} which is 3.3 ppm. This accuracy of the voltage measurement has to be fulfilled in principle over the whole measurement time of five years. As described in chapter 4 the KATRIN high voltage dividers have a monthly drift of less than

0.1 ppm/month. Over five years this will be 6 ppm and thus too high. But for KATRIN it is sufficient to know the retarding potential with that accuracy over a period of 2 months. This two months are needed for one single tritium run and its corresponding analysis. In this period the stability is about a factor 10 higher than required. Additionally further disturbances concerning the high voltage can lead to sources of uncertainties like AC components and RF noise (see section 3.4).

The influence of a wrong calibration of the high voltage divider and the voltmeter were investigated numerically by Kaspar et al. [Kas04]. For the high voltage divider the influence of a Gaussian fluctuation and an unknown shift of the scale factor in 50% of the measurement time was investigated[1]. The limit found by this numerical approach for a Gaussian broadening is also < 60 meV and in good agreement with the estimation above. For the digital voltmeter an unaccounted uncertainty of the calibration line was simulated. This was done in one case for a constant slope error and for a Gaussian one varying over time. The results are presented in figure 16. The outcome is that the maximum allowed relative deviation for the voltage measurement is $\delta < 10^{-3}$. For an analysing interval of 50 eV below the endpoint energy this corresponds to 50 mV accuracy in voltage measurement for the whole measurement chain of voltage divider and digital voltmeter [KC04].

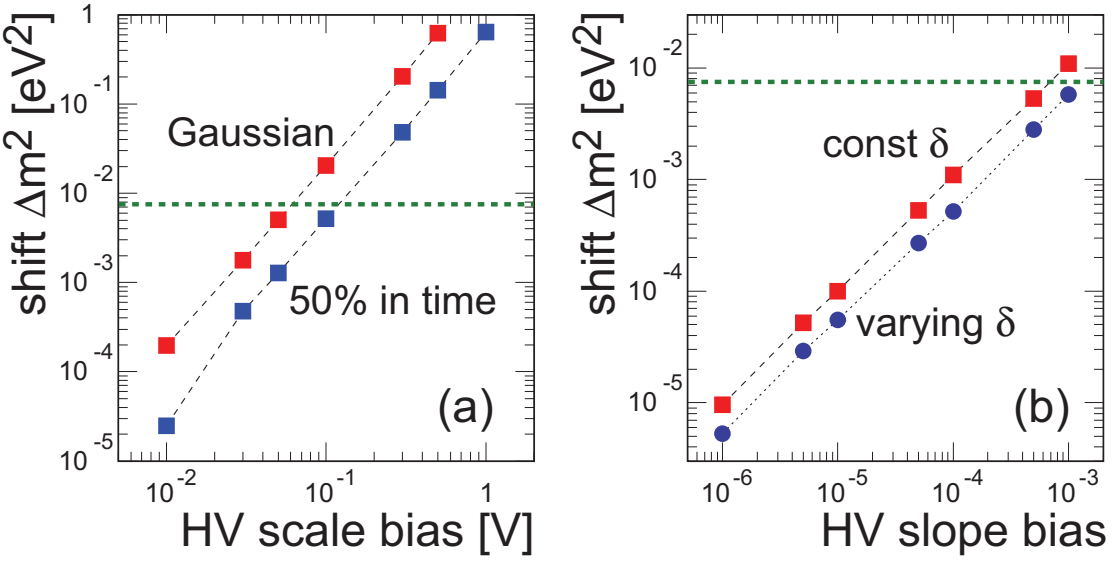

Figure 16: The shift in observed squared neutrino mass for a Gaussian fluctuation (red) and for an unknown shift in 50% of the measurement time (blue) is shown in **(a)**. The shift for a constant (red) error in the slope of the digital voltmeter and for an error varying over time (blue) is shown in **(b)**. In both plots the green dashed line represents the maximum allowed shift to the neutrino mass square of $\Delta m_\nu^2 = 0.0075\,\mathrm{eV}^2$. (Source: [KC04, Kas04])

[1] It should be noted that the absolute value of the scale factor is not of importance, since the end point of the β-spectrum is a fit parameter in the analysis.

2.8 Calibration and stability monitoring

In order to measure the β-spectrum at the KATRIN-experiment two procedures are possible:

- **Fixed retarding voltage at the main spectrometer:**
  For this method the voltage at the main spectrometer is kept constant and the potential of the source is scanned. The potential at the source can be measured with commercial devices with a precision of less than one ppm because of the low scanning voltage. The retarding voltage at the main spectrometer is measured with the KATRIN high voltage dividers (see chapter 4). In this case the potential difference is defined by the two voltage measurements relating to the ground potential.
- **Variable retarding potential at the main spectrometer:**
  The second solution to scan the β-spectrum is to fix the WGTS to ground potential and scan the retarding voltage at the main spectrometer. In this case only one voltage measurement is used to scan the energy of the electrons. For this scenario very high demands are placed to the high voltage power supply. Especially fine voltage steps and high stability. Therefore KATRIN has two custom made power supplies which fulfill these strict requirements.

Depending on the chosen method one or two voltages have to be measured with high accuracy. Because the scanning voltage for the WGTS can be measured by commercial devices with high precision only the methods for the high retarding potential at the main spectrometer will be discussed further. The schematic overview over the calibration and monitoring concept is shown in figure 17.

The retarding potential will be monitored on the one hand with the KATRIN high voltage dividers and on the other hand by the line position of ^{83m}Kr conversion electrons at the monitor spectrometer. Both methods of this redundant monitoring concept are investigated within this thesis. The KATRIN high voltage dividers are investigated and calibrated in order to improve the direct measurement of the retarding voltage (see chapter 4). At the monitor spectrometer dedicated measurements was carried out to compare the stability of implanted ^{83}Rb/^{83m}Kr sources and the KATRIN high voltage divider K35. Furthermore the possibility to determine the voltage dependence of the KATRIN dividers by the difference in γ energies, was tested (see chapter 5).

The absolute energy calibration is done by conversion electrons from ^{83m}Kr sources. This calibration sources are used in different states of aggregation. On the one hand ^{83m}Kr is used as gaseous source inside the WGTS on the other hand it is used as **C**ondensed **Kr**ypton **S**ource (CKrS) inside the CPS. The CKrS is presented in chapter 6. Furthermore, implanted sources are used at the monitor spectrometer to mainly monitor the stability of the retarding voltage but also to do energy calibration.

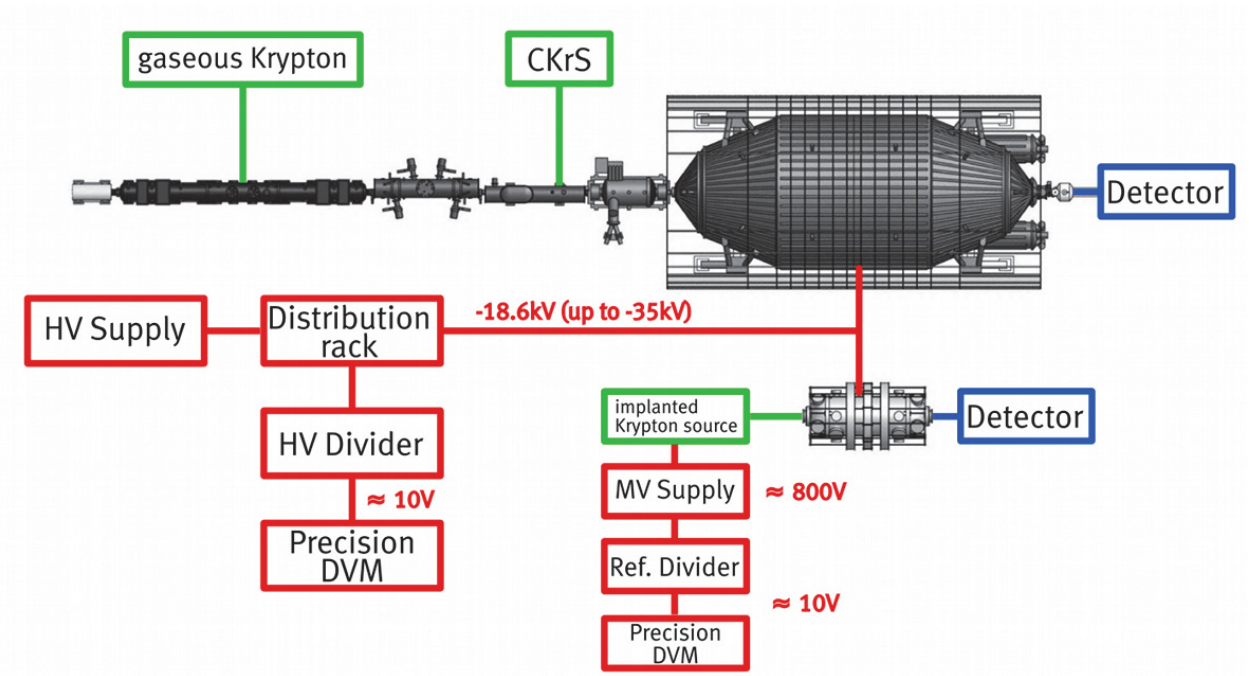

Figure 17: Schematic overview of the monitoring concept. Both spectrometers are supplied by the same high voltage by a precision high voltage power supply. This retarding potential is redundantly monitored by the one of the KATRIN high precision voltage divider and the monitor spectrometer. In order to scan the conversion electron line K-32, the implanted krypton source can be scanned via a dedicated power supply (MV Supply). This scanning voltage is monitored by a Fluke 752A reference divider and a precise digital voltmeter. Additionally to the monitor spectrometer the energy calibration can be carried out via krypton admixture in the WGTS or by the condensed krypton source inside the CPS.

Chapter 3

The high voltage system at KATRIN

For the KATRIN-experiment many different voltages have to be applied. Mainly this are the retarding potential for all three MAC-E-Filters, the potential WGTS and the post-acceleration of the detector. All needed potentials have specific requirements concerning stability, noise and the absolute value. An overview is given in figure 18.

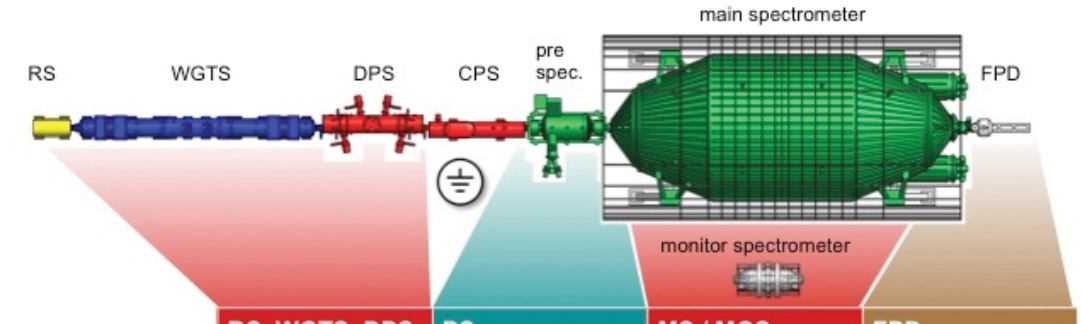

	RS, WGTS, DPS	PS	MS / MOS	FPD
Voltage	-1 kV	-35 kV	-35 kV	+25 kV
Stability	± 20 mV	uncritical	± 20 mV	uncritical
HF noise	compensated	uncritical	compensated	shielded
Relevance to m_ν	very high	low, bg reduction	very high	low, bg reduction
Safety aspects	HV on surface, interlock	HV on surface, interlock	HV on surface, interlock	no, grounded housing

Figure 18: Overview of the KATRIN high voltage system. The tabular shows the voltage, the needed stability, influences of noise, the relevance of the certain voltages to the neutrino mass as well as safety aspects. [Thü08]

Because the relevance of the high voltage at the detector and the pre-spectrometer to the neutrino mass is very low this will not be discussed further. The voltage at the source can be stabilized and measured with commercial devices to high accuracy. Thus the following sections will focus on the high voltage system for the main and monitor spectrometer. Especially the high voltage system for the main spectrometer is very complex. A system of wire electrodes, to which up to 48 voltages can be applied, is installed inside the main spectrometer. Before presenting the high voltage system an overview of the electrode system and its properties will be given in the next section.

3.1 The wire electrode system

In order to reduce the background caused by electrons generated at the inner surface of the KATRIN main spectrometer, a two-layer wire electrode system was installed. This wire electrode was designed taking many electromagnetic simulations into account [Hug08, Val09, Zac09]. The production of the whole electrode was done in the clean room of the Institut für Kernphysik at the University of Münster, Germany [Hil11, Pra11]. The basic concept is

to screen the flux tube from electrons starting at the inner surface of the main spectrometer vessel and to provide the retarding potential of the MAC-E-Filter. Electrons starting from the spectrometer wall can be generated by e.g. radioactive decays in the materials or by cosmic muons. This electrons can enter the flux tube and thus generate background. The screening of these electrons is done by applying a slightly more negative potential to the two layers of wires than to the vessel itself. By this electrostatic screening the electrons are reflected back to the vessel hull (figure 19).

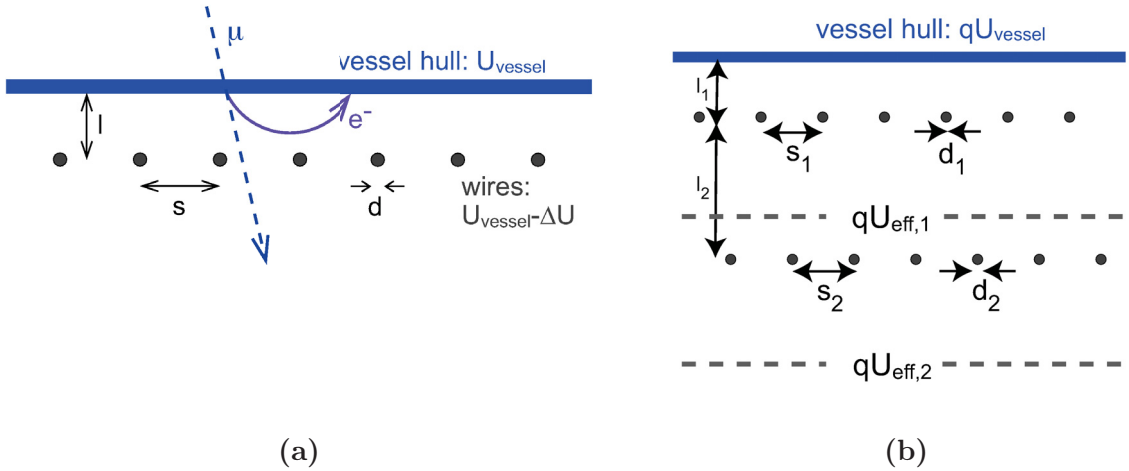

Figure 19: Principle of electrostatic screening. The simplest solution for the electrostatic screening is a single layer wire electrode with the distance l to the vessel hull, a wire diameter d and the distance between wires s. Electrons generated at the vessel hull are reflected by a more negative potential (ΔU) at the wires **(a)**. Because of the higher screening and hence better background reduction and in order to counteract mechanical uncertainties in the vessel hull a doubled-layered wire electrode was chosen for KATRIN **(b)**. The first layer with wire diameter $d_1 = 0.3\,\text{mm}$ is placed in the distance $l_1 = 150\,\text{mm}$ to the vessel hull. The second layer with wire diameter $d_2 = 0.2\,\text{mm}$ is placed in the distance $l_2 = 70\,\text{mm}$ to the first layer. The distance between the wires in each section is $s_1 = s_2 = s = 25\,\text{mm}$. (Source: [Pra11]).

The wire electrode system is also used to fine-tune the electric field inside the main spectrometer [Zac09]. This will avoid Penning-traps and will optimize the retardation and the radial field drop inside the analysing plane. For that purpose up to 48 different voltage can be applied to the different sections of the whole system. Therefore a high voltage distribution rack was designed and set up, which will be described in section 3.2.

The wire electrode system consists of 248 double layered modules and is organised in rings (see figure 20). Each layer of each ring can be supplied with an individual potential with two exceptions:

1. Ring 07 to 11, forming the central part inside the cylindrical part of the spectrometer, are connected. This is done in a way that for the central part one inner and one outer layer are realized.

2. At the steep cones the two potentials are split up into wire layer and frame because they consists only of one wire layer.

For the double layer modules (all rings except for ring 2, 3 15 and 16 in figure 20, "step cones") the potential of the outer layer is connected to the frame of the wire electrode module. In addition the whole system is divided into two dipole halves along the z-axis. This provides the option to apply a dipole field to remove stored particles by the $E \times B$ drift.

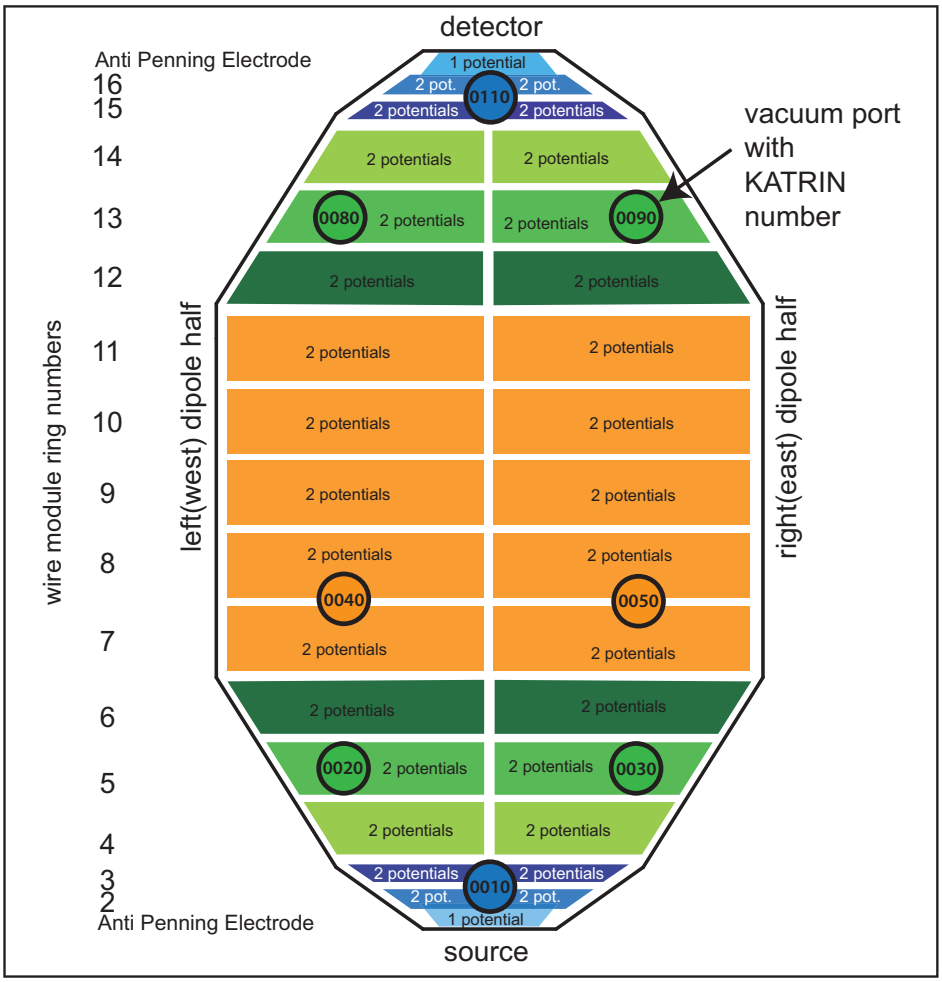

Figure 20: Overview of the module rings and the high voltage feedthrough flanges of the main-spectrometer. Module rings 2 - 16 are divided into the dipole halves east (right) and west (left). The full metal electrodes (Anti Penning Electrode, ring 1 and 17) are not divided into dipole halves. The voltages are guided into the spectrometer through eight vacuum ports. [Pra11].

Due to the high importance of the wire electrode system, a monitoring tool to check the integrity is needed. A short cut between electrode and vessel or between layers/rings can easily be measured by the resistance. But there is also the possibility that a broken wire will make no short cut but will hang down into the flux tube. These failures or a change in geometry can be investigated by electrons from an angular selective electron gun (eGun) at the outer radii of the flux tube [Zac14]. A different approach is to measure the capacitance of each electrode segment. This method and first measurements will be presented in section 3.5.

3.2 High voltage distribution system

As already mentioned in section 3.1 the electrode system is used to fine-tune the electric field. For that purpose 48 voltages have to be provided. In detail this are two times 11 voltages for each dipole half of the wire electrode (11 electrical separated rings with two different potentials / layers ⇒ 44 potentials, see figure 20). In addition two potentials for the anti-Penning electrodes and two potentials for the dipole mode. A very simplified schematic of this is given in figure 21. It shows the concept of using two independent power supplies, one for the vessel an all related parts and the second one for the analysing potential and as reference signal for all offset supplies for the remaining electrode channels. The retarding voltage will be looped through the so-called dipole supply where an additional voltage source can be switched onto by a relay. This allows to remove stored particles by the $E \times B-$drift.

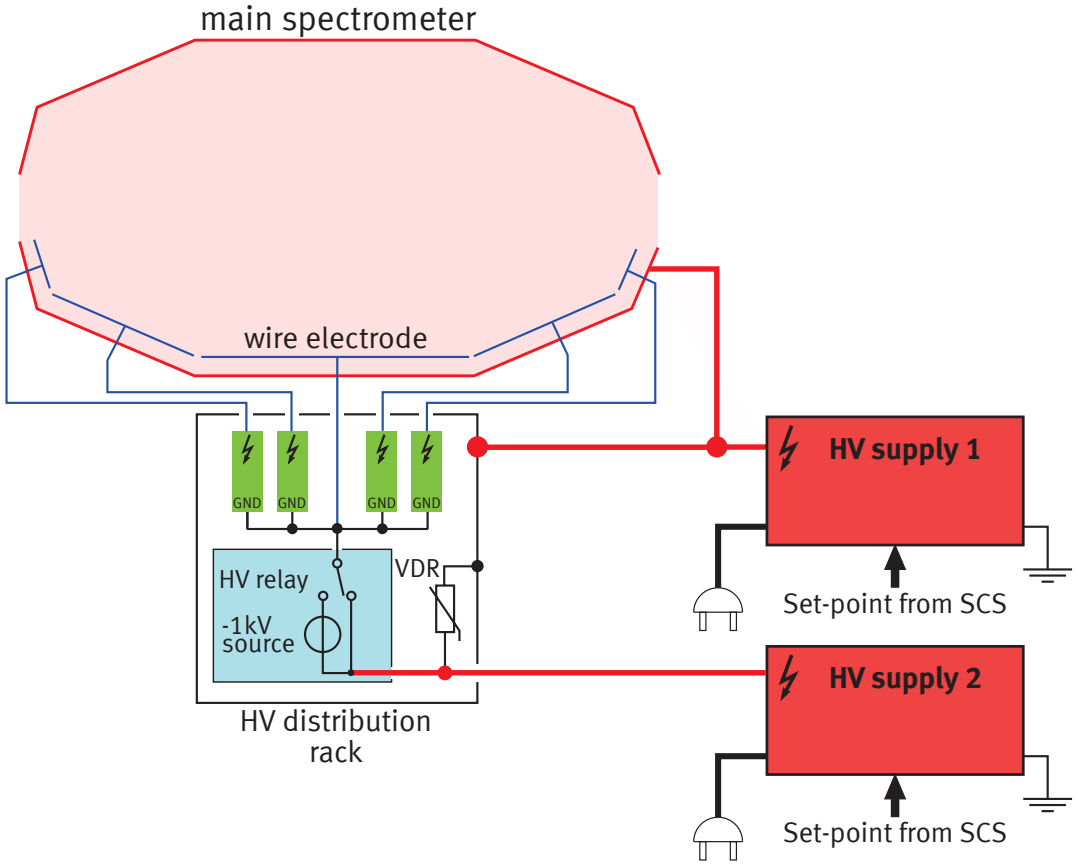

Figure 21: Simplified schematic overview of the wire electrode voltage supply. The schematic shows a simplified version with only five single layer rings (instead of 11 double layered) for one dipole half. One high voltage supply is used to supply the spectrometer vessel and all related parts (e.g. TMPs, HV distribution rack). The second high voltage supply is connected to the dipole power supply (light blue). The external voltage can be looped through the dipole supply or an additional potential of up to $-1\,\mathrm{kV}$ can be applied for the dipole mode. The output voltage of the two channel dipole supply goes directly to the central part of the inner wire electrode and serves as common signal for the offset supplies (green) of the remaining electrode channels. All power supplies get their set-point from the high voltage slow control system (SCS).

It is yet to test whether the two independent regulations of both power supplies affect each other in a negative way or not, especially since they are strongly coupled (from a certain cut-off frequency) by the high capacity of the wire electrode.

All 46[1] electrode voltages are provided by the high voltage distribution rack, which is shown in figure 22. This high voltage rack was developed and set up within the diploma thesis of S. Rosendahl [Ros10] and installed at the KATRIN experiment within this work. It is divided into to parts corresponding to the dipole halves. Within these halves the rack is divided into an isolated part and a non-isolated one. The isolated parts are identically in each dipole halve. They provide the power supplies for the wire electrode offset-voltage as well as the PXI-systems to control the power supplies and to measure the applied voltage. The non-isolated parts hold the isolated power supplies (DC/DC converter) to supply the isolated parts of the rack, the NIM-frame for the anti-Penning supply and the dipole power supply (see figure 22). Because of the fact that the rack is on the same potential as the vessel, the communication connection is realized by optical fibres and the mains supply by an insulating transformer.

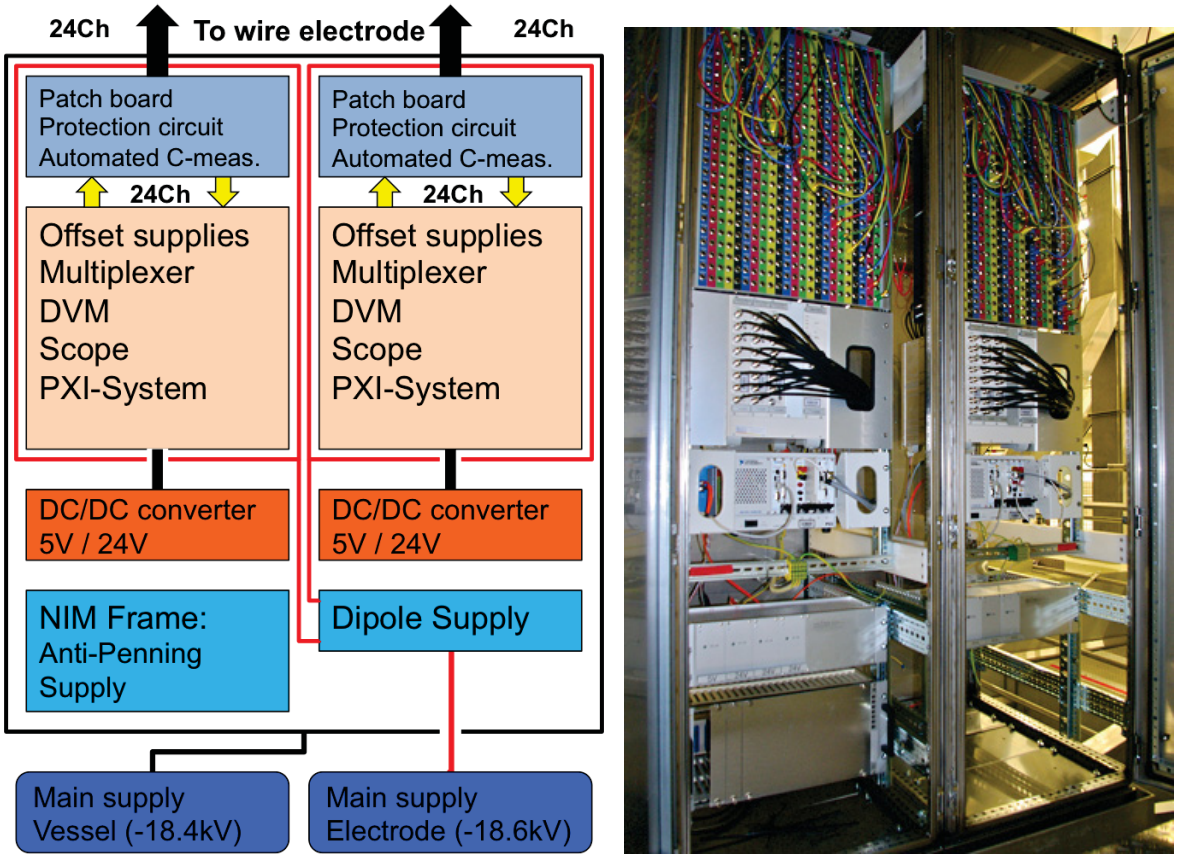

(a) (b)

Figure 22: Schematic overview of the high voltage distribution rack. The isolated parts for both dipoles are framed in red. These parts get their functional earth from the dipole power supply **(a)**. A real picture of the rack (dipole and anti-Penning electrode supply not installed)**(b)**.

[1]The retarding potential in the analysing plane will be provided by the external primary power supply, hence 46 of the 48 potentials will be provided by the high voltage distribution rack.

In the topmost part of the isolated section a patch board, protection circuits and circuit boards for an automated capacitance measurement of the wire electrode are installed (see 3.5). The patch board allows to connect each section to a specific channel of the offset voltage supplies. For that purpose a matrix of 6.3 mm audio jacks is used where each row represents one channel of the voltage supplies and each column one section of the wire electrode (see figure 23). If for example all plugs are placed in the first row, all electrode sections are connected to the first channel of the offset supplies.

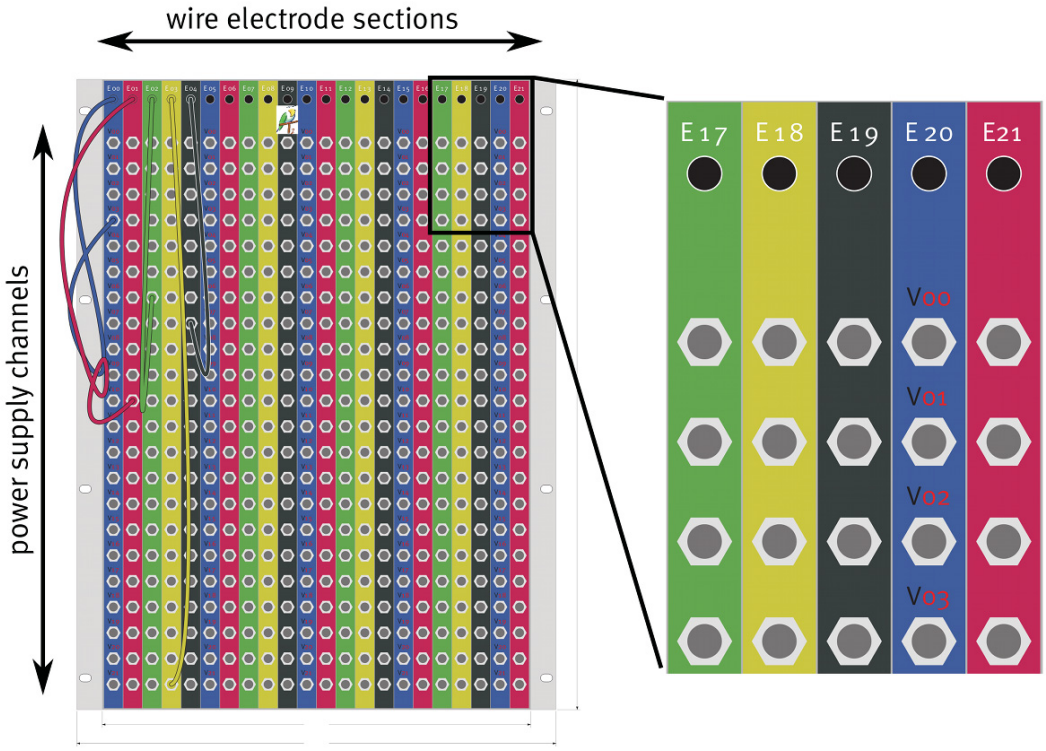

Figure 23: At the patch board the power supply channels are arranged in rows (V00 to V21) and the sections of the wire electrode in columns (E00 to E21). This allows to set all electrodes to an individual power supply or to connect multiple electrode segments to the same power supply.

A two staged protection circuit (see figure 24) protects the system against transient overloads. This protection circuit was developed by S. Wüstling and constructed in the electrical workshop of the Institut für Kernphysik in Münster. The first stage consists of a 50 Ω resistor in parallel to a gas discharge tube and is located at the circuit board of the relay circuit for the automated capacitance measurement. The 50 Ω resistors limit the maximum current, caused by transient overloads. The first resistor is protected by a gas discharge tube, which bridge the resistor if a voltage drop of 90 V is exceeded. The second stage holds a capacitor (4.7 nF), a voltage depended resistor (Panasonic ERZV14D182) and a second 50 Ω resistor. This stage is located on a separate board following the relay board as shown in figure 24. The capacitor makes a capacitive coupling to the potetnial of the spectrometer vessel ("local ground") and the voltage dependent resistors makes a low resistive connection to local ground if a voltage of appropriately 1500 V is exceeded. The circuit is terminated by a second 50 Ω resistor.

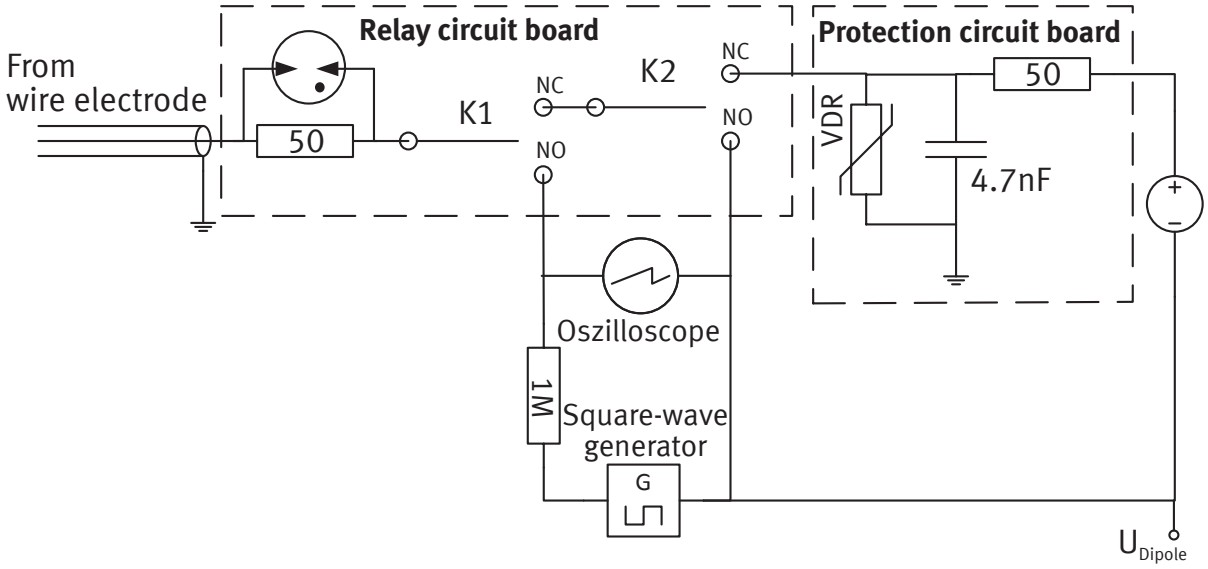

Figure 24: Input section for the wire electrodes. Each channel of the wire electrode system is connected to a relay and protection circuit. First protection stage is a 50 Ω resistor which is protected by a gas discharge tube. This is used to reduce the current of transients. This stage is followed by the relay circuit to switch the electrode channel to the capacitance measurement. It consists of a square wave generator, a 1 MΩ resistor and an oscilloscope to record the charge and discharge curves. The second protection stage consists of a voltage dependent resistor (VDR) to derive over-voltages to ground and a capacitor to short-cut AC components to the vessel potential. The last part is a terminating resistor of 50 Ω. During capacitance measurements both relays (K1 and K2) are switched to the position NO, else both are switched to the position NC.

The relay circuit for the capacitance measurement is placed in between both protection stages. During capacitance measurements the second relay (K2, see figure 24) of all channels is switched to the potential of the corresponding dipole, which itself is grounded during a capacitance measurement. By that stable and reproducible conditions for the measurements are provided. The first relay (K1) of each wire electrode channel allows to switch single or multiple electrode channels to the measurement device. The default position (NC = normally closed) of both relays is chosen that they connect the wire electrode via the protection circuit to the power supplies. This is the default connection if the capacitances are not measured.

3.3 High Voltage Slow control system

The High Voltage Slow Control System (HV-SCS) controls and reads every parameter of the high voltage system. This system is written in LabView and divided into three parts:

1. **Main control:**
   The main control can be operated by ZEUS[2] or by the local control terminal ("Experten-PC"). The ZEUS control is standard operation mode where the values are set by a ORCA[3] run control script. This will set all values needed for an automated measurement. All parameters have allowed limits which were defined in a HV recipe. If the requested values exceeds these limits they are ignored from the HV-SCS. The "expert mode" is for development and fault analysis and enables the full control over the system without any limit.

2. **High voltage control system:**
   The high voltage control system is based on a National Instruments compact RIO system (cRIO). This system distribute all data between the subsystems (distribution rack, high voltage dividers, and post regulation) of the high voltage system and the main control. It holds the HV recipe and enables the connection and data flow between all sub-components of the HV-SCS. It also controls the primary high voltage supplies and the digital voltmeters and is the interface to the safety system.

3. **PXI-System:**
   Due to the huge amount of controllable parameters inside the high voltage distribution rack two PXI-Systems are installed to control all installed components. Additionally the high potential difference of the dipole halves makes it necessary to have a dedicated control unit on each dipole potential. The electrical isolation is realized with optical fibres. The east PXI also controls the dipole supply and the west PXI the anti-Penning electrode supply. Both interfaces are realized via optical Ethernet. The basic functions of this software were already written within S. Rosendahls diploma thesis [Ros10] and the integration into the KATRIN SCS including the final version of this software are part of this work.

An overview of the complete HV-SCS network is given in figure 25. The software of both PXI-Systems of the "HV-Schrank Münster" was adapted and integrated in the HV-SCS within this work as well as the software for the compactFieldPoints of both high voltage dividers ("Spg. teiler 35kV" and "Spg. teiler 65kV"). The software and interfaces concerning the cRIO, the measurement devices and the main high voltage supplies were developed and programmed by the group "Mess- und Automatisierungstechnik" of T. Höhn (KIT).

All parameters for the high voltage distribution rack (see table 3.1) are set and read back within a cycle time of 1 s. For all secondary parameters like temperature inside the device or supply voltage there are warnings and errors defined. All monitor values are written into a database.

[2] **ZE**ntrale datenerfassung **U**nd **S**teuerung, central data acquisition and control
[3] **O**bject-oriented **R**eal-time **C**ontrol and **A**cquisition [ORC]

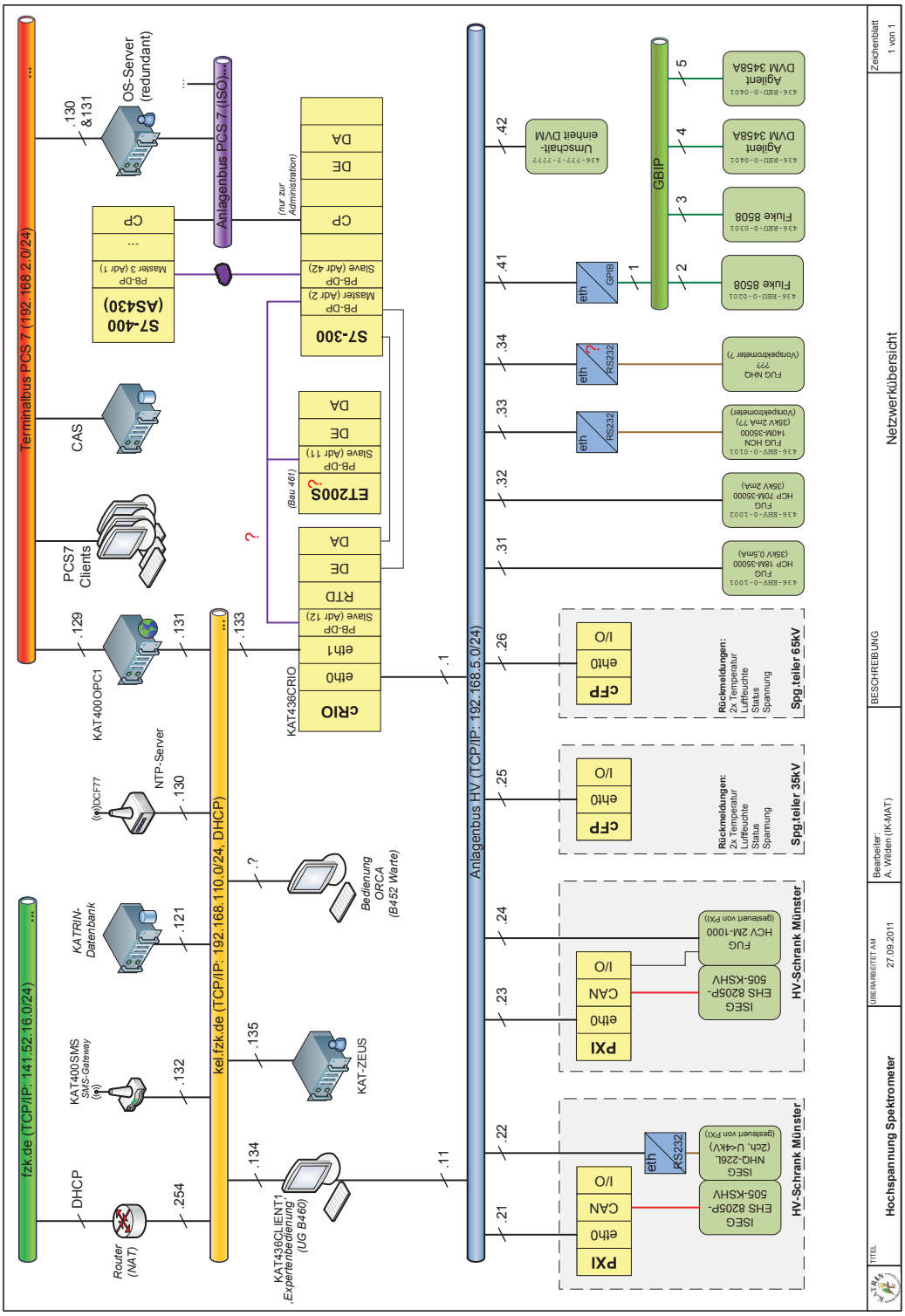

Figure 25: Overview of the high voltage slow control system. The high voltage experimental LAN ("Anlagenbus HV") controls and reads back all parameters needed for the high voltage of the pre and main spectrometer at KATRIN. The control of this system can be given either to the automated run control or the the "Experten PC" (KAT436CLIENT1). The systems enclosed in the dashed rectangles were developed in Münster.

Table 3.1: Overview of slow control data for the high voltage distribution rack. The numbers in brackets are the possible channels when two more modules of the offset voltages supplies are used. This is already realized in software but actual the additional hardware is not needed.

parameter	unit	channels to read	channels to write
set voltage	V	52 (68)	52 (68)
actual voltage	V	52 (68)	
current limit	mA	52 (68)	52 (68)
actual current	mA	52 (68)	
voltage ramp speed	V/s	10 (12)	10 (12)
module temperature	°C	6 (8)	
supply voltages of modules	V	6 (8)	
sum		230 (300)	114 (148)

3.4 Compensation of AC components and RF noise

Due to the fact that the TMPs and other connected devices are operated on high potential (spectrometer vessel will be on high potential up to −35 kV) high frequency noise is expected on this potential. Furthermore the spectrometer vessel itself acts as an antenna for electrical and electromagnetic alternating fields due to the fact that the vessel is not screened. To minimize the influence of these disturbances two complementary techniques are used for suppression. The first method is the use of two or three smoothing capacitors of 7 nF each. By this the noise in the high frequency range up to several MHz can be efficiently reduced. These capacitors will be coaxially arranged around the ceramic insulator between grounded beam tube and main spectrometer at the pre-spectrometer side (see figure 26). For the range from from DC to 1 MHz an active regulation via a triode shunt ("post regulation") was developed by S. Wüstling and will be installed at the KATRIN experiment. Figure 26 shows a schematic view of the system. The basic concept is to create a adjustable, low impedance path between the spectrometer and ground which is regulated in dependence of the noise amplitude measured on the spectrometer. The noise amplitude is measured via a pick-up probe directly at the high potential side of the ceramic insulator at the source side of the spectrometer. The grounded beam tube at the entrance of the main spectrometer serves as reference potential (GND). The AC component measured with the pick-up probe is then amplified and fed into the HV Post-Regulator, which in turn controls the triode shunt in order to counteract the noise signal. As the post-regulator also requires a DC path, an auxiliary high voltage divider is used to provide the actual HV DC value. This auxiliary divider will be a Julie-Research-Labs KV 50 from the former Mainz Neutrino Experiment.

Not only the noise can be suppressed by such a shunt, but also the DC value can be adjusted. For that the data obtained from the high precision divider are used to compensate drifts of the DC value. This information will be provided by the slow control system via software [Wüs13].

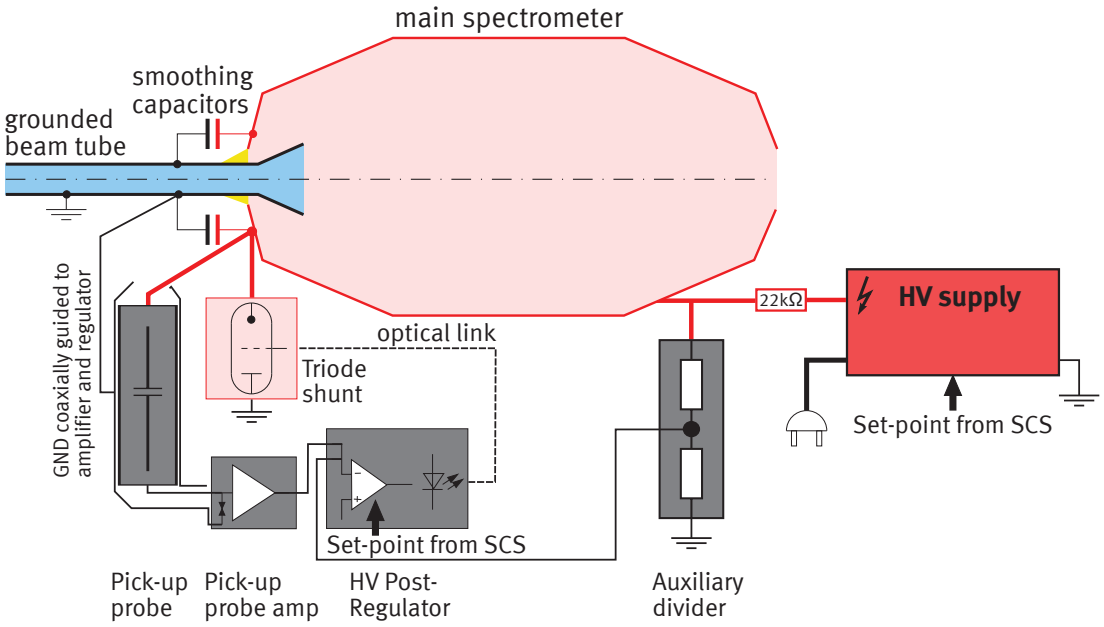

Figure 26: Schematic overview of the noise reduction methods used at KATRIN. The high frequent noise will be reduced by smoothing capacitors. These capacitors are connected to the beam tube (blue) which acts as reference potential. They will be arranged around the high potential side of the ceramic insulator (yellow). The noise in the frequency range from DC to 1 MHz will be reduced by a triode shunt regulator. The corresponding pick-up probe will tap the AC signal in the same point the smoothing capacitors are connected. This signal will be amplified and serves, in combination with the DC signal from the auxiliary divider, as input signal for the HV Post-Regulator. (Based on [Wüs13].)

3.5 Capacitance of the wire electrode system

The capacitance of the wire electrode system was measured in order to monitor the integrity of the wire electrode during bake-out cycles. The aim is to detect a change in geometry or at least a broken wire or insulator by a change in the capacitance. The measurements were done in three steps.

1. The capacitance was measured inside the high voltage distribution rack (this includes the capacitance of the connecting cable)
2. The capacitance was measured directly at the feed through without the cable to get the capacitance of the bare electrode section
3. The cable capacitances was measured to compare the values obtained at the feed-thoughts and at the high voltage distribution rack.

The last step is important because an automated measurement of the capacitances is almost ready and can only be realized inside the high voltage distribution rack. An automated measurement is necessary because frequently removing the cabling would cause a significant source of errors. The first measurements were done with an *Agilent U1732C* handheld LCR Meter. This device is able to measure inductances (L), capacitances (C) and resistors (R)

with AC voltages at frequencies of 100 Hz, 120 Hz, 1 kHz and 10 kHz. It auto-detects the properties of the circuit (e.g. mainly capacitive) and displays the value of the two-terminal device. Also the phase difference between current and voltage is displayed. This LCR meter has an uncertainty of less than 1%. In every step the following measurements were done (see figure 27):

1. Capacitance between inner wire and vessel
2. Capacitance between outer wire/frame and vessel
3. Capacitance between inner and outer wire/frame

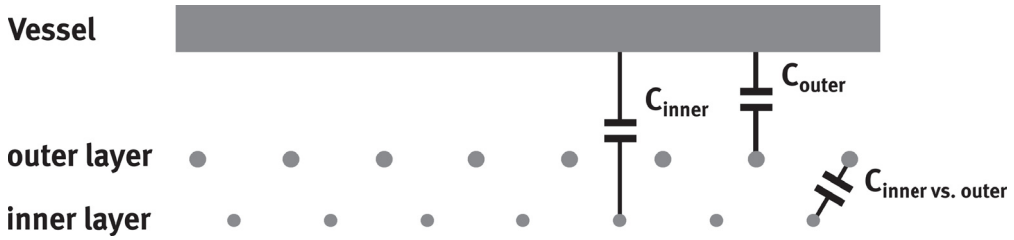

Figure 27: Schematic view of the three measured capacitances. The picture shows the equivalent circuit of the measured capacitances between the outer layer and vessel (C_{outer}), between the inner layer and vessel (C_{inner}) and between outer layer and inner layer ($C_{inner\ vs.\ outer}$).

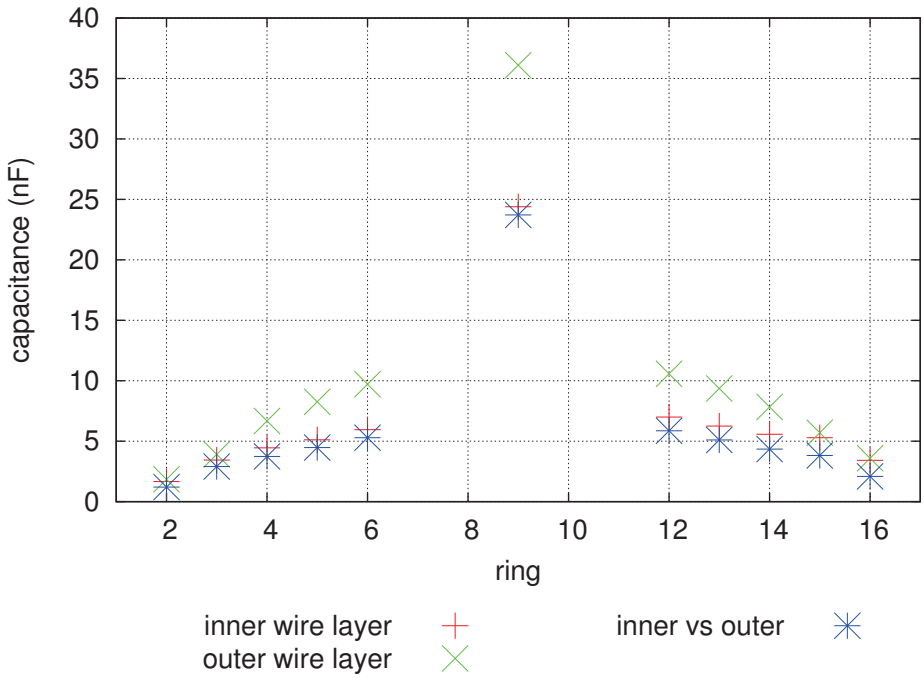

Figure 28: Capacitances at 1 kHz of all rings (only dipole 2) measured at the high voltage distribution rack. All three capacitances for each ring are shown including their cable capacitance. The central part (rings 7 to 11) is drawn at ring 9. (Source: [Bau13a])

This was also done for the measurements of the cable capacitances. A measurement for all rings of dipole two is shown in figure 28. These measurements were done inside the high

voltage distribution rack. Therefore these values include the capacitances of the cables. The measurements show a increase in capacitance towards the central part. This is due to the increasing radii and therefore an increasing number of wires. The capacitance of the central part is much higher because five rings (07-11) are connected by purpose. These five rings form the analysis plane of the main spectrometer. At the detector side the capacitances are slightly higher than at the source side because of longer cables connecting the wire electrode with the high voltage rack (source side of spectrometer).

Because all sections of the wire electrode, except for those, which is measured, are grounded, two additional points have to be considered:

- The capacitance C_{outer} is the not only the capacitance between outer layer and vessel but also an additional capacitance between the outer and inner layer has to be considered since the inner layer is grounded during this measurement.
- The capacitance C_{inner} is dominated by the capacitance between both layers because the outer layer screens the vessel hull.

The difference between both dipoles is expected to be small. These differences are caused by the wiring inside and outside the main spectrometer. Due to technical constraints they are not completely identical. The results are shown in figure 29.

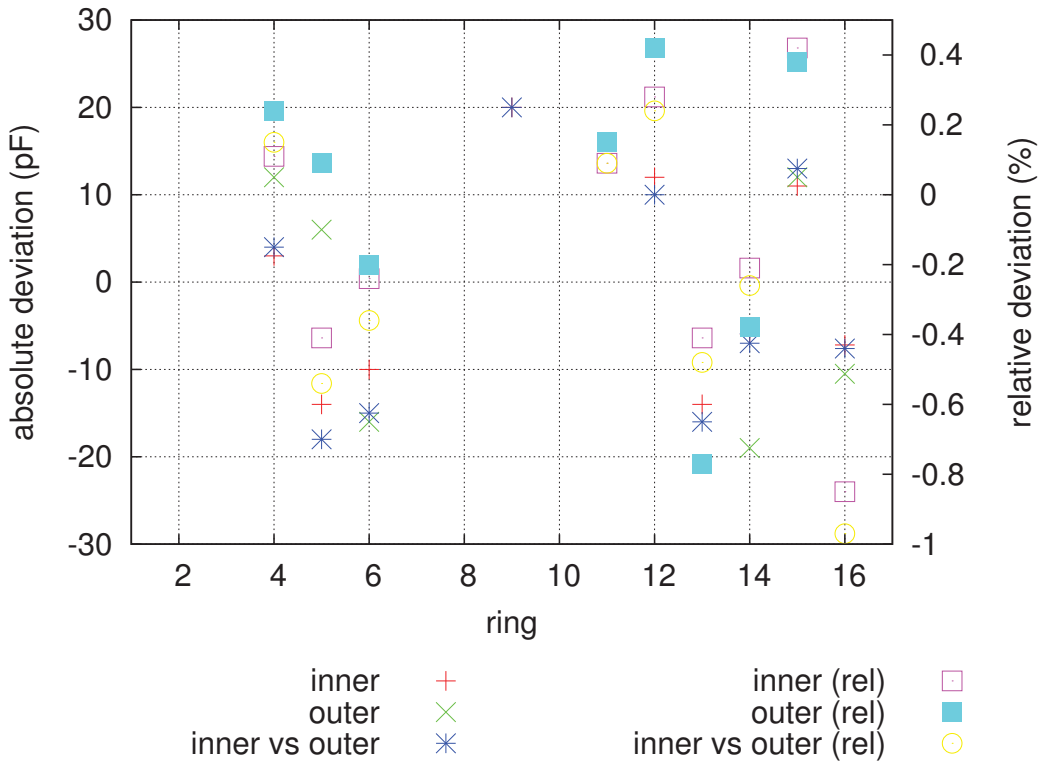

Figure 29: Difference between dipole one and two. The measurements are made with 1 kHz measurement frequency directly at the feed through. For ring two and three no measurements were done at the feed through, because no access was possible during the measurements. (Source: [Bau13a])

In order to reduce the measurement time a multiplexed automated capacitance measurement circuit was planed and installed inside the high voltage distribution rack (see figure 24). This multiplexing allows to switch the measured section to a capacitance measurement circuit. The measurement itself is a measurement of charge time with a square wave generator (Darlington transistor switching a 5 V source), a charging resistor to define the charging current and an oscilloscope to record the voltage across the capacitance during charge and discharge. With the knowledge of the square wave and the charging resistor the time constant $\tau = RC$ can be obtained from a fit to the data. More details concerning the control software and first tests at the main spectrometer will be given in [Res13].

The measurement circuit is shown in figure 30a. The voltage over the capacitor can be described for charging and discharging by the following equations:

$$U_{\mathrm{C,charge}}(t) = U_0 \cdot \left(\frac{R_{\mathrm{M}}}{R + R_{\mathrm{M}}}\right) \cdot \left(1 - e^{-\frac{t}{\tau}}\right) \tag{3.1}$$

$$U_{\mathrm{C,discharge}}(t) = U_0 \cdot \left(\frac{R_{\mathrm{M}}}{R + R_{\mathrm{M}}}\right) \cdot \left(e^{-\frac{t}{\tau}}\right) \tag{3.2}$$

$$\tau = \frac{R \cdot (C_{\mathrm{x}} + C_{\mathrm{M}})}{\frac{R}{R_{\mathrm{M}}} + 1}\,, \tag{3.3}$$

where τ is the time constant of the system, U_0 the voltage applied to the system, R the charging resistor, R_{M} the input resistance of the oscilloscope, C_{M} the input capacitance of the oscilloscope and the connecting cables and C_{x} the capacitance under test. The parameter under investigation is the capacitance C_{x} and since this parameter is only accessible via the time constant $\tau = R \cdot C$, the charging resistance R, the capacitance C_{M} and resistance R_{M} of the measurement device have to be determined and fixed for the fit.

A first test of the capacitance measurement circuit is shown in figure 30b. For this test a capacitor with a capacitance of 2.2072(5) nF was used to calibrate the system at one single point. The capacitance of the measurement circuit was fixed to 475 pF (449 pF for 4.4 m RG58 cable and 26 pF for the oscilloscope). About 40 charge and discharge curves were recorded for a second capacitor with 4.655(5) nF and a fit of equation 3.1 and 3.2 to all of these data sets leads to 4.545 nF. To obtain an absolute value with higher precision a more detailed calibration has to be carried out. This can be done recording the time constant τ for at least ten capacitors spread over the whole capacitance range which will be measured (1 nF to 40 nF). The values for C_{M} and R_{M} will be obtained by a fit to these data . The resistance R can be measured with high precision by an ohm-meter. Furthermore it has to be considered that for the discharge the current is not limited by the resistance R but by the resistance of the oscilloscope R_{M} and the resistance of the closed transistor inside the square wave generator. The simplest approach is to consider one resistance R_{M} for the case of charging and one R'_{M} for the case of discharge. To do so the time constant for discharging has to be expressed in this way:

$$\tau' = R'_{\mathrm{M}} \cdot (C_{\mathrm{x}} + C_{\mathrm{m}})\,. \tag{3.4}$$

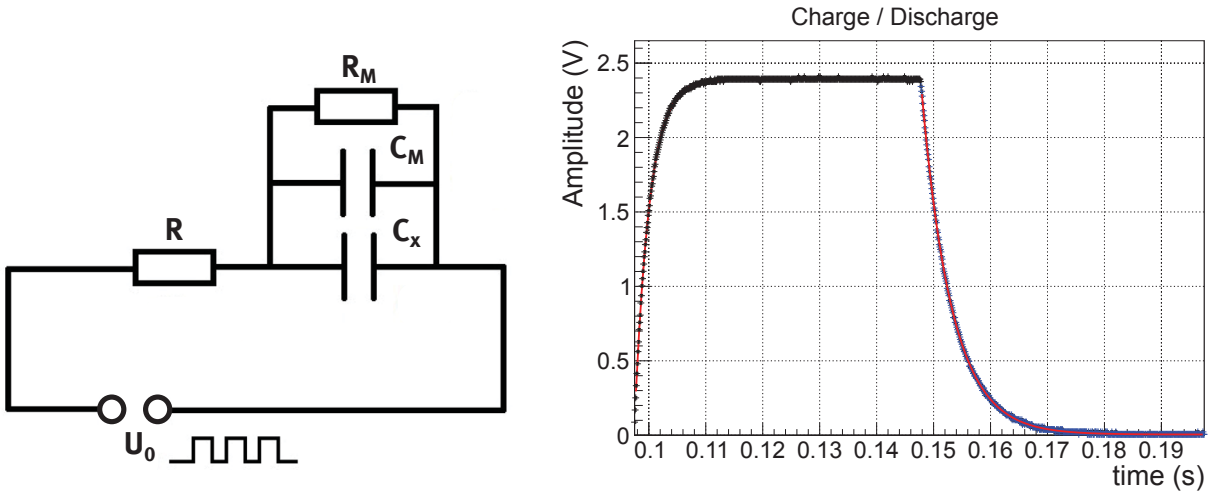

(a) (b)

Figure 30: Simplified measurement set-up of the capacitance measurement. The circuit consists of the square wave generator U_0, the charging resistor R, the input impedances of the measurement device (Oscilloscope) R_M and C_M and the capacitance under test C_x **(a)**. Measurement of a 4.655(5) nF capacitor with the automated measurement circuit. The charge and discharge time was measured 100 times. A detailed view of one charge and discharge curve is shown in **b**. Fits to all curves yielding a capacitance of 4.553 nF (without complete calibration of the system).

This can be done because the discharge current will be dominated by the oscilloscope resistance and only a little fraction will go through the closed transistor. This small fraction will than be considered by R'_M.

Fortunately the absolute value of the capacitances are not important for the measurements at KATRIN. Only the stability or reproducibility is of interest. During tests at Münster the maximum deviation between five measurements of the same capacitor was 7 pF. These measurements were spread over one day. More details about the calibration, stability and the implementation at KATRIN will be presented in [Res13].

During the bake out of the main spectrometer short cuts appeared at some wire layers. Thus not all capacitances could be measured again. The relay circuit boards for the multiplexer of the automated capacitance measurement were already installed. Hence almost all remaining capacitances (besides those electrodes being short-circuited) could be measured in a semi-automated way. The measurements were carried out with the Agilent LCR-Meter instead of the charge time measurement to make the values more comparable. For the installation of the relay boards the cables had to be stripped-down a bit. By this a reduction in capacitance of about 5 pF to 25 pF (which corresponds to about 5 to 25 cm cable) was expected. The absolute change after bake out is presented in figure 31. Due to the new circumstances, caused by the short cuts, the control board of the multiplexer was modified. In the first version it was only possible to switch one layer of one ring to the measurement circuit and all others were automatically connected to the vessel. By this no measurement of a module with a short cut was possible. The new version enables to switch multiple channel in parallel to the measurement circuit and hence to measure this combined capacitance against the vessel.

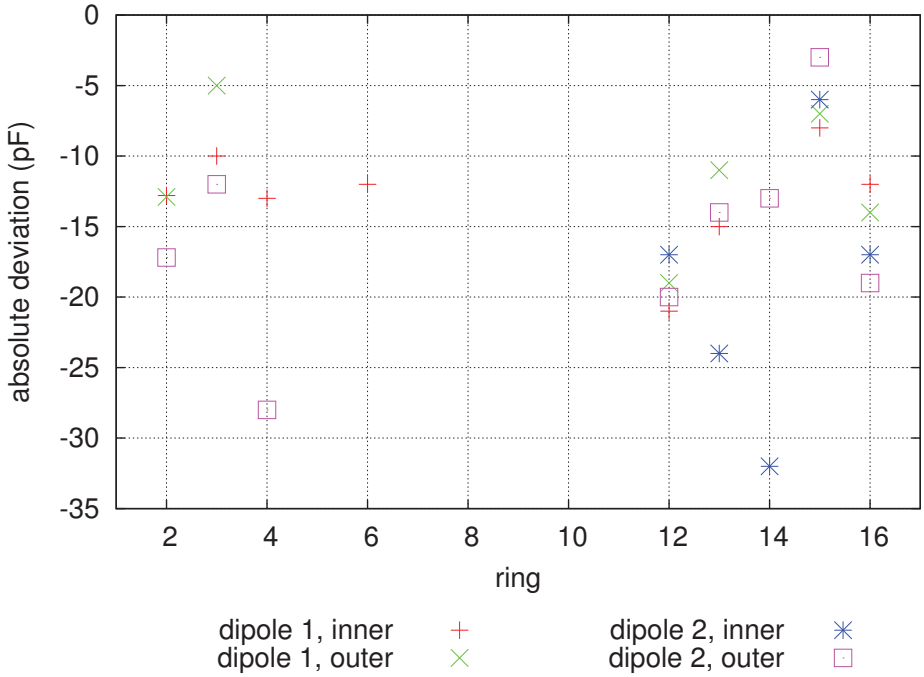

Figure 31: Difference of electrode capacitance before and after the bake out at 1 kHz measurement frequency. A reduction of 5 pF to 25 pF was expected due to changes at the set-up which can be confirmed by this measurement. (Source: [Bau13a])

All measured values except for two are within the expected range. The two channels with higher changes are not necessarily an indication for a broken wire or ceramic. Also first measurements with an angular selective electron gun shows no unexpected behaviour of the wire electrode system [Zac14].

3.6 Summary of the high voltage system

The KATRIN main spectrometer is equipped with a segmented, double-layered wire electrode system to reduce the background caused by secondary electrons. The complex system is also used to fine-tune the electric field inside the spectrometer. For that purpose up to 48 different voltages have to be applied. This is realized by a high voltage distribution rack [Ros10], which is set up isolated and referenced to the spectrometer potential. The installed power supplies for the electrode high voltage are referenced to the potential of the analysing plane, which is provided by a high precision high voltage supply. The whole system of power supplies and measurement devices is controlled via the high voltage slow control system (SCS). This system is split up in subsystems which communicate via optical fibres to overcome the high voltage differences between the systems. The SCS is written in LabView and controls and read back all of the appropriately 350 parameters. All necessary parameters can later on be set with a run script within defined ranges, which allows fully automated measurements.

To counteract noise on the high potential multiple compensation methods will be used including a HV post-regulator based on a triode shunt. This post-regulator measures the noise with a pick-up probe and controls the impedance of the triode shunt. In order to monitor the integrity of the wire electrode system an automated capacitance measurement system was installed. First test were successful but further investigations will be made in [Res13].

For the precise determination of the neutrino mass, the retarding potential of the MAC-E-Filter is of very high importance and one of the major sources of systematic uncertainties. Therefore the analysing potential will be monitored in a redundant way by the monitor spectrometer and the KATRIN ppm-class high voltage dividers. The latter will be described within in the next chapter.

Chapter 4

The high precision KATRIN voltage dividers

As presented in section 2.7 and 2.8, the precise monitoring of the retarding potential (−18.6 kV) is a crucial point for the determination of the neutrino mass with an electrostatic filter. But precision high voltage is not only of great interest for the neutrino mass determination with MAC-E Filter. Many different experiments in nuclear and particle physics make use of precision high voltage as for example experiments performing high-precision weak decay studies like aSpect [Zim00] or WITCH [Bec03]. Other applications of precision high voltage in physics are electron coolers in storage rings [Pot90], the accelerating voltage of ions in collinear laser spectroscopy (e.g. [Kri11]), or huge drift chambers or time projection chambers (e.g. [Alm10]). Of course precision high voltage applications are very important also for technical applications. For example, a high-precision high voltage divider has been developed for high voltage direct current (HVDC) electric power transmission systems [Li11]. Precision high voltage dividers are needed because voltages in the kV regime or above can usually not directly been measured but are divided into lower voltages with the help of high voltage dividers.

Since commercial available high voltage dividers do not offer the desired precision and stability, two high-precision voltage dividers were developed in cooperation with the Physikalisch Technische Bundesanstalt Braunschweig (PTB, the national metrology institute of Germany). The calibrations, especially the calibrations at low voltages (section 4.6) were carried out together with all maintenance and optimization of both dividers within this work. This chapter will describe the design, the performance and the low voltage calibration method of the two KATRIN high voltage dividers.

4.1 Basic concepts of precision high voltage dividers

The basic concept of a voltage divider is that two resistors are connected in series. For high voltage dividers the upper resistance R_{HV} usually consists of many resistors R_{i} connected in series in order to allow the requested maximum voltage (see figure 32). The output voltage (U_{out}) is measured over the low voltage resistor R_{LV}. Voltage dividers are usually characterized by a scale factor:

$$M := \frac{U_{\mathrm{in}}}{U_{\mathrm{out}}} = \frac{\sum_{i=1}^{n} R_{\mathrm{i}} + R_{\mathrm{LV}}}{R_{\mathrm{LV}}} \tag{4.1}$$

This scale factor describes the factor between input and output voltage. The total resistance of a high voltage divider is a compromise between different properties which has to be optimized for the particular application. In order to reduce the dissipated power of the divider and hence the influence of a temperature dependence of the resistors, the total resistance has to be as high as possible. On the other hand R_{LV} will also increase for higher total resistance in order to meet the desired scale factor and hence the thermal voltage noise $U_{n,eff} = \sqrt{4Rk_{\mathrm{B}}T\Delta f}$ over a frequency band Δf will also increase. Secondly, the current which flows through the voltage divider must be significantly higher than the leakage currents caused by the insulating resistance of the utilized insulators. High-precision high voltage

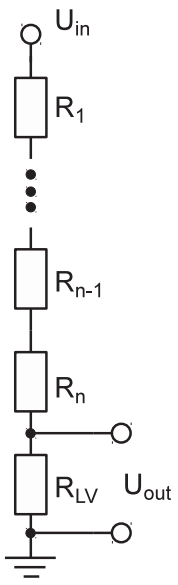

Figure 32: Simple realisation of a high voltage divider. The high voltage resistance consists of a set of resistors $R_\mathrm{i}, \mathrm{i} = 1 \ldots n$ connected in series. The ratio between input voltage U_in and output voltage U_out is described by the scale factor given in equation (1.1).

dividers typically use currents passing through the divider of about 100 µA. Therefore one has to find a suitable balance between high total resistance and a low R_LV.

For the requirements at the KATRIN-experiment, commercial high voltage dividers are not sufficient, since they do not surpass a precision of the scale factor of 10^{-4} to some 10^{-5} with a significant thermal dependence and non-neglible long-term drifts. Only the Fluke 752A "Reference Divider" offers high accuracy of 0.5 ppm [Flu83] by the use of a self calibration procedure, but this device is limited to 1 kV. Therefore the only solution is a custom-made device. But also for self-development, it is very difficult to get into the area of the desired accuracy and stability, as there are different effects to be considered. One point is the thermal behaviour of the resistors, as they have a temperature coefficient of resistance (TCR). The TCR is expressed as absolute change of resistance with temperature $\frac{\partial R}{\partial T}$ or as relative change $\frac{\partial R}{\partial T} R^{-1}$. An unbalanced change of all resistors will directly lead to a change in the scale factor of the voltage divider. In order to counteract the thermal behaviour the resistors have to be selected according to their thermal characteristics and combined in a way that the overall thermal behaviour sums up to nearly zero temperature dependence of resistance. This can be further improved by an additional thermal stabilization of the voltage divider. The first method is only possible if the resistors are available with both sign of temperature dependence. An other approach is to use selected resistors where the relative change of resistance of the low voltage and the high voltage resistor is identical and small. Thereby the scale factor keeps constant. The method applied for the resistor selection of both KATRIN dividers is described in section 4.3.

As already mentioned, disturbances caused by the high voltage, such as corona discharges or leakage currents, can change the scale factor of a high voltage divider as well. In order to reduce leakage currents, insulators with high volume and surface resistance have to be used for the mounting structure of the resistors. A very suitable material for that purpose is

PTFE[1]. To prevent corona discharges, high field gradients must be avoided and the electric field inside the divider has to be homogeneous, with low field strengths. The first voltage divider which considered this was set up by Park using special shielded resistors [Par62]. By this shielding the potential difference surrounding the resistors is equal to the voltage drop over the resistor. Additionally a huge set of resistors was investigated with respect to their temperature coefficient of resistance. It was found that one part shows a negative dependence and the other part a positive one. Therefore matched pairs were selected to achieve an average temperature coefficient close to zero. With the combination of both techniques, it was possible to set up a voltage divider ($R_{\text{total}} = 200\,\text{M}\Omega$) with an accuracy of 20 ppm at 100 kV [Par62]. Knight and Martin reached an accuracy of 5 ppm (1σ) at 100 kV with a similar set-up [Kni93]. The major differences were a total resistance of 1 GΩ and additional corona shields which obtain their voltages from the resistor chain itself. Further, actual voltage dividers with a set-up similar to that of Park, reaches accuracies of 30 ppm (k=2)[2] [DP10] and 66 ppm (k=2) [Mer09]. Both have a total resistance of 100 MΩ. The most precise system based on the design of Park is the divider of the National Measurement Institute, Australia (NMIA) [Li11]. This divider reaches accuracies better than 5 ppm (k=2) at 150 kV.

A slightly different approach was chosen for the MT100 which is the standard divider for DC voltages up to 100 kV of the PTB [Mar01]. This divider is equipped with 101 selected wire-wound resistors of 10 MΩ each. As it has already been done by Park, the resistors were also selected with respect to their temperature coefficient but with much higher accuracy. The resistors are arranged in a helix which is divided into five sections. These sections are separated by copper electrodes to shape the field inside the divider. Unlike the design of Park, the resistors themselves are not individually enclosed by a shield, but as groups of 20 by the copper electrodes. The copper electrodes obtain their potential from an independent control divider in parallel to the high precision divider. The control divider also contains capacitances to protect the high precision divider against transient overload, when the voltage is switched on or off. Further the divider is enclosed by a steel vessel and filled with compressed SF_6[3]. This Faraday cage additionally screens the divider from external disturbances like RF noise and enables a temperature regulation of the system. A comparison between the MT100 and the NMIA divider showed deviations of less than 2 ppm [Li03].

Following the design of the MT100 two high precision voltage dividers were developed at the University of Münster in cooperation with the PTB. The first divider for voltages up to 35 kV (further referred to as K35) is described in [Thü09]. The second one for voltages up to 65 kV (further referred to as K65) is a further development to higher voltages, an even higher precision and a better long-term stability w.r.t. the first divider (K35) and is presented in [Bau13c]. For the KATRIN-experiment these dividers will precisely measure the retarding potential (-18.6 kV) of the spectrometer over five years of measurement time in which the precision of 3 ppm is required for a period of two month [KC04]. The K35 and K65 were also used to calibrate the acceleration voltage of the ISOLDE facility at CERN [Kri11].

[1] Polytetrafluoroethylene

[2] $k = 2$ means a coverage factor of 2 which is equivalent to a $\pm 2\,\sigma$ region

[3] Sulfur hexafluoride. SF_6 is commonly used as insulation gas for high voltage application. The dielectric strength of SF_6 is approx. 10 kV/mm. Dry air has in comparison only 2 to 3 kV/mm.

4.2 Design of the KATRIN high voltage dividers

At the KATRIN-experiment the voltage under investigation is −18.6 kV. Because the most common reference voltage sources have an output voltage of 10 V and also the multimeter used (Agilent 3458A and Fluke 8508A) have the best performance in the 10 V (Agilent 3458A) to 20 V range (Fluke 8508A), the best scale factor would be around $M = 2000 : 1$. For the K35 [Thü09] it turned out that the best resistors, with respect to time stability and low TCR, were VISHAY Bulk Metal Foil® resistors (VHA518-11) [VIS07]. The highest available resistance of these resistors is 1.84 MΩ. In order to meet the approved current of 100 µA at the nominal high voltage of −18.6 kV, 100 resistors were chosen for the high voltage resistor chain leading to a total resistance of 184 MΩ. By this a current of 101 µA through the divider was achieved. In combination with the low voltage resistance $R_{\mathrm{LV}} = 93\,\mathrm{k\Omega}$ a scale factor of M=1972:1 was obtained. The second scale factor is the 3944:1 and the third one is the 95:1 (after upgrade in 2009 [Ros10]). The latter is important for calibration purposes since the commonly used reference divider Fluke 752A can measure, with its 100:1 scale factor, voltages up to 1 kV with an accuracy of 0.5 ppm (k=3) [Flu83]. This 95:1 scale factor is realized by the use of the last 1.84 MΩ resistor in the high voltage resistor chain.

At the K35 the high voltage resistor chain is divided into four sections of 25 resistors each, separated by copper electrodes which form a driven guard (see figure 33). The high precision resistors are arranged in a helix which changes direction after each section to minimize the inductance of the resistor chain. The resistors are arranged in pairs or in small groups in such a way that one resistor with positive TCR is placed next to one with a negative TCR of the same absolute value. By this it is ensured that both resistors have the same ambient temperature and their thermal behaviour adds to nearly zero, as presented in section 4.3. All resistors are mounted on nickel-plated brass mountings. These mountings are fixed on PTFE supports, which offer high-insulating resistances. The copper electrodes are mounted on supports made from POM[4] (see figure 33), which offers a higher mechanical strength as PTFE. The low voltage resistors for the scale factors 1972:1 and 3944:1 are placed in a closed box made from PMMA.

A second resistive-capacitive divider chain is connected parallel to the high precision divider chain. The resistive part is the control divider for the driven guard and it also enables low precision monitoring of the applied high voltage. The capacitive chain protects the high precision divider against transient overloads. A circuit diagram of the K35 divider is shown in figure 34.

The complete set-up is stored in a stainless steel vessel which works as a Faraday cage to reduce the influence of external disturbances like RF signals. Furthermore the vessel provides a sealed surrounding for an atmosphere of dry nitrogen gas at a slight overpressure of 70 mbar allowing a temperature stabilisation and avoiding humidity-driven leakage currents .

The temperature stabilisation is realized by a water circulation heating-cooling system. Thus the voltage divider is decoupled from the electrical components of the heating-cooling system and possible noise from external devices is avoided. The main components outside the high voltage divider vessel are a thermoelectric cooler, a resistive heater, both equipped with a

[4]Polyoxymethylene

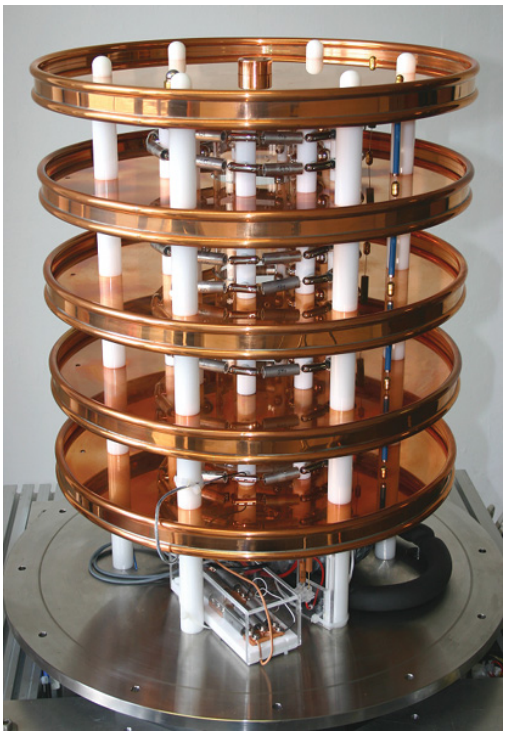

Figure 33: Picture of the K35 with removed vessel. The four sections are separated by copper electrodes which form a driven guard. The 100 resistors (grey) of the precision high voltage resistor chain are arranged in a helix structure. The resistors of the control divider (blue) are connecting the copper electrodes. The low voltage resistors are installed in a box made of PMMA. The cooper electrodes are mounted on POM rods and the resistors on PTFE supports.

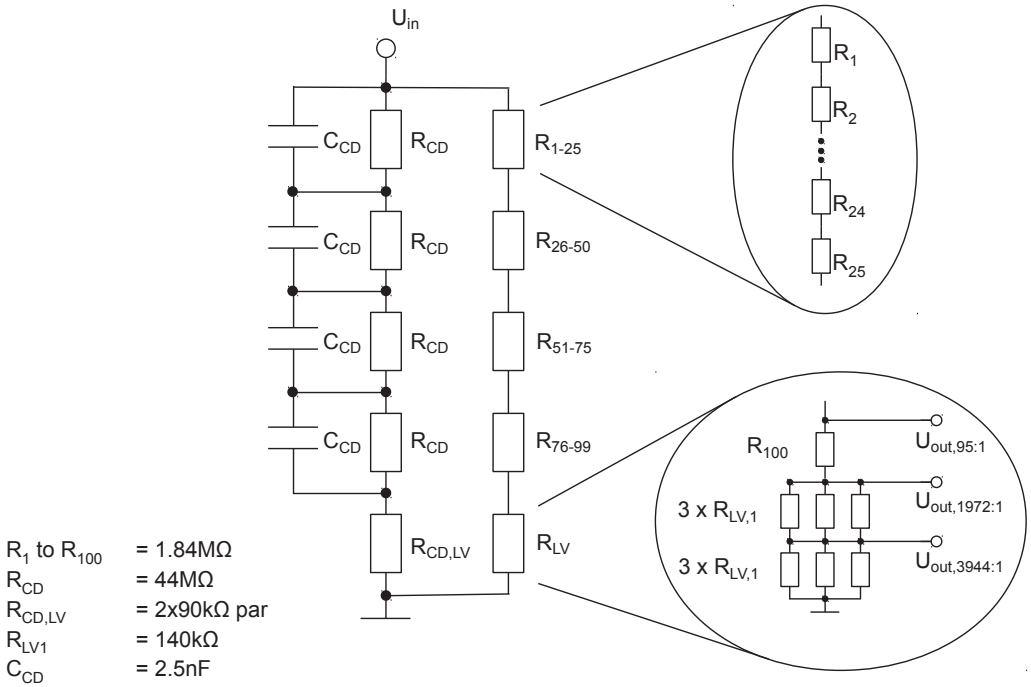

Figure 34: The equivalent circuit of the K35 divider. The low voltage part of the primary divider is shown in detail in the lower right inset. The corresponding values are listed in the lower left part of the picture.

separate heat exchanger and a power supply. The water is circulated by a pump. Inside the vessel a second heat exchanger connects the temperature of the water with the one of the dry nitrogen atmosphere. A fan transports the nitrogen through a tube made from PMMA[5] via bores in the tube wall to the resistors. The control of the system is done by a industrial PID[6] controller (WEST 4100). The humidity inside the stainless steel vessel is monitored by a humidity sensor. If the humidity is higher than 30% the nitrogen gas is exchanged. This sensor can also be used for detecting leaks in the water circuit, since the relative humidity will significantly increase if a leakage occurs within the vessel.

The K65 follows the design of the K35, which already fulfils the KATRIN requirements, but several improvements were made. The major improvements are firstly the usage of even improved resistors exhibiting a very low TCR by matching positive and negative temperature coefficients inside the resistor itself and an improved long-term stability (section 4.3). These newly developed resistors are limited in resistance to 880 kΩ. To reach a total resistance which is similar to that of the divider K35, a much higher number of resistors is requested leading, as the second advantage, to a lower thermal load per resistor at −18.6 kV. The larger number of resistors and a larger stainless steel vessel provided an additional feature: The maximum operating voltage of the high voltage divider K65 is increased to 65 kV expanding the field of possible applications, e.g. for further calibrations at the ISOLDE facility [Kri11]. Thirdly the thermal distribution inside the divider is improved by an optimized distribution of the bores inside the PMMA tube as described in [Bau13c] and [Bau09].

For the set-up of the K65 165 resistors of 880 kΩ were used (see figure 35). In principle a higher number of resistors would have been possible but would have significantly complicated and increased the size of the mechanical set-up. The 165 resistors were selected from a total of 194 resistors to obtain the smallest possible TCR. The load per resistor at the nominal high voltage of −18.6 kV was reduced from 19 mW (K35) to 14 mW. The chosen set of resistors leads to a total resistance of $\approx 147\,\mathrm{M\Omega}$ including the resistors of the low voltage section summarized as R_{LV}. The total resistance of K65 leads to a current through the precision divider chain of 127 µA.

The high voltage resistor chain is connected to the low voltage section. These section is equipped with resistors of the same type but lower values, providing different low voltage outputs (figure 35). In comparison to the K35 the low voltage resistors are placed in a dedicated section (low voltage section, lowermost section). By this, the resistors are within the nitrogen flow, which ensures a constant temperature of the low voltage resistors. By this the warm-up behaviour could be optimized as shown in section 4.5. The nominal values of the corresponding scale factors are 3636:1, 1818:1, 566:1 and 100:1. The exact values are determined in measurements at the PTB (see section 4.5) and at the Institut für Kernphysik, University of Münster. The scale factor to be used for standard measurements at KATRIN is the 1818:1 scale factor. For high voltage measurements above $|U|$ =36 kV the 3636:1 scale factor is used, because the high precision measurement range of the used multimeter (Fluke 8508A) is limited to 20 V. Additionally high resolution measurements for voltages up to 11 kV are possible because of the 566:1 scale factor.

[5] Polymethylmethacrylate, also known as acrylic glass under the trade name Plexiglass
[6] Proportional-integral-derivative controller

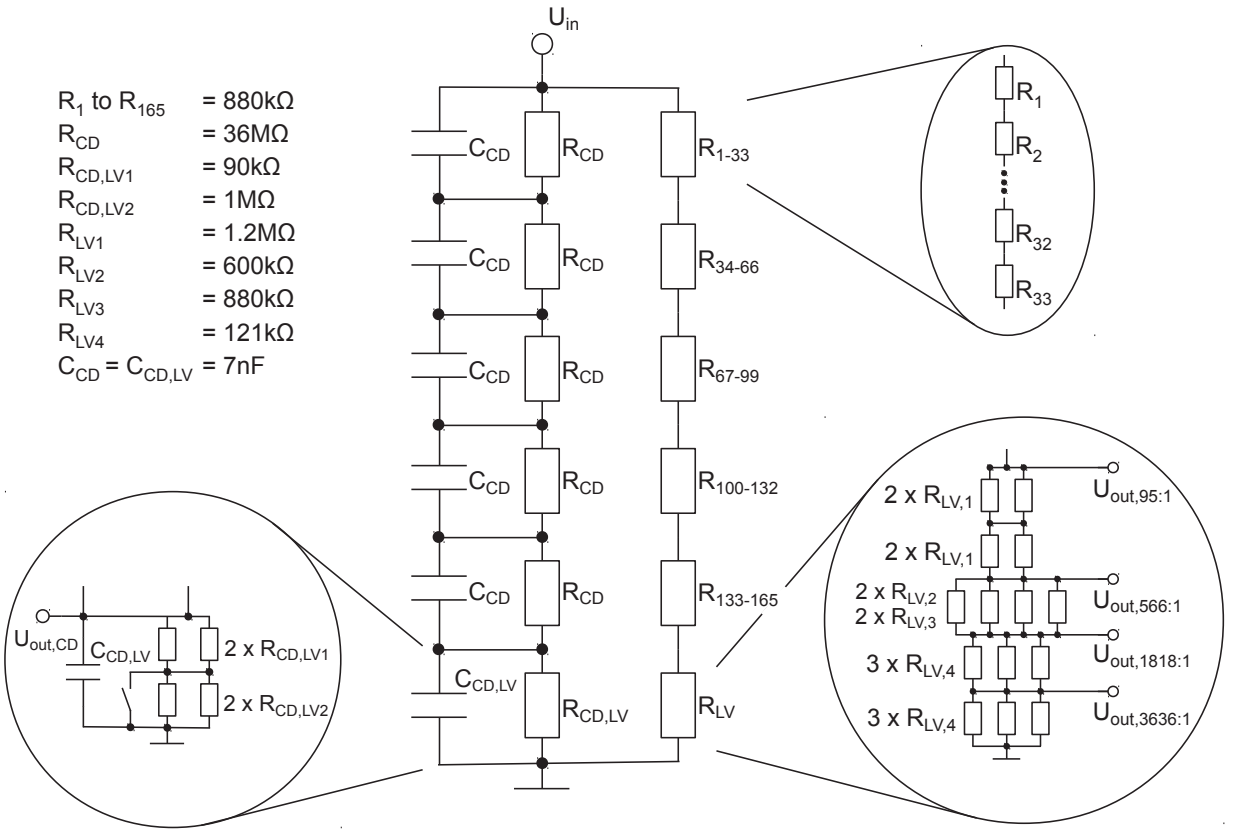

Figure 35: The equivalent circuit of the K65 divider. The low voltage part of the primary divider is shown in detail in the lower right inset. The tap of the built-in ripple probe including the additional resistor $R_{\mathrm{CD,LV2}}$ is shown in the lower left inset. The corresponding values are listed in the upper left part of the picture.

At the K65 the high voltage resistor chain is divided into five sections of 33 resistors each, also separated by copper electrodes to form a driven guard (see figure 36). The mechanical set-up is similar to that of the K35 except for the dedicated low voltage section (see figure 36). The divider is also stored in a stainless steel vessel inside a nitrogen atmosphere. The resistive-capacitive divider chain which is connected parallel to the high precision divider chain exhibits in the case of the K65, a built-in ripple probe (see section 4.4). An overview of the electrical properties of both dividers is given in table 4.1.

The temperature stabilisation of the K65 is also realized by a water circulation heating-cooling system but with a thermoelectric cooler/heater with one heat exchanger. In this case, the thermoelectric heater/cooler is supplied by a power supply with a polarity switch to enable cooling and heating with one device. The bores of the PMMA tube were optimized to control the thermal distribution inside the divider. The control of the system is done by a PID controller, but this time realized in software (LabView). A picture of the set-up with removed vessel is shown in figure 37.

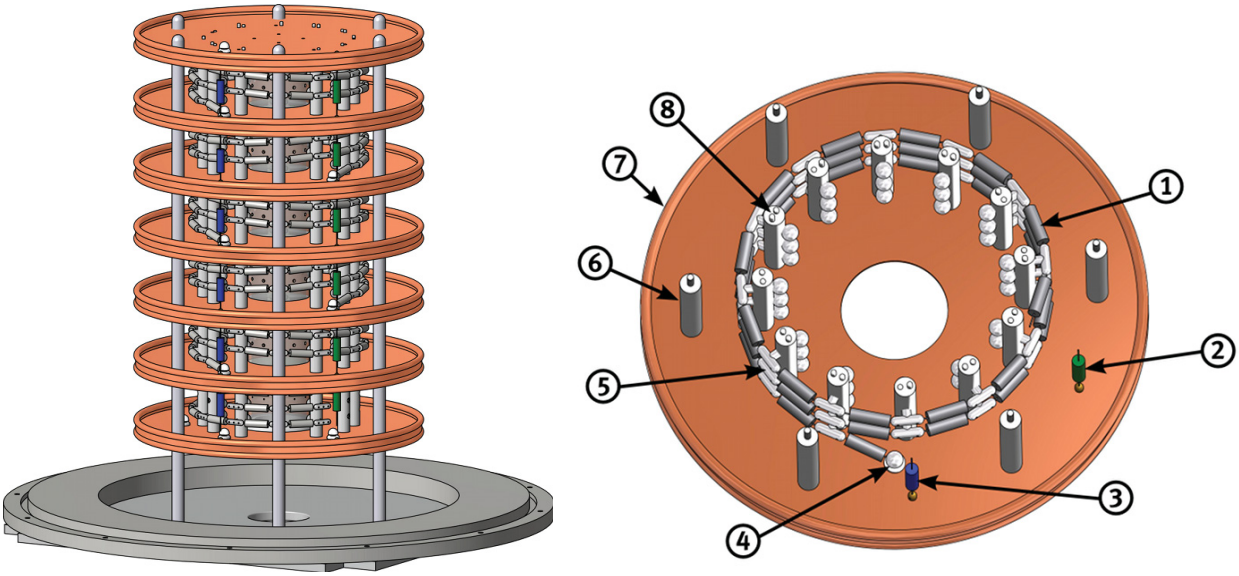

Figure 36: CAD model of the K65 divider and detailed view of one high voltage resistor section. The left picture shows the complete divider without the stainless steel vessel. The upper five sections house the 165 precision resistors and the lowermost section contains the low voltage resistors, which provide the different scale factors. In the center the PMMA tube of the heating/cooling system is shown in gray. The right picture shows one section of the high voltage resistor in detail. Each section contains the following parts: ① 33 precision resistors, ② one high voltage capacitor and ③ one high voltage resistor of the control divider, ④ insulated feedthrough for the precision resistor chain, ⑤ Nickel-plated brass mountings, ⑥ POM supports, ⑦ Copper electrode, ⑧ PTFE supports.

Table 4.1: Electrical characteristics of both dividers. The combined resistance of the precision divider chain and the control divider is stated as total resistance. The resistance of the precision divider chain is stated separately. The current denotes the current through the precision chain only.

Parameter	K35	K65
max Voltage (kV)	35	65
total resistance (MΩ)	90	81
Precision divider chain:		
resistance of precision chain (MΩ)	184	147
current at −18.6 kV (µA)	101	127
resistors in high voltage resistor	100	165
resistance of one resistor (kΩ)	1840	880
load per resistor at 18.6 kV (mW)	19	14
Control divider chain:		
resistance of control divider chain (MΩ)	176	180
resistance of one resistor (MΩ)	44	36
capacitance of each capacitor (nF)	2.5	7

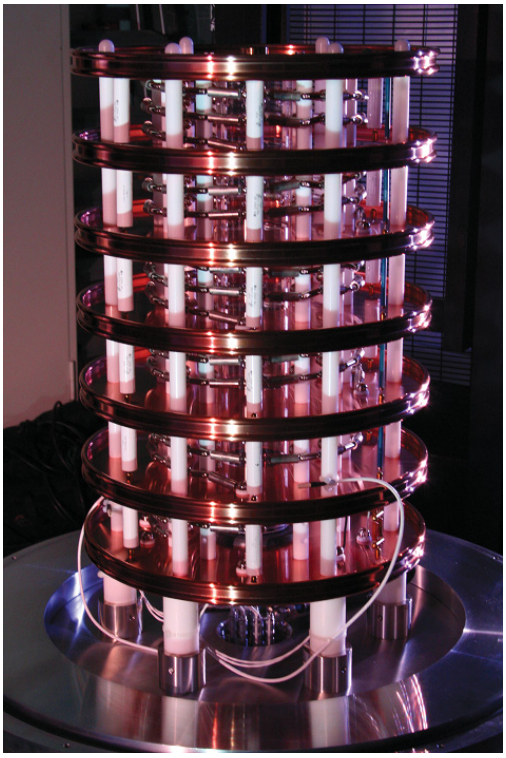

Figure 37: Picture of the K65 with removed vessel. Each of the six sections (five for the high voltage resistor and one section for the low voltage resistors) is separated by copper electrodes which form a driven guard. The 165 resistors of the precision high voltage resistor chain are arranged in a helix structure. The resistors of the control divider (blue) are connecting the copper electrodes. The cooper electrodes are mounted on POM rods and the resistors on PTFE supports.

4.3 Selection of resistors

Resistor technology

For both KATRIN high voltage dividers the same type of resistors are used, but for the K65 in an improved version. The improvements were realized through a close cooperation between the University of Münster and the company VISHAY. VISHAY's "Hermetically Sealed High Precision Bulk Metal Foil® Technology Resistors" consists of several chips mounted inside a tinned brass cylinder, which is filled with oil for a better heat transport from the chips to the cylinder. Each chip is made out of a ceramic substrate with a meander-type metal film on it. Since both materials have different thermal expansion coefficients, the metal film reacts on the mechanical stress due to temperature changes by a mechanical deformation which is a wanted feature. By designing the chip the deformation under temperature change can be controlled and thus temperature coefficients of resistances (TCR) of both signs can be realized by the manufacturing process. University of Münster's task within that cooperation was to characterize with its dedicated high-precision set-up resistors which were produced at VISHAY with certain production parameters. The aim was to build resistors consisting of chips with both positive and negative TCRs compensating each other such, that the overall TCR of the resistor becomes close to zero but with a defined sign. It should be mentioned that this compensation holds for a given operation temperature, which is in the case of the KATRIN dividers 25 °C.

The new manufacturing process in combination with the required ultra-low TCR was only possible for resistors of up to 880 kΩ. This fits in well with the already proposed increased number of resistors. The set of resistors of the new type were ordered to have the same

amount of slightly positive and negative TCRs. These resistors were additionally treated by VISHAY with a special procedure ("pre-ageing") to improve the long term stability. An overview of the specifications of the VISHAY resistors is given in table 4.2.

Table 4.2: Specification of the used VISHAY VHA518-11 resistors [VIS07]. The type of both sets of resistors is VHA518-11 but for the K65 these are manufactured according to the custom specifications. The values listed are those of the data sheet for the standard typ VHA518-11 and do not consider the internal TCR compensation and pre-ageing of the resistors for the K65.

parameter	value	comment
resistance (kΩ)	1840 / 880	K35 / K65
tolerance of resistance (%)	0.1	
max. Voltage (V)	600	
TCR ($\mathrm{ppm\,K^{-1}}$)	±2.0	−55 °C to 125 °C (T_{ref} = 25 °C)
	±0.2	24 °C to 26 °C (T_{ref} = 25 °C)
voltage coefficient ($\mathrm{ppm\,V^{-1}}$)	< 0.1	limited by test equipment ("essential zero")
inductance (µH)	0.08	typically, mainly caused by leads
capacitance (pF)	0.5	typically
load life at 2000 h (ppm)	20	at 0.1 W per chip and at 60 °C improved for K65 by pre-ageing

Selection procedure

To determine the relative change of resistance with temperature one can chose different methods. One can measure the temperature coefficient of resistance (TCR) directly by changing the temperature of the resistor while a constant voltage is applied. Another method is to determine the so called warm-up drift (WUD). Here the change of resistance over time is measured after applying a defined voltage while the ambient temperature is kept constant. For both methods the resistor under test R_{UT} is connected in series with a reference resistor R_{ref} to form a simple divider circuit (see figure 38). The chosen reference resistor has a resistance of R_{ref} =36.8 kΩ, thus the thermal load of this resistor is negligible. In order to not compromise the measurement precision, the reference resistor is also a high-precision Bulk Metal Foil® resistor from VISHAY.

The investigation of a representative set of resistors proved a strong correlation between WUD and TCR. Because the measurements of the WUD are much more simple to carry out, this method was chosen for the resistor selection of both KATRIN dividers [Thü09, Hoc08, Bau09]. A further advantage is, that the resistors are tested under conditions of operation. During operation the resistors will have a stable ambient temperature and a temperature gradient along its own profile. This gradient is caused by the heating of the resistor due to the power dissipation in combination with the limited thermal conductance of the oil inside the resistor.

The input voltage (U_{in}) was delivered by a Fluke 5720A Calibrator and the voltage drop (U_{out}) over the reference resistor was measured with an Agilent 3458A voltmeter. Both

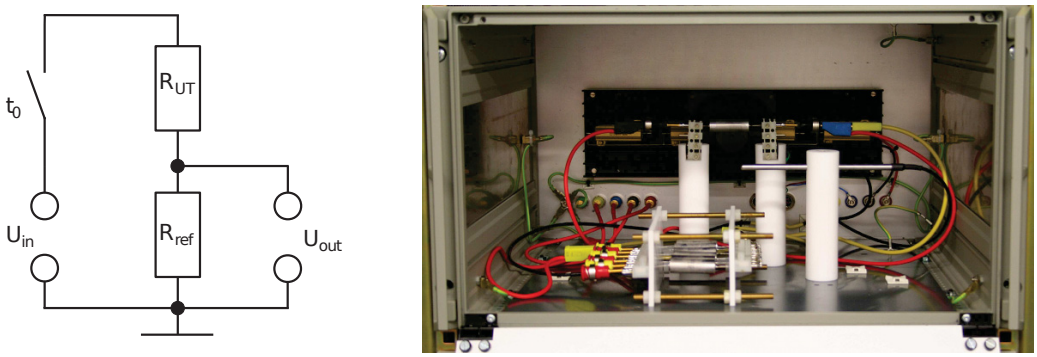

Figure 38: Arrangement to measure the WUD. The circuit of the voltage divider is shown in the left picture. During measurement this divider is placed in a temperature stabilized box at $(25.0 \pm 0.1)\,°C$ (right picture). The reference resistor is placed in the middle of the set-up onto two PTFE rods. The third rod holds the PT100 temperature sensor. The black heat sink at the back is equipped with high power resistors for heating. The resistors under test are mounted between to sheets of PTFE (fixed by threaded rod made out of brass) to easy change the resistors between the measurement.

devices was granted a warm-up time of at least four hours to achieve the maximum stability. Stable conditions during the WUD measurements are realized by placing the resistors in a temperature stabilized box at the default operation temperature of the resistors of $(25.0 \pm 0.1)\,°C$. This box also acts as Faraday cage and screens the set-up against external influences.

To measure the WUD the following procedure was chosen: After applying 255 V (600 V in the case of K35) at the time t_0 the voltage drop over the reference resistor was measured every 10 s over a period of 30 min. The relative change of the measured voltage is the relative change of resistance times a small correction factor considering the influence of the reference resistor:

$$\frac{\Delta U_{\text{out}}}{U_{\text{out}}} = \frac{\Delta R_{\text{UT}}}{R_{\text{UT}}} \cdot \frac{R_{\text{UT}}}{R_{\text{UT}} + R_{\text{ref}}} := \alpha_{\text{WUD}} \cdot \frac{R_{\text{UT}}}{R_{\text{UT}} + R_{\text{ref}}} \tag{4.2}$$

This change over time is the so called WUD coefficient α_{WUD} (see figure 39). The WUD coefficient was determined by fitting a constant to the data of the last 15 min. The short-term fluctuations of the measurement equipment is not well known, since the manufacturer usually provides the long-term drifts for 8 or 24 hours. Therefore the short-term fluctuations of the set-up was determined by requesting that the reduced χ^2 of the fits are about one yielding a measurement uncertainty of the relative change of resistance of 0.05 ppm (see error bars in figure 39). The results of the resistor selection for K35 is shown in figure 40 and for K65 in figure 41. The results for the selection of the resistors for K65 (see figure 41) also demonstrates that VISHAY indeed delivered resistors with positive and negative α_{WUD} as requested for the K65. In figure 40 one might think that the resistors of the K35 show a significant higher WUD as those of K65 but the resistors of K35 were measured with 600 V and those of K65 with 255.2 V. Since the WUD raises linearly with the dissipated power, these values become comparable.

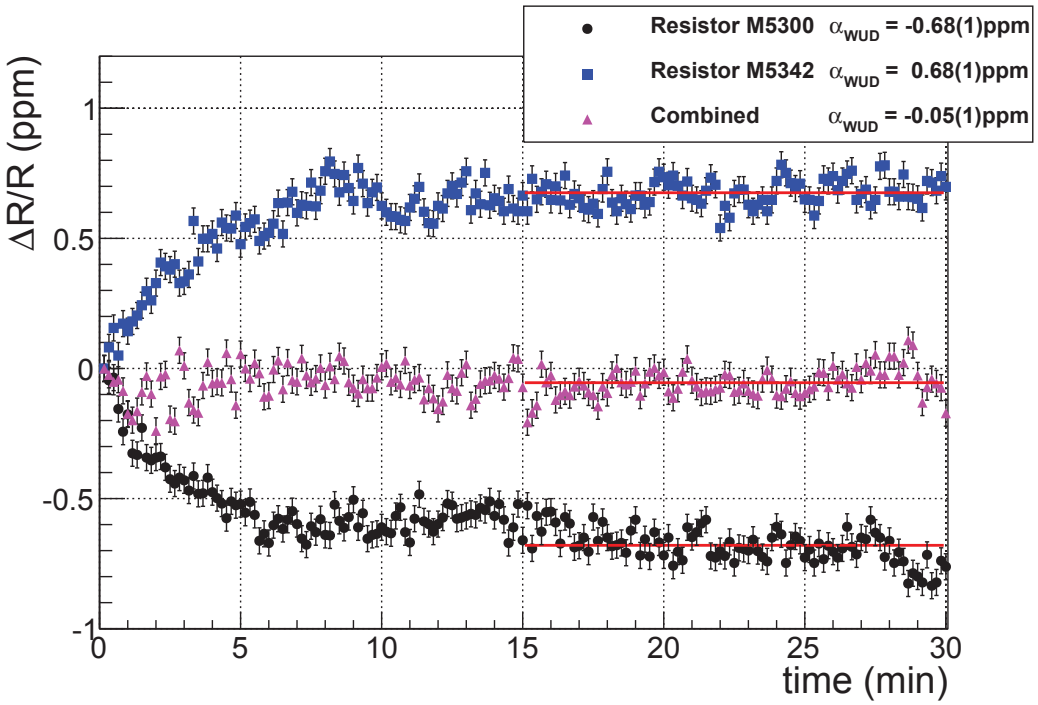

Figure 39: The warm-up drift α_{WUD} for $U_{\mathrm{in}} = 255.2\,\mathrm{V}$ for the resistors, named M5300 and M5342 is shown (all resistors for K65). The triangles show the residual warm-up drift α_{WUD} for $U_{\mathrm{in}} = 510.4\,\mathrm{V}$ after both resistors were connected in series. The red lines denotes the constant fit to the last 15 min. The legend exhibits the fits and its statistical uncertainties.

4.4 Built-in ripple probe of the K65

One additional feature of the K65 divider is the built in ripple probe. It can be used to investigate noise on DC high voltages. This can be done during the ppm precise measurement of high DC voltages of up to 65 kV. The ideal case of a ripple probe is a high-pass filter composed of a capacitor (C) and a resistor (R) connected in series. For frequencies much higher than the cut-off frequency ($f_{\mathrm{c}} = \frac{1}{2\pi RC}$) the scale factor of such a probe is equal to 1. The K65 uses the control divider tap as ripple probe with the consequence that for low frequencies the scale factor will be dominated by the resistive part of the control divider ("low precision HV-divider") and for high frequencies by the scale factor of the capacitive part ("capacitive divider"). This capacitive divider causes the scale factor for high frequencies to be around 6 instead of 1. For measurements with the ripple probe two additional resistors ($R_{\mathrm{CD,LV2}} = 500\,\mathrm{k\Omega}$, see figure 35) can be switched into the low voltage resistor chain of the control divider chain to reduce the cut-off-frequency to approx. 60 Hz. This allows to investigate noise also in the regime of the line frequency (50 to 60 Hz).

Figure 42 shows a measurement of the frequency response characteristic and phase difference of the built-in ripple probe. For this measurement the AC voltage of $3\,\mathrm{V_{RMS}}$ was delivered by a Fluke 5720A Calibrator and the output voltage was measured with a National Instruments PXI 5922 digitizer. The frequency was varied from 10 Hz to 400 kHz.

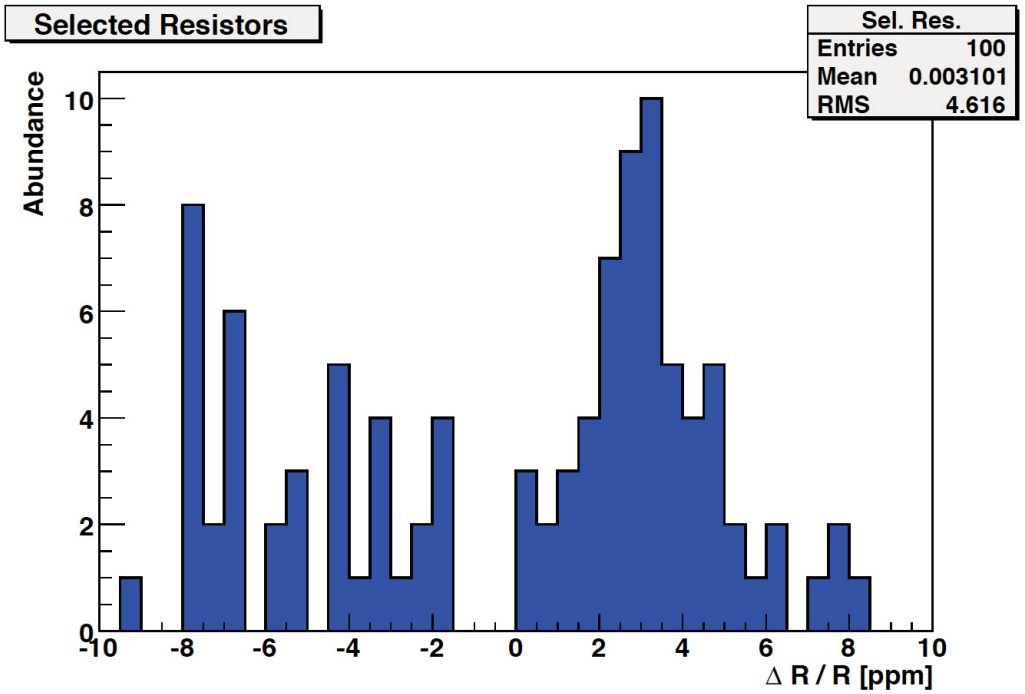

Figure 40: Results on warm-up drift at 600 V of the 100 selected resistors for the K35 divider. The α_{WUD} ($\frac{\Delta R}{R}$) of all resistors sums up to 0.31 ppm which corresponds to a mean α_{WUD} of 0.0031 ppm per resistor. (Source: [Thü07])

In order to find a simple description of the ripple probe the high voltage and the low voltage part of the control divider is combined to one equivalent resistance and one equivalent capacitance each:

$$R_{\mathrm{CD}}^{\mathrm{HV}} = 5\,R_{\mathrm{CD}} \qquad C_{\mathrm{CD}}^{\mathrm{HV}} = \frac{C_{\mathrm{CD}}}{5} \tag{4.3}$$

$$R'_{\mathrm{CD,LV}} = \frac{R_{\mathrm{CD,LV1}}}{2} + \frac{R_{\mathrm{CD,LV2}}}{2} \qquad C_{\mathrm{CD,LV}} = C_{\mathrm{CD}} \tag{4.4}$$

In figure 42 the theoretical description of this system was fitted to the measurements. For $R'_{\mathrm{CD,LV}}$ and $C_{\mathrm{CD,LV}}$ the influence caused by the impedance of the measurement device is considered in the theoretical description. Since the fit is only sensitive to the product of $R{\cdot}C$ the values for $R_{\mathrm{CD}}^{\mathrm{HV}}$ and $R'_{\mathrm{CD,LV}}$ were fixed to the values measured with a Fluke 8508A. The capacitances $C'_{\mathrm{CD}} = 1.4(2)$ nF and $C_{\mathrm{CD,LV}} = 7.1(2)$ nF were obtained by the fit. This is in nice agreement with the measured values of $C_{\mathrm{CD,meas}}^{\mathrm{HV}} = 1.4(1)$ nF and $C_{\mathrm{CD,LV,meas}} = 7.1(1)$ nF.

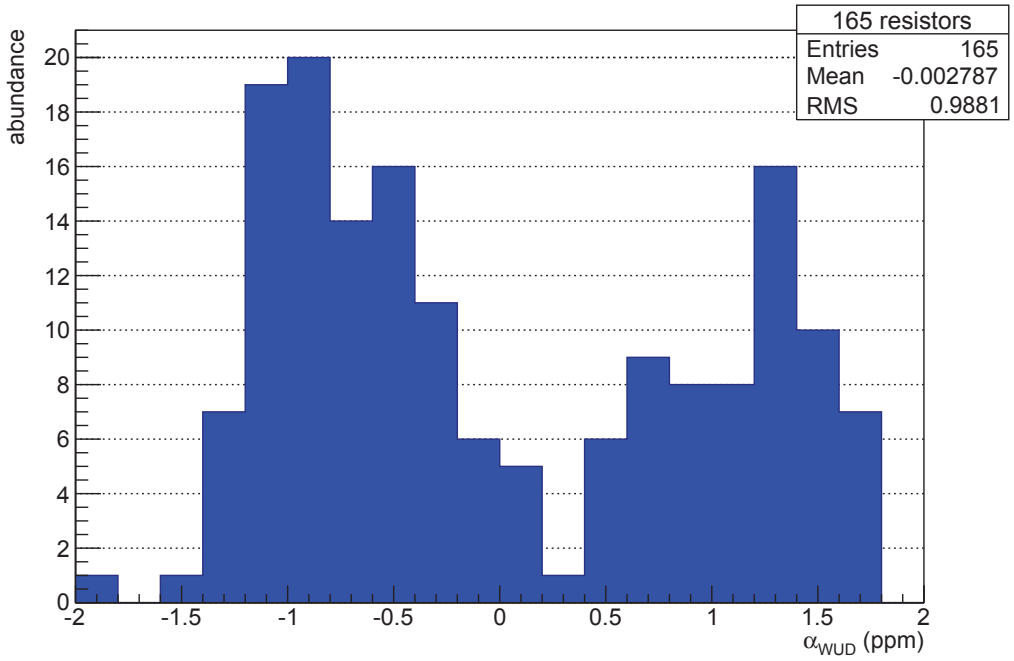

Figure 41: Results on warm-up drift at 255.2 V of the 165 selected resistor for the K65 divider. They were produced to have the same amount of resistors with a positive and negative α_{WUD}. The α_{WUD} of all resistors sums up to -0.46 ppm which corresponds to a mean α_{WUD} of -0.0028 ppm per resistor.

4.5 Calibration at PTB

Two calibrations of both KATRIN dividers were carried out at the laboratory for high-voltage metrology (working group 2.32) of the PTB Braunschweig. All measurements were done in comparison to the MT100 [Mar01], the standard divider of the PTB which is one of the most precise and most stable high voltage dividers in the world [Li03]. Each measurement was done for both polarities and the uncertainties in this section are always given in units of standard deviations σ. The calibration of the 100:1 scale factor was carried out at 1 kV directly with the Fluke 752A divider. Therefore its systematic uncertainty is 1.2 ppm ($k = 2$) because it only depends on the transfer uncertainties of the digital voltmeters and the uncertainty of the reference divider (see table 4.3). The systematic uncertainties for the remaining scale factors of the KATRIN dividers amount to 2 ppm ($k = 2$) as stated in [Thü09].

Calibration phase 2009

The first measurements of the K65 divider at the PTB were carried out from October to December 2009. During this phase the scale factors, the voltage dependence and the temperature dependence was measured. Although the voltage divider provides an additional 566:1 scale factor, this one has not been investigated. The determined parameters are shown

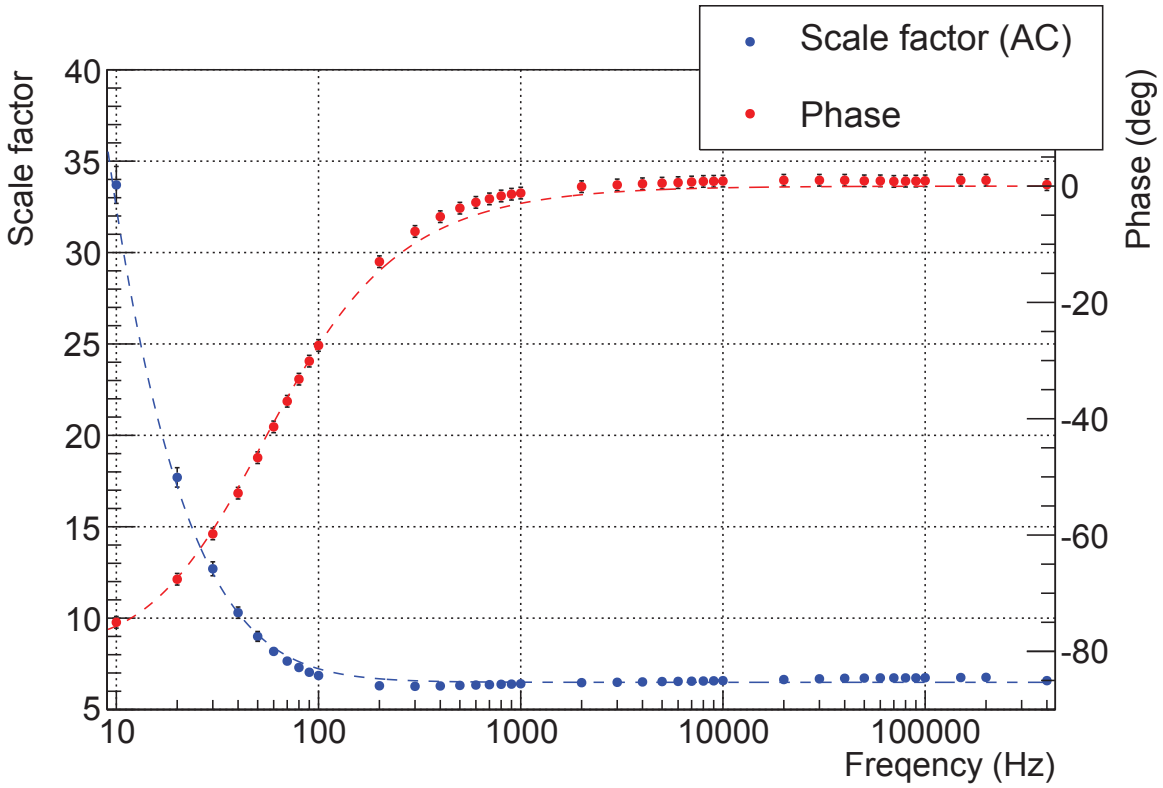

Figure 42: Measurement of the scale factor (blue points) and phase (red points) of the frequency response of the built-in ripple probe with the two additional resistors $R_{\mathrm{CD,LV2}}$ switched into the low voltage resistor chain. A fit to the data points is denoted as dashed lines.

Table 4.3: Summary of the uncertainties of the calibration of the 100:1 scale factor at 1kV. The uncertainties are taken from the corresponding specifications. For the Fluke 752A reference divider the uncertainty in normal distributed and the coverage factor is k = 3. For both digital voltmeter the uncertainty relative to calibration standards over 24 h was chosen. This is state in the manual of the Agilent 3458A with a rectangular distribution and for the Fluke 8508A with a normal distribution and a coverage factor of k = 2.

Instrument	device	probability distribution	divisor	rel. uncertainty (ppm)
Fluke 752A	ref. divider	Normal (k = 3)	3	$0.5/3 = 0.17$
Fluke 8508A	voltmeter	Normal (k = 2)	2	$0.9/2 = 0.45$
Agilent 3458A	voltmeter	Rectangular	$\sqrt{3}$	$0.56/\sqrt{3} = 0.32$
combined standard uncertainty				0.58

in tabular 4.5. The K35 was already measured in 2005 and 2006, but since the 100:1 scale factor was implemented in 2009 and hence the resistance of the divider chain was changed, these data can not be compared to those taken in 2009 and 2011.

Table 4.4: Summary of the results for K35 obtained at the calibration phase in 2009 at PTB. Listed are the scale factors determined at the given calibration voltage, their relative standard deviations over all measurements and their calibration uncertainties. The measurements were always done with voltages of both polarities and the results stated here are the mean of the values for both polarities. The linear voltage dependence is given as mean value for the scale factors 1972:1 and 3944:1.

Parameter	100:1	1972:1	3944:1
scale factor (at 1 kV for 100:1 else 35 kV)	95.20535	1972.4584	3944.9163
relative standard deviation	$3.7{\cdot}10^{-7}$	$5.5{\cdot}10^{-7}$	$5.0{\cdot}10^{-7}$
calibration uncertainty (k=2)	$1.2{\cdot}10^{-6}$	$2{\cdot}10^{-6}$	$2{\cdot}10^{-6}$
linear voltage dependence α' (8-32kV)		-6.1(2)·10^{-8}/kV	

Table 4.5: Summary of the results for K65 obtained at the calibration phase in 2009 at PTB. Listed are the scale factors determined at the given calibration voltage, their relative standard deviations over all measurements and their calibration uncertainties. The measurements were always done with voltages of both polarities and the results stated here are the mean of the values for both polarities. The temperature dependence was measured for the 1818:1 scale factor. The linear voltage dependence is given as mean value for the scale factors 1818:1 and 3636:1.

Parameter	100:1	1818:1	3636:1
scale factor (at 1 kV for 100:1 else 35 kV)	100.51484	1818.1096	3636.2743
relative standard deviation	$1.2{\cdot}10^{-7}$	$6.8{\cdot}10^{-7}$	$7.0{\cdot}10^{-7}$
calibration uncertainty (k=2)	$1.2{\cdot}10^{-6}$	$2{\cdot}10^{-6}$	$2{\cdot}10^{-6}$
temperature dependence (18 to 34 °C)		$< 1 \cdot 10^{-7}$/K	
linear voltage dependence α' (8-32kV)		-1.9(2)·10^{-8}/kV	

Calibration phase 2011

A second calibration phase was carried out from September to December 2011. The scale factors, the voltage dependence and the warm-up behaviour were investigated during this phase.

For the warm-up behaviour the change in scale factor was measured over 30 min after the high voltage was applied. To obtain a possible warm-up behaviour of the MT100, a dedicated

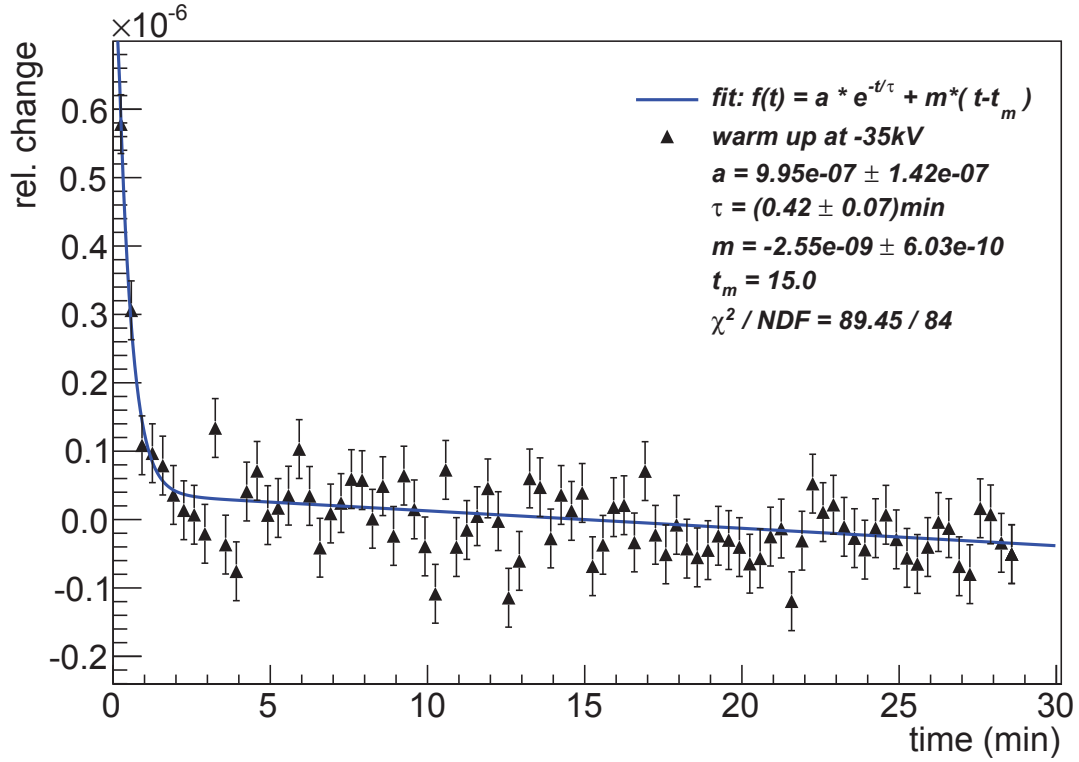

Figure 43: Relative change of the 1818:1 scale factor (K65) after applying −35 kV. The scale factor measurement in comparison to the scale factor of the MT100 started with the application of −35 kV. Before that the K65 divider was idle for at least 30 min. The plotted values are corrected for the measured warm-up behaviour of the MT100. The data set consists of the mean values of five independent measurements. The error bars represent the standard deviations between these five measurement series. The fit function was the sum of an exponential function and a 1^{st} order polynomial because a small linear drift was observed. This fit yields a time constant of 0.42(7) min. The first measurement point was discarded and the fit was done for the whole measurement period of 30 min. The small linear drift of $-2.6(6) \times 10^{-9}\,\mathrm{min}^{-1}$ cannot be used to estimate a long-term drift. It can be caused from a slow process during the thermalization of the divider and is not observed over longer periods of time.

measurement was made using the K65 as reference divider. This was done by connecting the MT100 via a vacuum circuit-breaker to the system. After the K65 was stabilized the voltage was ramped down fast, the MT100 was switched by the vacuum circuit-breaker to the system and the voltage was ramped up again. In all four measurements a slight deviation in the sub-ppm region was observed and all measurements were corrected for this warm-up behaviour. The warm-up behaviour of both dividers was measured for the 1972:1, 3944:1, 1818:1 and 3636:1 scale factors at voltages of 18.6 kV and 35 kV with both polarities. As an example the warm-up behaviour at −35 kV of the 1818:1 scale factor of K65 is shown in figure 43. The measurements at 18.6 kV did not exhibit any measurable warm-up deviation.

The voltage dependence of the dividers was investigated by multiple measurements between 5 kV and 35 kV in steps of 5 kV for both polarities. These data sets were fitted by a 2^{nd}

order polynomial. The quadratic term is motivated by the heating of the resistors due to the U^2/R loss and their temperature dependent resistance. The linear term is a combination of various effect. On the one hand leakage currents will go linearly with the applied voltage but also secondary effects of the heating of the resistors (like temperature dependent heat conduction) can cause a linear effect. Hence it is not possible to quantify the leakage current effect without further investigations. For a voltage step of 35 kV the relative change in scale factor is approximately 2 ppm for the K35 and approximately 1.5 ppm for the K65. In addition the data sets were fitted by a linear function in the range between 10 kV and 35 kV to compare these results to older ones. For the K35 the voltage dependence between 2009 and 2011 doesn't change significantly. But for K65 the dependence raises from −0.019 ppm for both scale factors to −0.049 ppm for the 1818:1 and −0.035 ppm for the 3636:1 scale factor. The reason for this is not clear and has to be investigated during the next calibration phase at PTB, which is scheduled for October 2013.

During calibration usually mid term stability is also investigated. Figure 46 shows the stability of both dividers over a period of 16 h. The K65 shows a very small warm-up behaviour of about 0.1 ppm in the first 30 min and in contrast K35 shows an initial deviation of approx. −0.3 ppm over the first 4 h. The lowermost histogram in figure 46 shows that for the K65 there is no difference in Gaussian width and position between the whole measurement run and the last 12 h. The slow warm-up effect of K35 is probably caused be the encapsulated low voltage resistors at the K35. Due to the surrounding PMMA box the thermalization is not that efficient. This shows that the optimization of the thermal distribution inside the divider is a measurable improvement. The measurement shows that it is possible to carry out measurements over several hours with an uncertainty in the sub-ppm range. Even the small warm-up effect of −0.3 ppm at the K35 is negligible for almost all applications. With the K65 it is possible to make mid term measurements with an uncertainty of less than 0.1 ppm (k=1) or 0.16 ppm (k=2) without the need of a warm-up phase. In order to make measurement in the sub-ppm range it is nevertheless meaningful to grant a warm-up of at least 1 min to let the measurement system stabilize as shown in figure 43. At least for a voltage change of more than 1 kV.

To determine the long-term stability of the divider, a linear time dependence between the two calibrations in 2009 and 2011 was assumed. For all scale factors of the K65 divider the obtained long-term stability was measured to be less than 0.1 ppm/month (see table 4.7).

Table 4.6: Calibration phase in 2011 at PTB for K35. Listed are the scale factors for the applied calibration voltage, their relative standard deviations over all measurements and their calibration uncertainties. The linear voltage dependence (measured for both polarities) is given for the 1972:1 and the 3944:1 scale factor. The warm-up deviation and time constant was measured for the 1972:1 and the 3944:1 scale factor.

Parameter	100:1	1972:1	3944:1
scale factor (at 1 kV for 100:1 else 35 kV)	95.22078	1972.4566	3944.9119
rel. standard deviation	$2.7{\cdot}10^{-7}$	$1.3{\cdot}10^{-7}$	$1.0{\cdot}10^{-7}$
calibration uncertainty (k=2)	$1.2{\cdot}10^{-6}$	$2{\cdot}10^{-6}$	$2{\cdot}10^{-6}$
linear voltage dependence α' (10-35kV)		$-6.34(5){\cdot}10^{-8}$/kV	$-4.88(9){\cdot}10^{-8}$/kV
warm-up deviation at 35kV		$<1{\cdot}10^{-6}$	
warm-up time constant at 35kV		<1min	
stability (per month)		can not be stated due to the exchange of one faulty resistor in August 2010	

Table 4.7: Calibration phase in 2011 at PTB for K65. Listed are the scale factors for the applied calibration voltage, their relative standard deviations over all measurements and their calibration uncertainties. The linear voltage dependence (measured for both polarities) is given for the 1818:1 and the 3636:1 scale factor. The warm-up deviation and time constant was measured for the 1818:1 and the 3636:1 scale factor.

Parameter	100:1	1818:1	3636:1
scale factor (at 1 kV for 100:1 else 35 kV)	100.51479	1818.1078	3636.2668
rel. standard deviation	$4.5{\cdot}10^{-7}$	$1.1{\cdot}10^{-7}$	$1.5{\cdot}10^{-7}$
calibration uncertainty (k=2)	$1.2{\cdot}10^{-6}$	$2{\cdot}10^{-6}$	$2{\cdot}10^{-6}$
linear voltage dependence α' (10-35kV)		$-4.88(5){\cdot}10^{-8}$/kV	$-3.46(5){\cdot}10^{-8}$/kV
warm-up deviation at 35kV		$<1{\cdot}10^{-6}$ (see figure 43)	
warm-up time constant at 35kV		<1min (see figure 43)	
stability (ppm/month)	$-0.02{\cdot}10^{-6}$	$-0.04{\cdot}10^{-6}$	$-0.09{\cdot}10^{-6}$

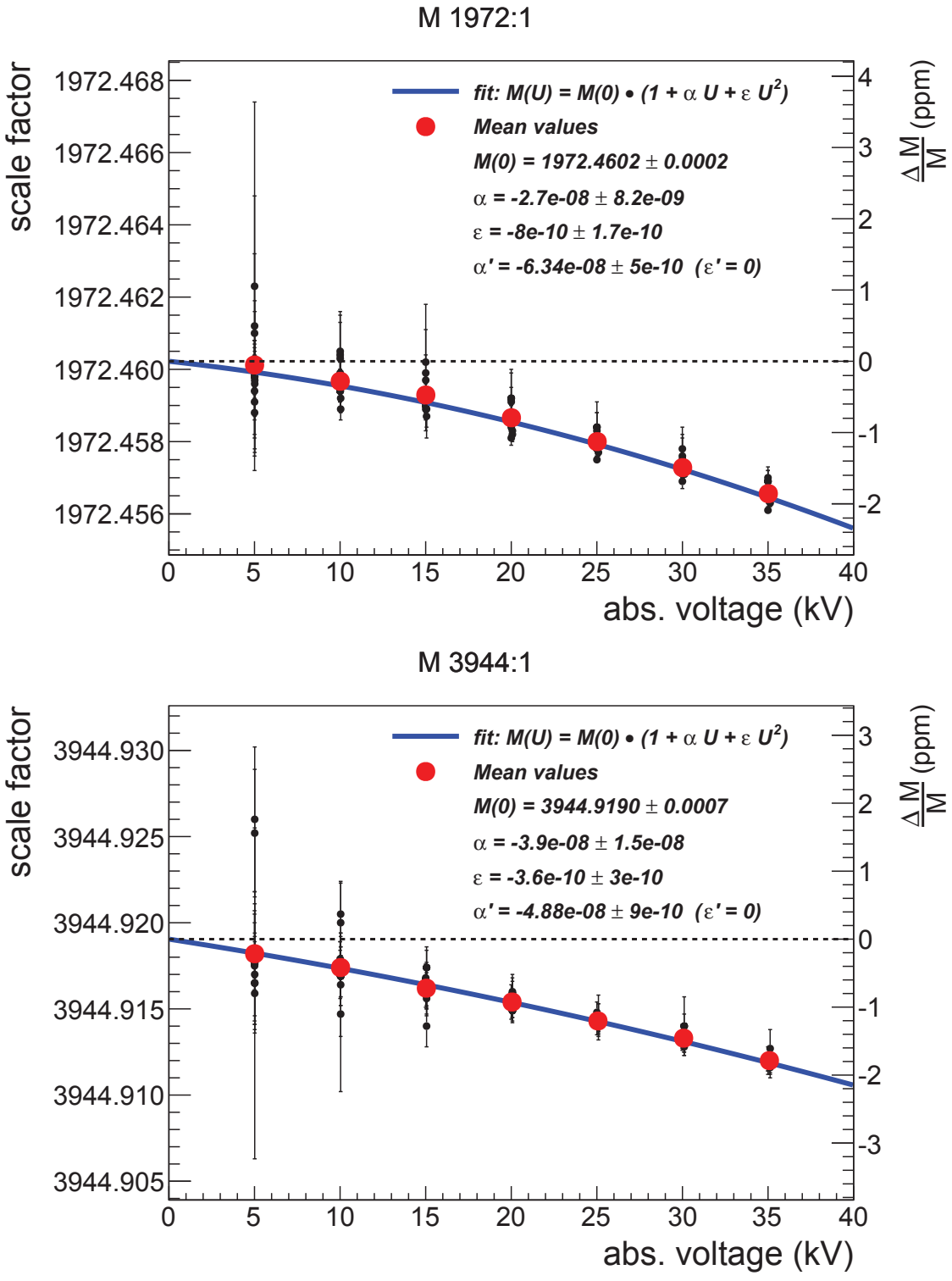

Figure 44: Voltage dependence of the 1972:1 and 3944:1 scale factors of the K35 divider. The data sets were fitted by a 2^{nd} order polynomial (blue line, coefficients α, ε) and by a linear function (not plotted, coefficients α', ε'). The relative change for both scale factors after a voltage step of 35 kV is below 2 ppm.

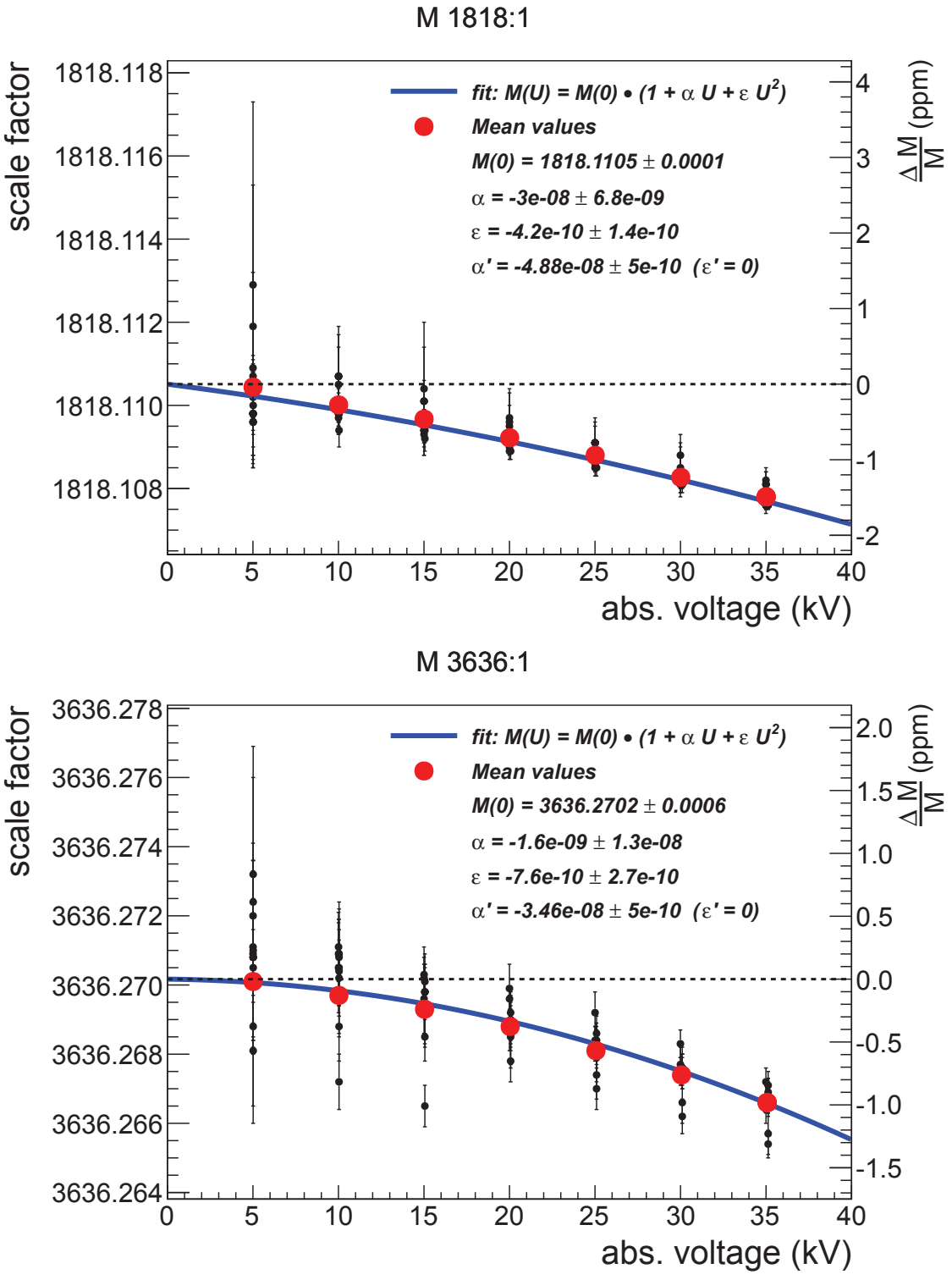

Figure 45: Voltage dependence of the 1818:1 and 3636:1 scale factors of the K65 divider. The data sets were fitted by a 2^{nd} order polynomial (blue line, coefficients α, ε) and by a linear function (not plotted, coefficients α', ε'). The relative change for both scale factors after a voltage step of 35 kV is below 1.5 ppm.

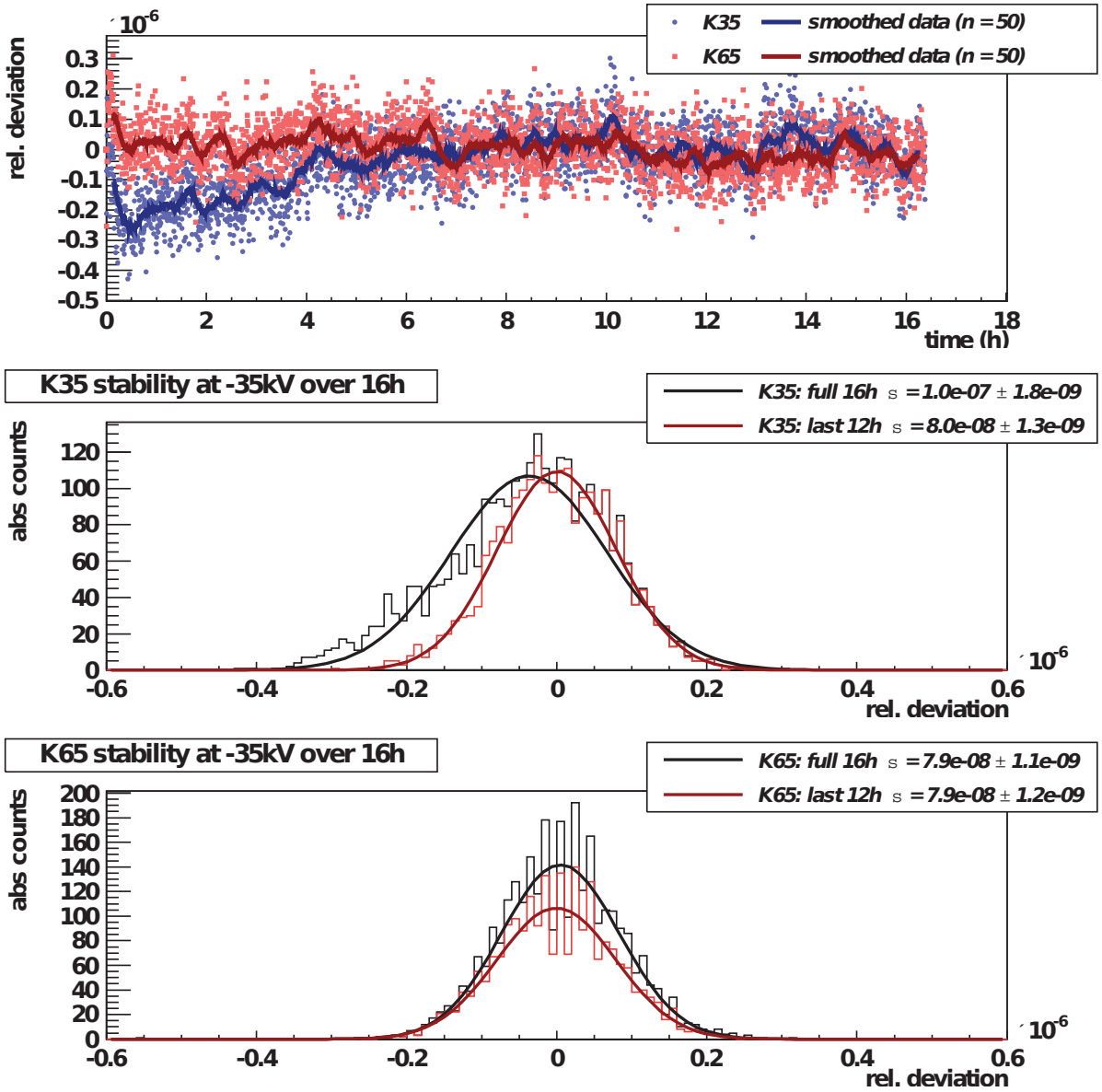

Figure 46: Stability of the 3944:1 and 3636:1 scale factors of K35 and K65 at −35 kV. The uppermost plot shows the stability for a 16 h run. The solid lines dote a moving average with a with of 50 data points. The two lower plots showing histograms with the distribution of the relative deviation. The distribution of K35 has a small tail towards negative deviations because of the 4 h warm-up of 0.2 ppm. A fit to the histograms gives a Gaussian width σ is for the K35 0.1 ppm and for the K65 0.08 ppm for the complete run and for the last 12 h both dividers show a σ of 0.08 ppm. The data are normalized to the mean value of the last 12 h. The error bars are not drawn for the sake of clarity.

4.6 Low voltage calibration

In order to have a simple monitor capability on the drift of the scale factors between the calibration phases with the MT100, the PTB suggested a calibration method using low voltages of up to 1 kV. This method makes use of the Fluke 752A Reference Divider (precision of 0.5 ppm) as reference and is dubbed "low voltage calibration". For this calibration method only commercial devices are needed. The basic idea behind this calibration method is that the temperature coefficient of the KATRIN high voltage dividers is so small that the difference in scale factor between 1 kV and 35 kV is only a few ppm. For the reason of clarity the scale factors 1818:1 and 1972:1 are referred to as 2000:1 and the scale factors 3944:1 and 3636:1 as 4000:1. The calibration works in the following order:

1. Calibration of the 100:1 scale factor with 1000 V and Fluke 752A Reference Divider.
2. 350 V are applied to the 100:1 scale factor and the output voltage of the 2000:1 (4000:1) scale factor is measured. This leads to a so called sub scale factor 20:1 (40:1).
3. To obtain the values of the 2000:1 and 4000:1 scale factors, the results for the 100:1 scale factor are multiplied with those results of the 20:1 and 40:1 respectively.

The results have a uncertainty of 1.6 ppm but can deviate from the scale factors obtained at high voltage, because this calibration does only apply 1 kV to the high voltage resistor. This neglects the thermal behaviour of the high voltage resistors chain. The thermal behaviour of the low voltage resistors is considered by applying 350 V to the 100:1 scale factor. This results in the same load at the low voltage resistor as if 35 kV are applied to the input of the high voltage divider. The advantage of this method is that one can use the Fluke 752A as reference divider and it can be carried out within a couple of hours. This allows to make on-site calibrations between the measurement runs at KATRIN. The disadvantage is that one measures the high voltage resistor only with 1 kV and the influences of thermal load and leakage currents are not considered. This causes the deviation between the values for the scale factors measured at high voltages and at 1 kV, which is typically between 0.5 to 2 ppm. This method is basically used to have a monitor on the divider drift over time.

The results for K65 of the low voltage calibration are compared to the results of the PTB calibrations in tabular 4.8 and 4.9. The value measured at PTB for the 1818:1 and 3636:1 scale factors are corrected for the voltage dependence determined in the corresponding calibration phase. Only the results for the 3636:1 deviates more than 1 ppm. Nevertheless these values all agree well within the error bars. Also the drift, obtained from these two phases of low voltage calibrations, leads to a negligible drift of the divider. Essential the divider is stable within the error bars.

The stability over time is shown in figures 47 and 48. The values measured over a period of about 3 years, scatter approximately 1 ppm around the mean value. For the calibrations, it is of crucial importance to provide stable experimental condition (screened rack, temperature stabilization ,...) and to avoid ground loops. This becomes apparent in figure 47. In August 2012 and May 2013 the low voltage calibration of K35 were carried out in the KATRIN main spectrometer hall. For the measurements in August the experimental conditions were not

Table 4.8: Comparison of the low voltage calibration of K65 at Münster measured in February and March 2010 with the results from high voltage calibration at PTB in December 2009. The last value denotes the relative difference between the low voltage calibration at Münster and the high voltage calibration at PTB.

	PTB		Münster		
2009	U_{cal} (kV)	scale factor	U_{cal} (kV)	scale factor	rel. difference (ppm)
100:1	1	100.51484	1	100.51484	0.0
1818:1	35	1818.1096	0.35	1818.1098	0.1
3636:1	35	3636.2743	0.35	3636.2725	-0.5

Table 4.9: Comparison of the low voltage calibration of K65 at Münster measured in December 2011 with the results from high voltage calibration at PTB in December 2011. The last value denotes the relative difference between the low voltage calibration at Münster and the high voltage calibration at PTB.

	PTB		Münster		
2011	U_{cal} (kV)	scale factor	U_{cal} (kV)	scale factor	rel. difference (ppm)
100:1	1	100.51479	1	100.51483	0.4
1818:1	35	1818.1078	0.35	1818.1094	0.9
3636:1	35	3636.2668	0.35	3636.2716	1.3

optimal (different machines were working inside the hall, no screened rack for the measurement equipment, no line filter). Hence the values scatter significantly. For the calibration in May 2013 these conditions were optimized with a clear result.

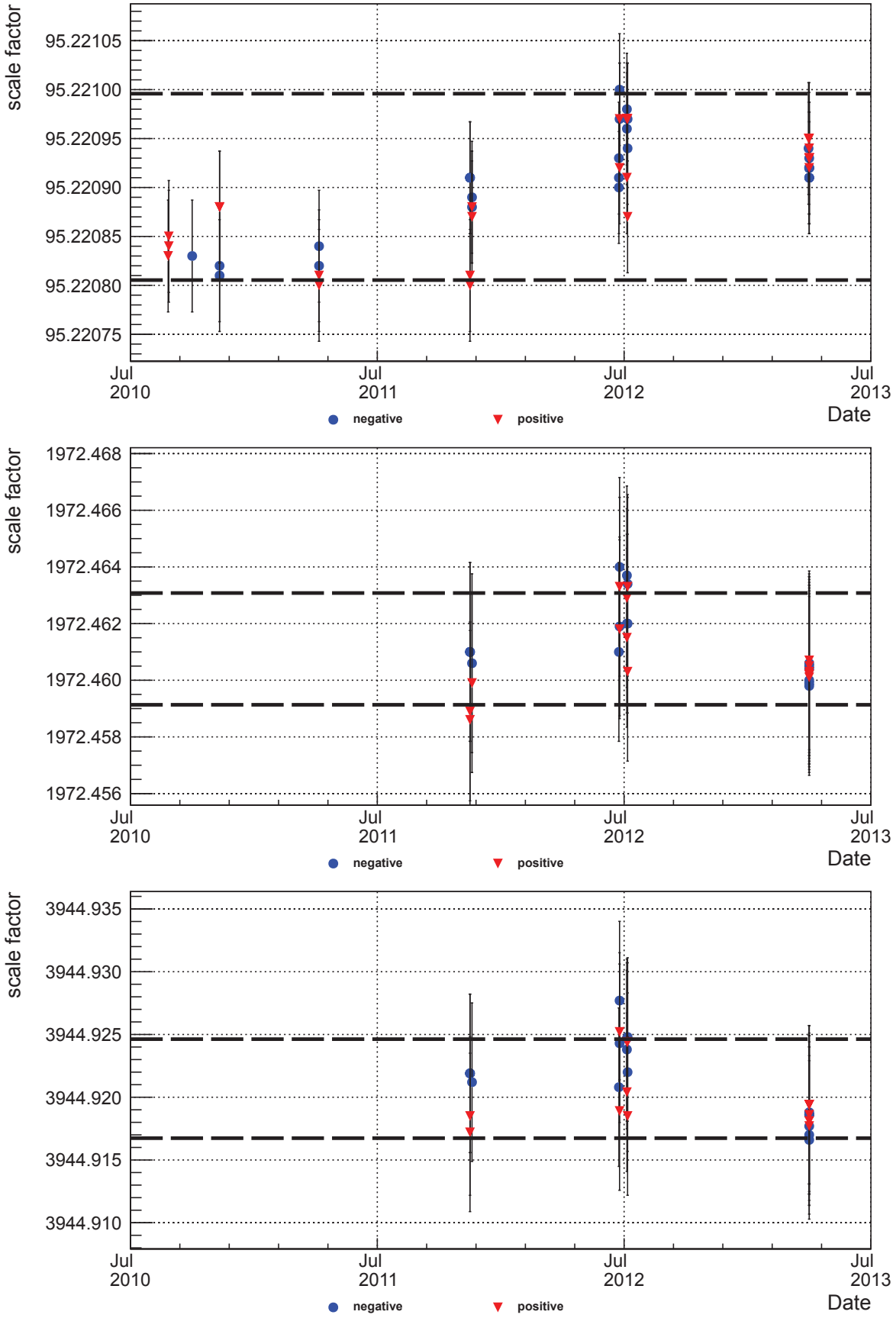

Figure 47: Results of the low voltage calibration of the K35. Shown is the scale factor measured with the low voltage calibration over time. The dashed black lines denote the ±1 ppm region around the mean value.

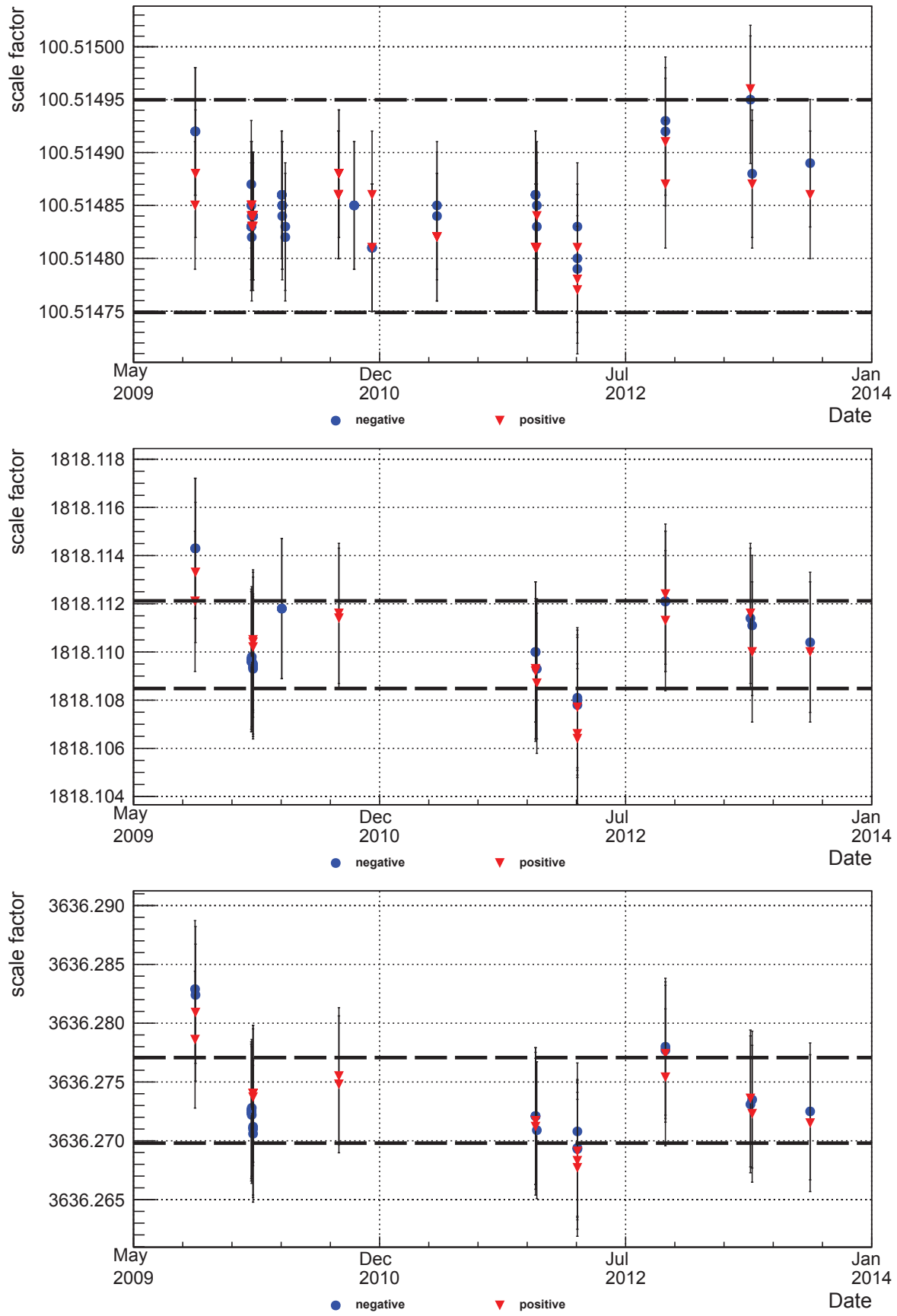

Figure 48: Results of the low voltage calibration of the K65. Shown is the scale factor measured with the low voltage calibration over time. The dashed black lines denote the ±1 ppm region around the mean value.

4.7 Summary of calibration results

Both KATRIN dividers show a very high stability also for mid term measurements. It was possible to reach sub-ppm accuracy for time period of several hours. The long term stability found for the K65 is $1\,\mathrm{ppm\,year^{-1}}$ for the 3636:1 scale factor. For the other scale factors the stability is even higher. With the results obtained in 2009 and 2011 for the K65 the divider can be stated as stable within the error bars. The stability of the K35 could not be obtained by the two calibration phases at PTB due to an exchange of one faulty resistor in 2010. But the low voltage calibration of K35 show a comparable drift over time as for K65.

The linear voltage dependence between 10 to 35 kV is 0.04 to $0.07\,\mathrm{ppm\,kV^{-1}}$, depending on the scale factor and divider. The voltage dependence also shows a quadratic term which is caused by the internal warming of the precision resistor chain.

The time dependent drift for K65 is less than 0.1 ppm/month and could also stated as stable within the error bars. A more precise value for the drift of both dividers can be specified after the next calibration phase starting in October 2013. In this phase again the scale factors, voltage dependence and stability of both KATRIN dividers will be measured. Also the low voltage calibration will be carried out intensively before and after the calibration at PTB at Münster and during the calibration phase at PTB.

For applications which do not need a precision of more than 5 ppm, it is possible to calibrate the dividers with low voltages and neglect the voltage dependence. For applications needing a higher precision a frequently calibration with high voltages is necessary. These calibrations can be carried out at PTB or at the KATRIN-experiment. A calibration without the PTB is possible because of the presence of two ppm-class dividers at KATRIN, therefore the calibration method of the PTB can be carried out. This method and also different ways to precisely calibrate ppm-class high voltage dividers is described in [Bau14].

Chapter 5

Measurements of ^{83m}Kr conversion electron lines at the KATRIN Monitor Spectrometer

The monitoring of the energy scale and stability for the KATRIN experiment is based on a redundant high precision measurement of the retarding high voltage. This monitoring system consists of the already presented precision high voltage dividers (chapter 4) and the use of a natural standard, namely the conversion electrons of ^{83m}Kr. The measurements of conversion electron lines covered within this work, were performed at the MAC-E filter of the former Mainz Neutrino Mass Experiment. The spectrometer is now located at the KATRIN experiment and dubbed **Mo**nitor **S**pectrometer (MoS). The measurement series started in January 2012 and ended in July 2012. During the measurement series the stability of line conversion electron line positions were investigated in comparison to the K35 divider. Further investigations were carried out by measuring conversion electron lines of different energies. Within this work only possible cross checks to the K35 are of interest. Detailed studies of the sources itself and the optimization of the analysis will be done in the PhD theses of M. Slezák [Sle15] and M. Erhard [Erh15]. First the principle of internal conversion and the ability of conversion electron sources for the calibration at KATRIN will shortly be introduced. After this the experimental set-up and the data analysis will be described before presenting the results.

5.1 Principle of internal conversion

The fact that an excited state of a nucleus can emit an orbital electron instead of a gamma quantum ("conversion of gamma radiation") was observed and described at the beginning of the 20^{th} century by O. von Baeyer, O. Hahn and L. Meitner [vB10, Hah24, Mei24]. The two competitive processes are the emission of γ radiation with the probability T_γ and the emission of one orbital electron with the probability T_e. The ratio of these probabilities gives the internal conversion coefficient:

$$\alpha_{IC} = \frac{T_e}{T_\gamma} \,. \tag{5.1}$$

The internal conversion coefficient depends on various parameters like the charge of the decaying nucleus, the energy of the nuclear transition, the orbital of the emitted electron and the multipolarity and parity of the nuclear transition.

The natural line width Γ (full width at half maximum, FWHM) of the conversion electron lines is given by the uncertainty relation $\Gamma \cdot \tau = \hbar$. In the case of internal conversion the width is given by [Zbo11]:

$$\Gamma = \frac{\hbar}{\tau_e} + \frac{\hbar}{\tau_\gamma} \,, \tag{5.2}$$

with the lifetime of the electron hole τ_e and the lifetime of the nuclear transition τ_γ.

The line shape of the conversion electron line is given by a Lorentz distribution:

$$L(E, E_0, \Gamma, A) = A \cdot \frac{\Gamma/2}{(E - E_0)^2 + (\Gamma/2)^2}\,, \tag{5.3}$$

in which A denotes the amplitude of the Lorentzian, E_0[1] the central energy, E the energy and Γ the FWHM. A more detailed introduction to the internal conversion is given in [Zbo11].

5.2 Conversion electrons of ^{83m}Kr and their use at KATRIN

A suitable electron calibration source for the KATRIN-experiment has to fulfil the following constraints:

- The energy of the emitted electrons should be as close as possible to the endpoint of the tritium β-decay.
- The energy spread should be narrow (small natural line width Γ) so that small changes in retarding voltage corresponds to high changes in count rate.
- The half-life of the radiative source has to be long enough to use one source for the calibration over more than one measurement run (two months) of KATRIN.
- The count rate must be high enough to provide sufficient statistics within a short period of time.

All this is fulfilled by calibration sources based on the conversion electrons of $^{83\mathrm{m}}$Kr [Zbo13]. The $^{83\mathrm{m}}$Kr is generated by electron capture of $^{83}_{37}$Rb ($T_{1/2} = 86.2\,\mathrm{d}$). The metastable state $I^\pi = \frac{1}{2}^-$ is populated by 77.6%, and decays into the $I^\pi = \frac{7}{2}^+$ via a highly converted ($\alpha_{\mathrm{IC}} = 2035$) process with the transition energy:

$$E_{32} = 32\,151.7(5)\,\mathrm{eV} \quad [\mathrm{Ven06}] \tag{5.4}$$

and a half-life of 1.83 h. The ground state is achieved after an other converted decay ($\alpha_{\mathrm{IC}} = 20$) with a half-life of 147 ns. The corresponding γ energy is in this case:

$$E_{9.4} = 9405.8(3)\,\mathrm{eV} \quad [\mathrm{Sle12}]\,. \tag{5.5}$$

Both transition energies were measured by gamma ray spectroscopy. Due to the populated K, L, M and N shells of krypton, many different conversion electron lines over an energy range of 7 to 32 keV can be used for calibration (see table 5.1).

[1] It should be mentioned that in the context of conversion electron lines E_0 denotes the central energy / peak position of the line and not the endpoint energy as it was the case for the tritium spectrum.

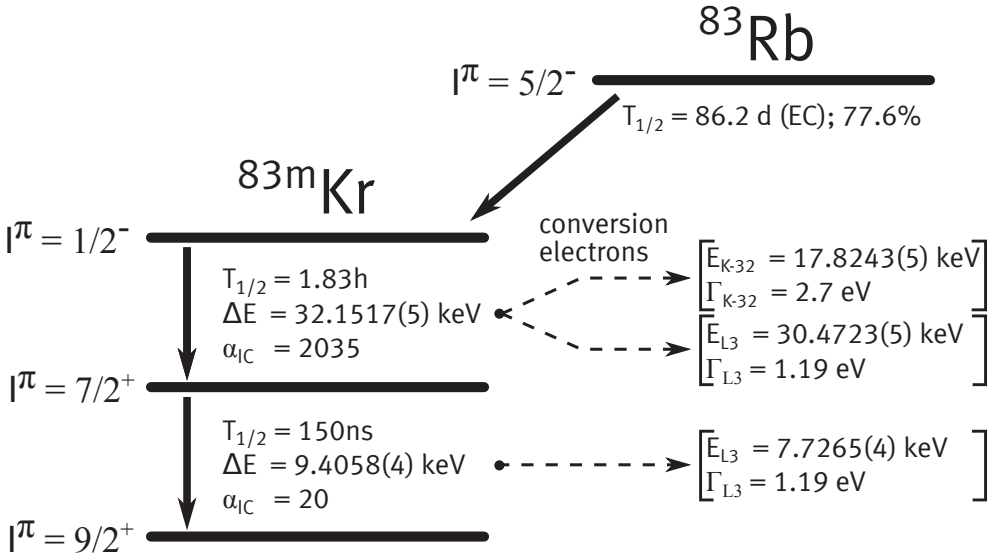

Figure 49: Decay scheme of ^{83m}Kr. The mother isotope ^{83}Rb decays by 77.6% via electron capture (EC) to the meta stable isotope ^{83m}Kr. This metastable state decays via two highly converted γ-transitions into the ground state. The electron energies and Lorentzian widths (Γ) for the K-32 and L_3 conversion are stated in the right part of the picture. Values taken from table 5.1. The values for the Lorentzian width are taken from column "recommended".

For a gaseous source the conversion electron energy measured with a MAC-E filter can be written as [Zbo11]:

$$E_{\mathrm{kin}}^{\mathrm{gas}}(i) = E_\gamma + E_{\mathrm{rec},\gamma} - E_{\mathrm{rec,e}}(i) - E_{\mathrm{bin}}^{\mathrm{vac}}(gas, i) - (\phi_{\mathrm{spec}} - \phi_{\mathrm{source}}) - C \tag{5.6}$$

with:

E_γ	: is the gamma ray energy,
$E_{\mathrm{rec},\gamma}$	: is the energy of the recoil atom after gamma ray emission and is equal to 0.007 and 0.002 eV for the E3 (32 keV) and M1 (9.4 keV) transitions, respectively,
$E_{\mathrm{rec,e}}(i)$	: is the energy of the recoil atom after emission of the conversion electron from shell i,
$E_{\mathrm{bin}}^{vac}(gas, i)$	: is the electron binding energy of the shell i(related to the vacuum level) of the free atom,
ϕ_{spec}	: is the work function of the spectrometer electrode,
ϕ_{source}	: is the work function of the source, and
C	: is an additional term accounting for possible space and surface charges within the gaseous source

Table 5.1: Overview of the conversion electron lines of ^{83m}Kr. All values of energy and line width are stated in eV. The energies of the M1 and E3 gamma transitions were taken from [Ven06] and [Sle11b], respectively. The intensities of the gamma transitions per ^{83}Rb decay are based on [Väi76] and [Wu57]. The electron kinetic energies are stated for gaseous krypton (cf. Equation 5.6) for $\phi_{\text{spec}} = \phi_{\text{source}}$, using the gamma transitions energies shown in the table and the binding energies summarized in [Zbo11]. The intensities of the electron lines per ^{83}Rb decay were determined using interpolated internal conversion coefficients tabulated in [Rös78a, Rös78b]. The experimental line widths were obtained from measurements with the condensed ^{83m}Kr at Mainz MAC-E filter. Remarks: **a** no recommended values stated in [Cam01]. **b** natural line width fixed to 0 in the analysis. **c** the lines N_2 and N_3-32 were analyzed as a single line $N_{2/3}$-32. Taken from [Zbo11].

Electron level and notation		**Atom rec. energy $E_{\text{rec},\,e}(i)$**	**Kinetic energy $E_{\text{kin}}^{\text{gas}}(i)$**	**Intensity $I(i)$ [%] per ^{83}Rbdecay**	**Lorentzian line width $\Gamma(i)$ recomm. [Cam01]**	**exp. (cond. Kr) [Pic92b]**	**[Ost08]**
γ transition M1			9 405.8(4)	5.86(134)			
$2s_{1/2}$	L_1	0.05	7 481.2(9)	70.32	3.75	5.30(4)	3.72(19)
$2p_{1/2}$	L_2	0.05	7 673.8(4)	7.91	1.25	1.84(5)	1.29(14)
$2p_{3/2}$	L_3	0.05	7 726.5(4)	5.07	1.19	1.40(2)	1.58(16)
$3s_{1/2}$	M_1	0.06	9 113.0(5)	11.60	3.5	4.27(5)	3.123(4)
$3p_{1/2}$	M_2	0.06	9 183.5(4)	1.30	1.6	1.99(32)	0.63(39)
$3p_{3/2}$	M_3	0.06	9 191.3(4)	0.98	1.1	1.66(8)	1.1(4)
$4s_{1/2}$	N_1	0.06	9 378.2(4)	1.43	0.4	0.19(4)	0.288(93)
$4p_{1/2}$	N_2	0.06	9 391.1(4)	0.12	- **a**	–	0 **b**
$4p_{3/2}$	N_3	0.06	9 391.7(4)	0.09	- **a**	–	0 **b**
γ transition E3			32 151.7(5)	0.035 8(45)			
$1s_{1/2}$	K	0.12	17 824.3(5)	17.07	2.71	2.83(12)	2.70(6)
$2s_{1/2}$	L_1	0.20	30 226.9(9)	1.13	3.75	–	–
$2p_{1/2}$	L_2	0.20	30 419.6(5)	17.61	1.25	1.84(5)	1.165(69)
$2p_{3/2}$	L_3	0.21	30 472.3(5)	27.42	1.19	1.40(2)	1.108(13)
$3s_{1/2}$	M_1	0.21	31 858.8(6)	0.19	3.5	–	–
$3p_{1/2}$	M_2	0.21	31 929.3(5)	2.99	1.6	1.99(32)	1.230(61)
$3p_{3/2}$	M_3	0.21	31 937.0(5)	4.65	1.1	1.66(8)	1.322(18)
$3d_{1/2}$	M_4	0.21	32 056.5(5)	4.69	0.07	–	–
$3d_{3/2}$	M_5	0.21	32 057.7(5)	6.59	0.072	–	–
$4s_{1/2}$	N_1	0.21	32 124.0(5)	0.02	0.4	0.19(4)	0.4
$4p_{1/2}$	N_2	0.21	32 136.8(5)	0.27	- **a**	0.59(4) **c**	0.608(13) **c**
$4p_{3/2}$	N_3	0.21	32 137.5(5)	0.41	- **a**		

For the calibration at KATRIN the K-32 conversion electron line is optimal. These conversion electrons are generated by the 32 keV transition energy and emitted from the K shell. The kinetic energy of these electrons is 17 824.3(5) eV and hence very close to the tritium endpoint. Also the width of $\Gamma = 2.7$ eV and the high intensity per ^{83}Rb decay (17%) allowing fast and precise calibrations.

Calibration sources using the conversion electron lines of ^{83m}Kr can be realised in different physical states. At KATRIN gaseous, quench condensed films and solid sources are used. The gaseous source will be used as admixture in the WGTS and allows an absolute calibration of the complete experimental set-up. The quench condensed films of sub-monolayer thickness, were already used at Mainz Neutrino Mass Experiment [Pic92a]. An improved system was tested also in Mainz showing a sufficient energy stability for the KATRIN experiment [Ost08]. This condensed source will be used at the CPS at KATRIN which allows to calibrate each pixel of the detector separately. An overview of this system and the modification needed for the use at the CPS are described in chapter 6. Vacuum evaporated sources and ion implanted sources are investigated as solid sources in [Zbo11] and results of the stability of the K-32 line of ion implanted sources are published in [Zbo13]. It turned out that for solid but non-condensed sources, ion implantation of ^{83}Rb yield the most stable sources, hence the next section will focus on these sources and their most important properties.

5.3 Implanted sources

The major advantage of ion implanted sources compared to quench condensed sources is the easy handling and their robustness against surrounding vacuum conditions. There is no need of cryogenic temperatures and and continuous surface monitoring like for condensed sources (see chapter 6). To implant ^{83}Rb into substrates like graphite or foils of noble metals a facility which provides the needed isotope and energy is needed. The sources investigated in this work are produced at the ISOLDE facility at CERN [Her10].

The measured energy of the conversion electrons of an implanted source can be written as [Zbo11]:

$$E_{\mathrm{kin}}^{\mathrm{impl}}(i) = E_{\gamma} + E_{\mathrm{rec},\gamma} - E_{\mathrm{rec,e}}(i) - \left(E_{\mathrm{bin}}^{\mathrm{vac}}(\mathrm{gas,i}) - \Delta E_{\mathrm{bin}}^{\mathrm{Fermi}}(\mathrm{impl,i})\right) - \phi_{\mathrm{spec}}\,, \tag{5.7}$$

where $E_{\mathrm{bin}}^{\mathrm{vac}}(\mathrm{gas,i})$ denotes the electron binding energy of gaseous krypton and $\Delta E_{\mathrm{bin}}^{\mathrm{Fermi}}(\mathrm{impl,i})$ the binding energy referenced to the Fermi level. In Eq. (5.7) the term ϕ_{source} is not explicitly written but it is actually included in the term $\Delta E_{\mathrm{bin}}^{\mathrm{Fermi}}(\mathrm{impl,i})$ [Zbo11].

In order to further investigate the implanted sources concerning their stability and to find possible cross checks for the reliability of the monitoring system, dedicated measurements at the KATRIN Monitor Spectrometer were performed. During this measurement four of these sources were installed into a source holder, which can hold up to four sources (see figure 50).

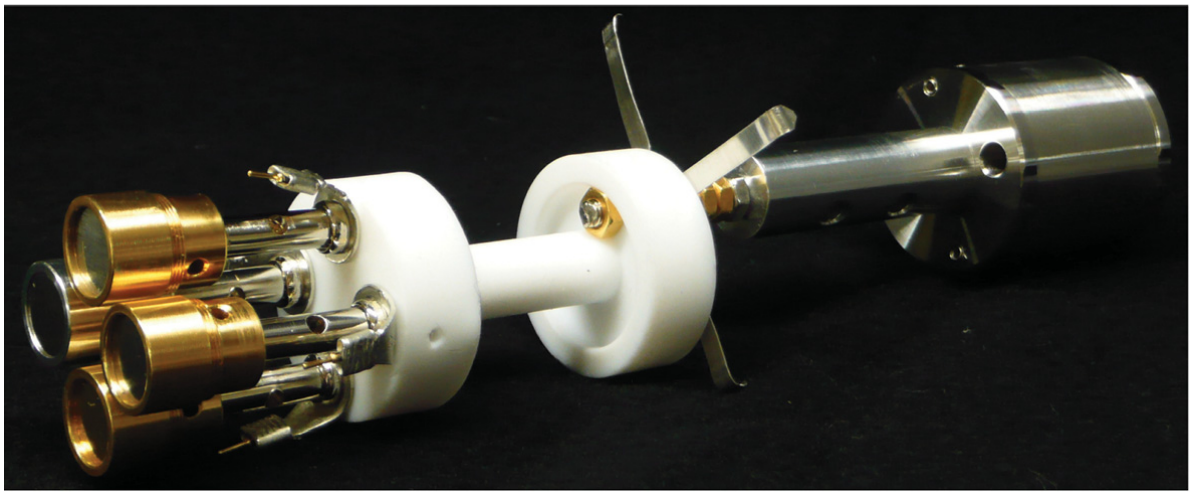

Figure 50: Source holder with four implanted sources installed. The holder can be installed on a xy-table into the source chamber of the MoS. The four sources (left part of the picture) are mounted onto an insulator to enable an independent electric potential for each source. The metal foil, containing the ^{83}Rb is installed into the source holder with a diameter of 12 mm. (Source: [Zbo11])

5.4 The KATRIN Monitor Spectrometer

5.4.1 Experimental set-up

KATRIN uses the spectrometer of the former Mainz Neutrino Mass Experiment as "monitor spectrometer". The monitor spectrometer will be connected to the same high voltage as the main spectrometer and monitor continuously the line position of the K-32 line. Thereby the applied voltage can be traced back to the measured position of the conversion electron line K-32 of ^{83m}Kr. The set-up consists of the spectrometer vessel and its vacuum system reaching a pressure of 10^{-10} mbar by the use of three TMPs. Superconducting solenoids are placed at each side of the spectrometer, providing the magnetic guiding field. These solenoids are working at 6 T in persistent mode at 50 A. At the center of the spectrometer four air coils are installed (see figure 51) to provide a homogeneous field of 3 G in the analysing plane. This leads to a resolution of the spectrometer of 0.9 eV for the K-32 line. The magnetic field configuration for this settings is shown in figure 52. Additionally, two sets of coils are installed to compensate the earth magnetic field (EMCS X and EMCS Y).

In order to provide the electric retarding field the MoS is equipped with two kind of electrodes inside the spectrometer vessel. The outer one is a full metal electrode and the inner one is a single layer wire electrode. The latter one allows to screen the flux tube from secondary electrons generated at the surface of the full metal electrode by setting it on a more negative potential. For the investigations within this work both electrodes were set to the same potential. This was done since during the measurements of high count rates (order of 100 Hz to 10 kHz) a low background is not needed. The retarding voltage is delivered by a precision high voltage power supply (FuG HCN140M-35000) and is monitored by the K35 divider (see chapter 4). The output voltage of the K35 is measured by a digital voltmeter (Fluke

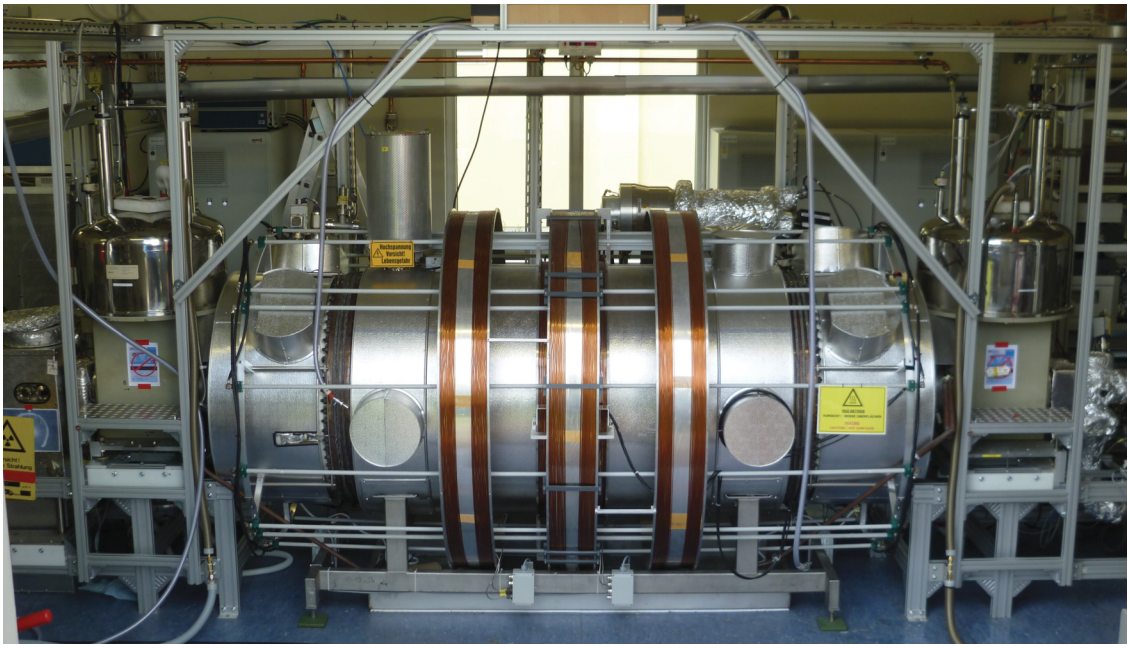

Figure 51: Set-up of the monitor spectrometer. Source chamber and source magnet are on the left side. Detector magnet and chamber on the right side. The four air coils surrounding the spectrometer (the fourth coil is inside the outer coil in the middle of the spectrometer) are visible in the central area.

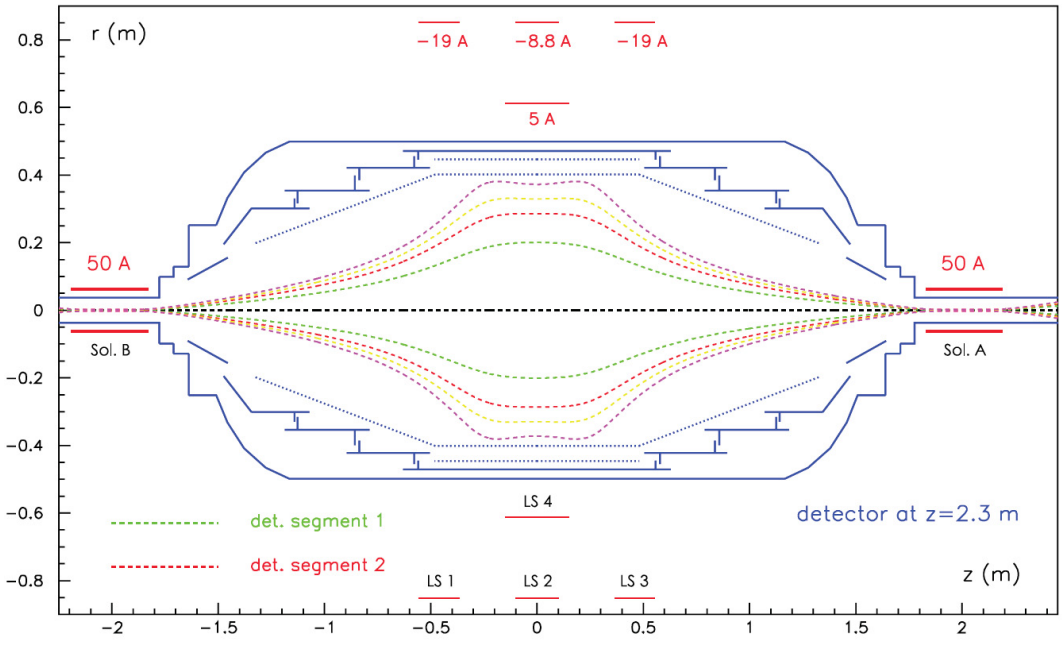

Figure 52: Magnetic field configuration of the MoS. Shown is flux tube of the monitor spectrometer for the magnetic setting of the "Mainz06" set-up, calculated in the PhD thesis of Th. Thümmler [Thü07]. The only difference at the KATRIN experiment is that the current of the outer air coils is −18 A instead of −19 A due to the maximum voltage of the power supply. The maximum magnetic field amounts to 6 T in the solenoids and the minimum is 300 µT in the analysing plane. This leads to an instrumental resolution of about 0.9 eV for the K-32 line. (Source: [Thü07])

8508A) and stored into a database. The offset and amplification of the voltmeter is regularly measured to ensure sub-ppm stability over one month.

The electron detector consists of five PIN diodes (see figure 53). For data analysis only the central pixel (Canberra PD150-12-500AM) is used. It has a size of 1.5 cm^2, an active thickness of 500 µm, an energy resolution of 7 keV and the dead layer is below 50 nm. The four outer pixels (Hamamatsu S3590-09 PIN diodes) are used for alignment of the electron source with respect to the detector. Their active area is 1 cm^2 and their depletion layer is about 300 µm [Gou10].

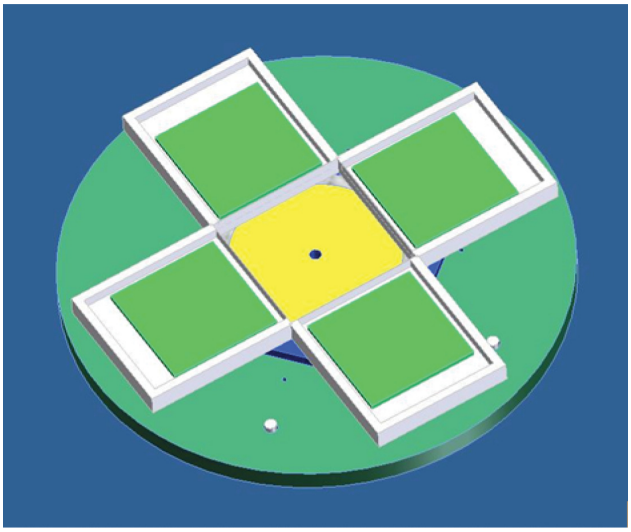

Figure 53: CAD model of the five pixel detector of the monitor spectrometer. The center one is used for analysis and the outer pixels for alignment purposes (Source [Gou10]).

5.4.2 Data acquisition

The conversion electrons are detected by the central detector pixel and amplified by a pre-amplifier mounted directly behind the detector inside the UHV chamber. In order to reduce noise this pre-amplifier is cooled by liquid nitrogen. These signals are digitized by a IPE-V4-Crate [Tch13] and stored into a database. For the correction of dead time effects of the detector system the signal of a 200 Hz pulser (Agilent 33220A) is recorded additionally.

The conversion electron spectrum is recorded by stepping of the retarding high voltage. In each step an electron spectrum is recorded for a given pre-set time (typically 20 to 120 s), depending on the signal rate. The count rate is determined and corrected for the dead time of the detector system.

5.4.3 Data analysis

For the stability monitoring the critical value is of course the line position. In order to determine this stability two methods are used in this work. The first method is to do a many-parameter fit of the theoretical line shape to the measured data. This is done within two different theoretical descriptions, which will be explained later in this section. The second method is not to fit a theoretical line shape to the data but to compare the measured spectra with a reference spectrum with the method of cross correlation. By this the line position is not determined, but its shift in position compared to a reference spectrum, which is sufficient for the stability monitoring. For all methods the χ^2_{red} is the measure of the goodness of the fit, together with the normalized residuals.

For the fit of theoretical line shapes also the transmission function and especially radial inhomogeneities of the electric and magnetic field inside the analysing plane have to be considered. This is done by the fit program of M. Slezák [Sle11a]. All three types of analysis in this work were carried out with this program. For the analysis with theoretical line shapes the Lorentzian width (Γ) was fixed to the recommended values in table 5.1.

Analysis using a Voigt profile

Since the width of the conversion electron line is broadened by different effects, e.g. noise on the applied high voltage, the spectra are not fitted by a pure Lorentzian (L) but by a Voigt profile, which is a convolution of a Lorentzian with a Gaussian (G) with the width σ:

$$V(E, E_0, \Gamma, \sigma, A) = L(E, E_0, \Gamma, A) \otimes G(E, \sigma) \tag{5.8}$$

Here E denotes the energy, E_0 the line position, Γ and σ the Lorentzian and Gaussian width respectively and A the amplitude. For the analysis of the data obtained at a MAC-E filter this Voigt profile has to be convoluted with the transmission function of the spectrometer. This line shape was already used for the analysis of conversion electron lines measured with a condensed source by B. Ostrick [Ost08] and also for implanted sources by M. Zbořil [Zbo11]. Unfortunately for implanted sources the low energy side of the line has enhanced count rates due to solid state effects (e.g. inelastic-scattering). This limits the analysis interval in the low energy region and for this work a lower limit of 17 825 eV was chosen for the K-32 line. This was also the lower limit applied in [Zbo11]. A typical result for a fit using a Voigt profile to a K-32 line is shown in figure 54.

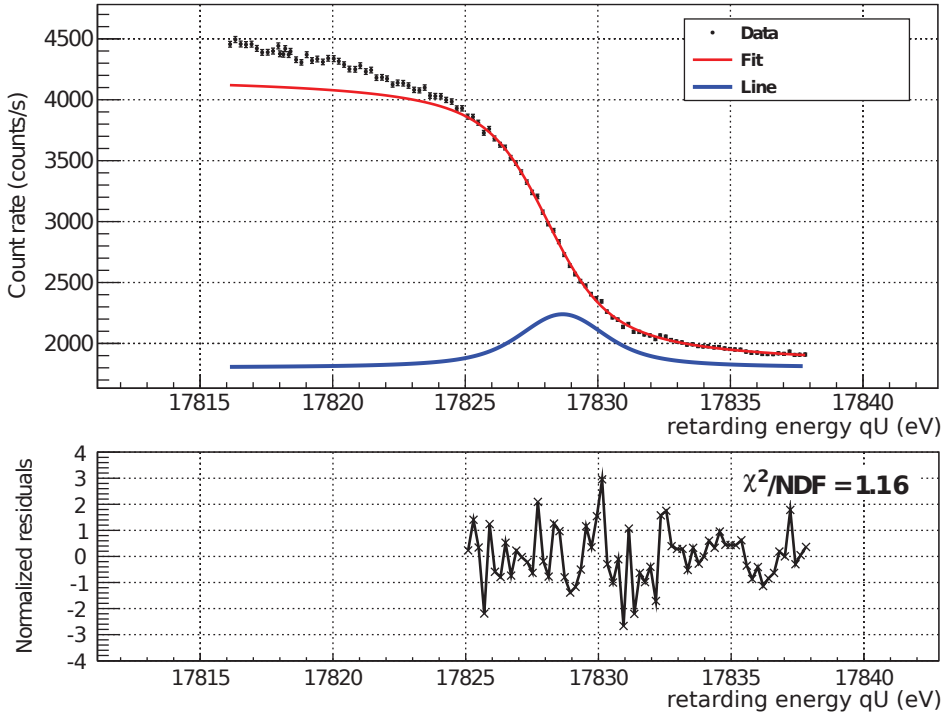

Figure 54: Results of a fit with a single Voigt profile to the K-32 of source Pt-10-1. The fit was done in the energy range [17 825 eV,17 840 eV] yielding a $\chi^2_{\text{red}} = 1.16$. The Lorentzian width Γ was fixed to 2.7 eV (see table 5.1) and the line position $E_0 = 17\,828.671(28)$ eV was obtained by the fit. The fit line (red) and the deconvolved line (blue) are extended to lower energies for the sake of example.

Analysis using a Doniach-Sunjic line shape

In order to describe the low energy part of the spectrum the use of a Doniach-Sunjic (DS) function was proposed in [Zbo11]. This line shape was described by Doniach and Sunjic for the description of a skew line shape of photoelectrons of metals [Don70]:

$$DS(E, E_0, A, \Gamma, \alpha) = \frac{A}{\pi((E-E_0)^2 + \Gamma^2/4)^{\frac{(1-\frac{\alpha}{1000})}{2}}} \tag{5.9}$$

$$\cdot \cos\left[\frac{\pi\frac{\alpha}{1000}}{2} + (1 - \frac{\alpha}{1000}) \cdot \arctan\left(\frac{E-E_0}{\Gamma/2}\right)\right], \tag{5.10}$$

where Γ is the width and E_0 is the centre of the peak. The skew parameter α describes the asymmetry in the low energy part of the spectrum. To make the values more convenient to read, the α is multiplied by 1000 in this work and also in the fit program. For $\alpha = 0$ the DS function will become a pure Lorentzian. The different line shapes are plotted in figure 55.

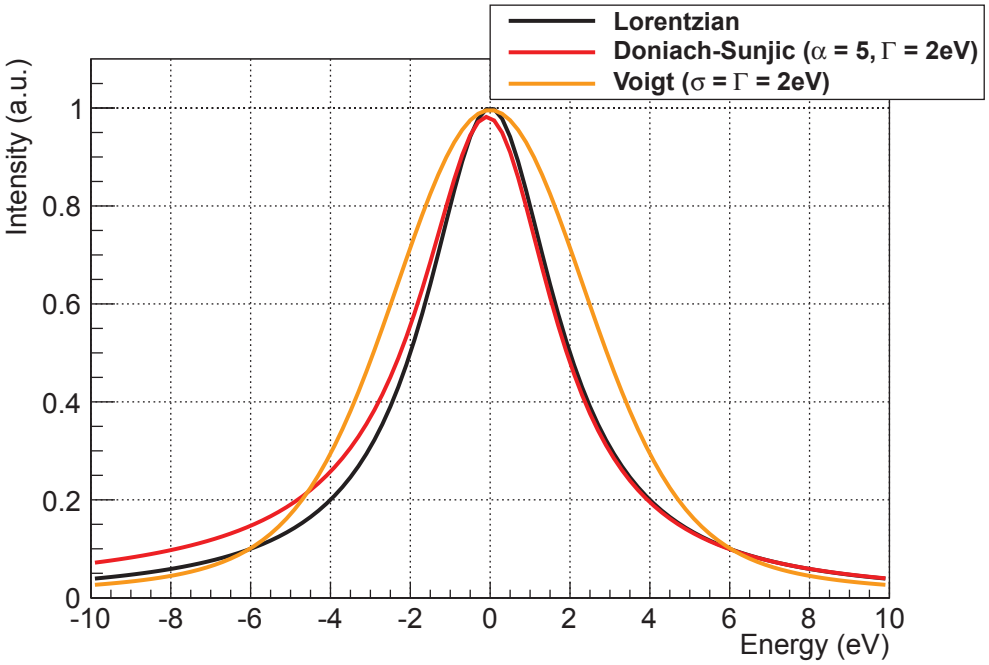

Figure 55: Lorentzian, Voigt and Doniach-Sunjic (DS) profiles. The plot shows the different line shapes for a central energy $E_0 = 0\,\text{eV}$. For all functions the Lorentzian width was set to $\Gamma = 2\,\text{eV}$. For the Voigt profile the Gaussian width was also set to $\sigma = 2\,\text{eV}$ and for the DS additionally the skew parameter was set to $\alpha = 5$. For $\alpha = 0$ the DS is identical to a pure Lorentzian.

For the MoS this function will be used to describe all solid state effects leading to an asymmetric line shape of the conversion electron lines. The physical motivation of this is that a suddenly created hole in an atomic subshell will be screened by conduction electrons of the metallic substrate. In this process, electron hole pairs are created with a range of energies that reduces the kinetic energy of the emitted electron [Sle13]. This DS function is also

convoluted with a Gauss in order to consider experimental effects like noise on high voltage and with the transmission function of the MAC-E filter. Typical results for the three lines investigated within this work (K-32, L_3(9.4 keV and L_3(32 keV) are presented in figures 56, 57 and 58. These fits describe the line shape well also in the low energetic part of the spectrum. The only drawback is that the parameters α and E_0 are strongly correlated, which will be discussed later on.

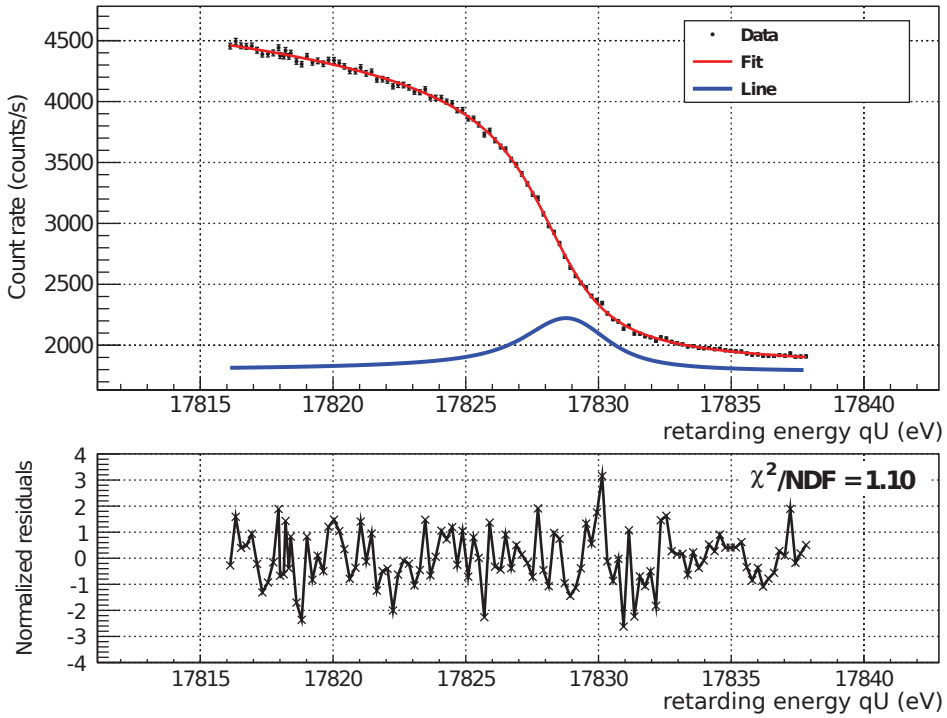

Figure 56: The plot shows a typical result of a Doniach-Sunjic fit to the K-32 line of the source Pt-10-1. The data points were fitted in the range [17 816 eV,17 838 eV]. Also the data in the low energy part are well described by this function (red curve). The Doniach-Sunjic profile is plotted in blue. The fitted line position $E_0 = 17\,828.977(30)$ eV, the Gaussian width $\sigma = 0.69(6)$ eV and the skew parameter $\alpha = 120(5)$. The Lorentzian Γ was fixed to 2.7 eV (see table 5.1).

Analysis using the cross correlation method

The cross correlation method compares two measured spectra to find the similarity. This can be done without a detailed knowledge of the theoretical line shape. As reference spectrum a fine stepped spectrum (200 meV step size, see figure 56), measured at 8$^{\text{th}}$ of February is used. The data points of the reference spectrum are interpolated by a smoothed cubic spline, as described in [Sle11a]. For this fit the amplitude, the shift of line position and the background are fitted with a least squares fit. This method offers very fast analysis, since no convolutions have to be done like for the Voigt or DS fit. But on the other hand this analysis assumes that the shape of the spectrum does not change over time. If the described asymmetry in the low energy part of the spectrum has a time dependence the cross correlation will lead to biased results.

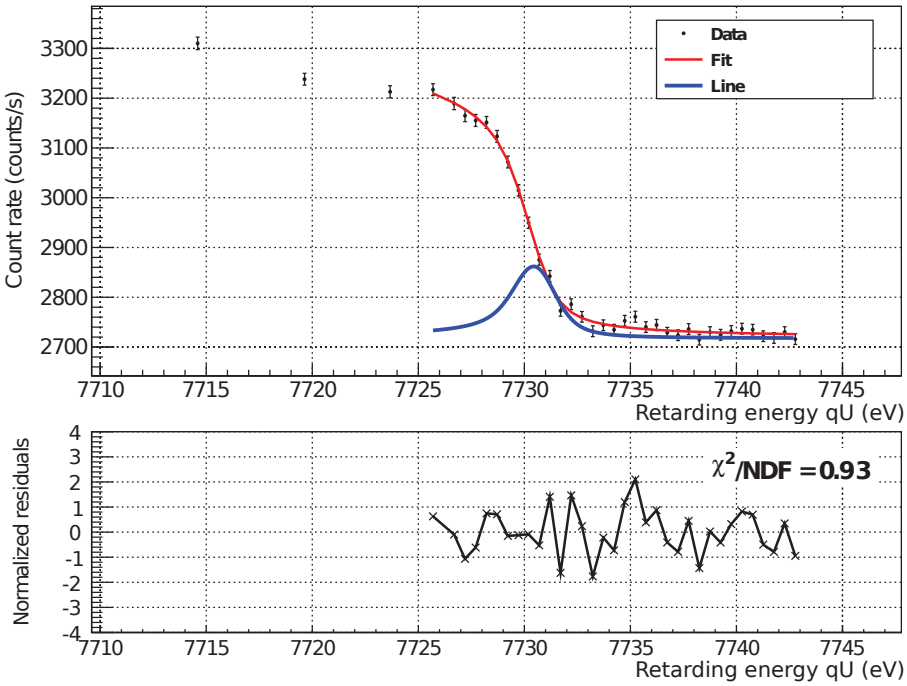

Figure 57: The plot shows a typical result of a Doniach-Sunjic fit to the L_3-9.4 line (Pt-10-1). The fit function is plotted in red and the Doniach-Sunjic profile is plotted in blue. The fitted line position is $E_0 = 7730.58(16)\,\text{eV}$, the Gaussian width $\sigma = 0.68(15)\,\text{eV}$ and the skew parameter $\alpha = 116(57)$. The Lorentzian Γ was fixed to 1.19 eV (see table 5.1).

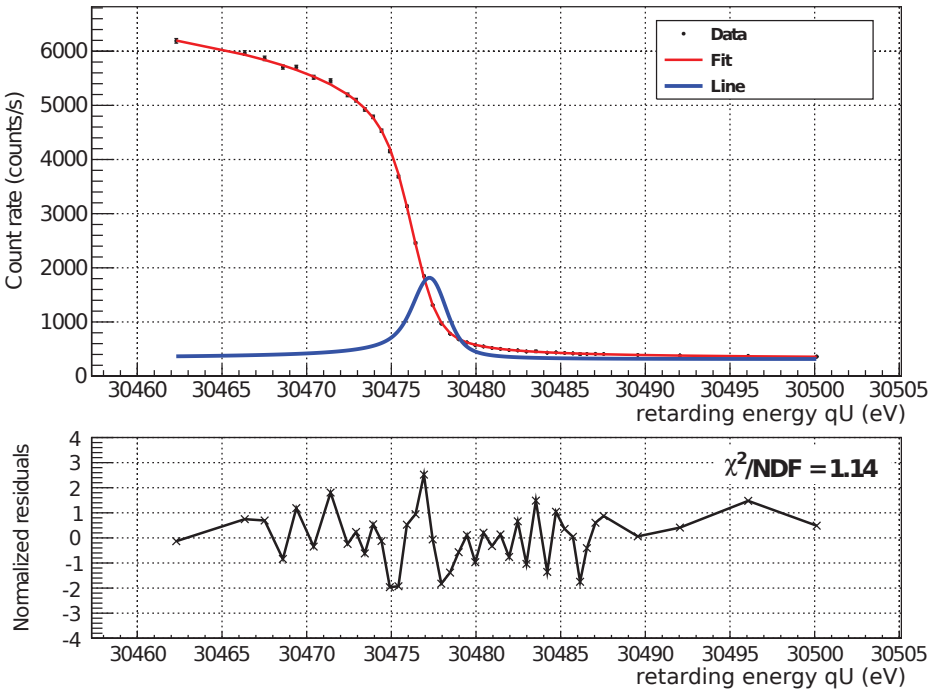

Figure 58: The plot shows a typical result of a Doniach-Sunjic fit to the L_3-32 line (Pt-10-1). The fit function is plotted in red and the Doniach-Sunjic profile is plotted in blue. The fitted line position is $E_0 = 30\,477.421(22)\,\text{eV}$, the Gaussian width $\sigma = 0.66(2)\,\text{eV}$ and the skew parameter $\alpha = 127(5)$. The Lorentzian Γ was fixed to 1.19 eV (see table 5.1).

5.5 Investigation of K-32 conversion electron line stability

The stability of ion implanted sources were investigated at the example of two sources, implanted with different energies. These are Pt-10-1 (^{83}Rb implanted into platinum with an energy of 10 keV) and Pt-15-5 (^{83}Rb implanted into platinum with an energy of 15 keV). Both sources were installed in the source holder so that they can easily be switched without braking the vacuum. For the Pt-10-1 all together 446 spectra of the K-32 line were analysed and for Pt-15-5 123 spectra. In the following plots four vertical dashed line denotes special events which occurred during this measurement series:

1. The installation of a zeolite based ^{83}Rb/^{83m}Kr source which emanates ^{83m}Kr (Emanator). This source was attached to the spectrometer but the valve between the source and the spectrometer was closed during the measurements described here.
2. A high voltage discharge caused by a test of the removal of stored electron by heating them by electron cyclotron resonance (ECR) [Mer12].
3. Venting the spectrometer by purpose in order to investigate the influence of a change in the work function of the spectrometer (Venting).
4. Baking of the spectrometer in order to check whether the work function of the spectrometer and hence the line position fully recovers or not (Baking).

The stability for the K-32 was analysed up to the day when the spectrometer was vented. All data points taken after the venting are only shown to demonstrate that after a full bake out of the spectrometer the work function seems to fully recover.

5.5.1 Results of the analysis with Voigt profile

For the analysis with the Voigt profile the spectra were fitted in an interval from 17 825 eV to 17 840 eV. Both sources showed a linear drift over time of 1.55(6) ppm/month for the case of the Pt-10-1 and 0.60(12) ppm/month for the Pt-15-5 source. An overview of all fitted line positions is given in figure 59.

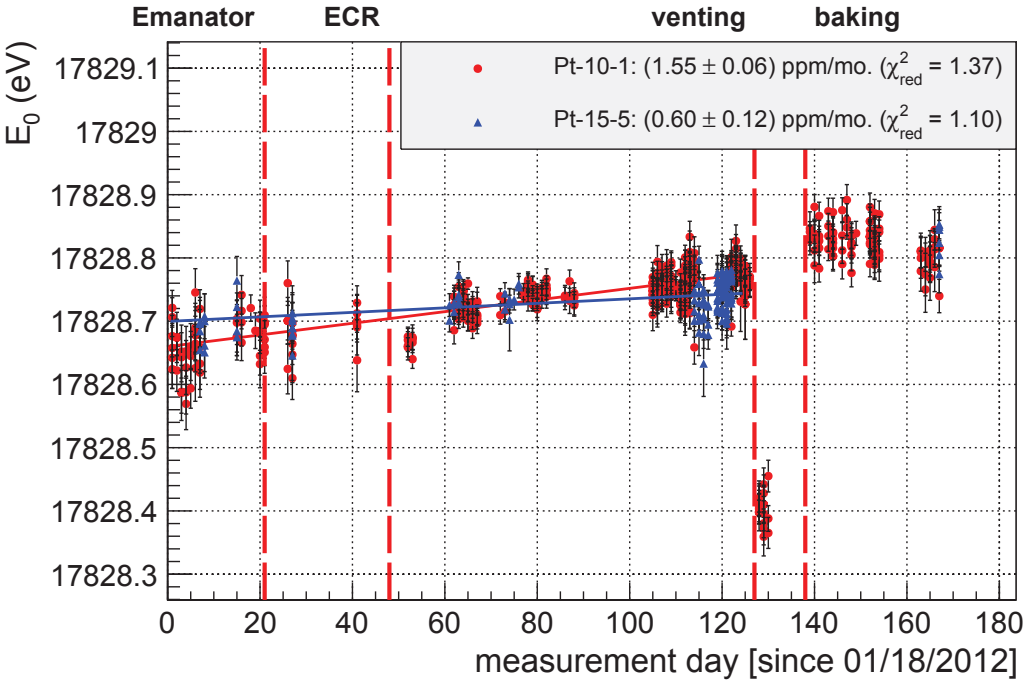

Figure 59: Results of the analysis with a Voigt profile for the K-32. All fits were carried out in an interval of [17 825 eV,17 850 eV]. The error bars denote the error of the position obtained by the fit, multiplied by $\sqrt{\chi^2_{\text{red}}}$ to take the goodness of fit results into account. Typical χ^2_{red} are around 1.4. The data points were fitted with a straight line up to the venting of the spectrometer (day 125).

5.5.2 Results for analysis with the cross correlation method

The stability of the K-32 line was determined with the cross correlation method in comparison to a 200 meV stepped reference spectrum, measured at the 8$^{\text{th}}$ of February. Therefore this analysis yields not a absolute line position but a shift of line position (ΔE_0) compared to the reference spüectrum.a For this reference spectrum the fit of a Voigt line shape yields a line position of E_0 = 17 828.671(28) eV. Also with this analysis a linear drift over time was found (see figure 60). This time 1.29(6) ppm/month for the case of the Pt-10-1 and 0.40(11) ppm/month for Pt-15-5.

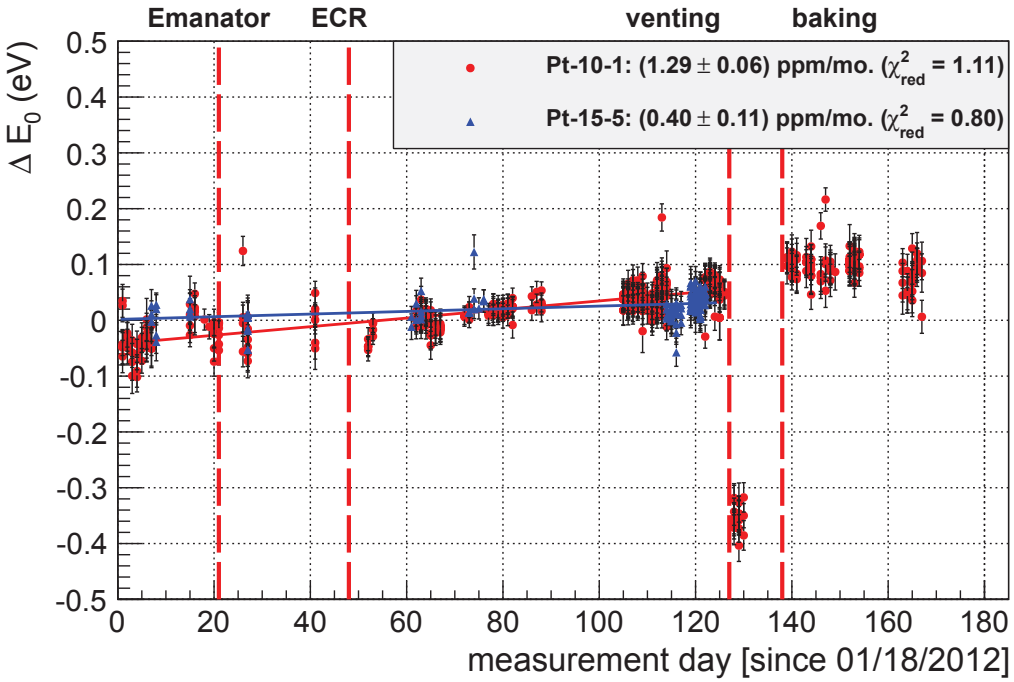

Figure 60: Results of the cross correlation method for the K-32. All fits were carried out in an interval of [17 825 eV,17 840 eV]. The error bars denote the error of the position obtained by the fit, multiplied by $\sqrt{\chi^2_{\text{red}}}$ to take the goodness of fit results into account. Typical χ^2_{red} are around 2.3. The data points were fitted with a straight line up to the venting of the spectrometer (day 125)

5.5.3 Results for analysis with Doniach-Sunjic line shape

In contrast to the analysis with the Voigt profile and the cross correlation method, the analysis with the DS shape showed within the first 80 days of measurement a very small drift for Pt-10-1 and a nearly zero drift for Pt-15-5 (dashed lines in figure 61). After this time the data starts to show a slight drift over time (see figure 61). The drift was also determined with a fit up to the day when the spectrometer was vented (solid lines in figure 61). These fits show slightly higher χ^2_{red} which may point to additional systematic uncertainties. Since the source is not expected to be stable for a certain time before it starts to drift and no significant change at the set-up was made, the secondary parameters like α were investigated further. Unfortunately the line position and the α parameter are strongly correlated (correlation coefficient around 0.92). The corresponding α parameter of each fit is also shown in figure 61.

In order to determine the correlation between the line position and the α parameter, the fits were repeated for both sources with fixed α parameter. This was done for α = 80, 90, 100, 110 and 120 and for two different measurement periods (see figure 62). The first one between 19$^{\text{th}}$ and 25$^{\text{th}}$ of January (day 1 to 7) and the second one between 30$^{\text{th}}$ of April and 18$^{\text{th}}$ of May (day 105 to 114). The results were fitted with a straight line. Both sources showed identical results for both periods which is shown in table 5.2. The weighted average of all four analyses gives the dependence of $\frac{dE_0}{d\alpha} = m_{\alpha,E_0} = 4.04(5)\,\text{meV}$.

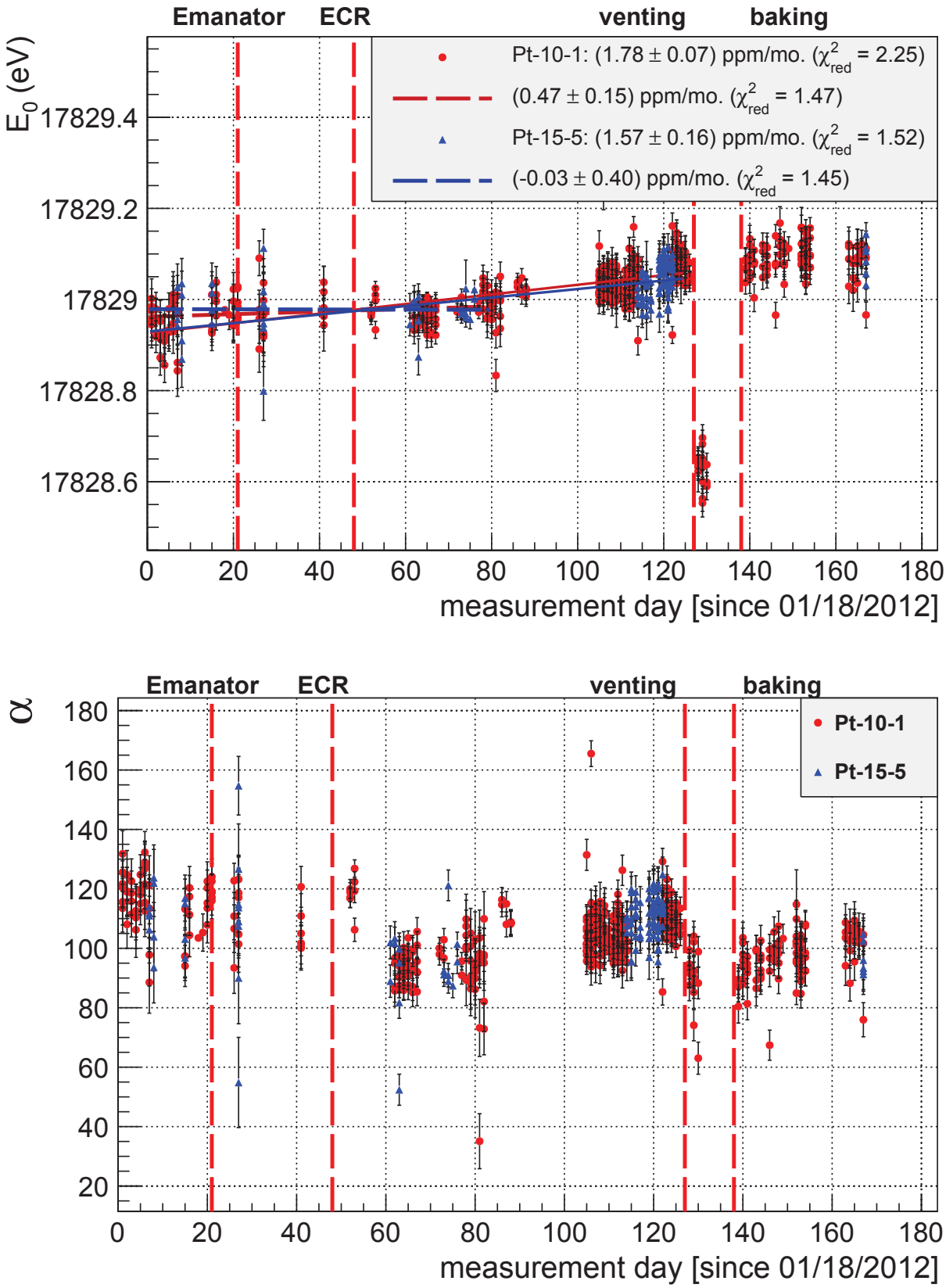

Figure 61: Results of the fit with a DS for the K-32 line. All fits were carried out in an interval of [17 815 eV,17 850 eV]. The error bars denote the error of the position obtained by the fit, multiplied by $\sqrt{\chi^2_{\mathrm{red}}}$ to take the goodness of fit results into account. Typical χ^2_{red} are around 1.2. The data points were fitted with a straight line up to the venting of the spectrometer (day 125) (solid line) and additionally up to day 80 (dashed line).

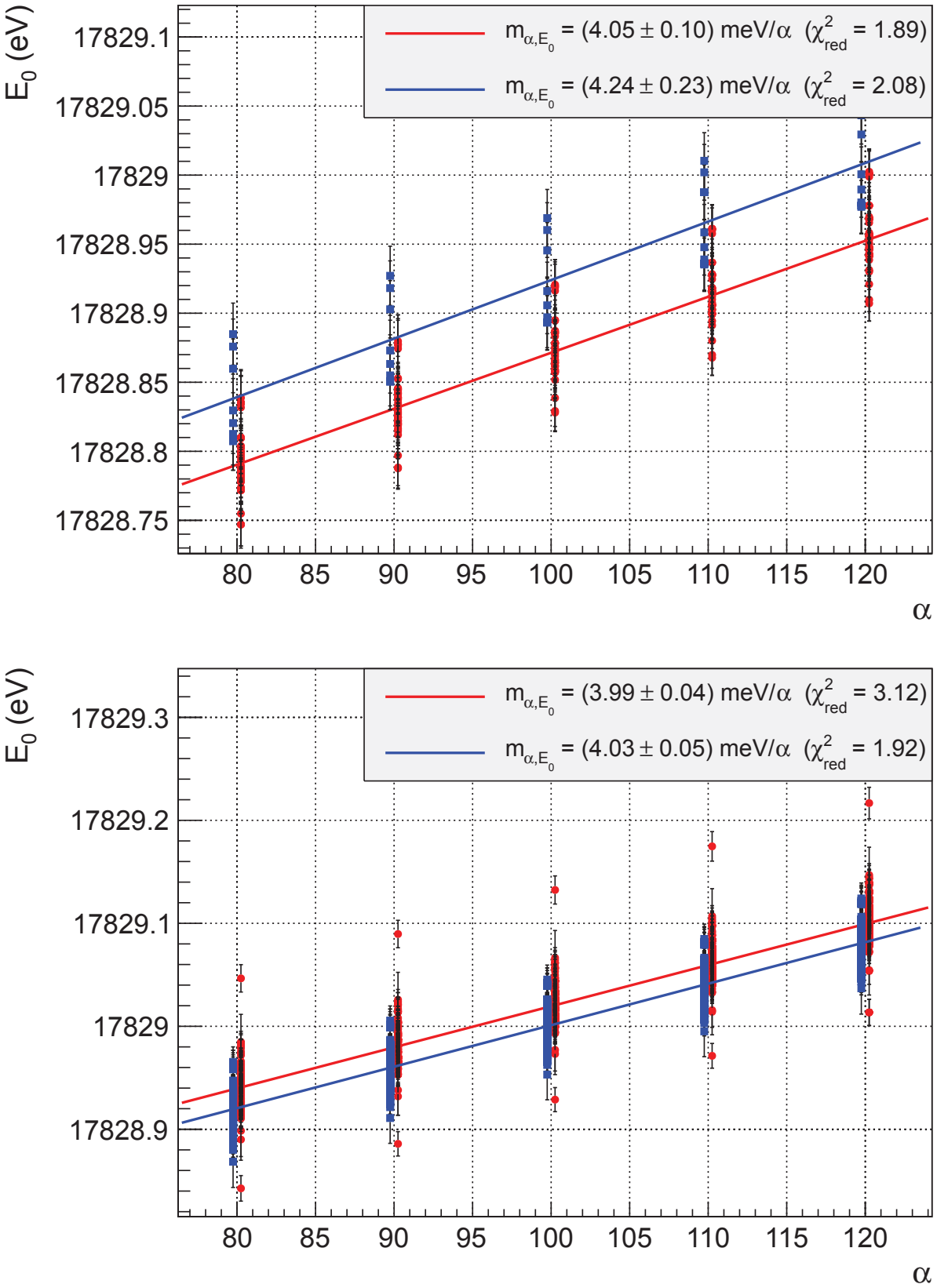

Figure 62: Results of DS fits with α fixed to 80, 90, 100, 110 and 120. The upper plot shows the results for a measurement series in January 2012 and the lower one those of May 2012. This analysis show a constant correlation between α and line position identical for both sources and stable over time.

Table 5.2: Correlation between line position E_0 and skew parameter α. The table shows the correlation between E_0 and α obtained from fits with fixed α for two sources at different times (see figure 62). The average was weighted according to the uncertainty of each results obtained from the fit.

Source	Date	$m_{\alpha,E_0}(\frac{meV}{1})$
Pt-10-1	January	4.05 ± 0.14
Pt-10-1	May	3.99 ± 0.07
Pt-15-5	January	4.24 ± 0.33
Pt-15-5	May	4.03 ± 0.07
weighted average		4.04 ± 0.05

In order to find a drift which is possibly masked by the α parameter, the data set showed in figure 61 was corrected by the following formula:

$$E_0' = E_0 - \Delta\alpha \cdot m_{\alpha,E_0} \,. \tag{5.11}$$

Here E_0' is the corrected line position, E_0 the line position found by the fit for a free α parameter, $\Delta\alpha = \alpha - \alpha_{\text{mean}}$ is the difference from the determined α to the mean value of α, which is in this case $\alpha_{\text{mean}} = 102.8$. Finally the dependence between α and line position is $m_{\alpha,E_0} = \frac{dE_0}{d\alpha} = 4.04\,\text{meV}/\alpha$. The results for this correction are shown in figure 63. After this correction is applied to the data, both sources show linear drifts which are comparable to the drift obtained by the two other methods. The drifts are 1.82(7) ppm/month for Pt-10-1 and 0.54(16) ppm/month for Pt-15-5.

5.5.4 Comparison of stability analysis results

The analysis carried out within this chapter shows a linear drift for both sources. An overview of the results is given in table 5.3. The results for Pt-10-1 are in the rage of 1.29 to 1.82 ppm/month. For the more deeply implanted source Pt-15-5 drifts ranges from 0.40 to 0.60 ppm/month were obtained, where the analysis with the DS function leads to a significantly different value of 1.57 ppm/month. After a correction of the correlation between line position and skew parameter the drift is in well agreement with the other results. All these values are not corrected for the drift of the K35 divider because the expected drift of the divider is of the order of less than 0.1 ppm/month and is equal for all measurements and analysis methods. All analysis methods showed a drift in the order of 1 ppm/month, which one order of magnitude higher than the drift of the K35 high voltage divider. Since both sources show different time-dependent drifts these drifts are not caused be a change in the work function of the spectrometer or by the high voltage divider but by the sources themselves. These drifts and especially the reproducibility of the ion implanted sources will be investigated in more detail in [Erh15] and [Sle15].

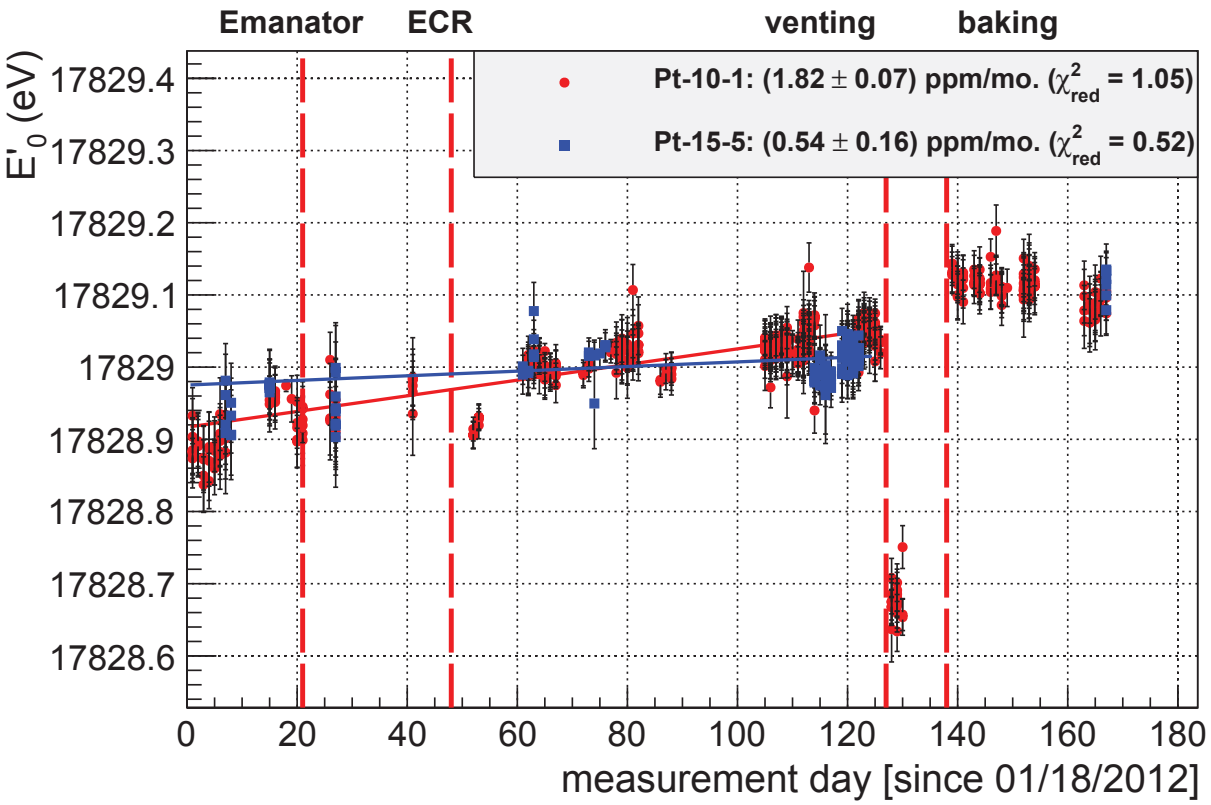

Figure 63: Line positions E_0' corrected for the correlation between α parameter and line position E_0. The correction was carried out with the results of table 5.2 and equation (5.11). With this correction the results for the drift over time get similar to those of the analysis with Voigt profile and cross correlation method, compare figures 59 and 60.

Table 5.3: Results for all three methods of stability analysis of sources Pt-10-1 and Pt-15-5. The results obtained from all method are comparable for each source. The only exception is the DS analysis for Pt-15-5. After the correction of the DS analysis for the correlation of α and E_0 also this results fits to the other methods. All errors are only statistical errors obtained from the fit. The systematic errors are identical for all analyses and will only cause a constant offset.

	Drift (ppm/month)	
Method	Pt-10-1	Pt-15-5
Voigt	1.55 ± 0.06	0.60 ± 0.12
CrossCorr	1.29 ± 0.06	0.40 ± 0.11
DS	1.78 ± 0.07	1.57 ± 0.16
DS corrected	1.82 ± 0.07	0.54 ± 0.16

In order to compare all three methods, the difference in fitted line position in comparison to the position obtained from a fit with a Voigt profile is shown in 64. Since all methods shows only minor deviations it is not obvious which analysis method is optimal. Detailed studies on the best analysis method will be carried out within the PhD theses of M. Slezák [Sle15] and M. Erhard [Erh15] and are not topic of this work.

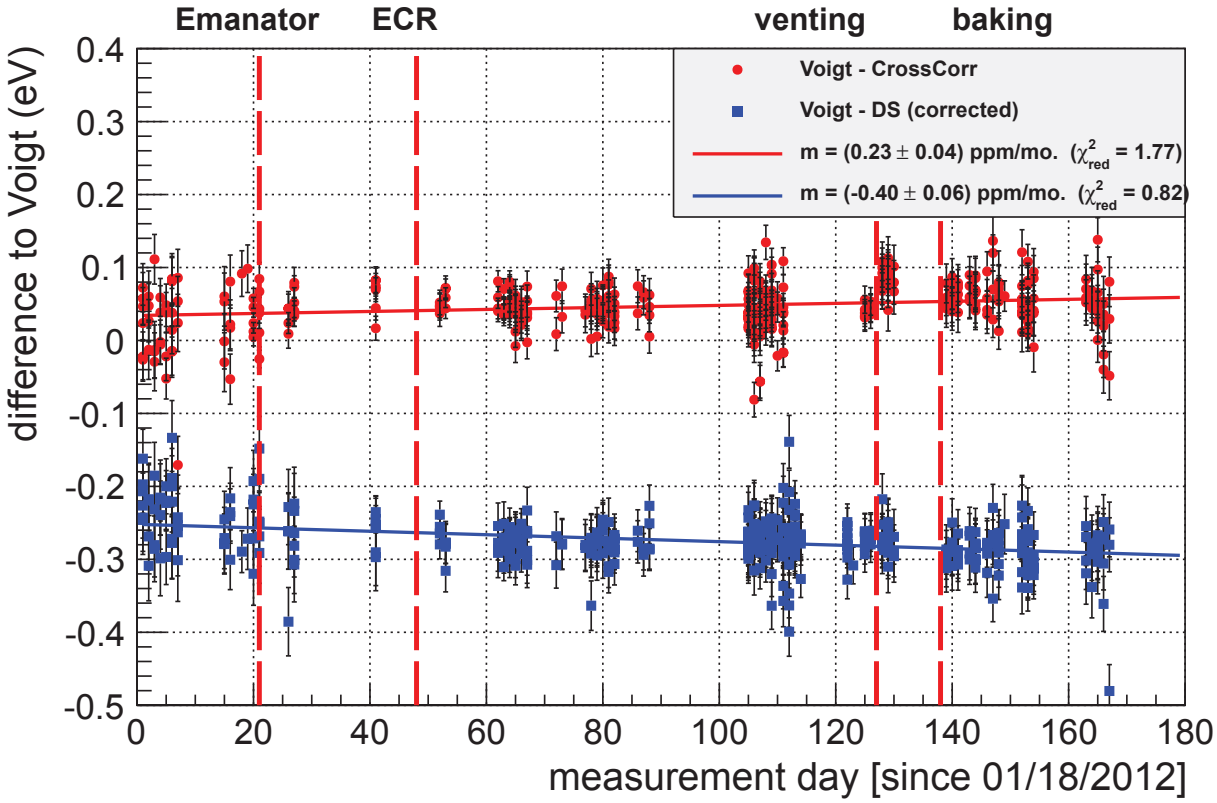

Figure 64: Difference in fit results of cross correlation and DS fit (corrected) in comparison to the analysis with a Voigt profile. This comparison was made for Pt-10-1. The plot shows only a sub-ppm deviation over one month and therefore no significant difference between those methods.

5.6 Difference of gamma energies

Beside the stability of the K-32 line, in this work also the difference in γ energies was investigated. This was done by measuring conversion electrons of the same shell, which was in this case the L_3 shell, for both transition energies. The atomic binding energy as well as correction $\Delta E_{\mathrm{bin}}^{\mathrm{Fermi}}(\mathrm{impl,i})$ (equation (5.7)) are expected to be the same for the same sub-shell which is in this case L_3. By only considering the difference of both line positions these effects and the spectrometer work function cancel out. Under the assumption that all conversion electron lines of one source are drifting to the same extent, the difference in γ energies should be constant. This is also the case if experimental conditions changes like the source or detector position or even the work function of the spectrometer. The difference in

γ energies will change if the scale factor of the voltage divider changes over time or if the voltage dependence of the voltage divider changes for some reason.

The difference of the kinetic energy for the L_3-32 keV and L_3-9.4 keV is than given according to eq. (5.7) by:

$$E_{\mathrm{kin}}^{\mathrm{impl}}(L_3\text{-}32\mathrm{keV}) - E_{\mathrm{kin}}^{\mathrm{impl}}(L_3\text{-}9.4\mathrm{keV}) = \Delta E_{\mathrm{kin}}^{\mathrm{impl}}(L_3) = \Delta E_\gamma + \Delta E_{\mathrm{rec},\gamma} - \Delta E_{\mathrm{rec,e}}\,, \qquad (5.12)$$

where in this case ΔE_γ is the difference in γ energies, $\Delta E_{\mathrm{rec},\gamma}$ the difference in recoil energy caused by the gamma ray emission and $\Delta E_{\mathrm{rec,e}}$ the difference between recoil energies caused by the emission of the conversion electron. All remaining terms cancel out. Hence the difference in γ energies can be written as:

$$\Delta E_\gamma = \Delta E_{\mathrm{kin}}^{\mathrm{impl}}(L_3) - \Delta E_{\mathrm{rec},\gamma} + \Delta E_{\mathrm{rec,e}}\,. \qquad (5.13)$$

The measurements were arranged such that different conversion electron lines were scanned multiple times within one measurement run which spanned 1-2 days. For example the L_3(9.4 keV) was first scanned four times, then K-32 four times and finally L_3(32 keV) line four times. This was also done with different repetitions and also with a different combination of electron lines. For the analysis each line position was fitted with the Doniach-Sunjic function (without the correction for the α parameter). Then the mean values of all scans (most times 3-4 scans) within one run were used to calculate the difference in γ energies. The results for both sources are plotted in figure 65. All in all 279 spectra of each conversion electron line were taken for this analysis.

The data points were fitted with a constant yielding to the following differences in in measured line positions:

$$\text{Pt-10-1: } \Delta E_{\mathrm{kin}}^{\mathrm{impl}}(L_3) = 22\,746.088(7)\,\mathrm{eV} \qquad (5.14)$$

$$\text{Pt-15-5: } \Delta E_{\mathrm{kin}}^{\mathrm{impl}}(L_3) = 22\,746.088(10)\,\mathrm{eV} \qquad (5.15)$$

The errors of these values have been multiplied with $\sqrt{\chi^2_{\mathrm{red}}}$. The difference in γ energies can now be calculated with the help of equation 5.13) with $\Delta E_{\mathrm{rec,e}} = 0.160\,\mathrm{eV}$ and $\Delta E_{\mathrm{rec,e}} = 0.005\,\mathrm{eV}$:

$$\begin{aligned}\Delta E_\gamma(\mathrm{L_3}) &= 22\,746.088\,\mathrm{eV} - 0.005\,\mathrm{eV} + 0.160\,\mathrm{eV} \\ &= 22\,746.243\,\mathrm{eV} \pm 0.012\,\mathrm{eV_{stat}} \pm 0.053\,\mathrm{eV_{sys}}\end{aligned} \qquad (5.16)$$

The difference is calculated using the mean value of both sources and already corrected for the scale factor of the K35 divider. This is necessary because there is only a preliminary value of 1972.5:1 stored in the data base. The scale factor used for this analysis is calculated

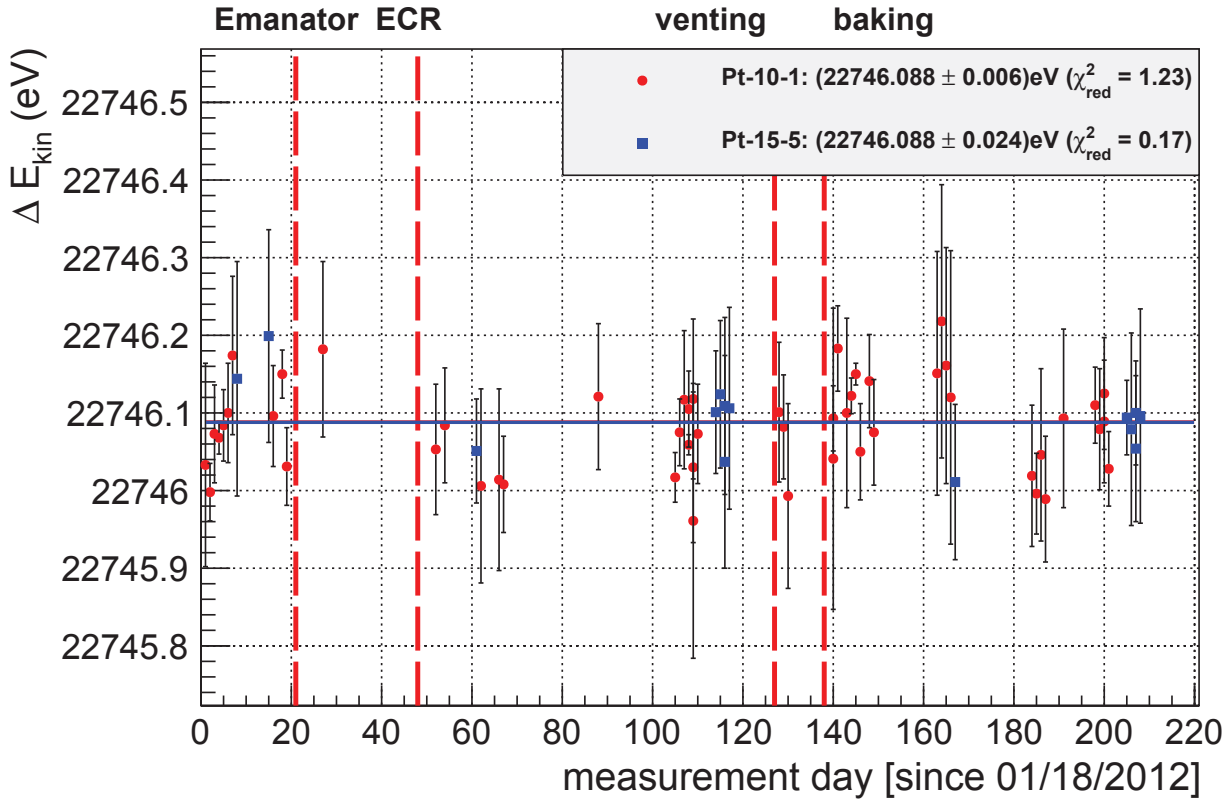

Figure 65: Difference in gamma energies. The plot shows the results for the difference of the measured line position of the L_3 shell. The data points denote the difference of the mean values of multiple scans measured within one measurement run. The error bars represent the quadratic sum of the standard deviations of the scans. To obtain the difference in measured line position (ΔE_{kin}) a constant was fit to the data for each source.

according to its quadratic voltage dependence (see section 4.5 figure 44) and is not corrected for the time depended drift of less than 0.1 ppm/month. The time dependent drift is treated as systematic error together with the calibration uncertainty of 2 ppm and the uncertainty of the 10 V reference source and hence the uncertainty of the voltage measurement. The latter was estimated to be about 1 ppm.

The expected difference in γ energies is given by the results of [Ven06] and [Sle12]:

$$\Delta E_\gamma(32 - 9.4) = 32\,151.7(5)\,\mathrm{eV} - 9405.8(3)\,\mathrm{eV} = 22\,745.9(6)\,\mathrm{eV}\,. \tag{5.17}$$

The difference of 348 meV is well within the error bar of the values obtained from gamma ray spectroscopy. The same analysis was done in [Zbo11] leading to a difference of 22 745.99(28) eV, which is also in good agreement with the values found in this work.

This difference in γ energies is not only of interest to investigate the calibration sources but by this also a malfunction of the high voltage dividers can be detected. If one of the resistors inside the dividers get damaged, the divider experiences in almost all cases a significant change in voltage dependence. Hence, if the difference of the γ energies changes drastically

at a certain time, this will be related to the high voltage divider. Since this is not the case in this analysis it is assumed that the divider is stable within its expected drift over time. If the by this method obtained difference of the γ energies changes slowly over time this could even be caused by the divider drift. In order to obtain the divider drift from these measurements the data shown in figure 65 were also fitted with a straight line which yield the following results:

$$\text{Pt-10-1} : 0.26(13)\,\text{ppm/month} \quad (\chi^2_{\text{red}} = 1.18) \tag{5.18}$$
$$\text{Pt-15-5} : -0.12(40)\,\text{ppm/month} \quad (\chi^2_{\text{red}} = 0.18) \tag{5.19}$$

Both results are compatible with a small positive drift in the order of $0.1\,\text{ppm}\,\text{month}^{-1}$ to $0.3\,\text{ppm}\,\text{month}^{-1}$ which corresponds to the same drift over time for the high voltage divider but with the opposite sign. This is in the same order as the expected drifts for the KATRIN high voltage dividers. As already mentioned in chapter 4 the drift over time of K35 is not yet determined at high voltages since a broken resistors was exchanged in 2010 and hence the scale factor changes. This time-dependent drift will be obtained from the next calibration at PTB in 2013. In order to obtain the voltage dependence of the K35 divider the difference in gamma energies must be known with high precision. Since this difference is only known with a precision of 0.6 eV the lowest change in scale factor (M) caused by a voltage dependence obtained from these measurements is:

$$\frac{\partial M}{\partial U} = \frac{0.6\,\text{V}}{22\,745.9\,\text{V}} = 26\,\text{ppm} \tag{5.20}$$

The expected change in scale factor for a voltage difference of 22 745.9 V is about 1 ppm and therefore can not be determined by this method. Nevertheless a malfunction which causes in many cases a drastically increase in voltage dependence can possibly be observed with this method.

5.7 Summary of the measurements at the monitor spectrometer

Between January 2012 and July 2012 two different ion implanted sources were measured. For the first source the ^{83}Rb was implanted with 10 keV implantation energy (Pt-10-1) and for the second source with 15 keV implantation energy (Pt-15-5). The measurements were carried out at the KATRIN monitor spectrometer. In this work the stability of the K-32 line was investigated with three different types of analysis. The first one was the fit of a Voigt profile to the measured spectrum, the second one a fit of a Doniach-Sunjic line shape and the last one was the comparison of all measured spectra to a reference spectrum with the method of cross correlation.

All methods showed a linear drift over time which was for the Pt-10-1 in the range from 1.29 to 1.82 ppm/month and for Pt-15-5 from 0.40 to 0.60 ppm/month. Especially the more

deeply implanted source Pt-15-5 fulfills the KATRIN requirements of 3 ppm/month. The drifts of the implanted sources found in this measurement series are one order of magnitude larger than the drift of the K35 divider, therefore the stability of the K35 divider could not be cross checked by the stability of the K-32 line position.

As additional check for the the integrity of the K35 divider, the difference of the line position of the conversion electrons of the L_3 shell was measured for both transition energies. By only considering the difference in energy all systematic effects cancel out and the difference in measured line position should be the difference of both γ energies. The latter was measured with gamma ray spectroscopy to be 22 745.9(6) eV. This difference in γ energies is constant over time as long as all conversion electron lines of one source drift to the same extend. If the experimental set-up could be stabilized even further and the analysis could be optimized this measurement shows high potential to be used to check or even determine the divider drift over time. First measurements showed already a drift which is expected for the K35 divider and has to be cross checked by calibrations at PTB in October 2013. Also the opportunity to measure the voltage dependence of the KATRIN high voltage dividers is limited to the accuracy of the gamma energies obtained from gamma ray spectroscopy.

Chapter 6

The condensed Krypton calibration source

An alternative approach to the ion implanted calibration sources, are condensed krypton sources. This type of source adsorbs ^{83m}Kr on a cold substrate ($T \approx 25\,\mathrm{K}$) instead of ion implanting ^{83}Rb into foils of noble metals as it is the case for the implanted sources presented in the previous chapter. The mother isotope ^{83}Rb is stored in an external container and the gaseous ^{83m}Kr is guided via a thin capillary to the substrate. The substrate is typically cooled by a cryocooler down to $\approx 30\,\mathrm{K}$ and placed inside an ultra-high vacuum (UHV) chamber. The substrate is additionally shielded by cold baffles ("cold shields") to avoid adsorption of residual gas. The cleanliness of the substrate surface is crucial for the stability and reproducibility of the conversion electron line position. Therefore the cleanliness is monitored by means of laser ellipsometry.

This concept of a quench **C**ondensed **Kr**ypton **S**ource (CKrS) was utilized the first time for a neutrino experiment at the Mainz Neutrino Mass Experiment [Pic92a]. A new condensed krypton calibration source for the KATRIN experiment was set up by B. Ostrick within her Ph.D. thesis [Ost08]. This source was successfully tested at the spectrometer of the former Mainz Neutrino Mass Experiment and showed the required stability on long-term scale. Also the long-term drift of the K35 high voltage divider (see chapter 4), measured between 2005 and 2006 at the PTB, could be verified by the stability of the line position over time [Ost08, Thü07].

The advantages of a condensed krypton source are:

- The preparation of the film and hence the line position is very reproducible.
- High stability of the line position over one week was shown in [Ost08] and is limited to vacuum conditions.
- Long-lived ^{83}Rb is stored in an external container which is separated by a valve, hence the risk of contamination of the spectrometer is minimized.
- Count rates in the order of $10^3\,\mathrm{s}^{-1}$ can be achieved by sufficiently strong ^{83}Rb sources ($\mathcal{O}$(MBq)). This requires an efficient transport of the ^{83m}Kr from the ^{83}Rb container to the substrate.

After the tests at Mainz, the set-up was transported to the Institut für Kernphysik at the University of Münster to investigate known issues and to prepare the calibration source for the application at the KATRIN experiment. This chapter gives an overview of the recent set-up and the improvements made. Finally, the new design developed in this work will be presented.

6.1 Set-up in Münster

The vacuum set-up consists of two chambers connected via a bellows. This bellows allows to move the substrate region, which is for example necessary at the CPS to move the source into the flux tube. The chamber in the front ("Elli-chamber") contains the front part of the cold finger with the substrate and the radiation shields on it (see figure 70). The cryocooler and

the turbomolecular pump (TMP) are attached via bellows to the second chamber ("cryo-section"). These bellows reduce vibrations on the substrate caused by the operation of the cryocooler and TMP. Further electrical feedthroughs and a gas preparation system are connected to the cryo-section. A CAD drawing of the vacuum chamber with the parts of the substrate region, the cryocooler and its attached cold finger is shown in figure 66 and a recent overview of the set-up is given in figure 67. The following sections will give details about the subcomponents of the CKrS.

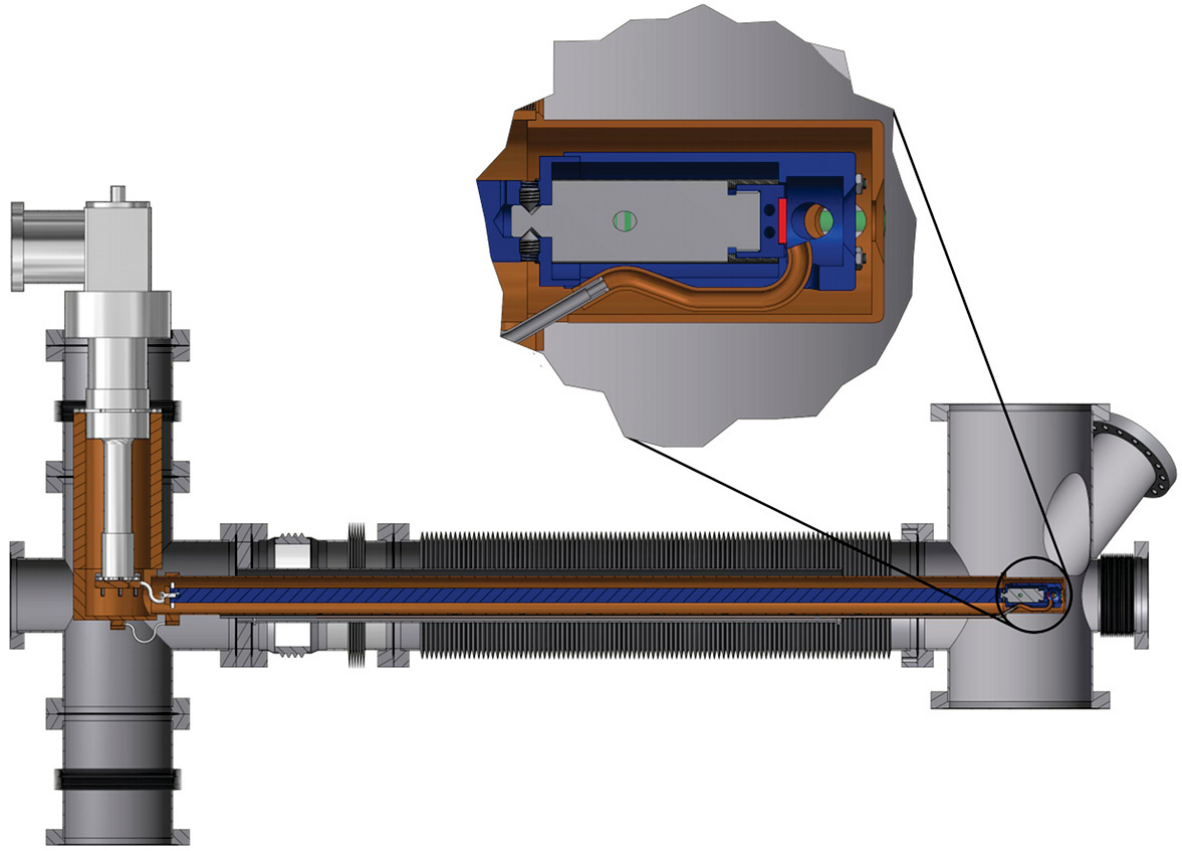

Figure 66: CAD drawing of the inner parts and vacuum system of the recent set-up at IKP Münster. Shown is the vacuum chamber (gray), the cryocooler (silver), the outer cold shield (copper) and the cold finger and inner cold shield (blue). The inset shows a magnification of the substrate region with stainless steel part (gray) to reduce the thermal conductivity and the nozzle (copper) for the krypton gas. The substrate is marked in red.

6.1.1 Vacuum system

The CKrS is evacuated by two cascaded turbomolecular pumps, backed by a dry fore pump. The pressure is measured with a Oerlikon Leybold Ionivac ITR 90 vacuum gauge, which can measure down to 5×10^{-10} mbar. This differential pumping is able to reach ultra high vacuum levels and is supported by the cold shield which acts additionally as a cryo pump. A schematic overview of the vacuum system is given in figure 68.

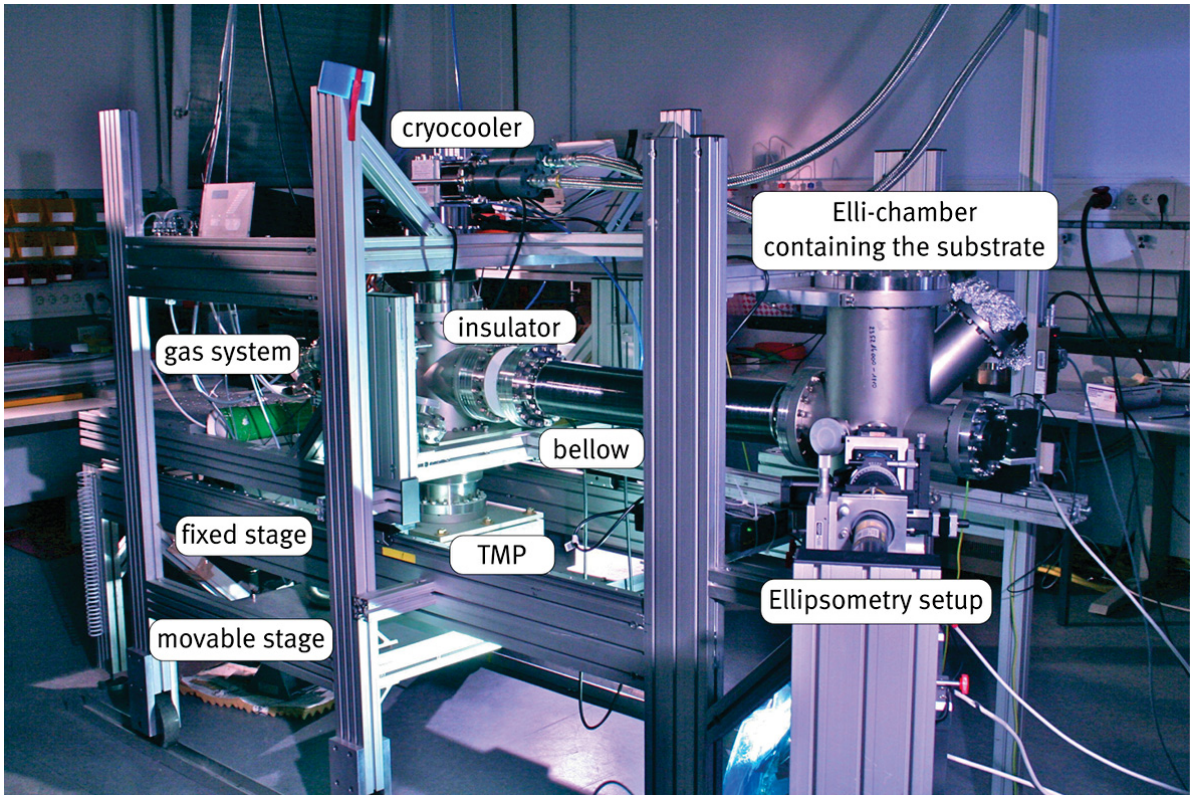

Figure 67: Side view of the CKrS set-up in Münster. The picture shows both vacuum chambers connected via a bellows. The front chamber contains the HOPG substrate and has an entrance window for the ellipsometry. The TMP and the cryocooler are connected to the second chamber. This second chamber is moveable (in z direction) with respect to the fixed front chamber. To apply high voltages to the substrate, the inner part and the second chamber are electrically insulated from the front chamber.

During the measurements at Münster it was possible to reach a pressure of $< 5 \times 10^{-10}$ mbar. The residual gas spectrum was dominated by hydrogen. The KATRIN requirement is a pressure in the 10^{-11} mbar region which can be reached by an additional non evaporable getter pump (NEG-pump, SAES GP100 MK5) with a pumping speed of 240 L/s for hydrogen. By this, most of the remaining hydrogen will be removed. This pump was purchased and will be installed at the CKrS set-up for the CPS which is described in section 6.2.

6.1.2 Crycooler and cold finger

The substrate is cooled by a two-stage cryocooler of the Gifford McMahon-type (Sumitomo Heavy Industries Ltd., model RDK 408D). The first stage of the cryocooler has a cooling power of 34 W at 40 K and the second stage 1 W at 4 K. The outer cold shield is connected to the first stage and acts as radiation shield for the cold finger itself. The second stage cools the cold finger and hence the substrate and the inner cold shield (see figure 66). With this cooling system the substrate can be cooled down to ≈ 15 K. An additional heater allows to chose slightly higher substrate temperatures, which are of advantage against condensation

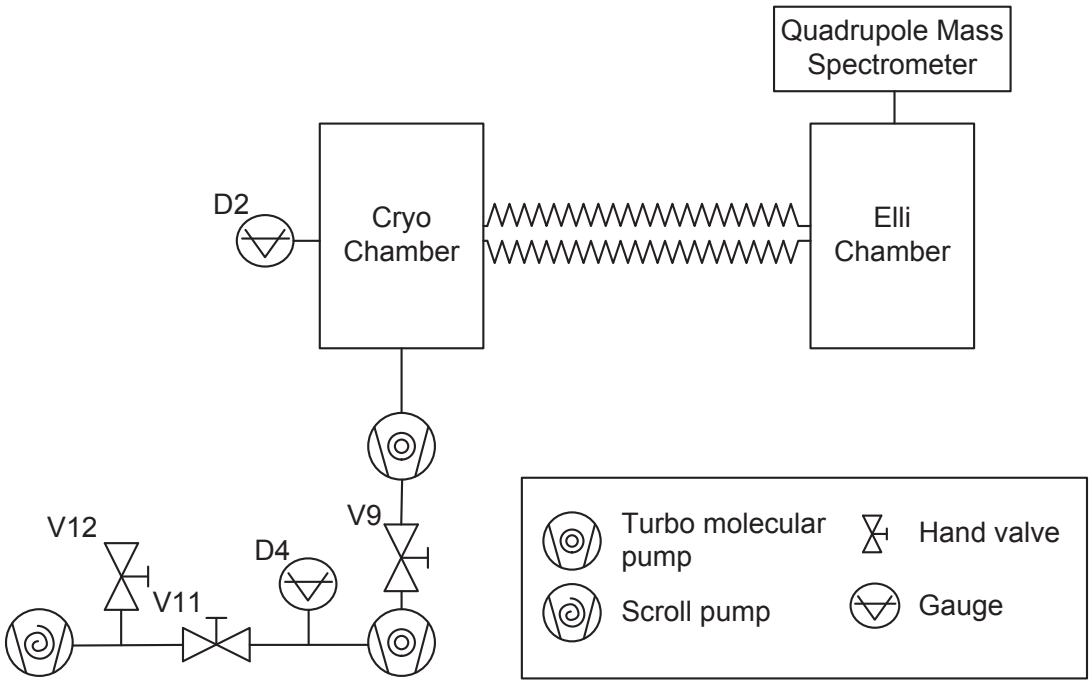

Figure 68: Vacuum system of the CKrS. Shown is a schematic view of the recent vacuum system. The two vacuum chambers are connected via a bellows. The system is pumped by two cascaded TMPs and a dry fore pump. The composition of the residual gas can be monitored by a quadrupole mass spectrometer. The cryocooler which acts as cryo pump is not shown.

of hydrogen gas.

In order to reduce the vibrations on the substrate, the connection between the cryocooler and the outer cold shield and the cold finger are realized by copper wires. Since copper has a high thermal conductivity the heat transport is high but due to the flexibility of the wire the vibrations are strongly damped. By this decoupling in combination with the afore mentioned decoupling of the TMP and the cryocooler from the set-up, almost all mechanical vibrations are avoided.

6.1.3 Substrate and substrate region

The substrate for the condensed krypton source was chosen to be **H**ighly **O**riented **P**yrolytic **G**raphite (HOPG), because it is on small scales atomically flat and electrically conductive. Hence the residual charges after a decay of the ^{83m}Kr will be discharged. Another special feature of HOPG is the significant difference of thermal conductivity in-plane and perpendicular (c-axis) to it. This offers perfect conditions for a cleaning of the substrate by means of laser ablation. This feature is strongly dependent on temperature and more details of laser ablation and the heat conductivity of HOPG will be presented in section 6.1.7. The

cleanliness of the substrate surface is of high importance in order to carry out high precision calibrations required by the KATRIN experiment.

HOPG is made of layers formed by carbon atoms arranged in a honeycomb structure (see figure 69). The distance between two atoms in this structure is 1.42 Å. The layers have a distance of 3.35 Å and since the layers hold together only by Van der Waals forces, a layer can easily be cleaved with adhesive tape. This way the surface of the HOPG substrate is prepared, before it is installed into the CKrS. The HOPG is polycrystalline thus the normal to the surface of the single crystals could have an non-zero angle with respect to the c-axis of the substrate. The HOPG is therefore classified by a "mosaic spread" which is determined by illuminating a significant part of the crystal with Cu-K_α radiation. The angle is than defined as the Full Width at Half Maximum (FWHM) of the rocking curve[1]. For the highest quality HOPG (SPI-1 or ZYA) this angle is $(0.4 \pm 0.1)°$. The electrical resistivity of HOPG at room temperature is $4 \times 10^{-5}\,\Omega\,\mathrm{cm}$ in-plane and $0.15\,\Omega\,\mathrm{cm}$ along c-axis [SPI].

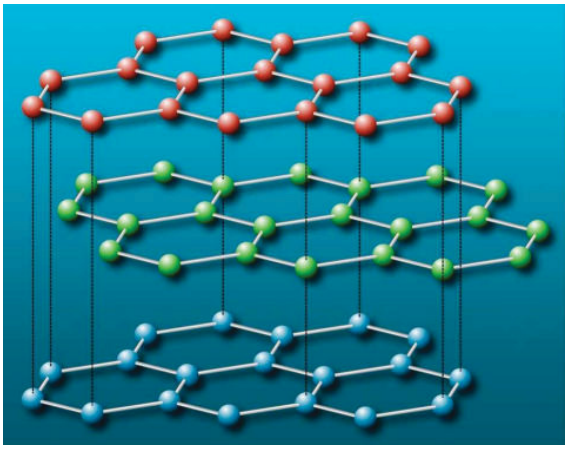

Figure 69: HOPG, like all graphites, consists of layers in which the carbon atoms are arranged in a honeycomb lattice. The distance between neighbouring atoms is 1.42 Å, the lattice constant is 3.35 Å and the distance between planes is 3.35 Å. (Source [Ost08]).

In the actual set-up of the CKrS the substrate is a $10 \times 10\,\mathrm{mm}^2$ grade SPI-2 (SPI supplies, mosaic spread $(0.8 \pm 0.2)°$) substrate and it is glued in a copper holder by electrically conductive silver epoxy (Polytec H20E). This electrically conductive glue ensure a good potential equalization. The copper mount is fixed to the cold finger via a middle section made from stainless steel, which reduces the heat load on the cold finger during heating of the substrate because of the poor thermal conductivity of stainless steel. The substrate is shielded by the inner and outer cold shield (see figure 70) in order to avoid the adsorption of residual gas. The temperature of the substrate is measured by a Si diode temperature sensor (LakeShore DT-670B-SD), which is mounted in the copper block that holds the substrate. The temperature of the substrate can be set to an arbitrary value above 20 K by means of resistive heating. To avoid birefringence of cold optical windows, both cold shields have free entrance and exit openings for the ellipsometry laser. Both cold shields have also an opening to the front through which the electrons are emitted.

[1] To measure a rocking curve, the detector is set at a specific Bragg angle and the sample is tilted. A perfect crystal will produce a very sharp peak. Defects like mosaicity create disruptions in the perfect parallelism of atomic planes [Spe].

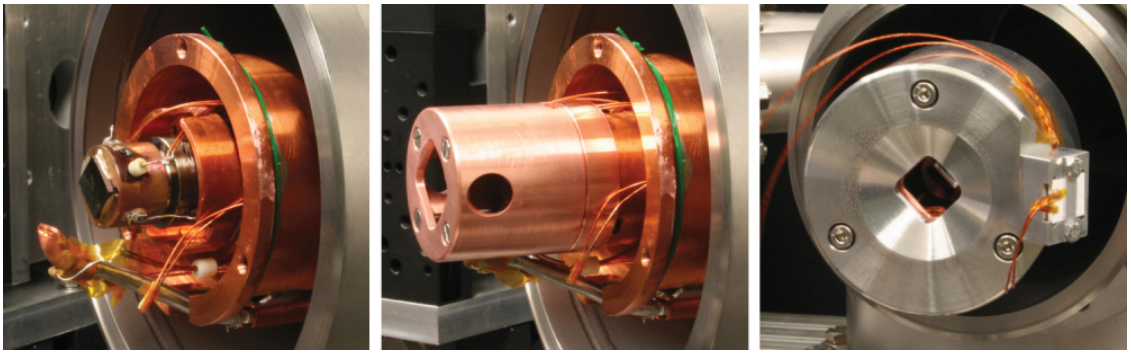

Figure 70: Head of the cryostat holding the substrate with two cold shields. Left: HOPG substrate glued on a copper block and the nozzle on the capillary for the gas inlet. Middle: Inner cold shield connected to the 1st stage of the cold head with the openings for the ellipsometry laser. Right: Outer cold shield and photodiode (for ellipsometry) connected to the 2nd stage of the cold head containing the analyzer and the detector.

6.1.4 Gas preparation system

The gas preparation system controls the gas flow from two possible sources towards the HOPG substrate. Improvements were made by T. Schäfer within his diploma thesis [Sch11]. These improvements are mainly in reducing the size and automating of the filling and evacuating of the system. During measurements at Mainz it turned out that the films are most stable if no other gas is frozen onto the substrate before the ^{83m}Kr [Ost08]. Therefore it is sufficient to have ^{83m}Kr and stable krypton as feed for the gas system. The stable krypton is needed in order to measure reference curves for the ellipsometry. Thus all parts needed for possible pre-plating layers e.g. neon were removed from the system. The actual version consists of a monitor volume (CF40 cross), two vacuum gauges (Oerlikon Leybold Ionivac, ITR 90 and Leybold CTR91 Ceravac), one valve (V4, see figure 71) for filling and two valves (V5 and V6) in combination with an inlay to reduce the conductance to prevent an overload of the TMP during the evacuation of the gas system (see figure 71 and 72). The system will be pumped by a TMP (Pfeiffer Vacuum TMU 071 P) in combination with a dry fore pump (Pfeiffer Vacuum TSU 071 E). The outgoing gas flow towards the substrate is regulated by a thermo-mechanical regulating valve (Pfeiffer Vakuum, UDV 146). The whole system is remote controllable via LabVIEW. More details about the gas system are presented in [Sch11].

6.1.5 Slow control system

The slow control system (SCS) controls and reads all parameters needed to operate the CKrS. The SCS is based on a PXI-system (National Instruments) and is written in LabVIEW. The front panel (figure 72) allows to control all valves and also the heater of the substrate. The software also allows to evacuate and fill the gas system and to do an automated condensation of films including the ellipsometry measurements. The number of condensation steps and the thickness of one layer can be set by the operator. The thickness of one layer is thereby controlled by the applied voltage and opening time of the regulating valve. This system

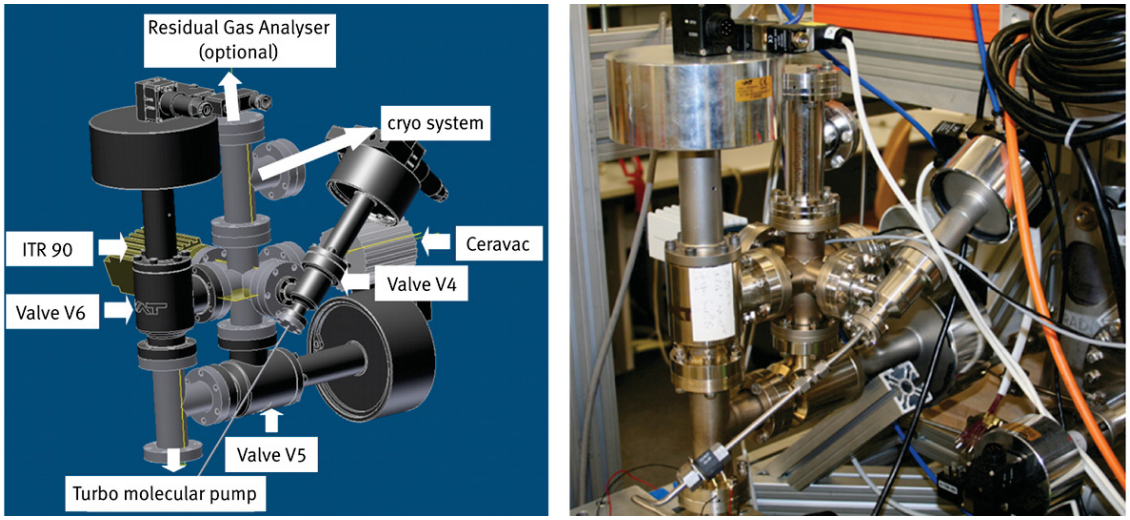

Figure 71: CAD drawing of the gas preparation system shows the monitor volume (CF 40 cross) and its connected valves and gauges (left). A real picture (right) of the gas system for the CKrS. (Based on [Sch11]).

also provides the complete data acquisition and instrument control needed to carry out the various types of reflection ellipsometry. More details on the ellipsometry SCS are presented in [Weg10].

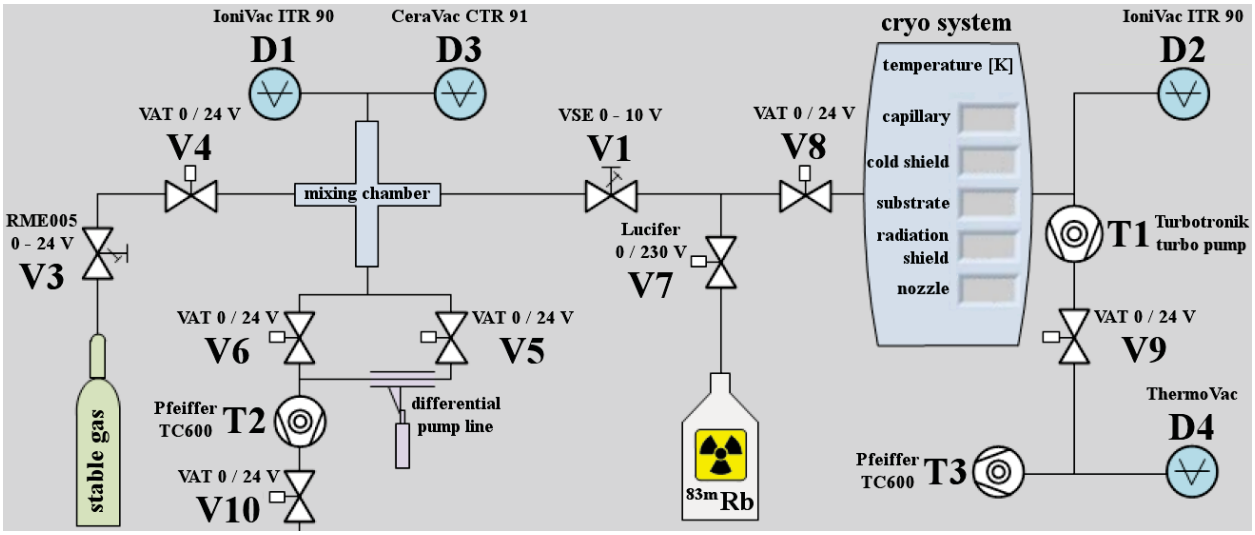

Figure 72: Front panel of the slow control system of the CKrS. The software gives an overview of the measured parameters and allows the control of the valves and the heater.

New sub-programs were developed within the diploma thesis of R. Bottesch [Bot12]. These sub-programs allow to control motors for the movement of the whole system and read back the current position. These developments are also preparations for the application of the CKrS at the CPS.

6.1.6 Ellipsometry set-up

The cleanliness of the substrate is monitored by means of laser ellipsometry (see chapter 7). This is a standard method in surface science for determining optical properties and thicknesses of thin solid films. Although ellipsometry offers sub-monolayer resolution, it is not possible to measure the thickness of the adsorbed ^{83m}Kr film. But contaminations caused by the residual gas can easily be detected by the ellipsometry. Thus the measurements with the ellipsometry set-up at Münster were carried out with stable krypton.

At Münster the system was upgraded to a green HeNe laser ($\lambda = 543.5$ nm, $P_{laser} = 0.5$ mW) in order to gain resolution. An addition the wavelength is closer to those of the ablation laser for which the optical windows are covered with an anti-reflection layer. Also new rotation tables (PI M-060.DG) for the optical components and a low noise current amplifier (Femto DLPCA-200) as readout of the laser ellipsometry detector were installed, tested and verified by A. Wegmann during her diploma thesis [Weg10]. The most recent ellipsometry set-up is presented in section 7.3. An overview of the front part of the CKrS, where the ellipsometry and ablation set-up is located, is given in picture 73. For the use at the CPS the ellipsometry

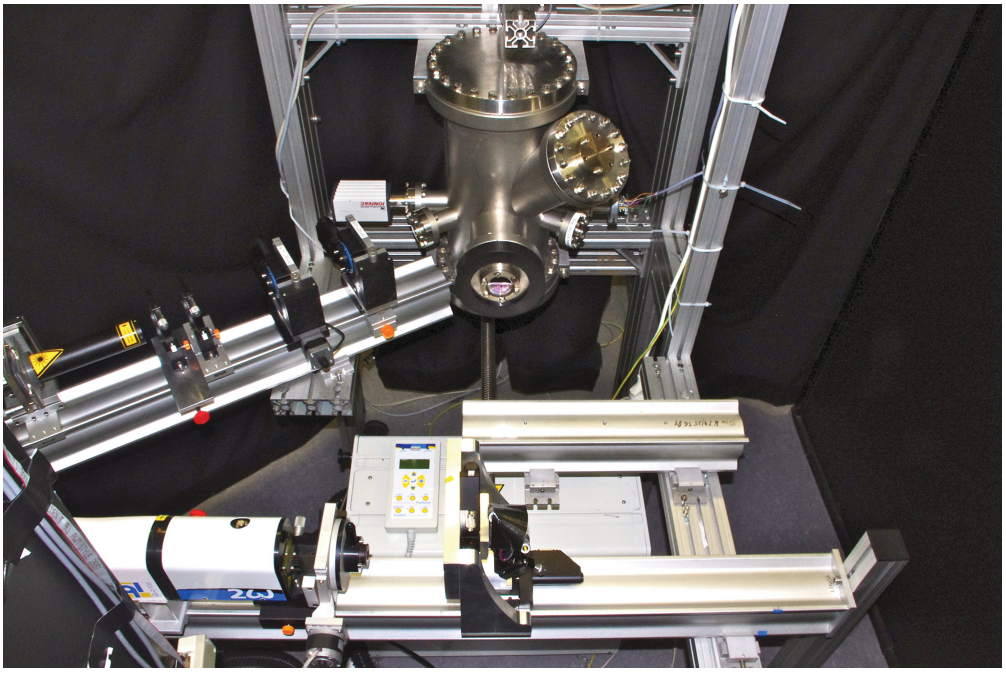

Figure 73: Picture of the front part of the CKrS. Shown is the ablation laser with the Glan-Laser polarizer to control the laser power and the mirror set-up in the lower part of the picture. In the left part is the ellipsometry set-up on its optical bench. The whole front part is enclosed by protection walls to ensure safe working conditions during the laser ablation.

has to be modified in a way that the laser beam enters the CKrS from the back and the reflected beam has to be analysed inside the vacuum chamber. This is necessary due to the large beam divergence caused by the optical properties of the HOPG (mosaic spread). Both constraints are due to the fact that no vacuum windows close to the substrate can be attached to the CPS. First concepts concerning this new set-up at the CPS were developed within this work and are presented in section 6.2. All details about ellipsometry and especially a novel

ellipsometry variant and its analysis which was also developed in this work, are presented in chapter 7.

6.1.7 Laser ablation

The surface cleanliness of the HOPG substrate is crucial for high precision calibrations with conversion electrons of condensed ^{83m}Kr, because possible contaminations will cause a shift in line position. In order to provide a clean surface, a combination of heating and laser ablation is applied. The heating up to 500 K is done via heating resistors, which are glued in the substrate holder. To induce more energy without heating the cryocooler too much the laser ablation is applied. By this cleaning method ultra-short pulses (≈5 ns) of a frequency-doubled Nd:YAG laser (λ = 532 nm, P_{laser} = 2 W) are used. This laser is guided via high reflective mirrors to the HOPG (see figure 74). These mirrors are mounted on linear stages which enables a scanning of the substrate by the laser beam.

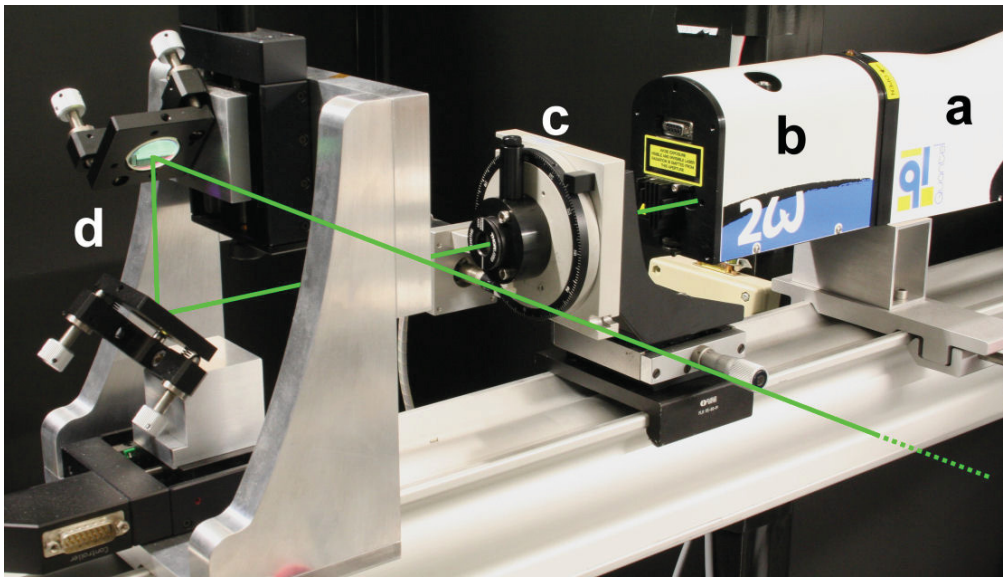

Figure 74: The ablation set-up consists of the laser (a) including the frequency doubler (b), a Glan-Laser polarizer with beam dump (c) to control the laser power and high reflective mirrors (d) to scan the surface of the HOPG with the laser beam. Not shown is the optional beam homogenizer which is placed in the optical path to provide a widened and homogeneous beam. (Source: [Bot12])

This cleaning method utilizes the high difference in thermal conductivity in-plane and perpendicular (c-axis) to the plane of HOPG. The difference depends strongly on the temperature which was investigated among others by [Iss83] and [Tay66]. When the thermal conductivity in-plane is much higher than in c-axis, the induced energy will be distributed over the surface of the substrate and only a little fraction goes into the bulk. To make use of this feature, the substrate temperature has to be above 200 K, otherwise the difference between both thermal conductivities gets similar as shown in figure 75. At the working temperature of the source (20 K to 25 K) the thermal conductivity in-plane is only four times higher than the conductivity in the c-axis.

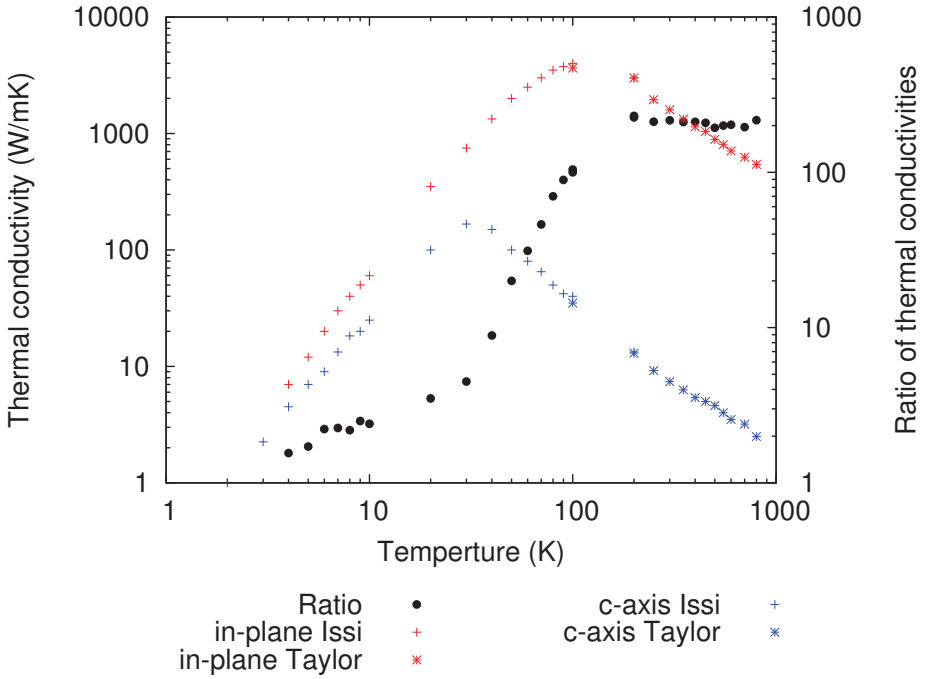

Figure 75: Thermal conductivity of HOPG in-plane (red) and perpendicular to the surface (c-axis, blue). The black dots denotes the ratio of the thermal conductivity perpendicular and in-plane. In the low temperature region both thermal conductivities become comparable. With increasing temperature the ratio also increases. Above 200 K the ratio keeps constant. Data for the temperature region up to 200 K are taken from [Iss83] and from 100 K to 800 K from [Tay66]

Because the ratio between the in-plane and c-axis thermal conductivity keeps constant above 200 K one expects that a heating temperature of 200 K in combination with laser ablation will be a good combination. During measurements at Münster it turned out that a further raise in temperature leads to cleaner surfaces (see chapter 7). For one measurement series the temperature was increased up to 500 K. The more efficient cleaning could be explained by the fact that at higher temperatures the probability for re-condensing of evaporated material is lower. Also the surrounding inner cold shield (see figure 70) is heated and thus cleaned by radiation heating. By that the local pressure will be improved.

The beam of the ablation laser can optionally be homogenized by a high-power laser beam homogenizer (SUSS 39 9935). This homogenizer has a divergence angle of $\pm 0.5°$. By this widening a scanning of the substrate is needless and the danger of too high intensities on the surface is reduced.

Too high laser intensities will destroy the surface of HOPG as reported in [Bot12]. The surface could be sufficiently cleaned at $300\,\mathrm{mW\,cm^{-2}}$ during the measurements at Mainz [Ost08]. A more detailed investigation was done in [Bot12] where it was found that the maximum allowable power density is $400\,\mathrm{mW\,cm^{-2}}$. During the latest measurements in this work it turned out that $180\,\mathrm{mW\,cm^{-2}}$ in combination with a heated substrate (500 K) are sufficient to clean the HOPG. For this measurements the ablation was carried out with the beam homogenizer over 180 s.

6.2 New set-up at the cryogenic pumping section

At the KATRIN experiment the CKrS will be used at the CPS to calibrate the KATRIN beam line. Due to technical constraints the actual set-up of the CKrS has to be modified to meet these requirements at the CPS. For this purpose the mechanical design was adapted to the installation at the CPS. The most obvious modification is that the CKrS must now be oriented vertically instead of horizontally as in Mainz and Münster. Also a new method of ellipsometry has to be used to monitor the surface cleanliness of the HOPG substrate (see section 7.2). This is caused by the fact, that at the CPS the reflected laser beam would have to be guided over approx. 2 m if the polarisation analysis of the reflected beam will be made outside the vacuum chamber. This is not possible due to the high beam divergence after the reflection at the HOPG.

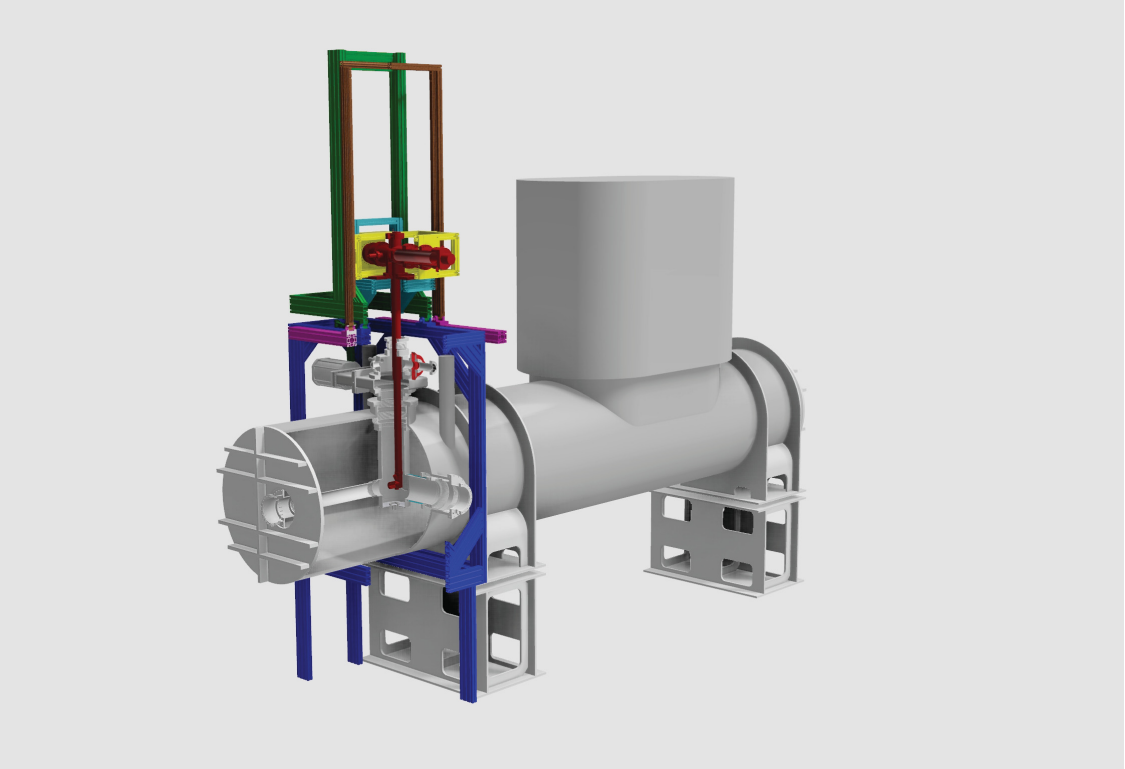

Figure 76: CAD model of the new CKrS mounted on top of the CPS. Shown is a sectional view of the CPS. The CKrS is inserted into the flux tube through pump port 2. The blue scaffold will be the base for the two movable scaffolds (green and brown). The CKrS itself is marked in red.

The CKrS will be mounted into a scaffold made from aluminium profiles (KANYA) on top of the CPS (see figure 76). This scaffold is split up into a part fixed to the floor and a movable part (see figure 77). The movable part is again split up into two segments as well. The one carries the TMP and the cold head of the cryocooler and the other the CKrS itself. By mounting the TMP and the cold head on a separate scaffold, in combination with bellows between those parts and CKrS, the transfer of vibrations to the substrate will be minimized as it is already the case for the existing CKrS.

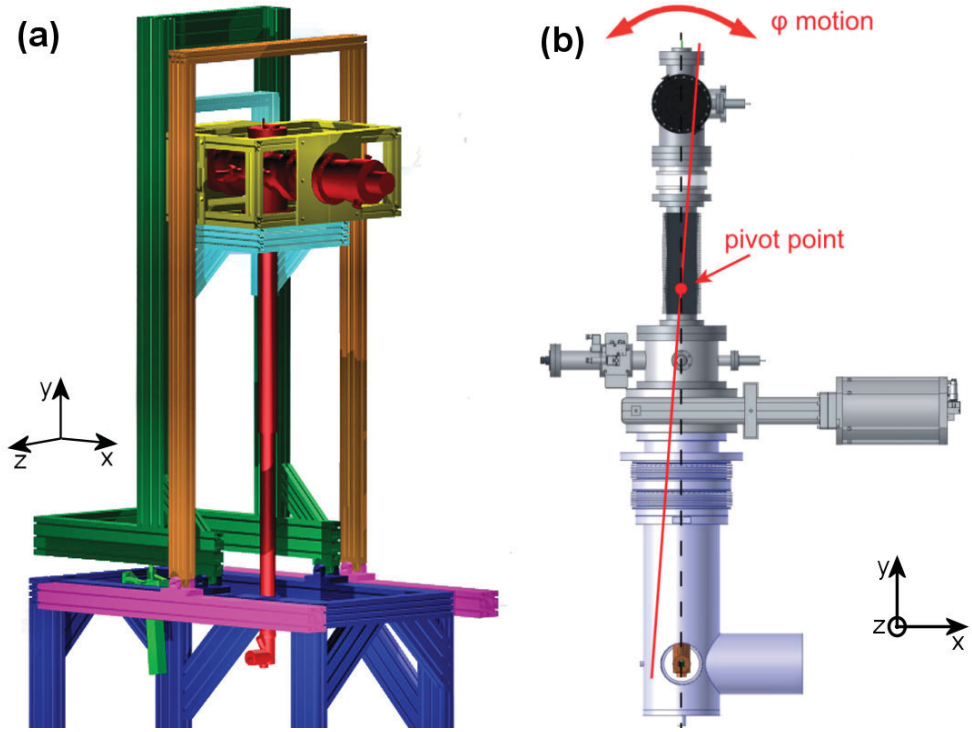

Figure 77: Scaffold and movement of the CKrS. The CKrS will be mounted on a scaffold made from aluminium profiles. The bottom part (blue and magenta) will be fixed to the hall ground. The top part will be split into one part to carry the TMP and cold head (yellow and brown) and the other part will carry the CKrS itself (light blue and green). This separation reduces the vibration on the substrate efficiently. Both top parts are pivot mounted onto the bottom part **(a)**. The movement to scan the flux tube will be split up into a vertical movement and a movement in φ-direction **(b)**.

In order to scan the flux tube the CKrS will be moved in y and φ-direction (see figure 77). By this the whole flux tube of the KATRIN experiment can be scanned and each detector pixel can be irradiated separately. The y-direction is realized by moving the CKrS on linear bearings on the scaffold (figure 77 green parts). In addition, the scaffold can be moved around a pivot point. By this the φ-direction is realized. Because of the drop of the magnetic field at the position of pump port 2 (figure 78) the movement of the CKrS has to cover a radius of about 70 mm. For that the movement in φ-direction has to cover an angle of $\pm 3.6°$.

At the CPS the substrate will be mounted under an angle of 90° with respect to the axis of the cold finger. This is because the CKrS enters the magnetic flux tube in a radial direction. This is shown in a sectional view in figure 79. Also the laser beam for the ellipsometry has to be guided inside the two cold shields due to the fact that there are no windows at the CPS. Hence the laser beam will enter the CKrS from the top (figure 79). In the substrate region the laser beam must be reflected via a mirror to the substrate (see figure 80). It was shown in [Spi11] that precise ellipsometry via mirrors is possible.

Because of the new orientation of the HOPG substrate the substrate region of the CKrS has to be redesigned. A first design developed within this work is shown in figure 80. The substrate for the new CKrS will be a $20 \times 20\,\mathrm{mm}^2$ HOPG of grade SPI-1 (SPI supplies, mosaic spread $(0.4 \pm 0.1)°$). The substrate holder will be fixed via a middle section made

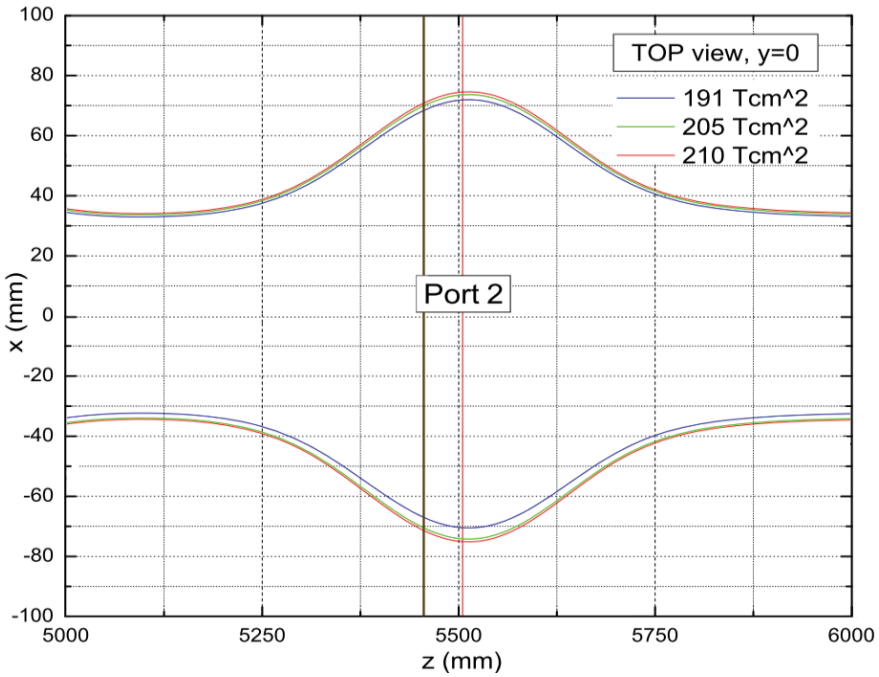

Figure 78: Magnetic flux tube inside the CPS at the position of pump port 2. The plot shows three different flux tubes. The KATRIN experiment is designed to transport a flux tube of 191 T cm^2 [KC04]. The red line denotes the position of the CKrS in z-direction in the middle of the split coil arrangement.

from stainless steel as in the existing set-up.

Before the removal of the condensed film the CKrS will be moved to the topmost position into an additional vacuum chamber ("ablation chamber") on top of the gate vale (see figure 81). During the laser ablation the gate valve towards the CPS will be closed. This ablation chamber holds the getter pump, the vacuum gauge and the optical window for the ablation laser. After the film is removed and the substrate is cooled down a new film can be prepared. After the preparation of the new film the source will be moved down to measurement position.

This new design of the CKrS for the application at the CPS uses most of the existing parts. After the finalization of the design the CKrS will be dismounted and reassembled in a new laboratory with sufficient ceiling height.

As already pointed out, it is not possible to utilize the same ellipsometry variant at the CPS, as at the recent set-up. Therefore a novel variant of the laser ellipsometry with polarisation analysis inside the UHV was investigated for the use at the CKrS. The basic principle and results of measurements of the novel ellipsometry variant at the CKrS at Münster are shown in the next chapter.

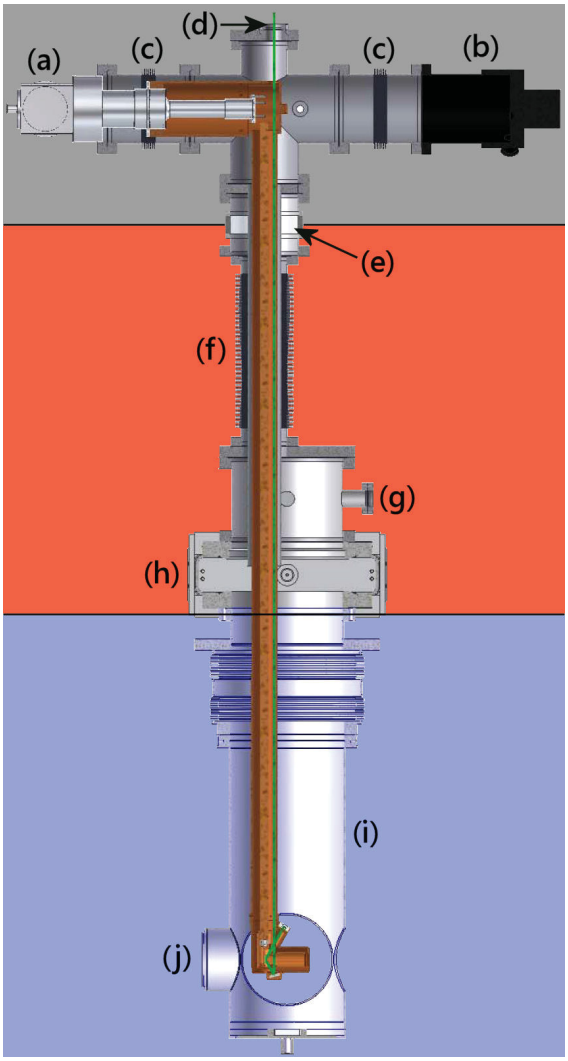

Figure 79: Side view of the CKrS at the CPS. The CKrS is divided into the section on high voltage (gray) and the grounded part (red). Both are connected on top of the CPS (blue). The top part consists of the cryocooler **(a)**, the TMP **(b)** both are connected via bellows **(c)** to reduce vibrations. The laser beam will be guided through a window on the top **(d)**. The insulation between the high voltage and the grounded part is done by a ceramic insulator **(e)**. To enable the vertical movement the insulator and the ablation chamber **(g)** are connected via a bellows **(f)**. The separation between the CKrS and the CPS is done by a CF250 gate valve **(h)**. The CKrS enters the pump port 2 **(i)** and scans the flux tube inside the beam tube **(j)**.

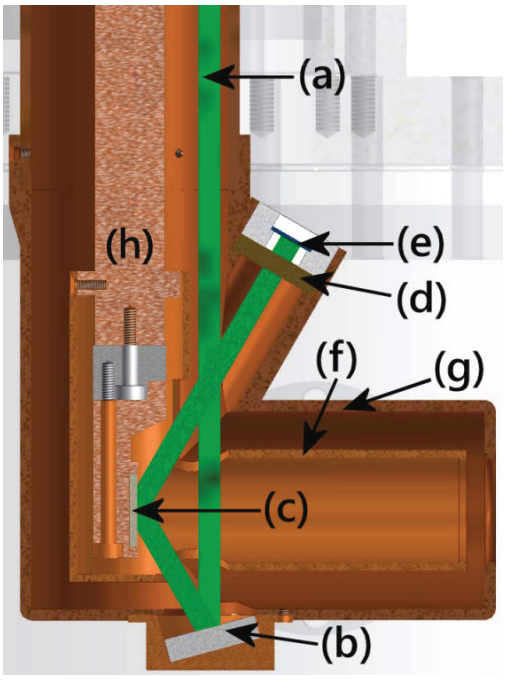

Figure 80: New design of the substrate region of the CKrS. The laser beam **(a)** comes vertically from the top of the system and is reflected via a dielectric mirror **(b)** to the substrate **(c)**. The reflected beam is analysed by the analyzer at fixed rotation angle **(d)** and the photodiode detector **(e)**. The system is enclosed by the inner **(f)** and outer **(g)** cold shields.

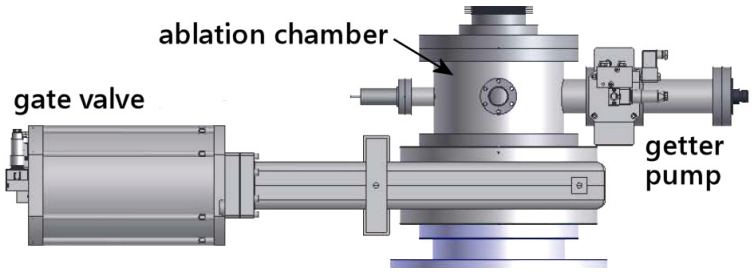

Figure 81: Ablation chamber on top of the pump port 2. For cleaning by laser ablation the substrate will be lifted into the ablation chamber. During the ablation the CF250 gate valve at the bottom will be closed.

Chapter 7

Novel ellipsometry variant at cryogenic temperatures

As already mentioned in the previous chapter the surface cleanliness of the HOPG substrate will be monitored by means of laser ellipsometry. The technique of laser ellipsometry is commonly used in many fields of surface science and also in semiconductor industries. It is a standard method to determine film thicknesses and optical properties of thin solid films. It makes use of the multiple beam interference of a multilayer system. By using a laser beam of well-defined polarisation as incident beam, the change of polarisation contains information on the optical system (multilayer system). There are many different types of ellipsometry but for reasons of clarity only two variants of reflection or surface ellipsometry will be discussed. As the name already implies, in this method, the polarization of the beam reflected at the optical system is under investigation. The change in polarisation is caused by the different Fresnel coefficients of the dissimilar layers of the optical system. For both variants the intensity of the reflected laser beam is extinguished. This null-ellipsometry was in both cases set up as arrangement with a linear **P**olarizer, a **C**ompensator (quarter-wave plate) before an optical **S**ystem followed by an **A**nalyzer. Because of this particular arrangement this set-up is called PCSA ellipsometer (see figure 82). The following chapter will give an introduction to the theoretical description and present the set-up and results of the novel ellipsometry variant with rotating compensator. A first proof of principle was done within the diploma thesis of D. Spitzer [Spi11] and further measurements and optimiziations of the analysis of this data were done in this work. The experimental results are also presented in [Bau13b].

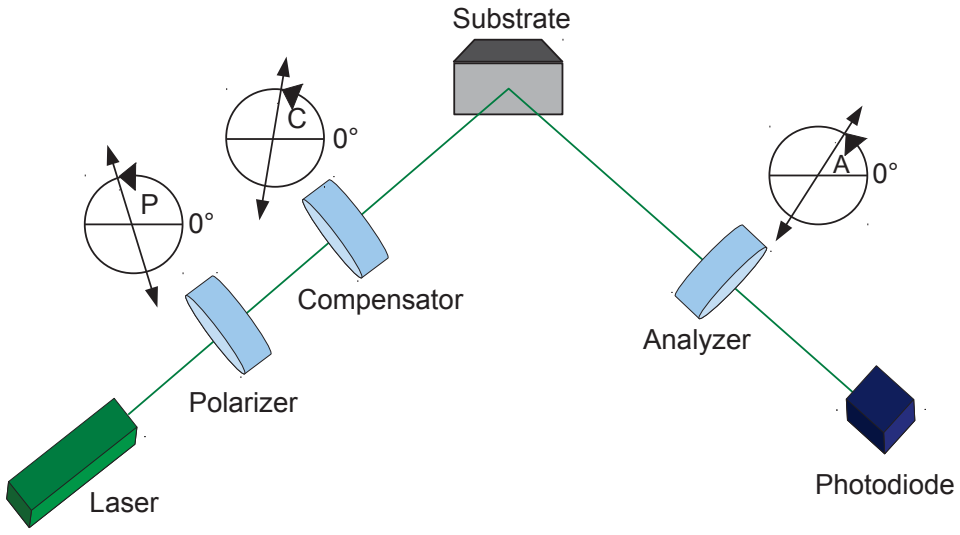

Figure 82: Schematic overview of the PCSA ellipsometer. The laser provides a circularly polarised beam at a fixed wavelength (here 543.5 nm). The polarisation of the incoming beam is defined by the angles of polarizer and compensator with respect to the plane of incident. The beam is reflected at the multilayer system built by the film condensed onto the substrate. The intensity of the reflected beam is monitored by the photodiode and minimized by the analyzer.

7.1 Principle of PCSA ellipsometry

7.1.1 Introduction to reflection ellipsometry

This section will give the most important equations needed to analyze and simulate ellipsometry data. It is a summary of the relevant chapters of [Azz87]. The first part will describe a simple optical system consisting of two different media. The applied three-layer system will be discussed later in section 7.1.2.

Light can be expressed as plane electromagnetic wave. A polarized wave which propagates in z-direction in an isotropic medium can be described as:

$$\vec{E}(z,t) = E_{\mathrm{x}}\hat{e}_{\mathrm{x}} \cdot e^{i(\omega t - k_{\mathrm{w}} z + \varphi_{\mathrm{x}})} + E_{\mathrm{y}}\hat{e}_{\mathrm{y}} \cdot e^{i(\omega t - k_{\mathrm{w}} z + \varphi_{\mathrm{y}})}\,, \tag{7.1}$$

where E_x and E_y are the amplitudes of the wave, $\hat{e}_x$ and $\hat{e}_y$ the basis vectors and φ_{x} and φ_{y} the phases. k_{w} is the length of the wave vector which can be written in the isotropic case (no birefringence) as:

$$k_{\mathrm{w}} = \frac{2\pi N}{\lambda} \tag{7.2}$$

where N denotes the complex refractive index and λ the vacuum wavelength. Therefore k_{w} can become a complex value to describe absorption too. In the following the notation of [Azz87] and [Hea91] is chosen. Thus the complex refractive index will be written as:

$$N = n - ik\,. \tag{7.3}$$

Here n is the index of refraction and k the extinction coefficient. Putting this into equation (7.2) leads to:

$$k_{\mathrm{w}} = \frac{2\pi n}{\lambda} - i\frac{2\pi k}{\lambda} \tag{7.4}$$

Hence the electrical field in transverse direction can be expressed as:

$$\vec{E}(z,t) = \underbrace{\left(E_x\hat{e}_x \cdot e^{i\varphi_{\mathrm{x}}} + E_y\hat{e}_y \cdot e^{i\varphi_{\mathrm{y}}}\right)}_{:=\vec{E}_0} \cdot e^{i(\omega t - k_{\mathrm{w}} z)} = \vec{E}_0 \cdot e^{i(\omega t - \frac{2\pi n}{\lambda} z)} \cdot e^{-\frac{2\pi k}{\lambda} z}\,. \tag{7.5}$$

The measurable quantity is the light intensity which is given by:

$$I = EE^* = E_0^2 \cdot e^{-\frac{4\pi k}{\lambda} z} \propto e^{-\alpha z}\,. \tag{7.6}$$

Thus the absorption coefficient α can be expressed as:

$$\alpha = \frac{4\pi k}{\lambda}\,. \tag{7.7}$$

By this an extinction coefficient $k > 0$ will lead to absorption of light and $k < 0$ to an amplification. Up to here the notation and the physical context was introduced. Now an optical system of two layers can be described by the complex refractive indices:

$$N_0 = n_0 - ik_0 \tag{7.8}$$
$$N_1 = n_1 - ik_1 \tag{7.9}$$

For ellipsometry, as for many other optical systems, a plane of incidence is defined as the plane spanned by the surface normal of the substrate and the propagation vector of the incoming beam. Now the electric field is split up into one part which is parallel (index p) to the plane of incident and one which is perpendicular (index s) to it. With this coordinate system one defines a polarised wave propagating in an isotropic medium by:

$$\vec{E}(z,t) = E_\mathrm{s}\hat{e}_\mathrm{s}\cdot e^{i(\omega t - k_\mathrm{w} z + \varphi_\mathrm{s})} + E_\mathrm{p}\hat{e}_\mathrm{p}\cdot e^{i(\omega t - k_\mathrm{w} z + \varphi_\mathrm{p})}\,, \tag{7.10}$$

where now E_s and E_p are the amplitudes of the wave, $\hat{e}_\mathrm{s}$ and $\hat{e}_\mathrm{p}$ the basis vectors and φ_s and φ_p the phases but now with respect to the plane of incidence. The two possible states of full linear polarisation will be further referred to as p and s polarized. At an optical interface some part of the incident wave will be reflected and the other part will be transmitted. For homogeneous and optically isotropic media the reflected and transmitted amplitudes can be calculated via the Fresnel coefficients [Azz87]:

$$\frac{E_{r,p}}{E_{0,p}} = r_\mathrm{p} = \frac{N_1\cos\phi_0 - N_0\cos\phi_1}{N_1\cos\phi_0 + N_0\cos\phi_1} = |r_\mathrm{p}|\, e^{i\beta_\mathrm{rp}} \tag{7.11a}$$

$$\frac{E_{r,s}}{E_{0,s}} = r_\mathrm{s} = \frac{N_0\cos\phi_0 - N_1\cos\phi_1}{N_0\cos\phi_0 + N_1\cos\phi_1} = |r_\mathrm{s}|\, e^{i\beta_\mathrm{rs}} \tag{7.11b}$$

$$\frac{E_{t,p}}{E_{0,p}} = t_\mathrm{p} = \frac{2N_0\cos\phi_0}{N_1\cos\phi_0 + N_0\cos\phi_1} = |t_\mathrm{p}|\, e^{i\beta_\mathrm{tp}} \tag{7.11c}$$

$$\frac{E_{t,s}}{E_{0,s}} = t_\mathrm{s} = \frac{2N_0\cos\phi_0}{N_0\cos\phi_0 + N_1\cos\phi_1} = |t_\mathrm{s}|\, e^{i\beta_\mathrm{ts}} \tag{7.11d}$$

$E_{0,x}$ denotes the amplitude of the incident part in the corresponding polarization, $E_{r,x}$ the reflected and $E_{t,x}$ the transmitted part.

Of course the angle ϕ_1 can be expressed by Snell's law:

$$N_0 \cos\phi_0 = N_1 \cos\phi_1 \,. \tag{7.12}$$

Reflection ellipsometry prepares the state of polarisation of the incident and measures the polarisation of the reflected beam. This leads to the determination of the ratio ρ_S of both complex Fresnel coefficients for reflection of p and s polarized waves. This results in the ellipsometric equation:

$$\rho_{\mathrm{S}} = \frac{r_{\mathrm{p}}}{r_{\mathrm{s}}} = \tan\Psi e^{i\Delta} \tag{7.13}$$

The right hand side represents the polar representation with the two ellipsometric angles Ψ and Δ:

$$\tan\Psi = \frac{|r_{\mathrm{p}}|}{|r_{\mathrm{s}}|} \tag{7.14}$$

$$\Delta = \beta_{\mathrm{rp}} - \beta_{\mathrm{rs}} \,. \tag{7.15}$$

This descriptions assumes perfectly smooth parallel-plane interfaces and homogeneous and isotropic media [Azz87]. The next section will show the theoretical description of the three-layer system used at the CKrS and that the two ellipsometric angles Ψ and Δ can be expressed by the angles of the polarizer and analyzer (or even by the compensator).

7.1.2 Reflection ellipsometry on a three-layer optical system

This section will focus on ellipsometry of a three-layer optical system like those of the CKrS. In particular these layers are HOPG as substrate, the condensed film of stable krypton and the ambient (vacuum) which is shown in figure 83.

Firstly the complex refractive indices will be expressed as:

$$Ambient : N_0 = \; n_0 - ik_0 = n_0 = 1 \tag{7.16a}$$

$$Film : N_1 = \; n_1 - ik_1 = n_1 \tag{7.16b}$$

$$Substrate : N_2 = \; n_2 - ik_2 \tag{7.16c}$$

For the vacuum the index of refraction is real and equal to 1. The film can be treated as non absorbing, hence the index of refraction is also real. Only for the substrate a complex refractive index is used. Because of the three-layer system the Fresnel coefficients for each

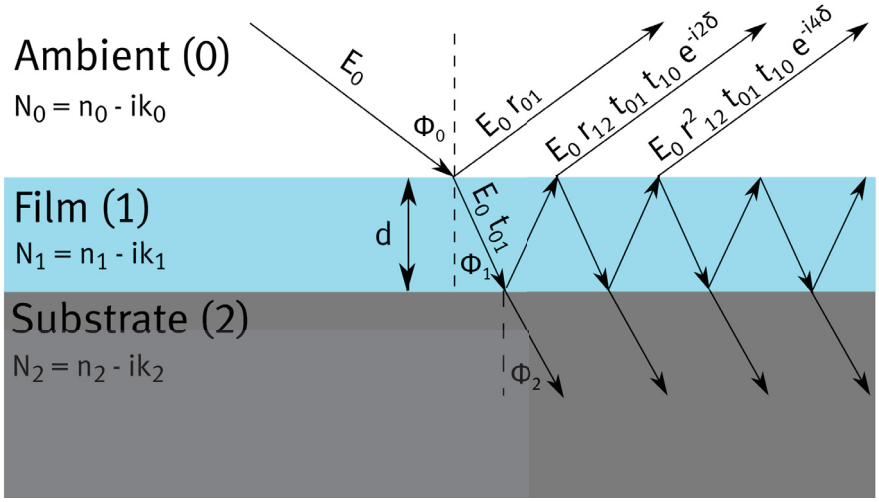

Figure 83: A multilayer system out of three layers (ambient, thin film of thickness d and substrate) is shown. The incoming beam is partially reflected and transmitted according to the optical properties of the system.

optical interface have to be calculated. This will be expressed by double indices e.g. for the interface ambient-film this index will be 01 (10 for the reverse direction) or for film-substrate 12 (21). The Fresnel coefficients are the same as in equations (7.11) but with the refractive indices equations (7.16) at the corresponding interfaces.

$$r_{01,\mathrm{p}} = \frac{N_1 \cos\phi_0 - N_0 \cos\phi_1}{N_1 \cos\phi_0 + N_0 \cos\phi_1} = \frac{n_1 \cos\phi_0 - \cos\phi_1}{n_1 \cos\phi_0 + \cos\phi_1} \tag{7.17a}$$

$$r_{01,\mathrm{s}} = \frac{N_0 \cos\phi_0 - N_1 \cos\phi_1}{N_0 \cos\phi_0 + N_1 \cos\phi_1} = \frac{\cos\phi_0 - n_1 \cos\phi_1}{\cos\phi_0 + n_1 \cos\phi_1} \tag{7.17b}$$

$$r_{12,\mathrm{p}} = \frac{N_2 \cos\phi_1 - N_1 \cos\phi_2}{N_2 \cos\phi_1 + N_1 \cos\phi_2} = \frac{N_2 \cos\phi_1 - n_1 \cos\phi_2}{N_2 \cos\phi_1 + n_1 \cos\phi_2} \tag{7.17c}$$

$$r_{12,\mathrm{s}} = \frac{N_1 \cos\phi_1 - N_2 \cos\phi_2}{N_1 \cos\phi_1 + N_2 \cos\phi_2} = \frac{n_1 \cos\phi_1 - N_2 \cos\phi_2}{n_1 \cos\phi_1 + N_2 \cos\phi_2} \tag{7.17d}$$

$$t_{01,\mathrm{p}} = \frac{2N_0 \cos\phi_0}{N_1 \cos\phi_0 + N_0 \cos\phi_1} = \frac{2\cos\phi_0}{n_1 \cos\phi_0 + \cos\phi_1} \tag{7.17e}$$

$$t_{01,\mathrm{s}} = \frac{2N_0 \cos\phi_0}{N_0 \cos\phi_0 + N_1 \cos\phi_1} = \frac{2\cos\phi_0}{\cos\phi_0 + n_1 \cos\phi_1} \tag{7.17f}$$

$$t_{12,\mathrm{p}} = \frac{2N_1 \cos\phi_1}{N_2 \cos\phi_1 + N_1 \cos\phi_2} = \frac{2n_1 \cos\phi_1}{N_2 \cos\phi_1 + n_1 \cos\phi_2} \tag{7.17g}$$

$$t_{12,\mathrm{s}} = \frac{2N_1 \cos\phi_1}{N_1 \cos\phi_1 + N_2 \cos\phi_2} = \frac{2n_1 \cos\phi_1}{n_1 \cos\phi_1 + N_2 \cos\phi_2} \tag{7.17h}$$

Because the angles ϕ_1 and ϕ_2 cannot be measured, they are expressed by Snell's law (equation (7.12)) as:

$$\cos\phi_1 = \sqrt{1 - \left(\frac{\sin\phi_0}{n_1}\right)^2} \tag{7.18a}$$

$$\cos\phi_2 = \sqrt{1 - \left(\frac{\sin\phi_0}{n_2}\right)^2} \tag{7.18b}$$

While the wave is travelling inside the film once, from one interface to the other, it experiences a phase change of:

$$\delta = \frac{2\pi d}{\lambda} n_1 \cos\Phi_1 \,. \tag{7.19}$$

In this case d is the film thickness, λ the wavelength and Φ_1 the angle between the normal to the substrate and the propagation direction of the wave (see figure 83). By replacing the angle Φ_1 by the incident angle Φ_0 via Snell's law and using the refractive indices of the particular three-layer system this phase shift becomes:

$$\delta = \frac{2\pi d}{\lambda} \sqrt{n_1^2 - \sin^2\Phi_0} \,. \tag{7.20}$$

To calculate the amplitude R of the reflected wave of a multilayer system one has to sum over all partial waves which leads to an infinite geometric series:

$$R = r_{01} + t_{01}t_{10}r_{12}e^{-i2\delta} + t_{01}t_{10}r_{01}r_{12}^2e^{-i4\delta} + t_{01}t_{10}r_{01}^2r_{12}^3e^{-i6\delta} + \ldots \tag{7.21}$$

which converges to the sum of:

$$R = r_{01} + \frac{t_{01}t_{10}r_{12}e^{-i2\delta}}{1 - r_{10}r_{12}e^{-i2\delta}} \,. \tag{7.22}$$

Taking into account that the Fresnel coefficient for reflection in the reverse direction has the opposite sign and that the transmitted part can be expressed in dependence of the reflected part one can set up the following equations:

$$r_{10} = -r_{01} \tag{7.23a}$$

$$t_{01}t_{10} = 1 - r_{01}^2 \,. \tag{7.23b}$$

Putting this into equation (7.22) the overall complex amplitude of reflection R for both states of polarisation is given by:

$$R_s = \frac{r_{01s} + r_{12s}e^{-2i\delta}}{1 + r_{01s}r_{12s}e^{-2i\delta}} \qquad \text{and} \qquad R_p = \frac{r_{01p} + r_{12p}e^{-2i\delta}}{1 + r_{01p}r_{12p}e^{-2i\delta}} \,. \tag{7.24}$$

For the overall transmitted amplitude the derivation is similar and given in [Azz87]. Now the ratio of the complex reflected amplitudes is:

$$\rho_{\mathrm{S}} = \frac{|R_{\mathrm{p}}|}{|R_{\mathrm{s}}|} = \tan\Psi e^{i\Delta} \tag{7.25a}$$

$$\tan\Psi = \frac{R_{\mathrm{p}}}{R_{\mathrm{s}}} \tag{7.25b}$$

$$\Delta = \Delta_{\mathrm{p}} - \Delta_{\mathrm{s}} \tag{7.25c}$$

Again $|R_{\mathrm{s}}|$ and $|R_{\mathrm{p}}|$ are the absolute values and Δ_{p} and Δ_{s} the complex phases of the reflection amplitudes R_{s} and R_{p}.

For the PCSA set-up with a quarter-wave plate as compensator, the measured intensity at the photodiode is given by [Azz87]

$$\begin{aligned} I \propto | \quad & R_{\mathrm{p}}\cos(A)[\cos(C)\cos(P-C) + i\sin(C)\sin(P-C)] \\ & + R_{\mathrm{s}}\sin(A)[\sin(C)\cos(P-C) - i\cos(C)\sin(P-C)]|^2 \,. \end{aligned} \tag{7.26}$$

In this case P,C and A are the azimuthal angles of the polarizer, compensator and analyzer, respectively. All these angles are measured in a counter-clockwise sense against the plane of incident (see figure 82). By measuring the angles (P, C, A) and the intensity one can also determine ρ_{S}.

7.1.3 Null ellipsometry

A very common method of ellipsometry is to find the set of angles (P, C, A), where the measured intensity is zero[1] $(I = 0)$. In this case the properties of the optical system can be expressed by the three measured angles.

$$\rho_{\mathrm{S}} = \frac{R_{\mathrm{p}}}{R_{\mathrm{s}}} = -\tan(A)\frac{\tan(C) - i\tan(P-C)}{1 + i\tan(C)\tan(P-C)} \,. \tag{7.27}$$

[1] In the experiment, the intensity minimum found will be assumed as 0.

Usually the compensator angle is set to $C = \pm\pi/4$. This in combination with the addition theorem ($\frac{1-i\tan\Theta}{1+i\tan\Theta} = e^{-i2\Theta}$) results in

$$\rho_S = \mp\tan(A)e^{\mp 2i(P\mp\frac{\pi}{4})} \quad \text{for} \quad C = \pm\frac{\pi}{4}. \tag{7.28}$$

Because the optical system is described by the two angles P and A, this system will be further referred to as PA ellipsometry. The application of this ellipsometry variant at the CKrS is described in detail in [Ost08, Weg10, Spi11]. A very common way to present ellipsometry data is to plot the ellipsometric angles (Ψ *vs.* Δ, see equation (7.25)). In this work the results will be presented as plots of the two angles (P, A).

7.2 Ellipsometry with rotating compensator and fixed analyzer

Due to already mentioned technical constraints at the CPS the PA ellipsometry cannot be applied. Therefore the analysis of the reflected beam has to be done at cryogenic temperatures inside ultra high vacuum. In principle three different alternatives are possible for the use at the CPS:

1. **Ellipsometry only with rotatable polarizer:**
   The simplest solution is to bring analyzer and detector inside the vacuum chamber and fix the analyzer at a certain angle. This was tested for film thicknesses up to 700 Å in [Spi11]. In principle this variant of ellipsometry can be used to monitor the surface cleanliness because the surface can be stated as "dirty" if the polarizer angle changes more than a certain value.

2. **Ellipsometry with rotatable analyzer in the vacuum:**
   To carry out the PA ellipsometry as done before one has to bring the analyzer and the detector into the vacuum chamber. Furthermore the analyzer has to be rotatable. This can be achieved by the use of vacuum-compatible rotational stages. This can be realized be the use of piezo drives like the ARN series from the company Attocube. This rotators are suitable for the use inside ultra-high vacuum, inside high magnetic field and at low temperatures. The ARN240 has a bore of 12.7 mm which makes transmission of the reflected laser beam possible.

3. **Ellipsometry with rotatable compensator and fixed analyzer:**
   For this third method the analyzer remains fixed at a certain angle A inside the vacuum and the compensator angle C is varied. By this full ellipsometry is still possible.

Of course, it is possible to combine all three alternatives by using rotational stage for all three major components (polarizer, compensator and analyzer). Thus one is able to use all variants of ellipsometry. The important drawbacks are that the rotator needs space within a narrow construction, it is very cost intensive and a malfunction may make it necessary to break the vacuum and open the CKrS. Hence, it was decided to use the last alternative of ellipsometry at the CPS. By this also the first alternative with only a rotating polarizer can be realised and no moveable parts are installed inside the vacuum chamber.

In this modified variant of PCSA ellipsometry the compensator is still considered to be a quarter-wave plate. Therefore, equation (7.27) still holds but not equation (7.28). In order to test that null intensity can be reached by varying the polarizer and compensator angles P and C an intensity map was calculated and plotted as function of P and C for different krypton film thicknesses d in figure 84.

It shows indeed, that for all film thicknesses regions with null-light intensity can be found. But figure 84 also illustrates that the minima might be flat, thus limiting the sensitivity. Like in PA ellipsometry again two minima are observed, now in the PC plane. Of course, figure 84 only shows some exemplary simulations to demonstrate these statements, but it is not a full mathematical proof. The minimum of the light intensity was determined as function of the polarizer and compensator angles P and C for a fixed analyzer angle A. Hence this method will referred to as "PC ellipsometry". Via equation (7.27) the angles P and C define a complex variable ρ_S. In order to facilitate the determination of the corresponding film thickness $d(P, C)$ two corresponding angles $\tilde{A}$ and $\tilde{P}$ are defined.

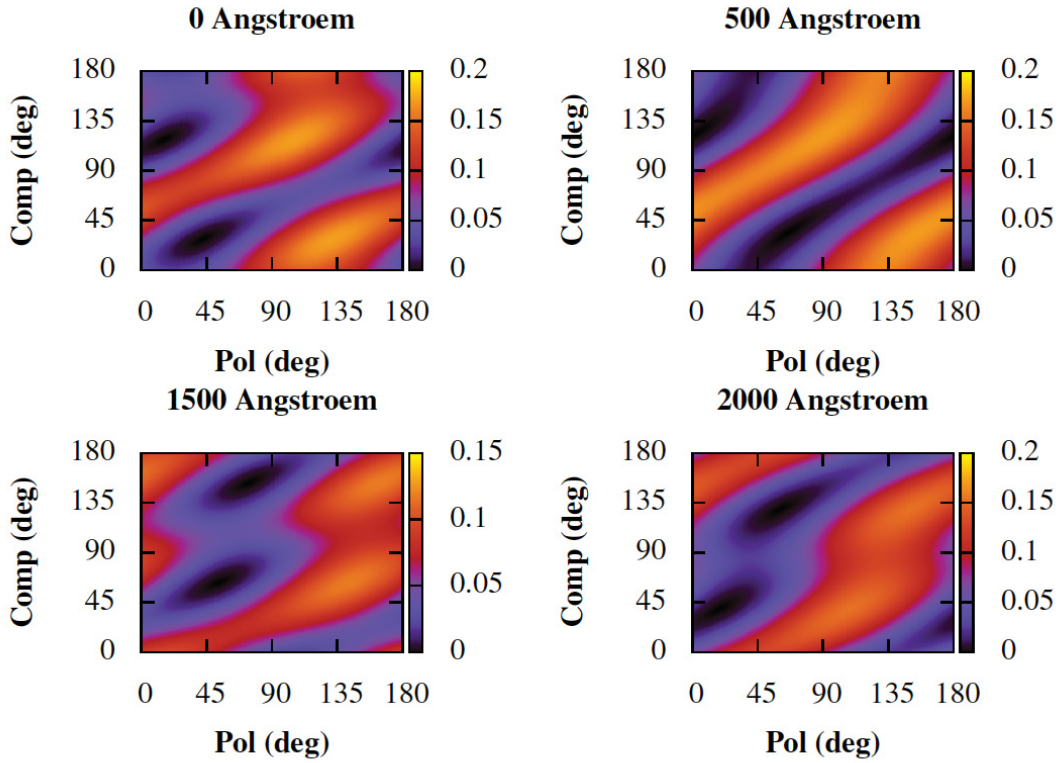

Figure 84: Intensity profile for a full scan of polarizer and compensator angles P and C for various film thickness $d = 0$ Å (upper left), $d = 500$ Å (upper right), $d = 1500$ Å (lower left) and $d = 2000$ Å (lower right). The analyzer angle was set to $A = 30°$ with respect to the plane of incidence. The simulations were made assuming a krypton film on a HOPG substrate in a vacuum environment ($N_0 = 1$, $n_1 = 1.28$, $n_2 = 2.645$, $k_2 = 0.964$) [Bau13b]. The laser wavelength in these simulations was set to $\lambda = 543.5$ nm (green HeNe laser) and the angle of incidence to $\Phi_0 = 60°$.

Similar to Euler's representation, any complex number ρ_S can generally be expressed by two angles $\tilde{A}, \tilde{P} \in [0, \pi[$ as

$$\rho_S = \tan(\tilde{A}) \cdot e^{i2(\tilde{P}+\pi/4)} . \tag{7.29}$$

Therefore it is possible to translate the angles P and C defining the intensity minimum for a given film thickness d into the corresponding angles $\tilde{A}$ and $\tilde{P}$ via:

$$\tan(\tilde{A}) \cdot e^{i2(\tilde{P}+\pi/4)} = \rho_S = -\tan(A)\frac{\tan(C) - i\tan(P-C)}{1 + i\tan(C)\tan(P-C)} . \tag{7.30}$$

The left-hand side of equation (7.30) looks identical to equation (7.28) for $C = -\pi/4$. This means, if a film thickness d would be characterized by a pair (P,C) in PC ellipsometry, the transformation with equation (7.30) describes which angles $\tilde{P}$ and $\tilde{A}$ would have been encountered in standard PA ellipsometry for the same film thickness. The advantage of this transformation is that one can use the same data analysis tools as for PA ellipsometry [Bau13b].

7.3 Ellipsometry set-up with fixed analyzer and rotatable compensator at the CKrS

A schematic overview of the PCSA set-up for the PC ellipsometry is given in figure 85. The light source is a HeNe laser (λ = 543.5 nm, P_{laser} = 0.5 mW) followed by a neutral density filter, a linear polarizer and a quarter-wave plate producing circularly polarized light. All these components are summarized in figure 85 as (a). The circular polarization of the laser light in combination with a second rotatable polarizer (b) allows to choose any angle of polarization without a change of intensity. After the polarizer the light beam passes the compensator (c). The latter two components are mounted on rotation tables (PI M-060.DG).

The substrate ($10 \times 10\,\mathrm{mm}^2$) is grade SPI-2 HOPG (SPI Supplies) with a mosaic angle of $(0.8 \pm 0.2)^\circ$. To avoid birefringence of cold optical windows, both cold shields have free entrance and exit openings for the ellipsometry laser. At the exit opening of the outer cold shield the analyzer and the detector are mounted as shown in figure 70. The analyzer is a linear polarizer of 12 mm diameter and 0.28 mm thickness (Thorlabs LPVISB050, not laminated). The temperature at the analyzer is about 90 K (with a maximum gradient of $0.6\,\mathrm{K\,min}^{-1}$ during cool down). The detector is a $9 \times 9\,\mathrm{mm}^2$ windowless Si-PIN photodiode (Hamamatsu S-3590-19) read out by a current amplifier (Femto DLPCA-200). The other relevant optical components are the polarizer (PGT 2.05 Bernhard Halle Nachfolger GmbH - optische Werkstätten) and the compensator (CVI Melles Griot QWPM-543-04-4-R10).

7.4 Analysis of PC-Ellipsometry data

During the measurement it turned out that the iterative online minima search from the PA ellipsometry was not precise enough to find the correct minima because of the rather flat

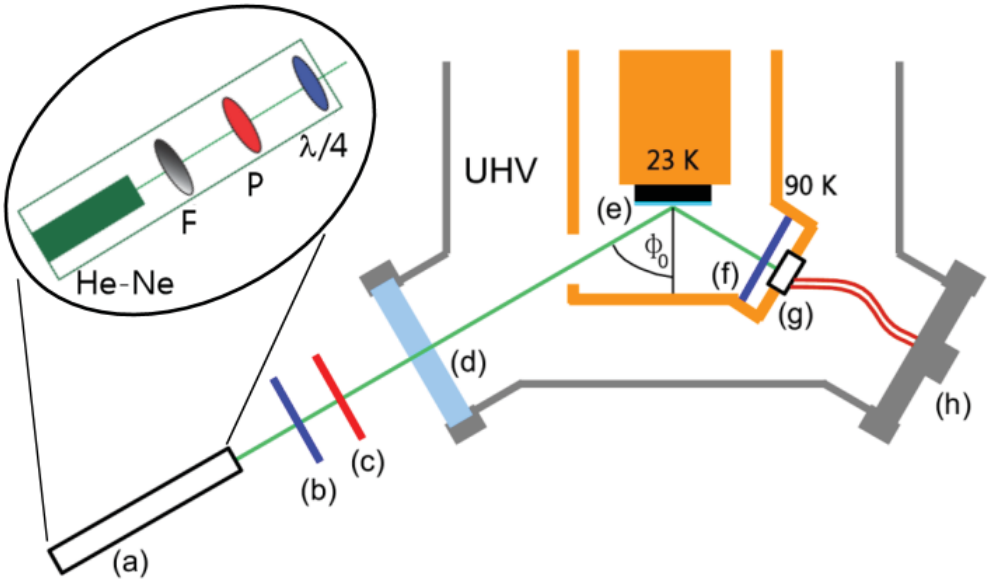

Figure 85: Ellipsometry set-up with analyzer and detector inside the UHV chamber. This set-up is a PCSA ellipsometer with the circular light source (a). This consists of a laser (He-Ne), a neutral density filter (F), a polarizer (P) and a quarter-wave plate ($\Lambda/4$). The light source is followed by the polarizer (b), the compensator (c) and the optical system (krypton film on HOPG) (e). The reflected beam is analyzed by the analyzer (f) and the intensity is measured by the photodiode (g). To guide the laser beam into the vacuum chamber an optical window with an antireflection coating (d) is used. The signal of the photodiode is accessible via the electrical feedthrough (h) . For the sake of clarity the inner cold shield, surrounding the substrate, is not shown. Figure combined from originals in [Bau13b] and [Weg10].

and broad PC minima (as shown in figure 84). Hence the area of $\pm 10°$ ($\pm 7.5°$) around the minima, found by the iterative method, was scanned with a typical step size of $1°$ ($0.25°$). The obtained data (see figure 87) were analyzed offline by fitting them, using a rotated paraboloid (equation (7.31)) locally around the minimum (see figure 88).

$$I = K + \frac{[cos(\theta) \cdot \Delta P + sin(\theta) \cdot \Delta C]^2}{a^2} + \frac{[-sin(\theta) \cdot \Delta P + cos(\theta) \cdot (\Delta C)]^2}{b^2} \quad (7.31)$$

K = Offset

θ = Rotation angle of paraboloid

$\Delta P = P - P_\mathrm{m}$

$\Delta C = C - C_\mathrm{m}$

P = Polariser angle

C = Compensator angle

P_m = Minimum in polarizer

C_m = Minimum in compensator

a, b = Constants defining curvature

This was done for a range in intensity starting from the minimum intensity in the data set to

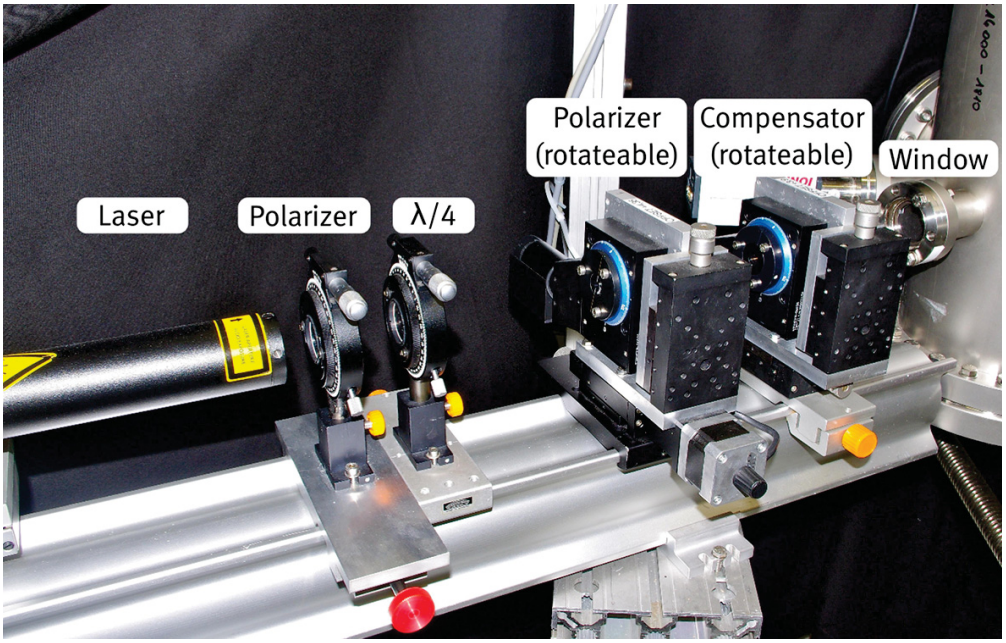

Figure 86: Picture of the PC ellipsometry set-up. Shown is the laser followed by the polarizer and the quarter-wave plate to provide circular polarized light. The second polarizer and compensator are mounted into rotatable stages which are controlled by software. Also shown is the entrance window of the vacuum chamber.

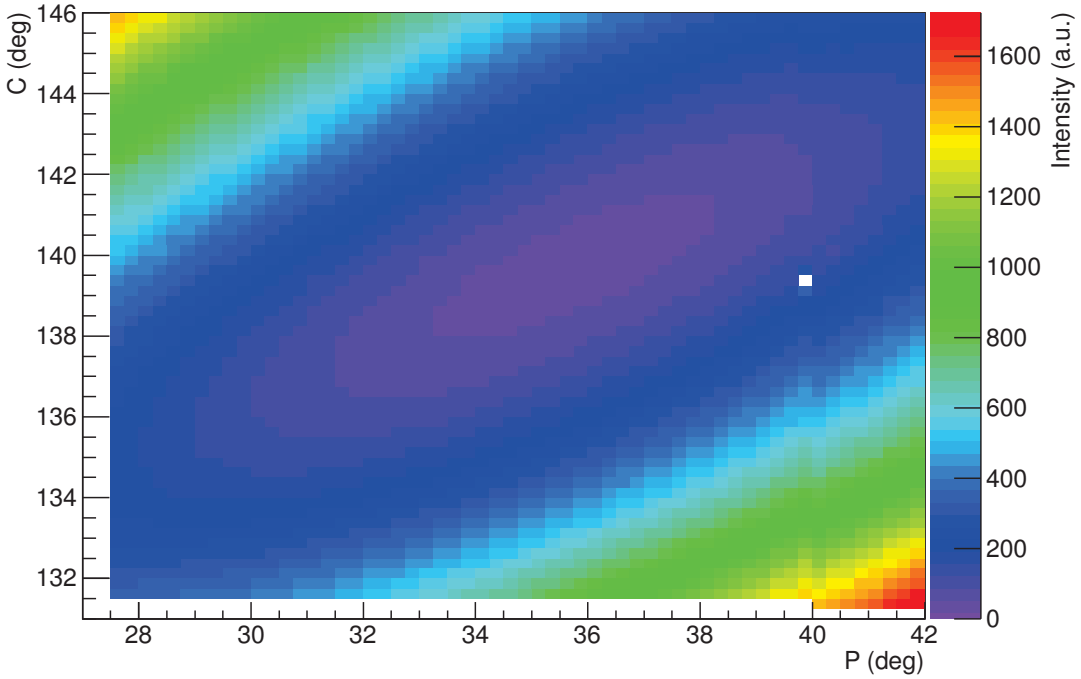

Figure 87: Scan in the PC plane of $\pm 7.5°$ in steps of $0.25°$ for one condensation step. Shown is the intensity against the angles P and C.

the minimum plus 60 units of intensity. The typical errors of the position in PC coordinates are below 0.1°. These errors are obtained from the least-squares fit and multiplied by $\sqrt{\chi^2_{\mathrm{red}}}$. This correction using $\chi^2_{\mathrm{red}} = \chi^2/N_{\mathrm{dof}}$ (N_{dof} is the number of degrees of freedom of the fit) is applied, since the size of the uncertainties of the intensity measurement is unknown but considered to be constant for all data points of a measurement. To obtain the uncertainties and the corresponding correlation coefficients after the transformation to $\tilde{P}\tilde{A}$-coordinates, the points of the error ellipse in PC coordinates were also transformed (figure 88 lower right). The two-dimensional ellipse centred at $(\tilde{P}_{\mathrm{m}}, \tilde{A}_{\mathrm{m}})$ represents the confidence level contour for a measurement with errors $(\Delta\tilde{P}_{\mathrm{m}}, \Delta\tilde{A}_{\mathrm{m}})$ and the correlation coefficient $\tilde{\rho}$ is given by:

$$f(\tilde{P}, \tilde{A}) = \left(\frac{\tilde{P}_{\mathrm{m}}}{\Delta\tilde{P}_{\mathrm{m}}}\right)^2 - \frac{2\tilde{\rho}\tilde{P}_m\tilde{A}_{\mathrm{m}}}{\Delta\tilde{P}_{\mathrm{m}}\Delta\tilde{A}_{\mathrm{m}}} + \left(\frac{\tilde{A}_{\mathrm{m}}}{\Delta\tilde{A}_{\mathrm{m}}}\right)^2 = 1 - \tilde{\rho}^2\,. \tag{7.32}$$

This error ellipse was fitted to the transformed data points yielding the errors and their correlation in the $\tilde{P}\tilde{A}$-coordinates. These analysis steps were done for each condensed layer of krypton to obtain the intensity minima $(\tilde{P}_{\mathrm{m}}, \tilde{A}_{\mathrm{m}})$, their uncertainties $(\Delta\tilde{P}_{\mathrm{m}}, \Delta\tilde{A}_{\mathrm{m}})$ and the correlation coefficient $(\tilde{\rho})$ for the whole condensation process.

7.5 Experimental results

For the investigation of the PC ellipsometry three different measurement series (H, HA, HAN - for their meaning see further below) were carried out. For all measurements a krypton film of about 3000Å thickness was condensed in about 15-30 steps. After each step PC ellipsometry was carried out yielding an intensity minimum $(P_{\mathrm{m}}, C_{\mathrm{m}})$ as presented in section 7.4. The results of a complete measurement are shown in figure 89. With the help of equation (7.30) these minima were transformed into the minima $(\tilde{P}_{\mathrm{m}}, \tilde{A}_{\mathrm{m}})$ in $\tilde{P}\tilde{A}$-coordinates as shown in figure 88. All datasets were corrected for a substrate tilt with respect to the plane of incident, as well as for angular offsets of the polarizer, compensator and analyzer, which is described in detail in [Gre12]. The uncertainties of these offsets were treated as systematic errors.

The conditions for the three measurement series are as follows:

1. **Measurements H1-H4:**
   For these measurements the substrate was cleaned only by heating the up to about 400 K.

2. **Measurements HA1-HA3:**
   A combination of heating the substrate to about 400 K and laser ablation was used to clean the surface of the HOPG.

3. **Measurements HAN1-HAN6:**
   To improve the reproducibility of the PC ellipsometry a new set of measurements was carried out as for HA1-HA3, but with these differences:

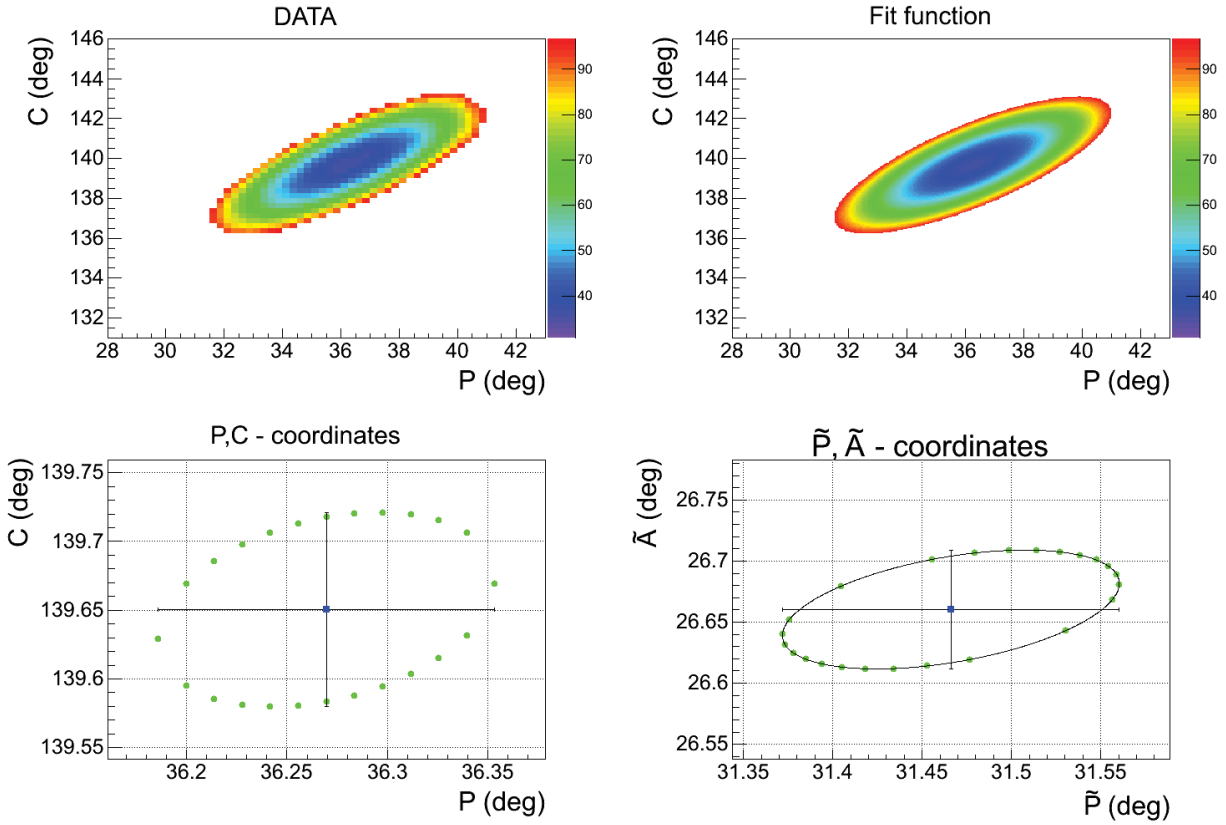

Figure 88: Scan in the PC plane of one condensation step and analysis at the example of measurement HAN3. The region around the intensity minimum of the data (upper left) was fitted with an elliptic paraboloid which is rotated in the PC plane (upper right) yielding the minimum $(P_\mathrm{m}, C_\mathrm{m})$ with the corresponding errors (lower left). The green dots show the 1σ error ellipse in the original (lower left) and in the transformed coordinates (lower right). The correlation coefficient $(\tilde{\rho})$ and errors $(\Delta\tilde{P}_\mathrm{m}, \Delta\tilde{A}_\mathrm{m})$ in the transformed coordinates were obtained from an elliptic fit to the transformed points (lower right).

a) The HOPG substrate was freshly cleaved.

b) P and C were scanned in a range of $\pm 7.5°$ with a step size of $\pm 0.25°$ instead of a range of $\pm 10°$ with a step size of $1°$.

c) The heating temperature was raised to approx. 500 K before and during ablation.

The optical constants of HOPG (n_2, k_2) as well as the index of refraction (n_1) of the condensed krypton films were also obtained from a fit to the measured intensity minima $(\tilde{P}_\mathrm{m}, \tilde{A}_\mathrm{m})$ as shown in figure 90. First many theoretical curves $(\tilde{P}_\mathrm{m}, \tilde{A}_\mathrm{m})$ or $(P_\mathrm{m}, A_\mathrm{m})$ respectively, were calculated and compared to the measurements. This was done by varying the optical constants of HOPG n_2, k_2 and the index of refraction of krypton n_1. The angle of incident Φ_0 and the absorption coefficient of krypton k_1 were kept fix during analysis. For each variation the ratio ρ_S of the two reflection coefficients (equation (7.27)) was calculated in 1 Å steps. From this the (P, A) values were derived using equation (7.28). The curve with the smallest distance to the intensity minima $(\tilde{P}_\mathrm{m}, \tilde{A}_\mathrm{m})$ yields the values for the optical constants. The

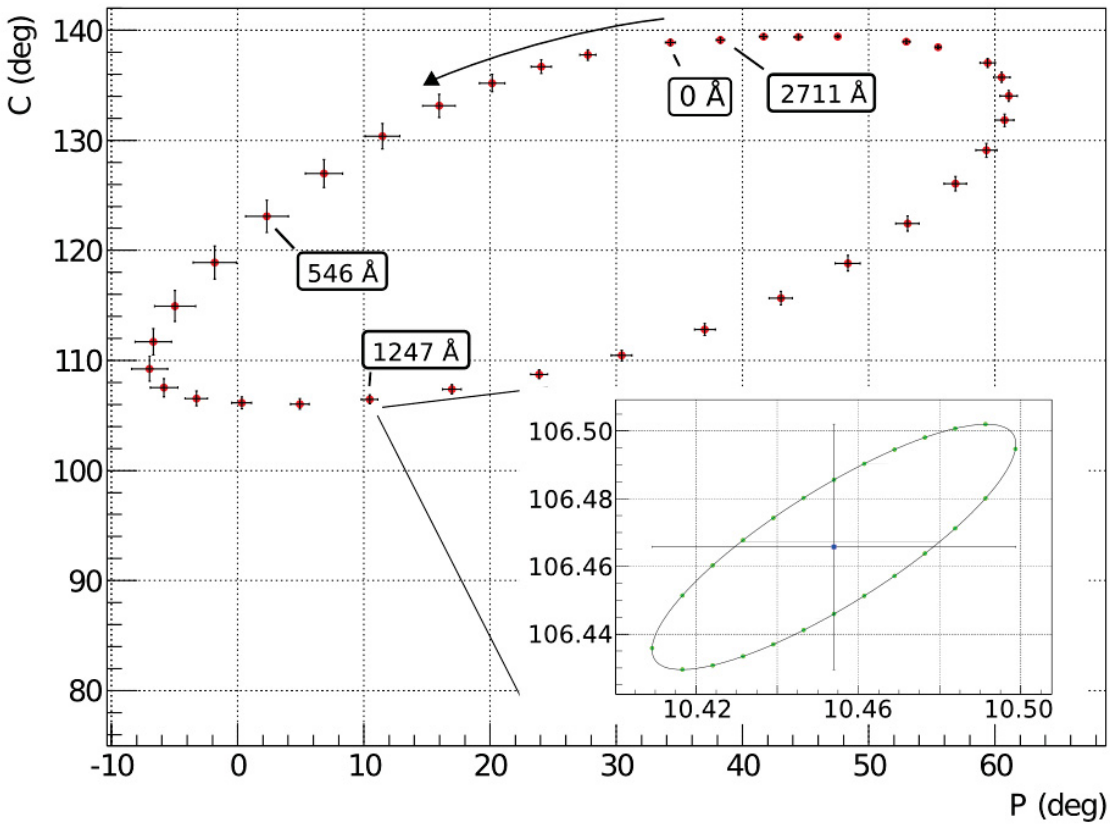

Figure 89: Intensity minima for polarizer and compensator $(P_\mathrm{m}, C_\mathrm{m})$ of PC ellipsometry of measurement HA1. In this plot the results of the off-line fits are shown for one complete film. The errors are multiplied by a factor of 20 for the sake of clarity. The substrate was cleaned by a combination of heating and ablation. The inserted plot shows the data point of step 16 with the corresponding error ellipse. The size of the error bars changes over the whole film because the shape of the minima changes with increasing film thickness (see figure 84).

correct distance between an intensity minimum $(\tilde{P}_\mathrm{m}, \tilde{A}_\mathrm{m})$ and the fit curve normalized to the uncertainties is given by:

$$\chi_i^2 = \frac{1}{(1-\tilde{\rho}_i^2)} \cdot \left[\frac{(\tilde{P}_{\mathrm{m},i} - P_{Fit,i})^2}{\sigma_{\tilde{P},i}^2} + \frac{(\tilde{A}_{\mathrm{m},i} - A_{Fit,i})^2}{\sigma_{\tilde{A},i}^2} - 2 \cdot \tilde{\rho}_i \cdot \frac{(\tilde{P}_{\mathrm{m},i} - P_{Fit,i}) \cdot (\tilde{A}_{\mathrm{m},i} - A_{Fit,i})}{\sigma_{\tilde{P},i}\sigma_{\tilde{A},i}} \right] \tag{7.33}$$

The distance calculations takes also the correlation coefficient $\tilde{\rho}_i$ of the uncertainties $\Delta\tilde{A}_{\mathrm{m},i}$ and $\Delta\tilde{P}_{\mathrm{m},i}$ into account. The summed distance $\chi^2 = \sum_i \chi_i^2$ is minimized in the fit. It should be noted that the fit uses relative values in PA and $\tilde{P}\tilde{A}$ coordinates by subtracting the corresponding values for zero film thickness P_0, A_0 and $\tilde{P}_0, \tilde{A}_0$ respectively. This detail is not considered in equation (7.33) for the sake of convenience to read this equation.

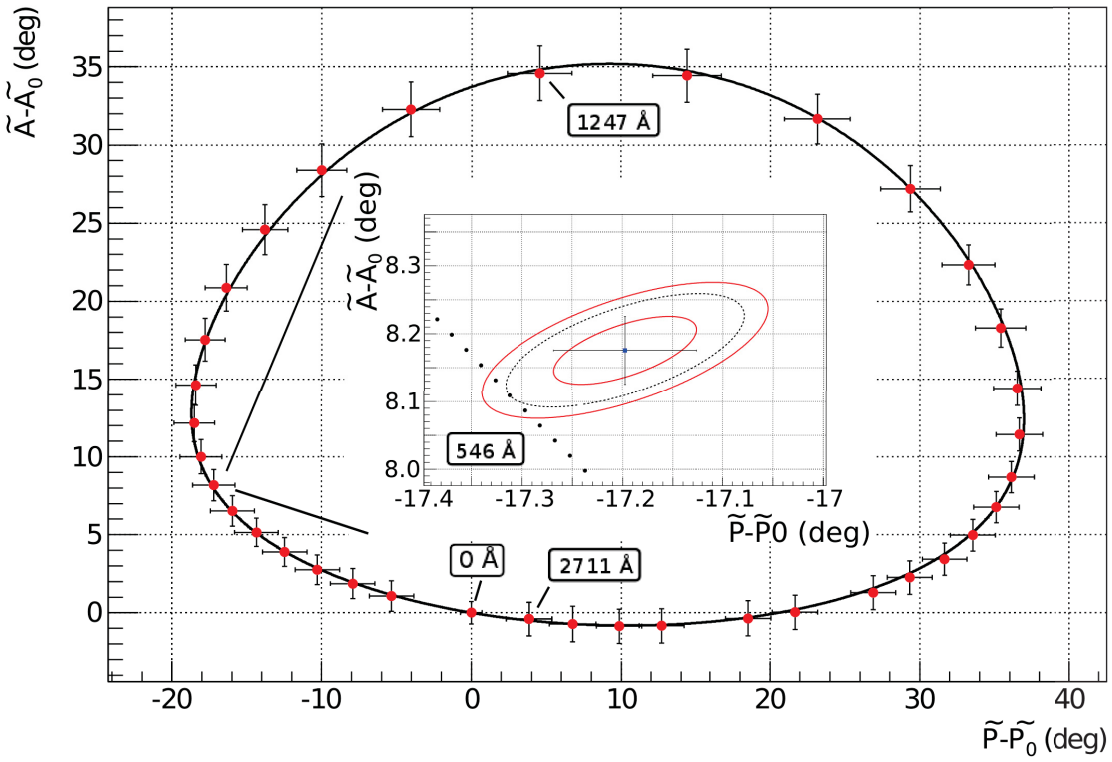

Figure 90: Intensity minima $(\tilde{P}_\mathrm{m} - \tilde{P}_0, \tilde{A}_\mathrm{m} - \tilde{A}_0)$ of the PC ellipsometry of measurement HA1 transformed into $\tilde{P}\tilde{A}$ coordinates according to equation (7.30). The line is a fit to the intensity minima were the parameters n_1, n_2 and k_2 were varied. The corresponding film thicknesses are marked by labels. The arrow denotes that the film thickness increases clockwise. The errors are multiplied by factor 20 for the sake of example. The inserted plot shows the data point of layer 7 together with the 1 sigma (red line), 1.67 (black dashed) and 2 sigma error ellipse (red line) to better illustrate how the distance χ^2_7 is calculated with the help of equation (7.33) (here $\chi^2_7 = 2.79 = 1.67^2$). The calculated curve is shown by black dots were each dot has a distance of 1Å. Finally we scale the uncertainties obtained by this fit with χ^2_red in order to account for unknown uncorrelated systematic uncertainties.

The fit to the corresponding angles $(\tilde{A}_\mathrm{m} - \tilde{A}_0, \tilde{P}_\mathrm{m} - \tilde{P}_0)$ yields the refractive indices of the condensed krypton film n_1 and the optical constants of the HOPG substrate n_2, k_2 (see table 7.1). Although HOPG is an anisotropic material in this work it is described only by one isotropic refraction index instead of ordinary and extraordinary refractive indices. The results of all three measurements of series HA are shown in figure 91.

In addition to the HA-series some HAN-series measurements were performed, in order to see whether our method could be improved further by increasing the heating temperature of the substrate to about 500 K. The increased substrate temperature during ablation can help to get a cleaner surface because the heat conductivity of HOPG out of plane decreases and the conductivity in plane increases with increasing temperature [Iss83]. Therefore, the energy of the ablation laser pulses are transferred less into the substrate and is dissipated mostly at the surface. In addition, the step size of the P- and C-scanning was reduced to 0.25° to

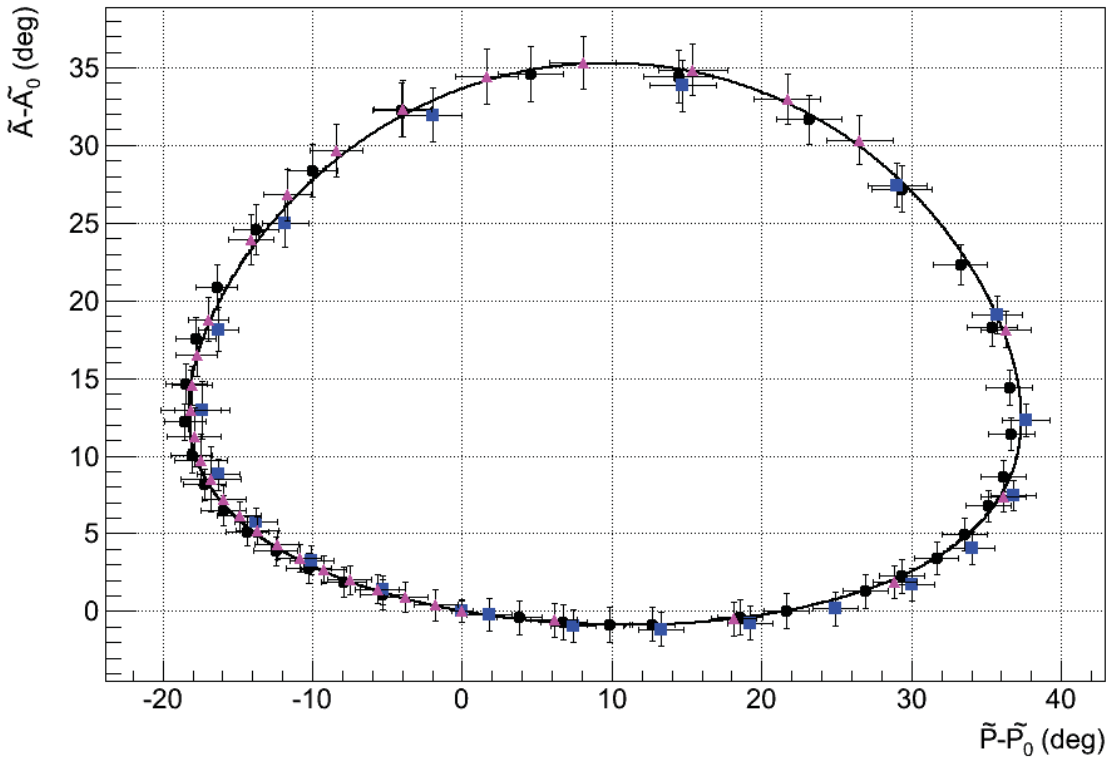

Figure 91: Results of three measurements HA1 - HA3. The solid line denotes the fit to all datasets and results in n_1=1.281, n_2=2.617 and k_2=1.001. The incident angle was fixed to 59.81° and k_1 to 0. All errors were multiplied by a factor of 20 for the sake of clarity.

obtain a more precise minimum.

Both changes lead to a higher reproducibility of the measured data but resulted in a much longer time span to measure one complete condensation of a film up to 3000 Å thickness. Unfortunately the residual gas pressure of water in the vacuum chamber was higher during this measurement series thus the data could not be analyzed for very large film thickness, because water was condensing onto the film. The whole condensing procedure took more than 24 hours due to the elaborate minimum search caused by the fine step size. This condensing water caused a non-closed curve in PC or $\tilde{P}\tilde{A}$ coordinates for a krypton film. Therefore we limited our analysis to film thickness up to 1400 Å only. The results of all analyzed data points are shown in figure 92.

Previous investigations showed that the combination of laser ablation and heating leads to the most stable measurements in comparison to other cleaning methods [2]. Figures 93 and 94 show the results of the optical parameters n_2, k_2 of HOPG and n_1 of krypton from all of our measurements. The results from the measurements within a series and between the three measurements series are consistent with each other. The averages obtained from figures 93 and 94 are compared with literature values in table 7.1.

[2]It should be noted, that the proper cleaning not only affects the index of refraction of HOPG but also those of the krypton film.

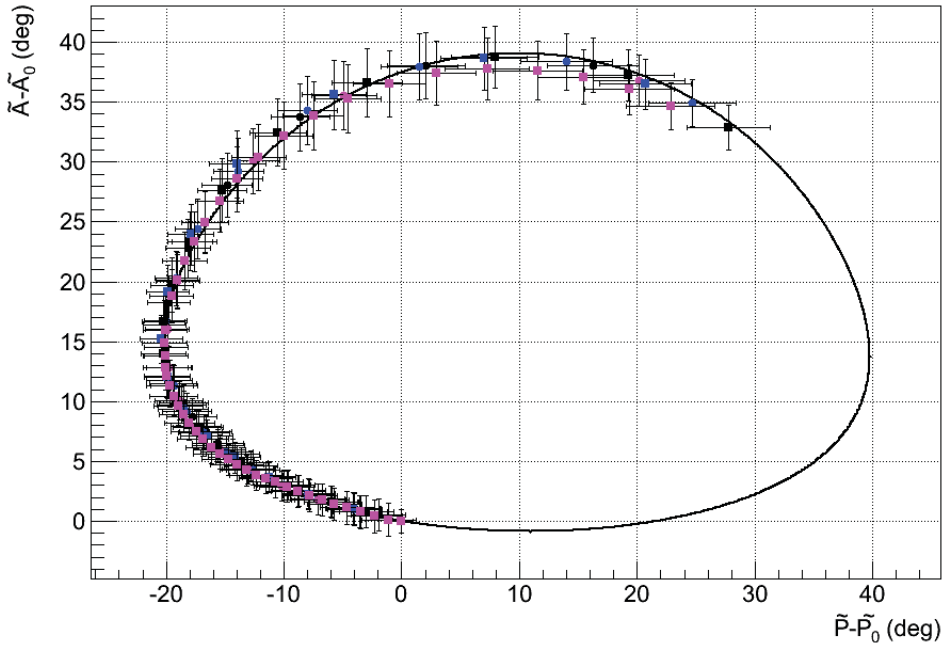

Figure 92: Results of six measurements HAN1 - HAN6. The solid line denotes the fit to all datasets and results in n_1=1.272, n_2=2.698 and k_2=0.813. The incident angle was fixed to 61.19° and k_1 to 0. All errors were multiplied by a factor of 20 for the sake of clarity. The last parts (thicknesses higher than approx. 1400Å) of all datasets were not analyzed because of the influence of a too high residual gas pressure of water in the set-up.

The refractive index n_1 of solid krypton deviates from most of the literature values. In the Mainz Neutrino Mass Experiment a similar deviation of the refractive index of tritium was observed, measured by ellipsometry as well as by measurements of the energy loss of electrons in quench condensed deuterium films [Ase00]. This observation was explained by a porous film due to the quench condensation of the tritium gas. One can calculate the density of the krypton films with the help of Clausius Mosotti‘s equation:

$$\frac{{N_1}^2 - 1}{{N_1}^2 + 2} = \frac{{n_1}^2 - 1}{{n_1}^2 + 2} = \frac{4\pi}{3}\alpha_{\mathrm{pol}}\frac{N_{\mathrm{A}}}{M}\rho_{\mathrm{Kr}} \tag{7.34}$$

Using the polarizability $\alpha_{\mathrm{pol}} = 2.46 \cdot 10^{-24}$ cm^3 [Kit05] and the molar mass (M) of krypton we obtain a density of our krypton film of:

$$\rho_{\mathrm{Kr}} = 2.369\frac{g}{cm^3}.$$

This is about 23% less than the expected value of $\rho_{Kr} = 3.081\frac{g}{cm^3}$ [Bea61]. Therefore the film can be assumed to be porous due to the quench condensation of the krypton gas, as in the case of the quench condensed tritium and deuterium films [Ase00]. The influence of surface roughness is also discussed in [Azz87]. A higher surface roughness leads to a lower index of refraction. A rough film can also be interpreted as porous because the density on

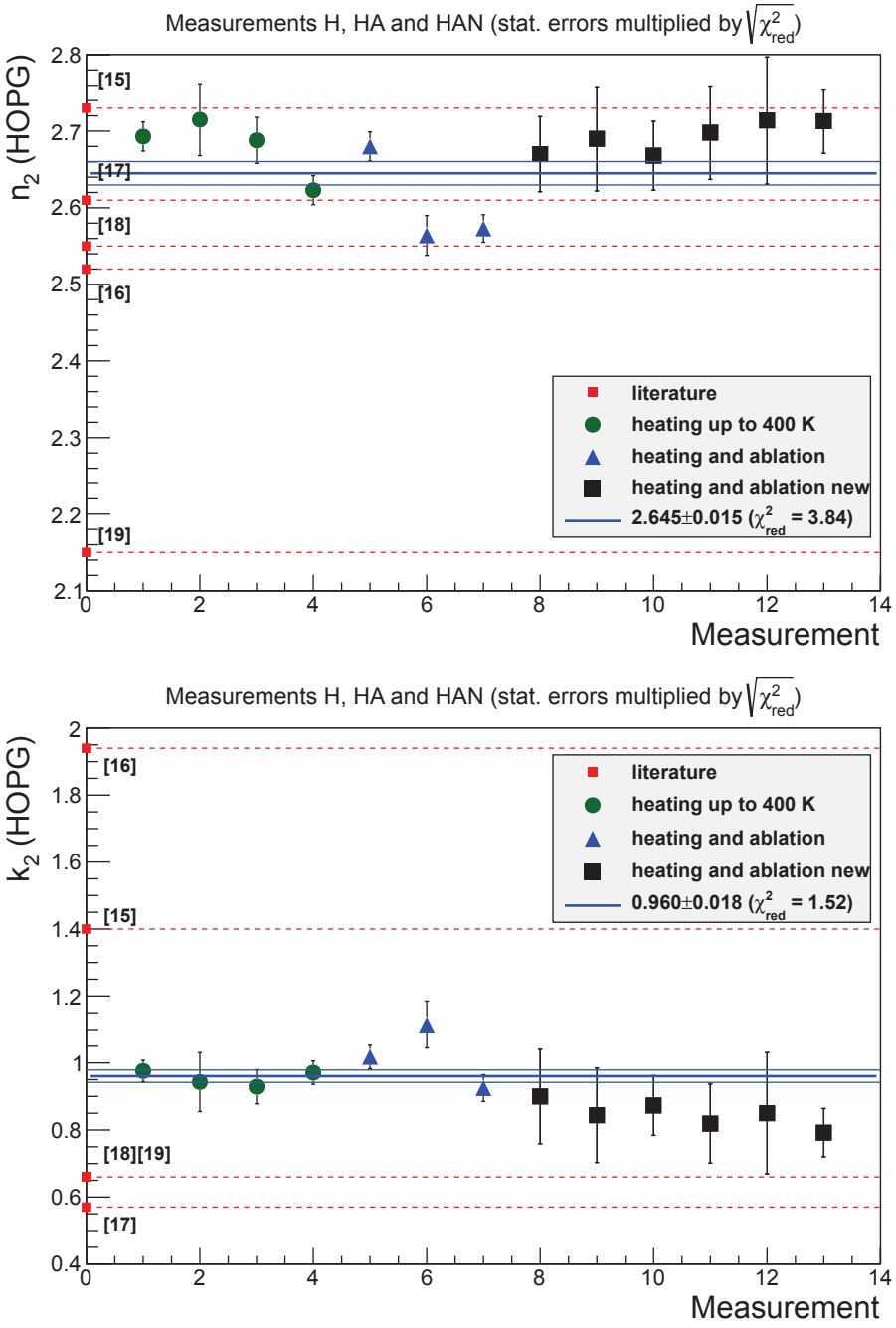

Figure 93: The index of refraction n_2 (top panel) and the extinction coefficient k_2 (bottom panel) of HOPG were determined by PC ellipsometry after different methods of cleaning the substrate were applied. The dashed lines denote the values found in literature [Gre69, Jel07, Taf65, Ber70, Erg67]. The solid blue lines show the mean value obtained from a fit to all measurements and the corresponding one sigma errors. The uncertainties of this average were obtained by scaling the fit error with $\sqrt{\chi^2_{\text{red}}}$

the top layers is drastically reduced. Hence it is not easy to distinguish between those two effects.

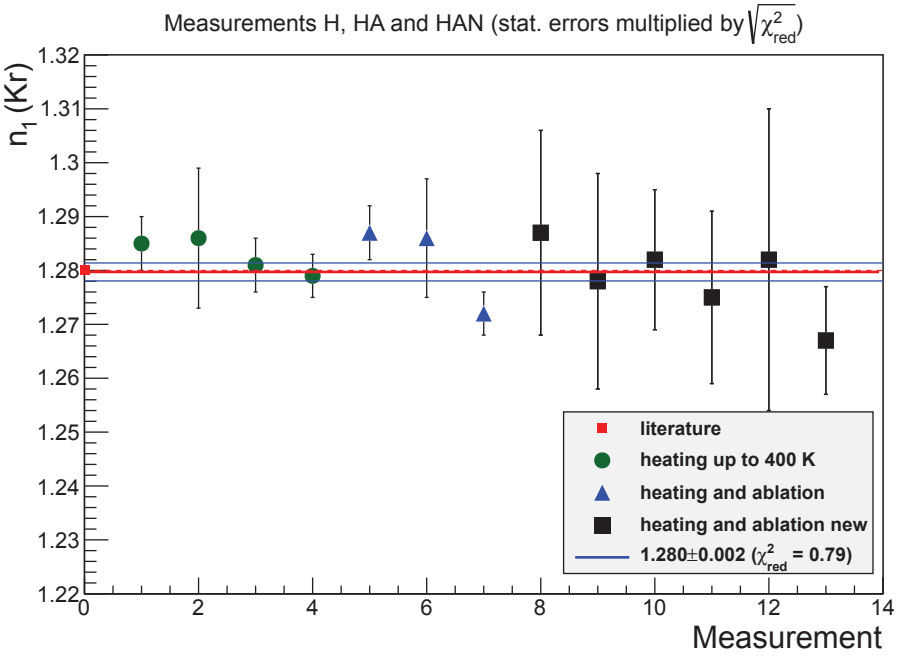

Figure 94: The index of refraction n_1 of the condensed krypton film determined by PC ellipsometry after different methods of cleaning the substrate were applied. The dashed line denote the values of Kruger [Kru59]. The solid blue lines shows the mean value obtained from a fit to all measurements and the corresponding one sigma errors. The uncertainty of this average was obtained by scaling the fit error with $\sqrt{\chi^2_{\text{red}}}$.

Table 7.1: Refractive indices of krypton $N_1 = n_1$ and the HOPG substrate $N_2 = n_2 - ik_2$. The second column gives the results from PC ellipsometry measurements at $T = 23$ K (the error is the quadratic sum of statistic and systematic error). The third column presents a range of literature values.

refractive index	this work	literature (table 7.2)
n_1	1.282 ± 0.008	1.28*
n_2	2.645 ± 0.030	2.15–2.73
k_2	0.964 ± 0.037	0.57–1.94

*For the refractive index of krypton k_1 only the results of Kruger [Kru59] are shown because it is also measured with quench condensed films.

The results show a reasonable agreement of our measured optical refractive indices for krypton and HOPG with values reported in the literature (see column 3 of table 7.1).

The values listed in table 7.2 yielding the ranges $n_2 = 2.15 - 2.73$ and $k_2 = 0.57 - 1.94$ (see table 7.1). For the refractive index of krypton k_1 only the results of Kruger [Kru59] are shown because most of the other values in literature are not measured with quenched condensed films and thus lead to different results. As already mentioned the krypton film might be porous and this might lead to a lower index of refraction. The values obtained

Table 7.2: Literature values for n_2 and k_2 of HOPG.

n_2	k_2	literature
2.73	1.40	(at 633 nm) [Gre69]
2.52	1.94	(at 546 nm) [Jel07]
2.61	0.57	(at 633 nm) [Taf65]
2.55	0.66	(at 633 nm) [Ber70]
2.15	0.66	(at 541 nm) [Erg67]

from different methods e.g. measurements with refractometers lead to an index of refraction of $n_1 = 1.375$ [Sin80].

7.6 Summary of the novel ellipsometry variant

A new variant of ellipsometry was presented, which is dubbed PC ellipsometry since the polarizer and the compensator are rotated to find the intensity minimum, where the analyzer behind the substrate remains at a fixed angle. This method allows a simple polarisation analysis close to the substrate even at cryogenic temperatures inside a vacuum chamber. The determined optical constants of condensed krypton and of the HOPG substrate are consistent with literature values. Also the determination of thicknesses of condensed krypton films up to 3000 Å was possible. The results show that PC ellipsometry can reach accuracies similar to that of standard PA ellipsometry. To use the same evaluation tools as for PA ellipsometry a transformation of the intensity minima $(P_\mathrm{m}, C_\mathrm{m})$ of PC ellipsometry into $\tilde{P}\tilde{A}$ coordinates was done.

Due to the temperature of 77 K at the site of operation inside a superconducting split-coil magnet (at CPS) the use of vacuum windows with direct sight onto the substrate is impossible. This new method will be used to carry out the polarisation analysis inside the set-up. The incoming polarized laser beam will be guided by one or two mirrors onto the substrate. The mirrors will be placed behind the polarizer and the compensator onto the substrate. It should be noted that in general dielectric mirror coating do influence the polarisation state of any incident light beam. However, for the high-precision mirrors (Laseroptik 11028J1) it was found in [Weg10], that these particular coatings preserved a defined polarization state and within the diploma thesis of D. Spitzer it was proven that accurate PA and PC ellipsometry via these mirrors are possible [Spi11].

Chapter 8

Conclusion and outlook

Since neutrino oscillation experiments showed that the neutrinos are not massless several experiments try to determine their mass. Different approaches were made with neutrinoless double β-decay experiments which assumes the neutrino to be a Majorana particle. Also cosmological constraints can give limits on the sum of all neutrino masses but they are dependent on the chosen model. A direct and model independent way to determine the average electron neutrino mass (m_{ν_e}) is to measure the β-decay spectrum in its endpoint region. Choosing tritium as β-emitter in combination with an electric retarding spectrometer of the MAC-E filter type provides the lowest upper limits for the neutrino mass measured in laboratory experiments up to now. These values are about 2 eV and were measured independently in Mainz and Troitsk. In order to improve the recent sensitivity by one order of magnitude the experiment has to be improved by two orders of magnitude, because the measured value is the squared neutrino mass.

This will be realized by the **KA**rlsruhe **TRI**tium **N**eutrino experiment (KATRIN) which will measure the neutrino mass with a sensitivity of 200 meV. KATRIN will measure the energy of β-decay electrons emitted in a **W**indowless **G**aseous **T**ritium **S**ource (WGTS) with the help of a tandem set-up of MAC-E filter spectrometers. The tritium flux coming from the source will be reduced by a factor 10^{14} utilizing a combination of differential and cryogenic pumping. The main spectrometer is equipped with a double-layer wire electrode system. This system is split up into rings and allows the electric field shaping. By applying a more negative potential to the electrode compared to the vessel, secondary electrons generated by cosmic muons and radiative materials in the vessel wall can be efficiently reduced.

The electrode system is supplied by up to 48 different voltages. These voltages are provided by a high voltage distribution rack, which is connected to the potential of the vessel. The distribution between the power supplies and the electrode system can be set via a patch board, which allows to put multiple electrode segments onto the same electric potential. In order to check the integrity of the wire electrode system an automated capacitance measurements system was installed. This system allows to measure the capacitance of each wire electrode segment via the charge time method. This system is now fully installed and first measurements were carried out. The measurement and analysis is being optimized and will be ready by the end of 2013.

The retarding voltage will be measured and monitored with a redundant system consisting of two custom made high precision voltage divider and a third MAC-E filter (monitor spectrometer), which measures the line position of ion implanted ^{83}Rb/^{83m}Kr sources.

Two high precision voltage dividers were developed in cooperation with the **P**hysikalisch **T**echnische **B**undesanstalt Braunschweig (PTB) in order to fulfill the requirements for the KATRIN experiment. These voltage dividers are designed to measure DC voltages of up to 35 kV (K35) and 65 kV (K65) with an absolute accuracy of 2 ppm, which ranks them among the most precise and most stable (0.1 ppm/month) high voltage dividers in the world. The main component of both dividers is a precision divider chain consisting of 100 (K35) and 165 (K65) high precision resistors selected and matched according to their **W**arm-**U**p **D**rift (WUD). By this the divider chain exhibit a negligible temperature dependence. This precision divider chain is placed between copper electrodes, which are connected via a second divider chain in order to ensure a homogeneous electric field surrounding the precision resistors (driven guard). This driven guard in combination with supporting structures with

high insulation resistances efficiently avoids corona discharges and reduces leakage currents. These voltage dividers also have negligible voltage and temperature dependence. With these specifications the KATRIN high voltage dividers exceed the KATRIN requirements (3 ppm over two months). The KATRIN dividers will again be calibrated at PTB in October 2013. This calibration will give more precise data on the time-dependent drift.

The KATRIN **Mo**nitor **S**pectrometer (MoS) utilizes the spectrometer of the former Mainz Neutrino Mass Experiment. This MAC-E filter will be connected to the same high voltage as the main spectrometer and measures the line position of the K-32 conversion electron line of ^{83m}Kr. The chosen sources are ion implanted ^{83}Rb/^{83m}Kr sources where ^{83}Rb is implanted into foils of noble metals. Two sources were investigated with the K35 divider at the MoS at **K**arlsruhe **I**nstitute of **T**echnology (KIT). The ^{83}Rb was implanted with 10 keV for the source Pt-10-1 and with 15 keV for the Pt-15-5. The data obtained in a measurement period from January 2012 to July 2012 were analyzed with three different methods (fitting of Voigt profile, Duniach-Sunjic line shape and by the cross correlation method). Both sources showed a different but linear drift which is for the Pt-10-1 about 1.5 ppm/month and for Pt-15-5 about 0.5 ppm/month. Since the drift is different for both sources, these drifts are most likely not caused by the work function of the spectrometer or by the high voltage divider but by the sources themselves. Additionally to the stability measurements of the K-32 line also the difference in measured energy of the L_3(9.4 keV) and L_3(32 keV) was measured and compared to the difference of gamma energies measured with gamma ray spectroscopy. The values obtained in this measurement phase with the help of the K35 divider are in good agreement with the values measured with gamma ray spectroscopy. This measurement can also be used in order to detect a malfunction like a broken resistor of one of the KATRIN dividers. After the calibration phase in 2013 at PTB the K35 divider will be shipped to KIT to measure new ion implanted calibration electron sources at the KATRIN **Mo**nitor **S**pectrometer (MoS). This new sources are produced at Bonn University.

An additional calibration source, which also makes use of conversion electrons of ^{83m}Kr, is the **C**ondensed **Kr**ypton **S**ource (CKrS). For this source the ^{83m}Kr is condensed onto a **H**ighly **O**rdered **P**yrolytic **G**raphite (HOPG). This source will be inserted into the **C**ryogenic **P**umping **S**ection (CPS) to measure transmission properties of the spectrometer and to calibrate the KATRIN experiment detector pixel by detector pixel. To ensure high reproducibility and stability the surface of the HOPG is cleaned by a combination of heating and laser ablation. The latter makes use of the high difference in thermal conductivity in-plane and along the c-axis of HOPG. The surface cleanliness is monitored by means of laser ellipsometry. With this method properties of thin solid films, like index of refraction and film thickness, can be determined by analysing the state of polarisation of a laser beam reflected at the optical system. The CKrS will be disassembled and rebuild according to the new design in 2013 and 2014. After a commissioning phase in Münster the set-up will be installed at the CPS in the KATRIN hall at KIT.

Due to technical constraints at the CPS the reflected beam of the ellipsometry laser either has to be guided over a distance of 2 m or analyzed inside the ultra high vacuum at cryogenic temperatures. Since the optical properties of the HOPG do not allow a long guidance of the reflected beam because of beam divergence, a new ellipsometry variant with polarization

analysis inside an ultra-high vacuum chamber at cryogenic temperatures has been established and tested. This variant rotates the polarizer and compensator (quarter-wave plate) and the analyzer remains at a fixed angle inside the vacuum chamber (PC ellipsometry). Because the minima in light intensity are rather flat, also a new method of minima search has to be applied for the PC ellipsometry. Thus the PC-plane was scanned in an area of $\pm 10^\circ$ ($\pm 7.5^\circ$) with a typical step size of 1° (0.25°). This data were fitted with a rotated paraboloid in order to obtain the minimal intensity $(P_\mathrm{m}, C_\mathrm{m})$. This minimum, its corresponding errors $(\Delta P_\mathrm{m}, \Delta C_\mathrm{m})$ and the correlation coefficient (ρ) were transformed into new coordinates $(\tilde{P}_\mathrm{m}, \tilde{A}_\mathrm{m}, \Delta\tilde{P}_\mathrm{m}, \Delta\tilde{A}_\mathrm{m}, \tilde{\rho})$ to make use of the existing programs for the analysis of the ellipsometry data. With this new ellipsometry variant it was possible to obtain the optical constants of the system under investigation (three-layer system of HOPG (substrate), krypton (film) and vacuum (ambient)) which are in good agreement with the values found in literature.

With the methods presented in this work it is possible to monitor the retarding potential of the KATRIN main spectrometer with a precision of:

$$\frac{\Delta U}{U} \leq 3\,\mathrm{ppm}\,,$$

for a KATRIN measurement and analysis run of 2 month. This monitoring precision corresponds to an uncertainty in the squared neutrino mass of:

$$\Delta m_\nu^2 \leq 0.0075\,\mathrm{eV}^2$$

These strict requirements are even exceeded by the KATRIN high voltage dividers by one order of magnitude.

Bibliography

[Aba11] K. Abazajian, E. Calabrese, A. Cooray *et al.* *Cosmological and astrophysical neutrino mass measurements.* Astroparticle Physics, **35(4)**, (2011), pp. 177 – 184. URL http://dx.doi.org/http://dx.doi.org/10.1016/j.astropartphys.2011.07.002.

[Ack13] K.-H. Ackermann *et al.* *The Gerda experiment for the search of* $0\nu\beta\beta$ *decay in* ^{76}Ge. The European Physical Journal C, **73(3)**, (2013), pp. 1–29. URL http://dx.doi.org/10.1140/epjc/s10052-013-2330-0.

[Alm10] J. Alme *et al.* *The ALICE TPC, a large 3-dimensional tracking device with fast readout for ultra-high multiplicity events.* Nucl. Instr. Meth. A, **622**, (2010), p. 316.

[Ase00] V. Aseev *et al.* *Energy loss of 18 keV electrons in gaseous* T_2 *and quench condensed* D_2 *films.* Eur. Phys. J. D, **10**, (2000), pp. 39–52.

[Aug12] M. Auger *et al.* *The EXO-200 detector, part I: detector design and construction.* Journal of Instrumentation, **7(05)**, (2012), p. P05010.

[Azz87] R. M. A. Azzam and N. M. Bashara. *Ellipsometry and polarized light.* (Elsevier), 1987.

[Bab12] M. Babutzka *et al.* *Monitoring of the operation paramters of the KATRIN Windowless Gaseous Tritium Source.* New Journal of Physics, **14**, (2012), p. 103046. URL http://dx.doi.org/10.1088/1367-2630/14/10/103046.

[Bau09] S. Bauer. *Aufbau und Inbetriebnahme des zweiten Präzisions-Hochspannungsteilers bis 65kV für das KATRIN-Experiment.* Diploma thesis, University of Münster, 2009.

[Bau13a] S. Bauer and O. Rest. *Capacitance of the wire electrode.* internal report, 2013.

[Bau13b] S. Bauer *et al.* *Ellipsometry with polarisation analysis at cryogenic temperatures inside a vacuum chamber.* arXiv:1307.5879 [physics.optics].

[Bau13c] S. Bauer *et al.* *The second KATRIN high precision voltage divider for voltages up to 65kV.* arXiv:1309.4955 [physics.ins-det].

[Bau14] S. Bauer, M. Schmidt, O. Rest *et al.* *Calibration of ultra-precise high voltage dividers on the ppm-level.* in prep.

[Bea61] Beaumont *et al.* *Thermodynamic Properties of Krypton. Vibrational and Other Properties of Solid Argon and Solid Krypton.* Proc. Phys. Soc., **78(6)**, (1961), pp. 1462–1481.

[Bea80] G. Beamson *et al.* *The collimating and magnifying properties of a superconducting field photoelectron spectrometer.* J. Phys. E, **13(1)**, (1980), pp. 64–66.

[Bec03] M. Beck *et al.* *WITCH: a recoil spectrometer for weak interaction and nuclear physics studies.* Nucl. Instrum. Meth. A, **503**, (2003), p. 567.

[Bec13] M. Beck *et al.* *An angular selective electron source for the KATRIN experiment.* in prep.

[Ber70] M. Berman, H. Kerchner and S. Ergun. *Determination of the Optical Properties of Absorbing Uniaxial Crystals from Reflectance at Oblique Incidence.* J. Opt. Soc. Am., **60**, (1970), pp. 646–648.

[Ber12] J. Beringer *et al.* *Particle Data Group Booklet.* Phys. Rev. D, **86**, (2012), p. 010001.

[Bla13] K. Blaum *et al.* *The Electron Capture ^{163}Ho Experiment ECHo.* arXiv:1306.2655 [physics.ins-det].

[Bot12] R. Bottesch. *Set-up of the motion control and characterization of the ablation laser for the condensed ^{83m}Kr conversion electron source of the KATRIN experiment.* Diploma thesis, University of Münster, 2012.

[Cam01] J. Campbell and T. Papp. *Widths of the Atomic K–N7 Levels.* Atom. Data Nucl. Data, **77(1)**, (2001), pp. 1–56.

[Cha14] J. Chadwick. *Intensitätsverteilung im magnetischen Spektrum der β-Strahlen von Radium B+C.* Verh. d. Deutsch. Phys. Ges., (pp. 383–391).

[Cha32] J. Chadwick. *The Existance of an Neutron.* Proc. R. Soc. London, **136(830)**, (1932), pp. 692–708.

[Che08] M. C. Chen. *The SNO+ Experiment.* arXiv:0810.3694 [hep-ex].

[Cow56] C. L. Cowan, F. Reines *et al.* *Detection of the Free Neutrino: a Confirmation.* Science, **124(3212)**.

[Dav96] R. Davis. *A Review of Measurements of the solar neutrino flux and their variation.* Nuclear Physics B, **48**, (1996), pp. 284–298.

[Don70] S. Doniach and M. Sunjic. *Many-electron singularity in X-ray photoemission and X-ray line spectra from metals.* Journal of Physics C: Solid State Physics, **3(2)**, (1970), p. 285. URL http://stacks.iop.org/0022-3719/3/i=2/a=010.

[DP10] C. K. D. Pattarakijkul and A. Charoensook. *Construction and evaluation of 100kV DC high voltage divider.* In *Conference on Precision Electromagnetic Measurements*, (pp. 677–679) (2010).

[Dre13] G. Drexlin, V. Hannen, S. Mertens *et al.* *Current Direct Neutrino Mass Experiments.* Advances in High Energy Physics, **2013**, (2013), p. 39. URL http://dx.doi.org/http://dx.doi.org/10.1155/2013/293986.

[Dun07] J. A. Dunmore. *Pixelation-Dependence of Transmission Function.* Technical report, KATRIN internal document, 2007.

[Erg67] S. Ergun. *Determination of Longitudinal and Transverse Optical Constants of Absorbing Uniaxial Crystals–Optical Anisotropy of Graphite.* Nature, **213**, (1967), pp. 135–136.

[Erh15] M. Erhard. *in preperation.* Ph.D. thesis, Karlsruher Intitut für Technologie, expected 2015.

[Fer34] E. Fermi. *Versuch einer Theorie der β-Strahlen.* Z. Phys., **88**, (1934), pp. 161–177.

[Fis12] S. Fischer *et al.* *Monitoring of tritium purity during long-term circulation in the KATRIN test experiment LOOPINO using laser Raman spectroscopy.* arXiv:1208.1605 [physics.ins-det]. URL http://arxiv.org/abs/1208.1605.

[Fis14] S. Fischer. *in preperation.* Ph.D. thesis, KIT, expected 2014.

[Flu83] Fluke Cooperation. *Fluke 752A Reference Divider instruction manual*, rev. 1 4/84 edition, 1983.

[Frä10] F. Fränkle. *Background Investigations of the KATRIN Pre-Spectrometer.* Ph.D. thesis, KIT, 2010.

[Fuk98] Y. Fukuda *et al.* ((Super-Kamiokande Collaboration)). *Evidence for Oscillation of Atmospheric Neutrinos.* Phys. Rev. Lett., **81**, (1998), pp. 1562–1567. URL http://dx.doi.org/10.1103/PhysRevLett.81.1562.

[Gan12] A. Gando *et al.* (KamLAND-Zen Collaboration). *Measurement of the double-*β *decay half-life of ^{136}Xe with the KamLAND-Zen experiment.* Phys. Rev. C, **85**, (2012), p. 045504. URL http://dx.doi.org/10.1103/PhysRevC.85.045504.

[Gil10] W. Gil *et al.* *The Cryogenic Pumping Section of the KATRIN Experiment.* IEEE TRANSACTIONS ON APPLIED SUPERCONDUCTIVITY, **20(3)**, (2010), pp. 316–319.

[Gou10] J. D. Goullon. *Installation and commissioning of the monitor spectrometer of KATRIN.* Diploma thesis, Karlsruher Institut für Technologien, 2010.

[Gre69] D. L. Greenway and G. Harbeke. *Anisotropy of the Optical Constants and the Band Structure of Graphite.* Phys. Rev., **178**, (1969), pp. 1340–1348.

[Gre12] B. Grees. *Verbesserung der Nullellipsometrie bei festem Analysatorwinkel für das KATRIN-Experiment.* Diploma thesis, University of Münster, 2012.

[Gro13] S. Grohmann, T. Bode, M. Hötzel *et al.* *The thermal behaviour of the tritium source in KATRIN.* Cryogenics, **55–56(0)**, (2013), pp. 5 – 11. URL http://dx.doi.org/10.1016/j.cryogenics.2013.01.001.

[Hah24] O. Hahn and L. M. (1924). *Das β-Strahlenspektrum von Radium und seine Deutung.* Z. Phys., **(26)**, (1924), pp. 161–168.

[Hea91] O. S. Heavens. *Otical propertiers of thin solid films.* (Dover Publications, New York), 1991.

[Her10] A. Herlert. *The ISOLDE facility.* Nuclear Physics News, **20(4)**, (2010), pp. 5–12.

[Hil11] B. Hillen. *Untersuchung von Methoden zur Unterdrückung des Spektrometeruntergrunds beim KATRIN Experiment.* Ph.D. thesis, University of Münster, 2011.

[Hoc08] F. Hochschulz. *Weiterentwicklung der Präzisions-Hochspannungs-Messung für das KATRIN-Experiment.* Diploma thesis, University of Münster, 2008.

[Hug08] K. Hugenberg. *Design of the electrode system for the KATRIN main spectrometer.* Diploma thesis, 2008.

[Iss83] J. P. Issi, J. Heremans and M. S. Dresselhaus. *Electronic and lattice contributions to the thermal conductivity of graphite intercalation compounds.* Phys. Rev. B, **27**, (1983), pp. 1333–1347.

[Jel07] G. E. Jellison, J. D. H. Jr and H. N. Lee. *Measurement of optical functions of highly oriented pyrolytic graphite in the visible.* Phys. Rev. B, **76**, (2007), p. 085125.

[Kas04] J. Kaspar *et al. Effect of energy scale imperfections on results of neutrino mass measurements from β-decay.* Nucl. Instr. and Meth., **A527**, (2004), pp. 423–431.

[Kay08] B. Kayser. *Neutrino mass, mixing and flavor change.* Particle data group booklet Chapter 13.

[KC04] KATRIN-Collaboration. *KATRIN Design Report 2004.*

[Kit05] C. Kittel. *Einführung in die Festkörperphysik.* (Oldenbourg Wissenschaftsverlag), 2005.

[Kni93] R. B. D. Knight and P. Martin. *A high voltage divider having an uncertainty of 5 ppm at 100 kV.* IEEE Trans. Instrum. Meas., **42**, (1993), pp. 568–570.

[Kod01] K. Kodama, N. Ushida, C. Andreopoulos *et al. Observation of tau neutrino interactions.* Physics Letters B, **504(3)**, (2001), pp. 218 – 224. URL http://dx.doi.org/http://dx.doi.org/10.1016/S0370-2693(01)00307-0.

[Kos12] A. Kosmider. *Tritium Retention Techniques in the KATRIN Transport Section and Commissioning of its DPS2-F Cryostat.* Ph.D. thesis, Karlsruher Intitut für Technologie, 2012.

[Kra05] C. Kraus, B. Bornschein, L. Bornschein *et al. Final Results from phase II of the Mainz Neutrino Mass Search in Tritium β Decay.* Eur. Phys. J., **40**, (2005), pp. 447–468. URL http://dx.doi.org/10.1140/epjc/s2005-02139-7.

[Kri11] A. Krieger *et al. Calibration of the ISOLDE acceleration voltage using a high-precision voltage divider and applying collinear fast beam laser spectroscopy.* Nucl. Instrum. Meth. A, **632**, (2011), p. 23.

[Kru59] J. Kruger and W. Ambs. *Optical Measurements on Thin Films of Condensed Gases at Low Temperatures.* J. Opt. Soc. Am., **49**, (1959), pp. 1195–1198.

[Leb10] M. Leber. Ph.D. thesis, University of Washington, 2010.

[Led62] L. M. Lederman, M. Schwartz, J. Steinberger *et al.* *Observation of high-energy neutrino reactions and the existence of two kinds of neutrinos.* Phys. Rev. Lett., **9(1)**, (1962), pp. 36–44.

[Li03] Y. Li and R. Marx. *Comparison of two ultra-precision DC high voltage dividers developed at PTB and NML.* In *XIIIth International Symposium on High Voltage Engineering* (2003).

[Li11] Y. Li. *Development of Precision DC High-Voltage Dividers.* IEEE Trans. Instrum. Meas., **60(7)**, (2011), pp. 2211–2216. URL http://dx.doi.org/10.1109/TIM.2010.2100655.

[Lob85] V. Lobashev and P. Spivak. *A METHOD FOR MEASURING THE ELECTRON ANTINEUTRINO REST MASS.* Nuclear Instruments and Methods in Physics Research, **A240**, (1985), pp. 305–310.

[Lob03] V. Lobashev. *The search for the neutrino mass by direct method in the tritium beta-decay and perspectivees of study it in the project KATRIN.* Nuclear Physics A, **719**, (2003), pp. 153–160.

[Mar01] R. Marx. *New Concept of PTBs Standard Divider for Direct Voltages of up to 100kV.* IEEE Transactions on instrumentation and measurement, **50(2)**, (2001), pp. 426–429.

[Mei24] L. Meitner. *Über die Rolle der γ-Strahlen beim Atomzerfall.* Z. Phys., **26**, (1924), pp. 169–177.

[Mer09] A. Merev and O. Kalenderli. *The construction of a DC high voltage precision divider.* Journal of Electrostatics, **67**, (2009), pp. 741–745.

[Mer12] S. Mertens, A. Beglarian, L. Bornschein *et al.* *Stochastic heating by ECR as a novel means of background reduction in the KATRIN spectrometers.* Journal of Instrumentation, **7(08)**, (2012), p. P08025. URL http://stacks.iop.org/1748-0221/7/i=08/a=P08025.

[Mon06] A. Monfardini *et al.* *The microcalorimeter arrays for a rhenium experiment (MARE): A next-generation calorimetric neutrino mass experiment.* Nuclear Instruments and Methods in Physics Research A, **559**, (2006), pp. 346–348.

[ORC] URL http://orca.physics.unc.edu/.

[Ost08] B. Ostrick. *Eine kondensierte ^{83m}Kr-Kalibrationsquelle für das KATRIN-Experiment.* Ph.D. thesis, University of Münster, 2008.

[Ott08] E. W. Otten and C. Weinheimer. *Neutrino mass limit from tritium β decay.* Reports on Progress in Physics, **71(8)**, (2008), p. 086201.

[Par] D. S. Parno *et al.* *Prototype focal-plane detector system for the KATRIN experiment.* in prep.

[Par62] J. H. Park. *Special shielded resistor for high-voltage DC measurements.* NBS J. Res., **66C**, (1962), pp. 19–24.

[Pau30] W. Pauli. *letter to a local meeting on radioactivity at Tübingen, Germany (dated December 4, 1930).* R. Kronig and V. Weisskopf, Eds., 1930.

[Phi12] D. G. Phillips *et al.* *The MAJORANA experiment: an ultra-low background search for neutrinoless double-beta decay.* Journal of Physics: Conference Series, **381(1)**, (2012), p. 012044. URL http://stacks.iop.org/1742-6596/381/i=1/a=012044.

[Pic92a] A. Picard, H. Backe, J. Bonn *et al.* *Precision measurement of the conversion electron spectrum of ^{83m}Kr with a solenoid retarding spectrometer.* Zeitschrift für Physik A Hadrons and Nuclei, **342(1)**, (1992), pp. 70–78. URL http://dx.doi.org/10.1007/BF01294491.

[Pic92b] A. Picard *et al.* *A solenoid retarding spectrometer with high resolution and transmission for keV electrons.* Nucl. Instr. Meth., **B63**, (1992), pp. 345–358.

[Pot90] H. Poth. *Electron Cooling: Theory, Experiment, Application.* Phys. Rep., **196**, (1990), p. 135.

[Pra11] M. Prall. *Background Reduction of the KATRIN Spectrometers: Transmission Function of the Pre-Spectrometer and Systematic Test of the Main-Spectrometer Wire Electrode.* Ph.D. thesis, University of Münster, 2011.

[Res13] O. Rest. *in preperation.* Master's thesis, University of Münster, 2013.

[Rob88] R. G. H. Robertson and D. A. Knapp. *Direct measurements of neutrino mass.* Ann. Rev. Nucl. Part. Sci., **38**, (1988), pp. 185–215.

[Rös78a] F. Rösel, H. Fries, K. Alder *et al.* *Internal conversion coefficients for all atomic shells.* Atomic Data and Nuclear Data Tables, **21(2–3)**, (1978), pp. 91 – 289. URL http://dx.doi.org/http://dx.doi.org/10.1016/0092-640X(78)90034-7.

[Rös78b] F. Rösel, H. Fries, K. Alder *et al.* *Internal conversion coefficients for all atomic shells.* Atomic Data and Nuclear Data Tables, **21(4–5)**, (1978), pp. 291 – 514. URL http://dx.doi.org/http://dx.doi.org/10.1016/0092-640X(78)90009-8.

[Ros10] S. Rosendahl. *Präzisionshochspannung für das KATRIN-Experiment.* Diploma thesis, University of Münster, 2010.

[SC00] SNO-Collaboration. *The Sudbury Neutrino Observatory.* Nuclear Instruments and Methods in Physics Research A, **449**, (2000), pp. 172–207.

[SC07] SNO-Collaboration. *Determination of the ν_e and Total ^8B Solar Neutrino Fluxes with the Sudbury Neutrino Observatory Phase I Data Set.* Phys. Rev. C, **75**, (2007), p. 045502.

[Sch11] T. Schäfer. *Aufbau eines automatisierten Gassystems für die kondensierte ^{83m}Kr-Kalibrationsquelle des KATRIN-Experiments.* Diploma thesis, University of Münster, 2011.

[Sim12] L. Simard and the Nemo-3 collaboration. *The NEMO-3 results after completion of data taking.* Journal of Physics: Conference Series, **375(4)**, (2012), p. 042011. URL http://stacks.iop.org/1742-6596/375/i=4/a=042011.

[Sin80] A. C. Sinnock. *Refractive indices of the condensed rare gases, argon, krypton and xenon.* J. Phys. C: Solid State Phys., **13**, (1980), pp. 2375–2391.

[Sle11a] M. Slezak. *Fit program of the KATRIN Monitor sectrometer User's manual*, 3rd edition, 2011.

[Sle11b] M. Slezak. *The source of monoenergetic electrons for the monitoring of spectrometer in the KATRIN neutrino experiment.* Diploma thesis, 2011.

[Sle12] M. Slezák, D. Vénos, O. Lebeda *et al. Precise energy of the 9.4 keV gamma transition observed in the 83Rb decay.* The European Physical Journal A, **48(2)**, (2012), pp. 1–9. URL http://dx.doi.org/10.1140/epja/i2012-12012-y.

[Sle13] M. Slezak, S. Bauer, O. Dragoun *et al. Description of conversion electron line shape from implanted ^{83m}Kr in terms of the Doniach-Sunjic asymmetrical function.* in prep.

[Sle15] M. Slezák. *in preperation.* Ph.D. thesis, 2015.

[Spe] S. A. Speakman. *Introduction to High Resolution X-Ray Diffraction of Epitaxial Thin Films.* URL http://prism.mit.edu.

[SPI] URL http://www.2spi.com/catalog/new/hopgsub.php.

[Spi11] D. Spitzer. *Alternative Ellipsometrie-Varianten bei kryogenen Temperaturen für das KATRIN-Experiment.* Diploma thesis, University of Münster, 2011.

[Ste13] N. Steinbrink *et al. Neutrino mass sensitivity by MAC-E-Filter based time-of-flight spectroscopy with the example of KATRIN.* arXiv:1308.0532 [physics.ins-det].

[Stu11] M. Sturm. *Status of the KATRIN experiment with special emphasis on source-related issues.* arXiv:1111.4773 [hep-ex]. URL http://arxiv.org/abs/1111.4773.

[Taf65] E. A. Taft and H. R. Philipp. *Optical Properties of Graphite.* Phys. Rev., **138**, (1965), pp. 197–202.

[Tay66] R. Taylor. *The thermal conductivity of pyrolytic graphite.* Philosophical Magazine, **13(121)**, (1966), pp. 157–166. http://www.tandfonline.com/doi/pdf/10.1080/14786436608211993, URL http://dx.doi.org/10.1080/14786436608211993.

[Tch13] D. Tcherniakhovski. *FLT V4 User Manual.* KATRIN, 3rd edition, 2013.

[Thü07] T. Thümmler. *Präzisionsüberwachung und Kalibration der Hochspannung für das KATRIN-Experiment.* Ph.D. thesis, University of Münster, 2007.

[Thü08] T. Thümmler. *Schematic overview KATRIN high voltage.* used in different presentations, 2008.

[Thü09] T. Thümmler, R. Marx and C. Weinheimer. *Precision high voltage divider for the KATRIN experiment.* New J. Phys., **11**, (2009), p. 103007.

[Väi76] S. Väisälä, G. Graeffe, J. Heinonen *et al. Levels of* ^{83}Kr *populated in the decay of* ^{83}Rb *and* ^{83}Br. Phys. Rev. C, **13**, (1976), pp. 372–376. URL http://dx.doi.org/10.1103/PhysRevC.13.372.

[Val09] K. Valerius. *Spectrometer-related background processes and their suppresion in the KATRIN experiment.* Ph.D. thesis, University of Münster, 2009.

[vB10] O. von Baeyer and O. Hahn. *Magnetische Linienspektren von P-Strahlen.* Phys. Z., **11**, (1910), pp. 488–493.

[Ven06] D. Venos, O. Dragoun, A. Spalek *et al. Precise energy of the weak 32-keV gamma transition observed in* ^{83m}*Kr decay.* Nuclear Instruments and Methods in Physics Research, **A(560)**, (2006), pp. 352–359.

[VIS07] VISHAY. *Hermetically Sealed High Precision Bulk Metal ©Foil Technology Resistors.* Data sheet, 2007.

[Weg10] A. Wegmann. *Laserellipsometrie für die kondensierte* ^{83m}*Kr-Konversionselektronenquelle des KATRIN-Experiments.* Diploma thesis, University of Münster, 2010.

[Wei03] C. Weinheimer. *Laboratory limits on neutrino masses.* in G. Altarelli and K. Winter (Eds.) Neutrino masses (Springer), 2003.

[Wei10] C. Weinheimer. *Neutrino oscillations with a polarized laser beam: An analogical demonstration experiment.* Progress in Particle and Nuclear Physics, **64(2)**, (2010), pp. 205 – 209. Neutrinos in Cosmology, in Astro, Particle and Nuclear Physics, International Workshop on Nuclear Physics, 31st course, URL http://dx.doi.org/10.1016/j.ppnp.2009.12.011.

[Wei13] C. Weinheimer and K. Zuber. *Neutrino masses.* Annalen der Physik, **525(8-9)**, (2013), pp. 565–575. URL http://dx.doi.org/10.1002/andp.201300063.

[Wol09] J. Wolf. *Size Matters: The Vacuum System of the KATRIN Neutrino Experiment.* Journal of the Vacuum Society of Japan, **52(5)**, (2009), pp. 278–284.

[Wu57] C. S. Wu, E. Ambler, R. W. Hayward *et al. Experimental Test of Parity Conservation in Beta Decay.* Phys. Rev., **105**, (1957), pp. 1413–1415. URL http://dx.doi.org/10.1103/PhysRev.105.1413.

[Wüs13] S. Wüstling. *Discussion on high voltage post-regulation circuit.* private communication, 2013.

[Zac09] M. Zacher. *Electromagnetic design and field emission studies for the inner electrode system of the KATRIN main spectrometer.* Diploma thesis, University of Münster, 2009.

[Zac14] M. Zacher. *in preperation.* Ph.D. thesis, University of Münster, expected 2014.

[Zbo11] M. Zbořil. *Solid electron sources for the energy scale monitoring in the KATRIN experiment.* Ph.D. thesis, Westfälische Wilhelms-Universität Münster, 2011.

[Zbo13] M. Zbořil *et al. Ultra-stable implanted* $^{83}Rb/^{83}Kr$ *electron sources for the energy scale monitoring in the KATRIN experiment.* JINST, **8**. URL http://dx.doi.org/10.1088/1748-0221/8/03/P03009.

[Zim00] O. Zimmer *et al. aSpect – a new spectrometer for the measurement of the angular correlation coefficient a in neutron beta decay.* Nucl. Instrum. Meth. A, **440**, (2000), p. 548.